Search for Electroweak Supersymmetry in final states with three electrons or muons plus missing transverse momentum in $13\,\text{TeV}$ proton-proton collisions at the Large Hadron Collider with the ATLAS Detector

A thesis submitted to The University of Sussex
for the degree of
Doctor of Philosophy
(PhD)

Nicola Louise Abraham

Submitted: June 2018

US

**UNIVERSITY
OF SUSSEX**

Declaration

I hereby declare that this thesis has not been and will not be submitted in whole or in part to another University for the award of any other degree.

Nicola Louise Abraham

Abstract

Name of the university	The University of Sussex
Candidate name	Nicola Louise Abraham
Degree title	Doctor of Philosophy
Thesis title	Search for Electroweak Supersymmetry in final states with three electrons or muons plus missing transverse momentum in 13 TeV proton-proton collisions at the Large Hadron Collider with the ATLAS Detector.
Submission date	June 2018

A search for the electroweak production of charginos and neutralinos decaying into final states involving three electrons or muons is presented. The analysis is based on $36.1\,\mathrm{fb}^{-1}$ of $\sqrt{s} = 13\,\mathrm{TeV}$ proton–proton collisions recorded by the ATLAS detector at the Large Hadron Collider. Scenarios considered are based on simplified models with the associated production of the next-to-lightest neutralino and the lightest chargino, followed by their decays into final states with leptons and the lightest neutralino via either sleptons or Standard Model gauge bosons. No significant deviations from Standard Model expectations are observed and stringent limits at 95% confidence level are placed on the masses of relevant supersymmetric particles. For a massless lightest neutralino, masses up to $1.13\,\mathrm{TeV}$ are excluded for the associated production of the next-to-lightest neutralino and the lightest chargino, assuming slepton mediated decays, whereas for gauge-boson-mediated decays, masses up to $380\,\mathrm{GeV}$ are excluded.

Acknowledgements

Over the course of my PhD, countless people have done so much for me, and their support really made this thesis into what it is. Therefore, my deepest gratitude to all of you.

Foremost, I would like to thank my supervisor, Professor Antonella De Santo, for without your initial and continuing belief in me, I would not be here writing this. You have always supported me throughout my studies, giving both constructive criticism and valuable encouragement and guidance, which has all led me to where I am today. You are an incredibly inspirational person, in more ways than one. And I look forward to continuing to work with you in our quest to find SUSY! I would also like to thank my second supervisor, Fabrizio Salvatore, for always being a constant positive presence and coordinator within the EPP group.

A big thanks to Yusufu Shehu for being my mentor during the first few years (I'm sure I still owe you a beer for that), Nicky Santoyo who supported and guided me in the latter few years, and Fabrizio Trovato, who always managed to be available to work (even from your phone while on a night out in Geneva)! As for Kerim Suruliz, Giuseppe Lerner and Carlos Chavez Barajas, I thank you for always being so approachable, and providing constant computing assistance, no matter what unreasonable hour of the day.

I am also thankful for the influence of fellow peers, Zara Grout who was a library of information when I first started, Tina Potter for always emanating supportiveness, Sarah Williams for your ongoing support throughout the (still ongoing) publication of our analysis, and Batool Safarzadeh, who I am looking forward to working with in the future. Emma, Fabio, Tom, Giovannis, Mario and Mario, you made being at Sussex a pleasure.

Additionally, a big thank you to Fabrizio Miano for providing lots of office laughs (and teaching me many Italian swear words), Sam and Anne Jones for sharing many a beer in O'Brassuer, and Olly Winston for always offering a cup of tea, chat, and a well-deserved break. And, not least, Mark Sutton, who not only supported me in a big way academically throughout my qualification task, but was always there for a much needed drink in R1, and on a number of occasions to give me a (rather wobbly) lift home on the back of your bike!

I would also like to thank everyone who I shared my undergraduate years at the University of Kent with: Jamie Ryan, Danny Smith, Kieran Selvon, Martin Anslow,

Science cannot solve the ultimate mystery of nature. And that is because, in the last analysis, we ourselves are a part of the mystery that we are trying to solve.

- Max Planck

Preface

All the work in this thesis was performed during the four years of my PhD at the University of Sussex as a member of the ATLAS Collaboration. The ATLAS Collaboration comprises over 3,000 scientific authors from 182 institutions around the world, many of whom have implicitly contributed to this thesis, in some ways shaping the contents presented in it.

My main contributions to the advancement of science within the ATLAS Collaboration have been to search for evidence of new supersymmetric particles, known as charginos and neutralinos. I have worked as part of a team of around 20 analysts, with the bulk of this thesis being based on searches using $36.1\,\mathrm{fb}^{-1}$ of data recorded by ATLAS in 2015 and 2016. In these searches, I played a pivotal role in defining new kinematic signal regions that enhanced the discovery power, as well as having involvement in defining kinematic regions to validate Standard Model background modelling. Furthermore, I took a lead role in utilising the statistical analysis software framework to interpret results. I made similar earlier contributions to results based on the first $13.3\,\mathrm{fb}^{-1}$ of new data. The full analysis strategy and outcomes are presented in Chapters 5 and 6, respectively.

As an ATLAS author, I also have performed a technical task designed to maintain an aspect of the ATLAS detector, and the work is presented in Appendix A.

My early physics-analysis contribution to the collaboration, presented in Appendix B, was a study on the re-optimisation of new kinematic signal regions targeting the standard model $t\bar{t}V$ process, with the objective of constraining its production cross-section using increased collision energies at the Large Hadron Collider.

Contents

1. Introduction

Particle physics has come a long way since particles were considered to be solid, indivisible and indestructible spheres; particles are now seen as a constant flow of transformation and change. It is arguably the most abstract field in modern physics focusing on phenomena at imperceptible small scales only accessible by the most intricate and evermore complex devices known to humankind. With the Large Hadron Collider (LHC) at CERN providing a unique insight into this sub-atomic world of dynamical processes and interactions, experimental particle physics is at the forefront of modern physics and is a very exciting area of study. It is key to our endless curiosity of understanding the most fundamental questions, and is essential for our comprehension of the very early universe.

The Standard Model (SM) of elementary particle physics is one of the most successful theories in physics, providing a framework that describes known elementary particles and their interactions. Its establishment has been an ongoing development of work performed over the past half century, continually improving and extending by collaboratively standing on the shoulders of giants. The work presented in this thesis aims to contribute to the search for supersymmetry, an extension of the SM. It does this by building on previous results obtained using data from earlier data-taking periods at the LHC.

The most recent data-taking period at the LHC, known as LHC Run-II, began in 2015, delivering proton-proton collisions at a centre-of-mass energy of $\sqrt{s} = 13\,\text{TeV}$, almost twice the maximum energy of $8\,\text{TeV}$ that had been achieved in the previous data-taking period, known as LHC Run-I (2010-2012). This is the highest energy ever reached in human-made collisions of particles. At this increased collision energy, thanks to increased production cross-sections, supersymmetric particles, if they exist, are expected to be more accessible than ever.

This thesis presents searches for supersymmetry focusing on a range of supersymmetric scenarios, each producing exactly three electrons or muons plus high missing transverse momentum in the final state. Data recorded by ATLAS during 2015 and 2016 is used. The structure of this thesis is as follows. Chapter 2 begins by introducing the theoretical concepts, including a description of the SM of particle physics, as well as its shortcomings, in turn motivating the need for its extension, such as Supersymmetry, which is also discussed. It also provides a summary of the current experimental status of relevant theoretical scenarios. The experimental setup, namely the LHC and the ATLAS detector, are the topic of Chapter 3. Chapter 4

describes the event generation, detector simulation and physics object reconstruction methods used in this analysis of ATLAS data. The three-lepton final state search strategy that was performed is the subject of Chapter 5, including the choice of event samples, physics object definitions and preselections, an overview of signal region optimisation techniques, and the estimation of SM background processes and associated uncertainties. It also provides a discussion on the conventional methods used by the ATLAS Collaboration for the statistical interpretation of results. Chapter 6 gives details of the implementation of the analysis strategy and presents results and their interpretation. Finally, concluding remarks are presented in Chapter 7.

Natural units $\hbar = c = 1$ are used throughout this thesis.

2. Theory and Experimental Landscape

This chapter gives a brief overview of the theoretical framework required, in the context of this thesis, to describe *elementary particles* and the way they interact with matter via *forces*, where the forces are themselves described by the exchange of elementary particles. This includes a summary of the most successful theory in particle physics, the SM. The SM, developed in the 1960's and 1970's, predicts measurable quantities that have been verified experimentally to very high precision. However, the SM is not a complete theory and cannot account for certain known phenomena occurring at high energies, such as the unnaturalness of quantum corrections to the Higgs mass. Also, it only incorporates three of the fundamental forces, electromagnetic, weak and strong, while omitting the gravitational force. Consequently, a wide range of theories have been developed as extensions to the SM with the intention to resolve its shortcomings. One of the most accredited of these theories, *Supersymmetry* (SUSY), is the topic of this thesis.

Described in Section 2.3, SUSY postulates an additional symmetry between fermions and bosons that forecasts the existence of a set of heavier particles, giving rise to new physics phenomena at high energies. In addition to the theoretical background, an overview of recent experimental results relevant to provide a theoretical landscape for this thesis are provided.

2.1 The Standard Model of Particle Physics

The SM of particle physics [1] provides a unified picture to describe an array of distinct elementary particles and their interactions. It comprises three generations of fermions, four force-mediating gauge bosons, and the Higgs boson, all of which are distinguishable by intrinsic physical properties, such as mass, and other quantum numbers, which will be described in Section 2.1.1. SM particles are treated as point-like (i.e. without internal structure), arising from excitations in their corresponding quantum fields. A description of the three fundamental forces included in the SM is given in Section 2.1.2, with Section 2.1.2.4 dedicated to introducing the "Higgs Mechanism".

2.1.1 Elementary Particles

The intrinsic quantum property that distinguishes fermions from bosons is known as spin. Spin is measured in units of $\hbar$, where fermions take half-integer values and bosons take integer values. The gauge and Higgs bosons can be further categorised as either vector bosons (with spin equal to one), or scalar bosons (with spin equal to zero). A depiction of the SM particles is presented in Figure 2.1.

Fig. 2.1: An overview of elementary particles described by the SM, with twelve fermions arranged into three generations of matter particles, gauge bosons in the fourth column, and the Higgs boson in the fifth. The masses given are approximate only [2].

The concept of spin also introduces two further particle properties: helicity and chirality. Helicity is defined as the projection of spin on the particles momentum, which is denoted "right-handed" if in the same direction of momentum, or "left-handed" if in the opposite direction. The helicity of a massive particle can change depending on the inertial reference frame of the observer. Chirality is closely related to helicity, but is somewhat more of an abstract concept, being an intrinsic quantum property that describes the phase of a particle's wavefunction, which influences the particle's behaviour when it undergoes a complex rotation.

The four gauge bosons mediate three of the fundamental forces; the gluon and photon mediate the strong and electromagnetic forces, respectively, while the weak force is mediated by the W and Z bosons. All particles that experience the strong force have a physical property known as "colour charge", which is discussed in Section 2.1.2, while particles that experience the electromagnetic force carry the electric charge Q, measured in units of elementary charge $e = 1.602 \times 10^{-19}$ coulombs. Analogously, weak isospin T is the charge of the weak force. Table 2.1 summarises the properties of all bosons described by the SM.

Fermions are also subdivided into either quarks or leptons, depending on their couplings with gauge bosons, and subsequent interactions with the fundamental forces. Quarks, which can couple with all gauge bosons, experience all three forces, and possess colour, weak isospin and electric charge. They are the fundamental building blocks of all *hadronic* matter. Quarks also carry a quantum number known as a "baryon number" equal to $+1/3$. The generations of quarks are ordered in ascending values of mass, with the first generation consisting of the up and down quarks, the second generation consisting of strange and charm, and the third generation being the bottom and top quarks. An alternative mode of categorising quarks is by charge, denoting those with $Q = +2/3\,e$ as "up-type", and those with $Q = -1/3\,e$ as "down-type". Both baryon number and total electric charge of bound physical states must be integers, thus, imposing limitations on quark combinations. Table 2.2 summarises the properties of all quarks described by the SM.

Leptons have electric charge and weak isospin, but not colour, meaning that they cannot couple with gluons or experience the strong force. They are also ordered into three generations based on ascending mass: the electron e, muon μ, and tau τ. Each of the fore-mentioned has an associated lepton neutrino, which, due to having zero electric charge, only interact via the weak force. Leptons carry quantum numbers, designated the electron (L_e), muon (L_μ) and tau (L_τ) lepton numbers. Table 2.3 summarises the properties of all leptons described by the SM.

All particles have an associated antiparticle with the same mass but opposite electric

Type	Spin	Particle	Symbol	Mass [GeV]	Electric Charge [e]
Vector Bosons	1	Gluon	g	0	0
		Photon	γ	0	0
		W boson	W	80.385 ± 0.015	± 1
		Z boson	Z	91.1876 ± 0.0021	0
Scalar Bosons	0	Higgs	H	125.09 ± 0.24	0

Tab. 2.1: A summary of all elementary bosons described by the SM. All mass measurements have been taken from the Particle Data Group [3] and are in units of GeV unless stated otherwise.

Fermion	Symbol	Mass [GeV]	Electric Charge [e]	Baryon Number
Up	u	$0.0022^{+0.0006}_{-0.0004}$	$+2/3$	$1/3$
Down	d	$0.0047^{+0.0005}_{-0.0004}$	$-1/3$	$1/3$
Charm	c	1.28 ± 0.03	$+2/3$	$1/3$
Strange	s	$0.096^{+0.008}_{-0.004}$	$-1/3$	$1/3$
Top	t	173.1 ± 0.6	$+2/3$	$1/3$
Bottom	b	$4.8^{+0.04}_{-0.03}$	$-1/3$	$1/3$

Tab. 2.2: A summary of all quarks described by the SM. All mass measurements have been taken from the Particle Data Group [3] and are in units of GeV unless stated otherwise.

Fermion	Symbol	Mass [GeV]	Electric Charge [e]	L_e	L_μ	L_τ
Electron	e	0.000511	-1	1	0	0
Electron Neutrino	ν_e	$< 2\,\text{eV}$	0	1	0	0
Muon	μ	0.106	-1	0	1	0
Muon Neutrino	ν_μ	< 0.00019	0	0	1	0
Tau	τ	1.777	-1	0	0	1
Tau Neutrino	ν_τ	< 0.0182	0	0	0	1

Tab. 2.3: A summary of all leptons described by the SM. All mass measurements have been taken from the Particle Data Group [3] and are in units of GeV unless stated otherwise.

charge, and baryon and lepton numbers. Typically, quantum numbers and physical properties must be conserved during particle interactions and decays, however there are known instances, discussed later, where this is violated.

2.1.2 Fundamental Interactions

The mathematical basis of the SM uses Quantum Field Theory [4], in which particles represent the excitations of fields, the dynamics of which are described by Lagrangian field densities $\mathcal{L}$. The general form of $\mathcal{L}$ is

$$\mathcal{L} = \mathcal{L}(\psi, \partial_\mu \psi), \tag{2.1}$$

where ψ is a fermion field and $\partial_\mu \psi$ is the partial derivative four-vector of all generalised spatial coordinates. Where symmetries in nature exist, the Lagrangian density of a system is symmetrically invariant under certain phase transformations ϑ of ψ, such as:

$$\psi \rightarrow e^{-i\vartheta}\psi. \tag{2.2}$$

A global symmetry is defined if the phase transformation has no dependence on the system's spatial coordinates. However, the SM requires symmetries to be local *gauge symmetries*, requiring that they remain invariant even when there is phase dependence on spatial coordinates, such that

$$\psi(x) \rightarrow e^{-i\vartheta(x)}\psi(x). \tag{2.3}$$

In this instance, it is clear that the partial derivative in Equation 2.1 will also act on the local dependence of the transformation, introducing extra terms. To counteract this variance, and to restore *gauge invariance*, the partial derivative can be replaced with a *covariant derivative D_μ*,

$$\partial_\mu \rightarrow D_\mu = \partial_\mu + iA_\mu, \tag{2.4}$$

where A_μ is an additional vector field that transforms and absorbs these extra terms in such away that $\mathcal{L}$ remains invariant:

$$A_\mu \rightarrow A'_\mu = A_\mu - \partial_\mu. \tag{2.5}$$

The result of introducing A_μ is that the gauge-invariant $\mathcal{L}$ contains an additional term that describes the interaction of particles (represented by ψ) with the excitations in the vector field (the force carrying bosons). An element of this description are the coupling constants α, which determine the strength at which fermions can couple with bosons. Coupling constants are in fact dependent on the given energy scale, which is known as the *running of the coupling*, or simply *running coupling*.

The full gauge symmetry group of the SM is given as

$$SU(3)_C \otimes SU(2)_L \otimes U(1)_Y, \tag{2.6}$$

where each term represents a symmetry group that comprises unitary base matrices, known as *generators*. These generators are subsets which can be combined to express many more elements of the group's local phase transitions. Each term will be discussed in the following.

2.1.2.1 Quantum Electrodynamics

The electromagnetic force is described in the SM by the relativistic quantum field theory *Quantum Electrodynamics* (QED), and is perhaps the best understood of the three forces described by the SM. QED is an *abelian* gauge theory with symmetry group $U(1)_Q$, meaning that the 1×1 generator commutes (albeit just with itself), resulting in electrical neutrality of the photon, and an inability to self-interact. $U(1)_Q$ describes the interactions of massless photons originating from the A_μ vector field, which govern all charged particles and can act over an infinite range. The coupling constant in an electromagnetic interaction at zero momentum transfer is given by

$$\alpha_{EM} = \frac{e^2}{4\pi} \sim \frac{1}{137}, \tag{2.7}$$

where e is the electric elementary charge.

2.1.2.2 Weak Interaction

The $SU(2)_L$ symmetry group consists of three 2×2 generators of a *non-abelian* gauge theory which describe the weak force. The non-abelian nature means the generators do not commute, corresponding to interactions between the bosons. Responsible for radioactive β-decay, weak interactions couple to weak isospin T, and are mediated by the exchange of massive W and Z bosons, corresponding to either charged or neutral currents. These arise from the $W_\mu^\pm$ and Z_μ vector fields, respectively. The projection of weak isospin along the z-axis, T_Z, is conserved in weak interactions. T_Z is related to chirality, where left-handed chiral-fermions have $T_Z = \pm 1/2$ and can be grouped into the following isospin doublets:

$$\begin{pmatrix} u_L \\ d_L \end{pmatrix}, \begin{pmatrix} c_L \\ s_L \end{pmatrix}, \begin{pmatrix} t_L \\ b_L \end{pmatrix}, \tag{2.8}$$

$$\begin{pmatrix} \nu_{e,L} \\ e_L \end{pmatrix}, \begin{pmatrix} \nu_{\mu,L} \\ \mu_L \end{pmatrix}, \begin{pmatrix} \nu_{\tau,L} \\ \tau_L \end{pmatrix}, \tag{2.9}$$

where the subscript L refers to the left-handedness of the fermions. The W boson has $T_Z = \pm 1$, which results in particles transforming weakly from $T_Z = +^1/_2$ to $T_Z = -^1/_2$, and vice versa. Conversely, right-handed fermions have $T_Z = 0$, and remain as the following singlets:

$$u_R, \ d_R, \ c_R, \ s_R, \ t_R, \ b_R, \ e_R, \ \nu_{e,R}, \ \mu_R, \ \nu_{\mu,R}, \ \tau_R, \ \nu_{\tau,R}, \tag{2.10}$$

where the subscript R refers to the right-handedness of the fermion. These right-handed fermions do not couple with the W boson, meaning that they do not undergo weak transformations. However, the Z boson, with $T_Z = 0$, couples to both left- and right-handed fermions. The consequence of the W boson's coupling selectiveness generates two unique features of the SM: it is the only interaction which can change the flavour of quarks; and, it violates parity conservation. Although right-handed neutrinos have been listed amongst the singlets in Equation 2.10, they are not known to couple to any interactions, and so neutrinos are only present in the SM as left-handed chiral fermions (or right-handed chiral fermions for anti-neutrinos).

The relatively large mass of the mediating W and Z bosons, as previously detailed in Table 2.1, means that they are short-lived with a mean lifetime of $\mathcal{O}(10^{-25}\,\text{s})$. Consequently, they act over a relatively short range of $\mathcal{O}(10^{-18}\,\text{m})$. The coupling constant of weak interactions at zero momentum transfer is found to be

$$\alpha_{weak} \sim \frac{1}{30} . \tag{2.11}$$

2.1.2.3 Electroweak Unification

The fundamental interactions detailed above are very good at describing the universe at energies below $\mathcal{O}(10^{10}\,\text{GeV})$, however, in the early universe they were merged together as one unified electroweak force [5–7], with electroweak symmetry group $SU(2)_L \otimes U(1)_Y$. Of note, the single QED symmetry group $U(1)_Q$ amends to $U(1)_Y$, introducing the quantum number Y, the weak hypercharge, a combination of the projection of isospin on the z-axis and electric charge, given as

$$Y = 2(Q - T_Z). \tag{2.12}$$

To remain invariant, in a similar way that A_μ was introduced in Equation 2.4, the Lagrangian of the unified electroweak force introduces: a triplet gauge field with three component gauge bosons, $W_\mu^{i=1,2,3}$, associated with weak isospin which mediate the weak force; and, a single gauge field with a corresponding gauge boson B_μ, which couples to weak hypercharge, mediating the electromagnetic force. All four gauge bosons are massless. The linear combination of the W_μ^1 and W_μ^2 forms the $W^\pm$ boson, while the Z and photon vector fields are mixings of B_μ and W_μ^3, all given by the following:

$$W_\mu^\pm = \frac{1}{\sqrt{2}}(W_\mu^1 \mp W_\mu^2), \tag{2.13}$$

$$Z_\mu = W_\mu^3 \cos\theta_W - B_\mu \sin\theta_W, \tag{2.14}$$

$$A_\mu = B_\mu \cos\theta_W + W_\mu^3 \sin\theta_W, \tag{2.15}$$

where $\sin\theta_W$ is the experimentally determined Weinberg, or weak mixing angle [8]. The spontaneous symmetry breaking of this unified theory introduces an additional complex scalar field, the Higgs field, which couples to fermions and bosons giving them their mass. The mechanism for this follows.

2.1.2.4 The Higgs Mechanism

The Higgs mechanism [9, 10] describes the spontaneous symmetry breaking of $SU(2)_L \otimes U(1)_Y$ by the introduction of the complex scalar Higgs field Φ, given in its simplest form as

$$\Phi = \frac{1}{\sqrt{2}}(\Phi_1 + i\Phi_2), \tag{2.16}$$

where Φ_1 and Φ_2 are the real and imaginary parameterisations, respectively, of the Higgs potential $V(\Phi_1, \Phi_2)$, depicted in Figure 2.2. The Higgs potential can be seen to be comparable to a "Mexican hat", and would have taken the central *vacuum expected value* (VEV) while the symmetry remained unbroken, corresponding to $V(0,0)$. The spontaneous breaking of the symmetry occurs when the field minimises and selects a random non-zero VEV corresponding to v, shown as the trough of the Mexican hat. This non-zero vaccum state can be chosen to be in the real direction so that $V(\Phi_1, \Phi_2) = V(v, 0)$. The Higgs field can be further parameterised by expanding about v with additional scalar fields η and ξ, modifying Equation 2.16 to:

$$\Phi = \frac{1}{\sqrt{2}}((\eta + v) + i\xi), \tag{2.17}$$

Fig. 2.2: Visualisation of the Higgs potential in the complex "imaginary" plane. The lowest-energy state corresponds to a randomly chosen non-zero point in the trough of the "Mexican hat". The movement from the centre of the potential to this trough corresponds to the massive Higgs boson [11].
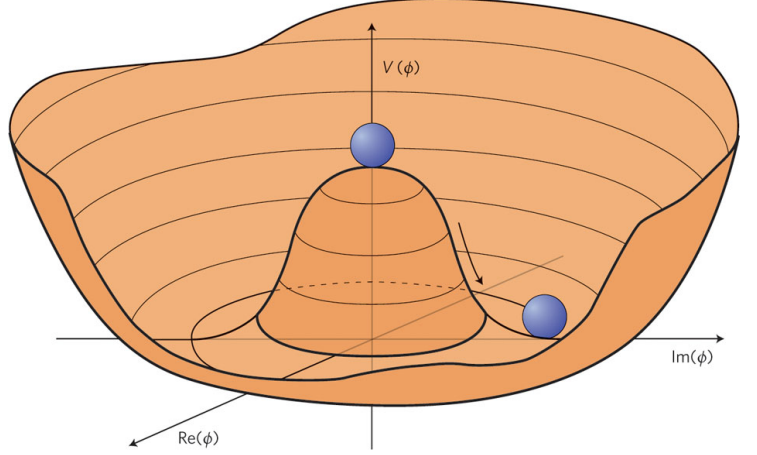
where $\eta + v$ describes excitations (bosons) in the η field, and ξ describes excitations (bosons) in the direction where the potential does not change, as indicated in Figure 2.3.

The inclusion of this parameterisation in the Higgs Lagrangian produces kinematic energy terms and interactions of the η, ξ and gauge fields, a coupling term between a gauge field and ξ, along with a mass term of η, and the introduction of a mass term that makes the $W_\mu^{i=1,2,3}$ and B_μ gauge bosons from the electroweak force massive. In this scenario, η represents the Higgs field, and its excitations correspond to a massive Higgs boson, a particle that was recently discovered in 2012 at the LHC (detailed in Section 2.1.3). The ξ term corresponds to massless "Goldstone" scalar bosons. Goldstone bosons, which cannot exist in nature due to the inability of a gauge boson to transform to a scalar boson, can be eliminated by making an appropriate gauge transformation.

The mass of $W^\pm$, given in Equation 2.13 as the linear combination of W_μ^1 and W_μ^2, is determined by the coupling constant of the $SU(2)_L$ gauge interaction and the VEV of the Higgs field. Additionally, Equations 2.14 and 2.15, which show that
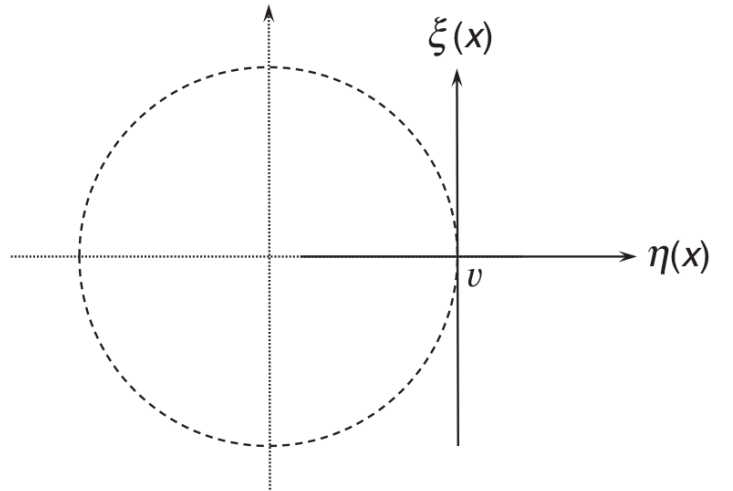
Fig. 2.3: The directions of the η and ξ fields which expand about the non-zero VEV of the Higgs potential where $\Phi = (\Phi_1, \Phi_2) = (v, 0)$. The dotted circle corresponds to the trough of the Mexican hat in Figure 2.2 [1].

W_μ^3 and B_μ mix, results in the masses of the Z boson and photon being described by matrices; the Z boson receives net mass, while the photon remains massless. Meanwhile, fermions are expected to gain mass from the Higgs field VEV interacting with Yukawa couplings of the particles.

2.1.2.5 Quantum Chromodynamics

Quantum chromodynamics (QCD) describes the final symmetry group incorporated in the SM, $SU(3)_C$. The group comprises eight 3×3 generators that describe the interactions of eight gluon gauge fields. Quarks possess a quantum property known as colour (red, blue, or green) that allows quarks to be described as colour triplets:

$$\mathbf{q} = \begin{pmatrix} q_r \\ q_b \\ q_g \end{pmatrix}. \tag{2.18}$$

Differing colour charge allows two quarks of the same flavour to exist in the same bound state without violating the Pauli exclusion principle, for example the two up quarks in a proton. Colour *confinement* is the requirement that all quarks are bound in colourless hadrons, because states with a net colour charge are not invariant under $SU(3)_C$ transformations. This can be achieved with: the combination of three quarks $|qqq\rangle$ with all three colours or anticolours, known as *baryons*, with a net baryon number of ± 1; or, by quark-antiquark pairs $|q\bar{q}\rangle$, where the colour and baryon number cancel, known as *mesons*. Subsequently, the net spin of a meson becomes an integer, making it a boson.

Although gluons are massless, the range of the strong force is only $\mathcal{O}(10^{-15}\,\mathrm{m})$. This is because gluons are non-abelian, meaning they can self-interact and generate virtual gluons in quantities proportional to the distance between two interacting quarks. The result is that the strong force becomes increasingly stronger with increasing distances. As increasingly higher energies are introduced to separate two quarks, there comes a point where it is energetically more favourable to produce an additional quark-antiquark pair instead of increasing the distance any further. This will continue until the energy is low enough to form bound hadron states (baryons or mesons). This entire process is known as *hadronisation*, forming cones of hadrons, known as *jets*. Due to the short timescale of hadronisation, only bound state hadrons can be observed experimentally.

The strong force, as its name suggests, is the strongest of all forces with a coupling constant at zero momentum transfer of $\alpha_S = 1$. At such low energies, unlike QED

and the weak force, QCD processes cannot be described using perturbation theory. However, the strong force's running coupling is highly sensitive to energy scale, meaning that α_S has the largest variation when compared to α_{EM} and α_{weak}. At high energies, α_S becomes sufficiently small that perturbation theory can be applied. A more detailed description of how the strong interaction is simulated is given in Chapter 4. At very high energies, α_S becomes negligible, enabling quarks to behave as free particles, known as *asymptotic freedom.*

2.1.3 Higgs Boson Discovery

The following is included to give an overview of the Higgs boson discovery at the LHC, the experimental setup of which is detailed in-depth in Chapter 3. On the 4th July 2012, two collaborations from the LHC, ATLAS and CMS, together announced the independent discoveries of a new SM particle consistent with the Higgs boson [12, 13], the elusive particle that had been postulated approximately 50 years previously. The detection of the Higgs boson meant it was the first elementary scalar particle discovered in nature. Figure 2.4 shows the results presented by ATLAS and CMS, displaying observed p_0 values as a function of Higgs mass m_H, whereby p_0 is indicative of the likeliness of observed deviations being random, and is detailed further in Section 5.6. Both results indicate that the mass of the Higgs boson agreed with expectation, $\sim$125 GeV. The mass has since been measured with greater precision and is now known within $\sim$0.2% uncertainty [14, 15]. The discovery of the Higgs is of particular relevance to this thesis because it is a significant SM background process that can replicate a three-lepton signature in the final state, detailed in Section 5.1. A preliminary first-look at searches with intermediate decays which include a Higgs boson is also presented in Section 6.3.
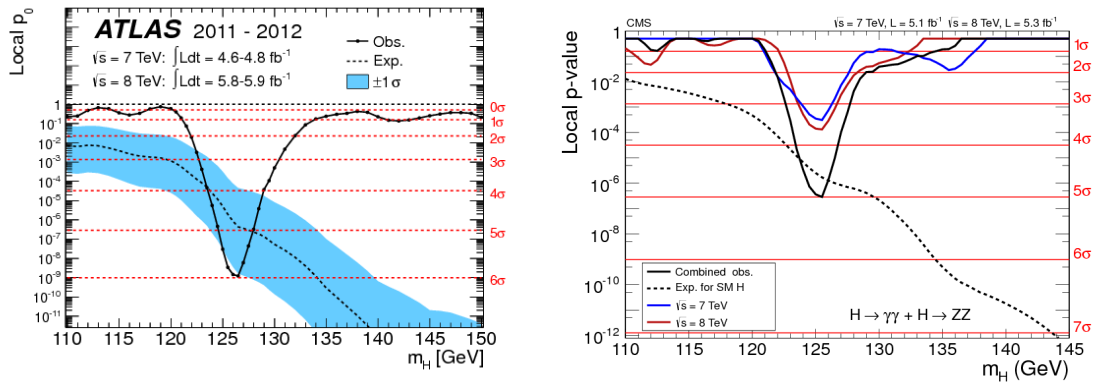
Fig. 2.4: Observed local p_0 as a function of m_H for ATLAS (left) [12] and CMS (right) [13].

2.2 Standard Model Shortcomings

Despite the experimental success of the SM, there still remain several fundamental deficiencies which suggest that it is incomplete. Sections 2.2.1 to 2.2.3 describe three main issues that could be solved with the theoretical extension known as supersymmetry.

2.2.1 The Hierarchy Problem and Naturalness

The experimentally observed Higgs mass m_H^2 consists of both a *bare*, or inherent, mass term m_0^2, and a Δm_H^2 term describing the quantum loop corrections from the coupling of every particle to the Higgs field, an example is shown in Figure 2.5. The full expression of the quantum loop contributions from a fermion field takes the form

$$\Delta m_H^2 = -\frac{\lambda_f^2}{8\pi^2}\Lambda_{UV}^2 + ..., \tag{2.19}$$

where λ_f is the Yukawa coupling of the fermion field, and Λ_{UV}^2 is the highest mass scale at which the theory is valid. This in itself is not a problem, however if Λ_{UV}^2 is of the order of the Planck scale $\mathcal{O}(10^{19}\,\text{GeV})$, its quadratic nature would cause it to be drastically larger than the observed Higgs mass ($\sim 125\,\text{GeV}$). The SM solution would be to fine-tune m_0^2 so that large corrections are cancelled out. However this goes against *naturalness*, a property that states ratios between free parameters must not be more than one or two orders of magnitude, and that the fine-tuning of free parameters is indicative of some missing ingredient in the theory [16].

Fig. 2.5: An example of a one-loop quantum correction described by Δm_H^2.
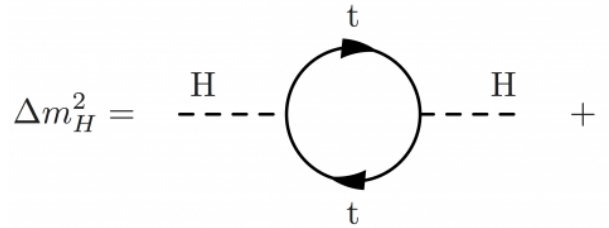
2.2.2 Gauge Coupling Unification

The SM predicts that gauge running coupling constants, as mentioned in Section 2.1.2, are dependent on the energy scale Q, as shown in Figure 2.6. In the SM, the electromagnetic couplings increase with energy while the weak and strong forces decrease. Although the electromagnetic and weak force unify into the electroweak force, no mechanism to unify the strong force exists within the SM. This goes against the idea of a Grand Unified Theory (GUT) [17] and would require new physics in order for all of the interactions to converge at one singular point.

Fig. 2.6: Running coupling constants for the three fundamental interactions of the SM, electromagnetic (blue), weak (red) and strong (green) [18].
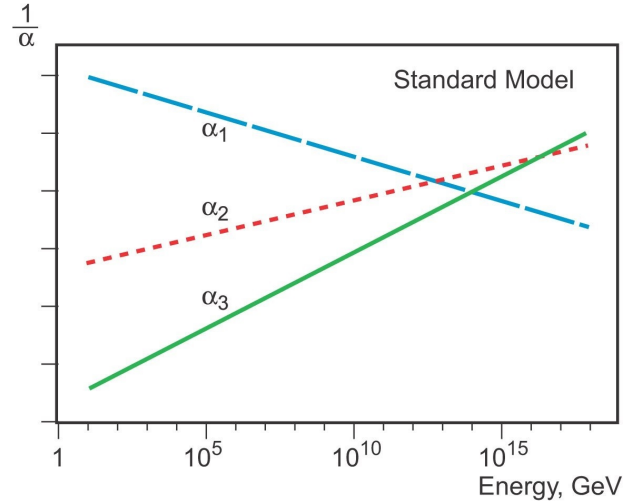
2.2.3 Dark Matter

The rotational curves of galaxies in our universe, which are functions of the rotational velocity and radial distance of the galaxy spiral arms, are observed to be considerably higher than what would be expected from visible matter alone. Figure 2.7 shows that with the addition of extra *dark matter* found in halos around galaxies, the theory will fit observations. Gravitational lensing [20] and measurements of the cosmic microwave background [21] are also consistent with the dark matter hypothesis, the alternative being a modified theory of general relativity on galactic scales. Dark matter, which has been calculated to make up ∼27% of the universe and ∼85% of matter, can be hypothesised as Weakly-Interacting Massive Particles (WIMPs), that interact with gravity and the weak force, but not with the electromagnetic force, and thus are extremely difficult to detect. Although the SM neutrino fulfills some of the WIMP criteria, they are not massive and can not solely account for the galaxy rotational curve observations. No other SM particle is a suitable dark matter candidate.

Fig. 2.7: Fit of expected disk (visible matter) and halo (dark matter) to the observed rotation curve (dots with error bars) [19].
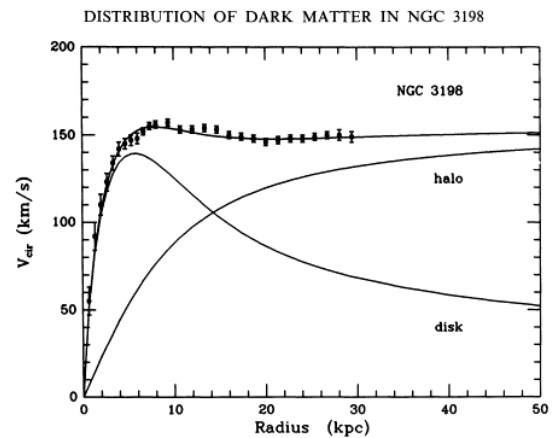
2.2.4 Other Issues

Gravity: the SM of particle physics does not currently incorporate quantum gravity, which is hypothesised to be mediated by the graviton elementary particle and could dominate at the Planck energy scale [22].

CP-Violation: charge-parity violation is one of the three Sakharov conditions [23] postulated as the origin of the net content of baryonic matter in our universe, which would have otherwise annihilated with antiparticles in the very early universe. The only measured source of CP-violation in the SM occurs in the Cabibbo-Kobayashi-Maskawa (CKM) matrix that describes the mixing of quark generations [24]. However, this measurement does not account for the total amount of baryons in the universe today, implying new physics beyond the SM is required for CP-violation to be explained.

Neutrino Oscillations: the SM predicts three massless neutrino generations, however, experimental observations show that neutrinos oscillate between flavours, implying that they have mass. This oscillation between flavours violates lepton number conservation [25]. An extension to the SM is required to account for this.

2.3 Supersymmetry

Supersymmetry (SUSY) [26–28] introduces a new space-time symmetry that transforms a particle's spin by $\Delta s = 1/2$ via a quantum operator Q. All SM fermions will have a bosonic superpartner and vice versa such that:

$$
\begin{aligned}
Q|\text{Boson}\rangle &= |\text{Fermion}\rangle \\
Q|\text{Fermion}\rangle &= |\text{Boson}\rangle.
\end{aligned}
\tag{2.20}
$$

The supersymmetric superpartners are referred to as *sparticles*, aquiring the suffix "ino" for boson naming conventions, and prefix "s" for scalar fermions. Their symbols are the same as their SM counterparts, only with a tilde on top.

Each particle-sparticle pair is arranged as a *supermultiplet*. Left- and right-handed chiral spin-$1/2$ fermions (f_L, f_R) and their equivalent spin-0 sfermions ($\tilde{f}_L$, $\tilde{f}_R$) are known as *chiral supermultiplets*. The Higgs boson and superpartner higgsino are also a chiral supermultiplet, and are the only particles to require two supermultiplets, each coupling to either up- or down-type fermions (H_u-$\tilde{H}_u$, H_d-$\tilde{H}_d$). Spin-1 gauge bosons and their corresponding spin-$1/2$ gauginos (all assumed to be massless) are known as *gauge supermultiplets*. The relationships between the supermultiplets and the operator Q, should mean that particles and sparticles have identical mass and

quantum numbers, with the exception of spin. However, no sparticles have been discovered at the mass scale of their SM partners, indicating their mass is of much larger scale and that SUSY must be a broken symmetry [29]. SUSY breaking can occur in many ways, the standard mechanism being *gauge-mediated* breaking. This mechanism introduces a separate *hidden sector* of SUSY where the breaking occurs, and uses gauge, or *messenger*, fields to mediate the breaking to the visible sector. The breaking of the symmetry is spontaneous, in the same way as electroweak breaking, whereby the scalar fields gain a non-zero VEV.

SUSY also offers a solution to the gauge coupling unification problem introduced in Section 2.2.2. By introducing new particle content into the theory, the scale dependence of the running couplings will be modified in a way that all three can approximately converge, shown in Figure 2.8. However, this could be accidental, and unification is predicted at energies currently unaccessable to probe experimentally, yet it can also be considered a strong indication that SUSY can provide the basis of a GUT.


Fig. 2.8: Running coupling constants for the three fundamental interactions of the SM when SUSY is included, electromagnetic (blue), weak (red) and strong (green) [18].
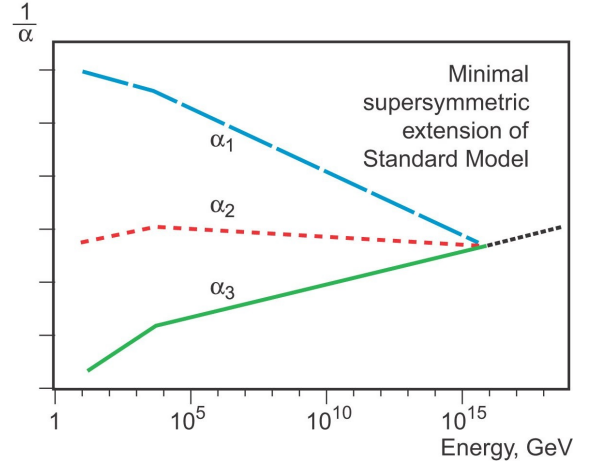
2.3.0.1 The SUSY Higgs Sector

As mentioned above, the Higgs boson has two supermultiplets, denoted either up- or down-type Higgs bosons. Each type has a separate VEV, v_u and v_d, where, in order to reproduce the known masses of the W and Z bosons, m_W and m_Z, respectively, the following must apply:

$$v = \sqrt{v_u^2 + v_d^2}. \tag{2.21}$$

where v is the VEV of the SM Higgs. The ratio of the VEV can be expressed as $v_u/v_d = \tan\beta$, and is important in calculating the squark and slepton masses, described in the next section.

2.3.1 The Minimal Supersymmetric Standard Model

The Minimal Supersymmetric Standard Model (MSSM) [30] is the extension to the
SM requiring the minimal amount of supersymmetric partners to solve the hierarchy
problem. The MSSM particle content is listed in Table 2.4. The gauge supermultiplets
are the gluino ($\tilde{g}$), wino ($\tilde{W}_i$) and bino ($\tilde{B}$) for the $SU(3)_C \otimes SU(2)_L \otimes U(1)_Y$ symmetry
groups, respectively.

2.3.1.1 MSSM Masses

As previously discussed, the Higgs mechanism, that occurs during electroweak
symmetry breaking, is responsible for giving SM particles mass, something that is
forbidden otherwise. However sparticles are allowed to have mass before this breaking
occurs. The total Lagrangian describing SUSY is defined as

$$\mathcal{L} = \mathcal{L}_{\text{SUSY}} + \mathcal{L}_{breaking}, \tag{2.22}$$

where $\mathcal{L}_{\text{SUSY}}$ contains the invariant interactions that preserve SUSY, and $\mathcal{L}_{breaking}$
contains new mass terms that are present due to the symmetry breaking. These new
mass terms give additional quantum loop corrections to the Higgs mass in the form

$$\Delta m_H^2 = \frac{\lambda_S}{16\pi^2}\Lambda_{UV}^2 + ..., \tag{2.23}$$

Supermultiplet	Name		Spin-0	Spin-$1/2$	Spin-1
Chiral	Squarks-Quarks	Q_i	$(\tilde{u}_L,\ \tilde{d}_L)$	$(u_L,\ d_L)$	$-$
		$\bar{u}_i$	$\tilde{u}_R$	u_R	$-$
		$\bar{d}_i$	$\tilde{d}_R$	d_R	$-$
Chiral	Sleptons-Leptons	L_i	$(\tilde{\nu},\ \tilde{e}_L)$	$(\nu,\ e_L)$	$-$
		$\bar{e}_i$	$\tilde{e}_R$	e_R	$-$
Chiral	Higgs-Higgsino	H_u	$(H_u^+,\ H_u^-)$	$(\tilde{H}_u^+,\ \tilde{H}_u^-)$	$-$
		H_d	$(H_d^+,\ H_d^-)$	$(\tilde{H}_d^+,\ \tilde{H}_d^-)$	$-$
Gauge	Gluino-Gluon		$-$	$\tilde{g}$	g
Gauge	Winos-W bosons		$-$	$\tilde{W}^{\pm},\ \tilde{W}^0$	$W^{\pm},\ W^0$
	Bino- B bosons		$-$	$\tilde{B}^0$	B^0

Tab. 2.4: Supermultiplet particle content of the MSSM. Here, $i = 1, 2, 3$, and indicates the
generation index with all generations following the same convention. The bars indicate that
the sparticle is the superpartner of a right-handed chiral particle.
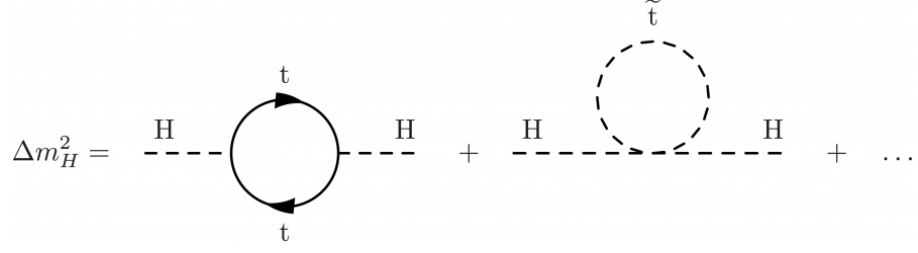
Fig. 2.9: Combination of a one-loop fermion field quantum correction (top quark) and equivalent scalar field quantum correction (stop squark) introduced by SUSY.

where λ_S is the Yukawa coupling of the new scalar field. The mass terms have opposite sign to their fermionic counterparts, resulting in the cancellation of the quadratic divergencies when a fermion is accompanied by two scalars, solving the hierarchy problem that was introduced in Section 2.2.1. A depiction of the modified Δm_H^2 term, previously shown in Figure 2.5, is presented in Figure 2.9.

The breaking is *soft*, meaning that SUSY remains a natural theory. It does this by requiring sparticle masses to not be much more than $\sim 1\,\text{TeV}$, therefore preserving it as a solution to the hierarchy problem. The additional mass terms introduced by the breaking include [31]:

- Three gaugino masses of the bino, wino and gluino: M_1, M_2, M_3;
- Five scalar masses for squarks and sleptons: $M_{\tilde{q}_L}$, $M_{\tilde{u}_R}$, $M_{\tilde{d}_R}$, $M_{\tilde{L}_L}$, $M_{\tilde{e}_R}$;
- Higgsino mass parameters squared: $m_{H_u}^2$, $m_{H_d}^2$.

The new mass terms can mix to form the eigenstates of sparticles, detailed in the following. Table 2.5 summarises the gauge and mass eignestates of SUSY.

Name	Spin	Gauge Eigenstates	Mass Eigenstates
Squarks ($\tilde{q}$)	0	$\tilde{u}_L$, $\tilde{u}_R$, $\tilde{d}_L$, $\tilde{d}_R$	(same)
		$\tilde{s}_L$, $\tilde{s}_R$, $\tilde{c}_L$, $\tilde{c}_R$	(same)
		$\tilde{t}_L$, $\tilde{t}_R$, $\tilde{b}_L$, $\tilde{b}_R$	$\tilde{t}_1$, $\tilde{t}_2$, $\tilde{b}_1$, $\tilde{b}_2$
Sleptons ($\tilde{\ell}$)	0	$\tilde{e}_L$, $\tilde{e}_R$, $\tilde{\nu}_e$	(same)
		$\tilde{\mu}_L$, $\tilde{\mu}_R$, $\tilde{\nu}_\mu$	(same)
		$\tilde{\tau}_L$, $\tilde{\tau}_R$, $\tilde{\nu}_\tau$	$\tilde{\tau}_1$, $\tilde{\tau}_2$, $\tilde{\nu}_\tau$
Higgs Bosons	0	H_u^0, H_d^0, H_u^+, H_d^-	h^0, H^0, A^0, $H^\pm$
Neutralinos ($\tilde{\chi}_j^0$)	$\frac{1}{2}$	$\tilde{B}^0$, $\tilde{W}^0$, $\tilde{H}_u^0$, $\tilde{H}_d^0$	$\tilde{\chi}_1^0$, $\tilde{\chi}_2^0$, $\tilde{\chi}_3^0$, $\tilde{\chi}_4^0$
Charginos ($\tilde{\chi}_j^\pm$)		$\tilde{W}^\pm$, $\tilde{H}_u^+$, $\tilde{H}_d^0$	$\tilde{\chi}_1^\pm$, $\tilde{\chi}_2^\pm$
Gluino	$1/2$	$\tilde{g}$	(same)

Tab. 2.5: Gauge and mass eigenstates of supersymmetric particles in the MSSM.

Higgs Bosons: the two Higgs supermultiplets introduced earlier, generate eight degrees of freedom: two charged Higgs states $H^{\pm}$, three neutral Higgs bosons, A^0, h^0 and H^0 (where one of the latter two must be the SM Higgs), and three giving rise to the masses of the $W^{\pm}$ and Z bosons of the SM, as discussed in Section 2.1.2.4.

Gauginos: higgsinos and electroweak gauginos mix with each other. *Neutralinos* are combinations of the neutral higgsinos ($\tilde{H}_u^0$ and $\tilde{H}_d^0$) and neutral gauginos ($\tilde{B}$ and $\tilde{W}^0$), while *charginos* are mixtures of the charged higgsinos ($\tilde{H}_u^+$ and $\tilde{H}_d^-$) and winos ($W^{\pm}$). The neutralino and chargino mass eigenstates are denoted as $\tilde{\chi}_{i=1,2,3,4}^0$ and $\tilde{\chi}_{i=1,2}^{\pm}$, respectively, where i indicates the masses in ascending order. The mass mixings can be represented by the following matrices:

$$\begin{pmatrix} \tilde{\chi}_1^0 \\ \tilde{\chi}_2^0 \\ \tilde{\chi}_3^0 \\ \tilde{\chi}_4^0 \end{pmatrix} = \begin{pmatrix} M_1 & 0 & -c_\beta m_Z s_W & s_\beta m_Z s_W \\ 0 & M_2 & c_\beta m_Z c_W & -s_\beta m_Z c_W \\ -c_\beta m_Z s_W & c_\beta m_Z c_W & 0 & -\mu \\ s_\beta m_Z s_W & -s_\beta m_Z c_W & -\mu & 0 \end{pmatrix} \begin{pmatrix} \tilde{B}^0 \\ \tilde{W}^0 \\ \tilde{H}_u^0 \\ \tilde{H}_d^0 \end{pmatrix}, \quad (2.24)$$

$$\begin{pmatrix} \tilde{\chi}_1^{\pm} \\ \tilde{\chi}_2^{\pm} \end{pmatrix} = \begin{pmatrix} M_2 & \sqrt{2}m_W s_\beta \\ \sqrt{2}M_W c_\beta & \mu \end{pmatrix} \begin{pmatrix} \tilde{W}^{\pm} \\ \tilde{H}^{\pm} \end{pmatrix}, \quad (2.25)$$

where $c_\beta = \cos\beta$, $s_\beta = \sin\beta$, $c_W = \cos\theta_W$, $s_W = \sin\theta_W$, and m_W and m_Z are the W and Z boson mass, respectively. Gluons and gluinos do not mix due to carrying the colour charge.

Squarks and Sleptons: although squarks and sleptons are labeled left- or right-handed, they do not carry chirality, and the label instead refers to the chirality of their supermultiplet partner. Without chirality, squarks and sleptons are able to mix. However, first and second generations have relatively low Yukawa couplings resulting in very small mixing angles and mass eigenstates the same as their gauge eigenstates. Conversely, the larger Yukawa effects cause the third generation to have much larger masses, resulting in significant mixings and altered mass eigenstates.

2.3.2 R-Parity

SUSY introduces many new interactions not found in the SM, some of which directly violate total baryon and lepton numbers. To remove these violations, a new symmetry, known as R-parity is often introduced, giving a multiplicative conserved quantum

number for each particle, given as

$$P_R = (-1)^{3(B-L)+2S}.$$

(2.26)

P_R will have a value of $+1$ for SM particles and -1 for their SUSY partners, and is conserved when the product of P_R is of the same-sign before and after the interaction. Although there are scenarios in SUSY where R-Parity is violated, this thesis focuses on scenarios were it is conserved. This means that the production of SUSY particles must occur in pairs from a SM particle, while SUSY particles themselves will continue to decay to both a SM and SUSY particle until the Lightest Supersymmetric Particle (LSP) is reached. This LSP is stable and would be a weakly-interacting massive particle, making it a suitable candidate for dark matter, introduced in Section 2.2.3. The detailed decays of sparticles is presented in the next section.

2.3.3 Sparticle Decays

The following gives a brief overview of the R-parity conserving decay patterns of the MSSM electroweak sparticles relevant to this thesis: charginos, neutralinos and sleptons.

2.3.3.1 Chargino and Neutralino Decays

Winos are able to couple to left-handed fermions and sfermions along with the up- and down-Higgs and higgsino doublets, while binos can also couple to the right-handed particles. Decays to lepton-slepton pairs are favoured due to their expected light masses, however decays are also expected to be to quark-squark pairs, as well as lighter charginos or neutralinos with a Higgs scalar or electroweak gauge boson, displayed in Figure 2.10. Possible two-body decays are:

$$\tilde{\chi}_i^0 \to Z\tilde{\chi}_j^0,\ W\tilde{\chi}_j^\pm,\ h^0\tilde{\chi}_j^0,\ \ell\tilde{\ell},\ \nu\tilde{\nu},\ [A^0\tilde{\chi}_j^0,\ H^0\tilde{\chi}_j^0,\ H^\pm\tilde{\chi}_j^\mp,\ q\tilde{q}],$$

(2.27)

$$\tilde{\chi}_i^\pm \to W^\pm\tilde{\chi}_j^0,\ Z\tilde{\chi}_1^\pm,\ h^0\tilde{\chi}_1^\pm,\ \ell\tilde{\nu},\ \nu\tilde{\ell},\ [A^0\tilde{\chi}_1^\pm,\ H^0\tilde{\chi}_1^\pm,\ H^\pm\tilde{\chi}_j^0,\ q\tilde{q}'],$$

(2.28)

where the final states in brackets are energetically less favourable. Charginos and neutralinos have higher branching fractions to tau leptons in the final state, however this thesis only targets final states with light leptons (electrons and muons).
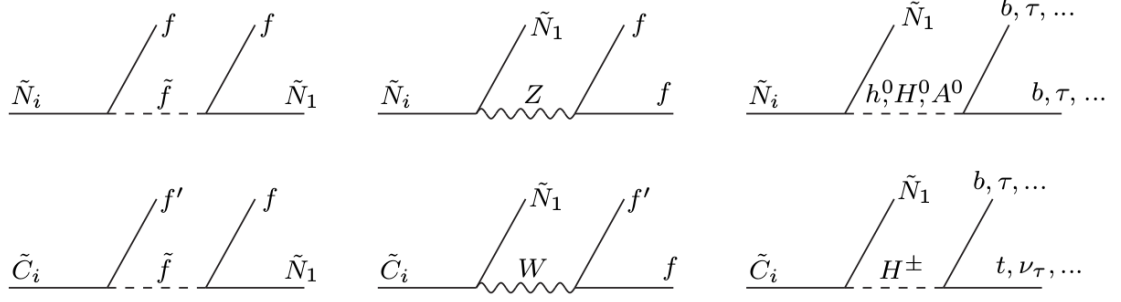
Fig. 2.10: Feynman diagrams of possible electroweak decays of the neutralino $\tilde{N}_i$ (top) and chargino $\tilde{C}_i$ (bottom) with the lightest neutralino $\tilde{N}_1$ in the final state [27].

2.3.3.2 Slepton Decays

Sleptons are able to decay to the following two-body states:

$$\tilde{\ell} \to \ell\tilde{\chi}_i^0, \ \nu\tilde{\chi}_i^{\pm}, \tag{2.29}$$

$$\tilde{\nu} \to \nu\tilde{\chi}_i^0, \ \ell\tilde{\chi}_i^{\pm}. \tag{2.30}$$

Right-handed sleptons will favour decays to the bino-like lightest neutralino, while left-handed sleptons prefer decays to wino-like charginos and neutralinos due to the higher weak interaction couplings (mediated by winos), compared to the smaller electromagnetic coupling (mediated by binos).

2.3.4 SUSY Production

SUSY particles can be produced in different modes which can be explored experimentally. Strong production refers to the direct production of the gluinos and first and second generation squarks, while the production of stop and sbottom squarks are referred to separately as third generation production. Examples of each production are shown in Figure 2.11. This thesis considers electroweak production, referring to the direct production of sleptons, charginos and neutralinos, all of which are displayed in Figure 2.12, with a focus on the direct production of a lightest chargino with a next-to-lightest neutralino.

Each production mode has different cross-sections, as seen in Figure 2.13, with the strong production having the highest, and electroweak the lowest. The motivation for searching for the lower cross-section electroweak SUSY is presented in Section 2.3.6.2.
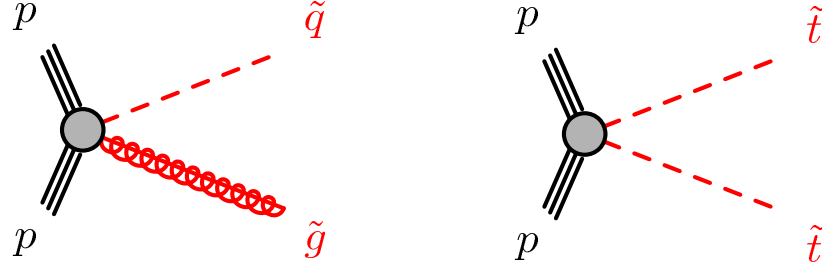
Fig. 2.11: Example schematic diagrams for: strong SUSY production of a gluino and squark (left); and, third generation SUSY production of two stops (right).
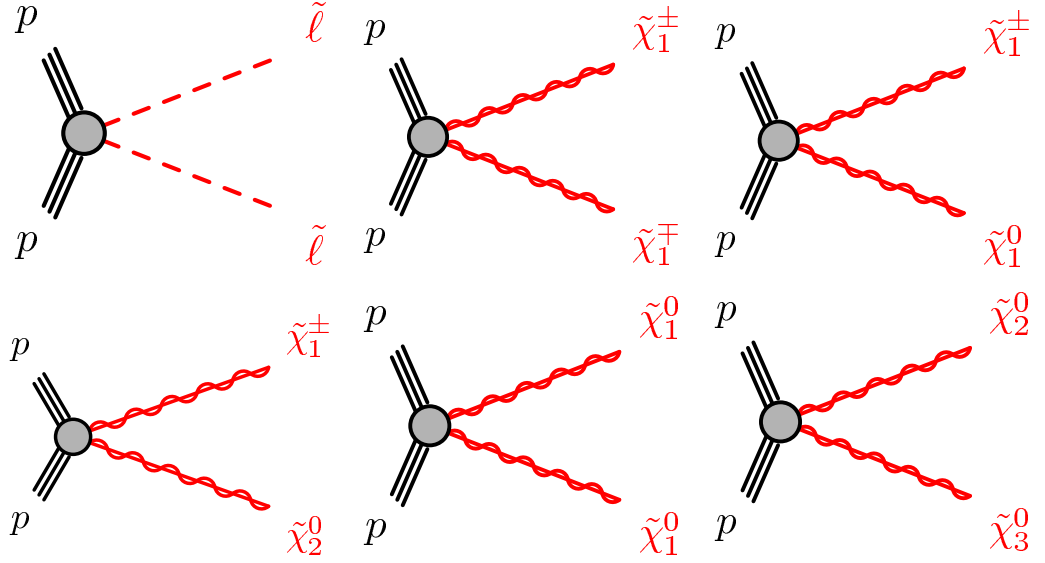
Fig. 2.12: Schematic diagrams for electroweak SUSY production: two sleptons (top left); opposite-sign lightest chargino pair (top middle); lightest chargino and neutralino (top right); the focus of this thesis, a lightest chargino and next-to-lightest neutralino (bottom left); a lightest neutralino pair (bottom middle); and, next-to-lightest and next-to-next-lightest neutralino (bottom right).

2.3.5 Simplified Models for Electroweak SUSY

Experimentally, SUSY can be simplified by reducing the particle content of decay chains to focus on only two or three particle masses and branching ratios. Such models cannot be exactly realised, however due to fewer assumptions on the nature of new physics, they prove sufficient in experimental searches.

The direct pair production of the lightest chargino $\tilde{\chi}_1^{\pm}$, and next-to-lightest neutralino $\tilde{\chi}_2^0$, are considered in this thesis, producing three electrons or muons and the lightest neutralino $\tilde{\chi}_1^0$, in the final state. Both $\tilde{\chi}_1^{\pm}$ and $\tilde{\chi}_2^0$ are mass degenerate consisting of wino and higgsino eigenstates, while the $\tilde{\chi}_1^0$ consists of binos and higgsinos. The first two simplified electroweak scenarios detailed in the following are the primary topic of this thesis, while the third scenario is the focus of a preliminary look into future
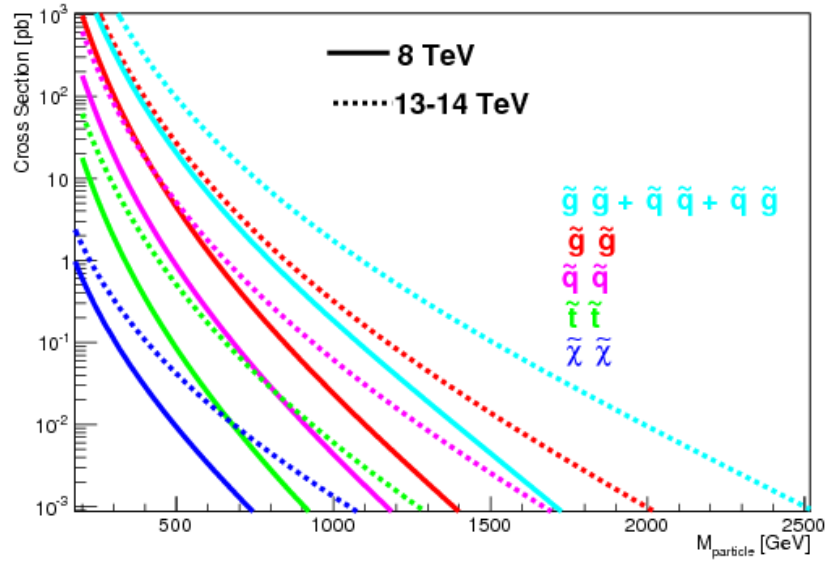
Fig. 2.13: Cross-sections for the different SUSY production modes with a centre-of-mass energy $\sqrt{s} = 8$ TeV (solid lines) and the increased 13-14 GeV (dashed lines) [32].

electroweak SUSY searches. Each are classified according to their intermediate decay chains.

$\tilde{\chi}_1^\pm \tilde{\chi}_2^0$ via Sleptons

The intermediate decay of $\tilde{\chi}_1^\pm$ $\tilde{\chi}_2^0$ via sleptons or sneutrinos has the highest branching ratio of the three considered, and is presented in Figure 2.14. In this scenario, left-handed sleptons or sneutrinos are assumed to be light, while their right-handed counterparts are assumed to have masses at the TeV scale. This results in the $\tilde{\chi}_1^\pm$ $\tilde{\chi}_2^0$ decaying dominantly via the left-handed sparticle. All slepton flavours are considered, however only electrons or muons are searched for in the final state. The branching ratio to either sleptons or sneutrinos is taken to be 50%.

$\tilde{\chi}_1^\pm \tilde{\chi}_2^0$ via W and Z Bosons

Figure 2.15 displays the scenario whereby all slepton and sneutrino masses are assumed to be at the TeV scale, resulting in the dominant $\tilde{\chi}_1^\pm$ and $\tilde{\chi}_2^0$ decay with a 100% branching ratio to W and Z bosons, respectively. Three leptons, a neutrino and $\tilde{\chi}_1^0$ are in the final state.

$\tilde{\chi}_1^{\pm}\tilde{\chi}_2^0$ via W and Higgs Bosons

The final scenario considered is a preliminary look at the lowest branching ratio process with intermediate decays via W and SM Higgs bosons, shown in Figure 2.16.[1] The masses of the slepton and sneutrino are also assumed to be at the TeV scale.

Fig. 2.14: A schematic diagram for $\tilde{\chi}_1^{\pm}\tilde{\chi}_2^0$ simplified models with intermediate sleptons decays producing three leptons in the final state.
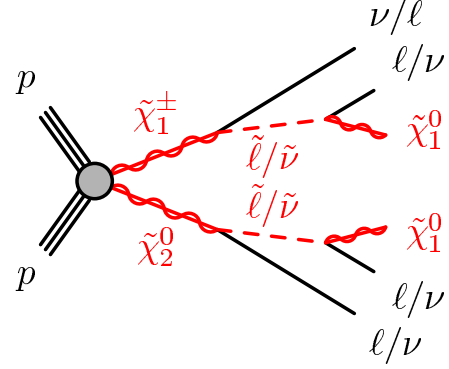
Fig. 2.15: A schematic diagram for $\tilde{\chi}_1^{\pm}\tilde{\chi}_2^0$ simplified models with intermediate W and Z boson decays producing three leptons in the final state.
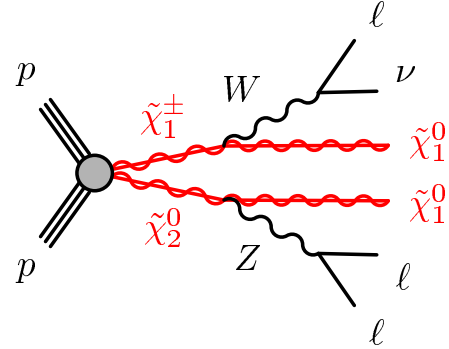
Fig. 2.16: A schematic diagram for $\tilde{\chi}_1^{\pm}\tilde{\chi}_2^0$ simplified models with intermediate W and Higgs boson decays producing three leptons in the final state.

---
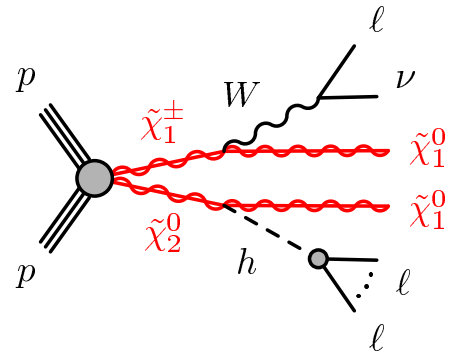
[1] In SM physics, the capital letter H is used to denote the light Higgs boson, while in supersymmetry a lowercase h is used.

2.3.6 Current Status of SUSY Searches at the LHC

The following is included to give an overview of relevant experimental SUSY results achieved by the LHC. The status of SUSY searches prior to the commencement of this thesis is presented in Section 2.3.6.1, followed by an overview of the motivations of this thesis to search for electroweak supersymmetry at the LHC in Section 2.3.6.2.

2.3.6.1 SUSY Mass Limits at the end of Run-I

To date, no evidence of SUSY particles has been detected. In the absence of a signal, upper limits (detailed in Section 5.6) on the masses of the $\tilde{\chi}_1^\pm \tilde{\chi}_2^0$ and $\tilde{\chi}_1^0$ can be set. Figure 2.17 shows the limits obtained in Run-I using $20.3\,\mathrm{fb}^{-1}$ of data at $\sqrt{s} = 8\,\mathrm{TeV}$ by the ATLAS experiment [33, 34], for scenarios with the intermediate decays detailed in Section 2.3.5. Although W and Z boson models with exactly two-leptons in the final state are not considered in this thesis, they can be combined with the three-lepton channel to generate a combined limit including both models. The W and Higgs boson limits also consider reconstructed taus in the final state, which means the limits will not be directly comparable to this thesis.

These results show that mass limits for slepton scenarios have been excluded up to $\sim\!720\,\mathrm{GeV}$ for $\tilde{\chi}_1^\pm \tilde{\chi}_2^0$ and up to $\sim\!380\,\mathrm{GeV}$ for $\tilde{\chi}_1^0$. The $\tilde{\chi}_1^\pm \tilde{\chi}_2^0$ and $\tilde{\chi}_1^0$ masses have been excluded up to $\sim\!350\,\mathrm{GeV}$ and $\sim\!130\,\mathrm{GeV}$, respectively, for intermediate decays via W and Z bosons with exactly three leptons in the final state. When this is combined with the results from the two lepton search, the upper limits increase to $\sim\!430\,\mathrm{GeV}$ and $\sim\!160\,\mathrm{GeV}$, respectively. Masses for the $\tilde{\chi}_1^\pm \tilde{\chi}_2^0$ and $\tilde{\chi}_1^0$ would be excluded up to $\sim\!150\,\mathrm{GeV}$ and $\sim\!18\,\mathrm{GeV}$, respectively, for the W and Higgs boson scenario.

Figure 2.18 presents Run-I limits using $19.5\,\mathrm{fb}^{-1}$ of data at $\sqrt{s} = 8\,\mathrm{TeV}$ from CMS [35]. The limits are directly comparable to analyses in this thesis for scenarios with intermediate decays via sleptons and W and Z bosons. The W and Higgs boson limits include a combination of the three lepton final state model, with two further separate models, meaning that it is also not directly comparable.

The CMS results for the slepton channel excluded $\tilde{\chi}_1^\pm \tilde{\chi}_2^0$ masses up to $\sim\!720\,\mathrm{GeV}$ and $\tilde{\chi}_1^0$ masses up to $\sim\!350\,\mathrm{GeV}$, almost identical to results obtained by ATLAS. The W and Z boson channel was able to excluded $\tilde{\chi}_1^\pm \tilde{\chi}_2^0$ masses up to $\sim\!220\,\mathrm{GeV}$ and $\tilde{\chi}_1^0$ masses up to $\sim\!60\,\mathrm{GeV}$. The combined W and Higgs boson channel excluded $\tilde{\chi}_1^\pm \tilde{\chi}_2^0$ and $\tilde{\chi}_1^0$ masses up to $\sim\!220\,\mathrm{GeV}$ and $\sim\!60\,\mathrm{GeV}$, respectively.
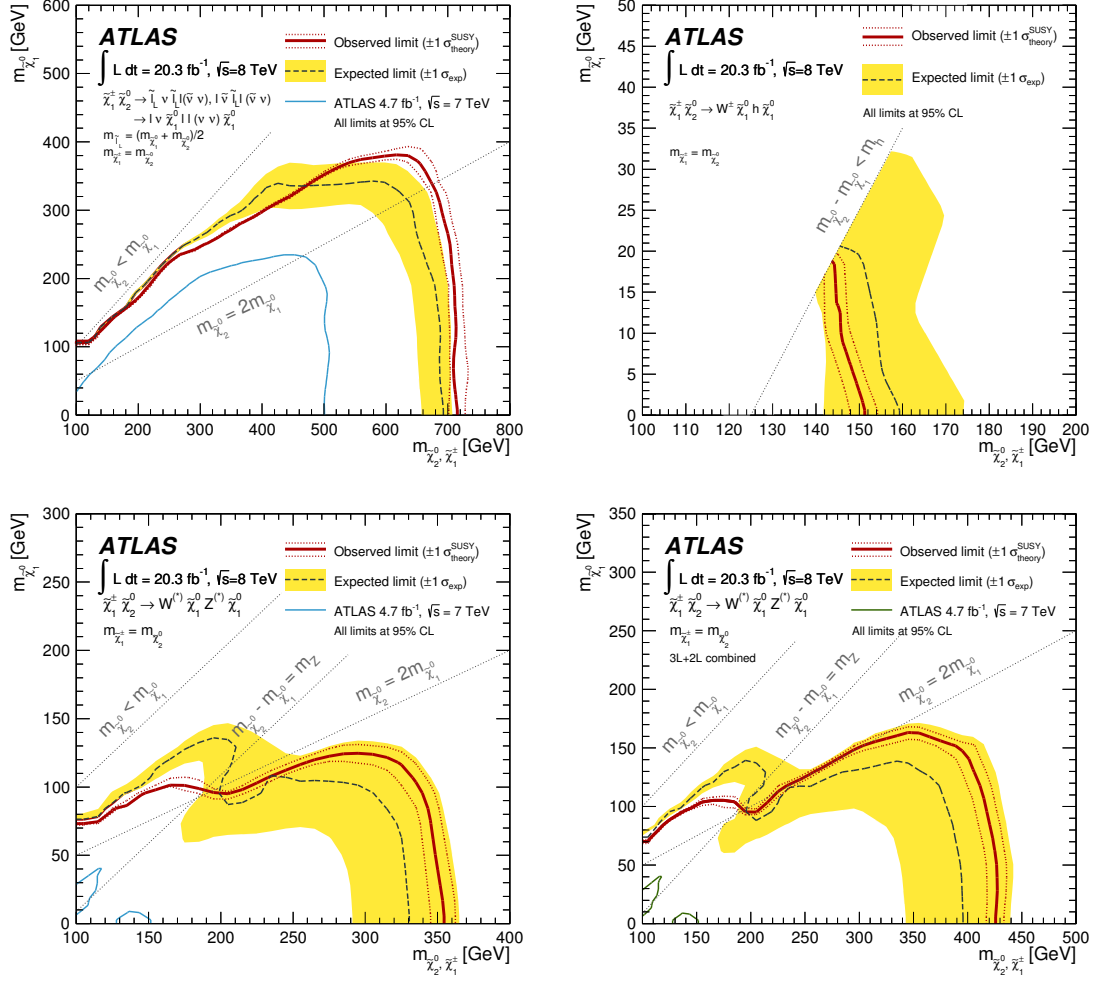
Fig. 2.17: Observed and expected exclusion limits on the $\tilde{\chi}_1^\pm \tilde{\chi}_2^0$ and $\tilde{\chi}_1^0$ masses in the context of SUSY scenarios with simplified mass spectra [33, 34]. Scenarios include intermediate decays via sleptons (top left), W and Higgs bosons (top right), W and Z bosons with exactly three leptons in the final state (bottom left) and a combination of this result with requiring two leptons in the final state (bottom right). The yellow band corresponds to the $\pm 1\,\sigma$ variations in the expected limit, including all uncertainties except theoretical uncertainties in the signal cross-section. The dotted lines around the observed limit illustrate the change in the observed limit as the nominal signal cross-section is scaled up and down by the theoretical uncertainty. All limits are computed at 95% confidence level. The observed limits that were obtained from ATLAS using $4.7\,\mathrm{fb}^{-1}$ of data at $\sqrt{s} = 7\,\mathrm{TeV}$ are also shown as blue or green lines [36].

2.3.6.2 Electroweak SUSY Search Motivation

Due to higher data statistics in Run-II, there is still clear motivation to continue the search. The increased centre-of-mass energy at the LHC ensures increased production cross-sections of all sparticles, previously shown in Figure 2.13, giving access to previously inaccessible masses, especially in the electroweak sector. The exclusion of squark and gluino masses well beyond the TeV scale [37] could also mean that they are too massive to be found at the LHC, meaning the direct production
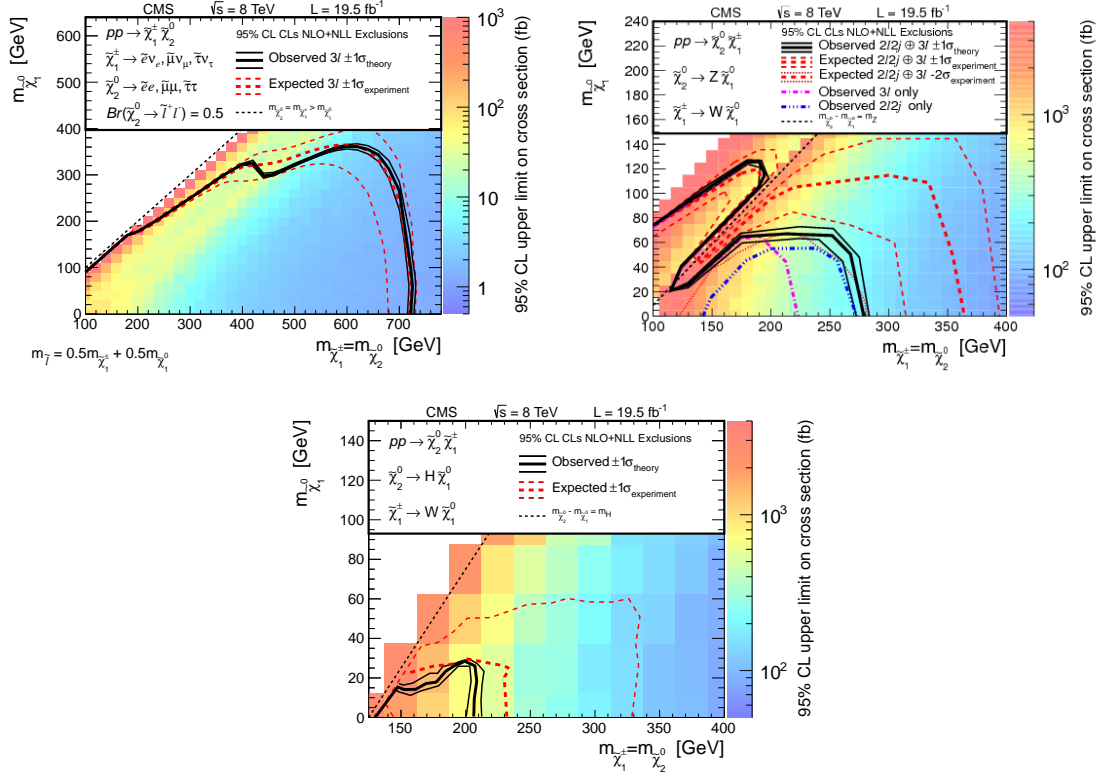
Fig. 2.18: Observed exclusion limits on the $\tilde{\chi}_2^0 \tilde{\chi}_1^\pm$ and $\tilde{\chi}_1^0$ masses in the context of SUSY scenarios with simplified mass spectra. Scenarios include intermediate decays via sleptons (top left), W and Z bosons (top right), and W and Higgs bosons (bottom). All limits are computed at 95% confidence level [35].

of electroweak gauginos and sleptons could dominate SUSY production, driving searches in this area. The electroweak signature with three leptons in the final state is also experimentally "clean" with little hadronic activity.

This chapter details the experimental setup of the acceleration process and the detector technologies used for identifying, measuring and selecting particles with the ATLAS experiment at the LHC.

3.1 The Large Hadron Collider

The LHC [38] is the world's largest and most powerful particle accelerator. Based at the European Organisation for Nuclear Research (CERN), it is located in a 27 km circular tunnel at varying depths between 45-170 m below the Franco-Swiss border.

The LHC was initially turned on in September 2008 with the first full data-taking period, known as Run-I, beginning in 2010 [39]. Although the LHC was originally designed to accelerate protons to a beam energy of 7 TeV, Run-I mainly operated with beam energies of 4 TeV and a centre-of-mass energy of $\sqrt{s} = 8$ TeV. In early 2013, a little later than originally planned due to the discovery of the Higgs Boson in 2012, the LHC went into a 2 year shutdown so that essential upgrades could be undertaken. In 2015, the upgraded LHC was restarted, now operating with beam energies of 6.5 TeV and a centre-of-mass energy of $\sqrt{s} = 13$ TeV. This new period of data-taking is known as Run-II and is due to continue until late 2018 [40].

3.1.1 Acceleration and Injection Chains

Protons that have been extracted from an ionised hydrogen source are gradually accelerated through a chain of smaller accelerators before reaching the energies

required to enter the LHC. The protons begin their acceleration journey in the linear accelerator, LINAC 2, where they are accelerated to energies of 50 MeV. They are then passed into the Proton Synchrotron Booster (SPB), taking them up to 1.4 GeV, followed by the Proton Synchrotron (PS), increasing them further to 25 GeV. The final accelerator before reaching the LHC is the Super Proton Synchrotron (SPS). The SPS accelerates the protons from 25 to 450 GeV before injecting two oppositely travelling beams into ultra-high vacuum pipes around the LHC's 27 km circumference. The typical time it takes from entering LINAC 2 to reaching the LHC is around 16 minutes. Once the beams enter the LHC it takes an additional 20 minutes for them to reach their nominal energy of 6.5 TeV.

The LHC also operates heavy ion runs, beginning the acceleration process in LINAC 3 and the Low Energy Ion Ring (LEIR), before following the same cycles for the proton run by entering the PS, SPS and LHC. Figure 3.1 depicts the full injection chain.

A time-oscillating electromagnetic field is employed at various points around the LHC which acts on both oppositely travelling beams. The beams are supplied in bunches of $\sim 10^{11}$ particles, which are synchronised to pass the electromagnetic fields during stages of maximum induced acceleration, which makes reaching energies of
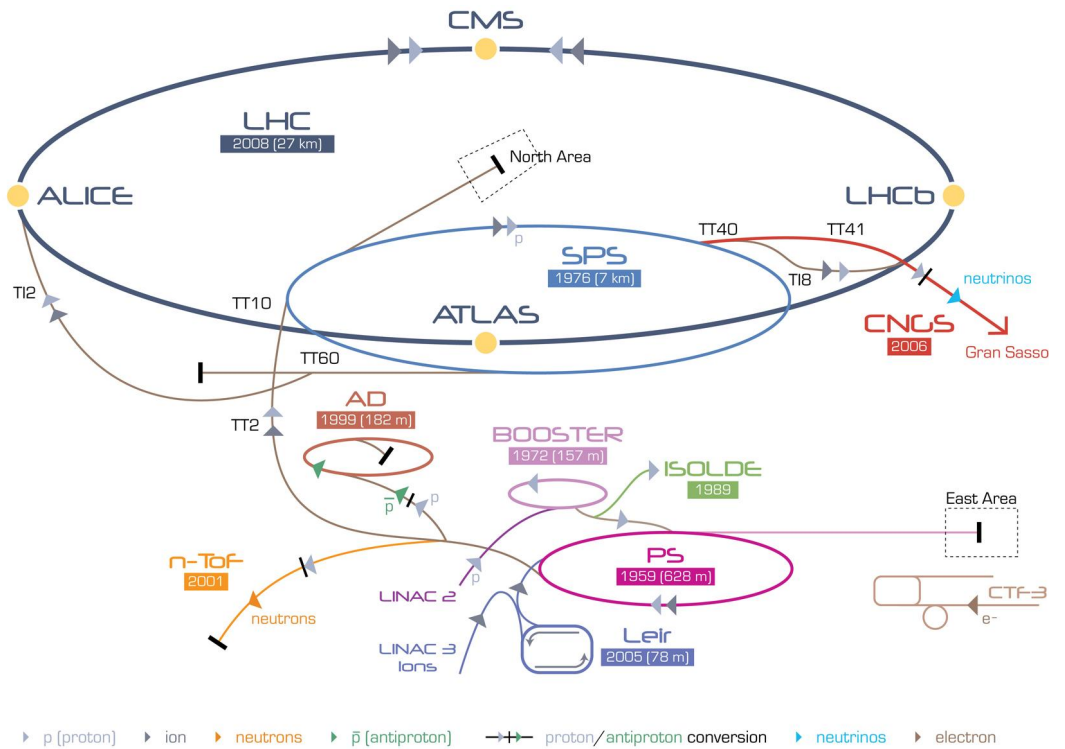
Fig. 3.1: Overview of the layout of the different accelerators and detectors at the CERN complex [41].

6.5 TeV possible. Once at the nominal energy, the beams can be stored and are able to travel around the LHC for several hours during data taking before needing to be replenished.

3.1.2 Collider Magnet System

The LHC uses superconducting magnets to keep the proton beams on a circular trajectory. There are 1,232 dipole magnets, each approximately 15 m long, which are responsible for bending the beams around the circular complex. The magnets are cooled by superfluid helium to temperatures as low as 2 K, giving rise to magnetic fields as large as 8 T which act perpendicularly to the direction of the beams.

During this process the beams can diverge. To remedy this a total of 392 superconducting quadrupole magnets, each 5-7 metres long, and 688 smaller sextupole magnets are employed to refocus the beam. The quadrupole magnets act like a lens to refocus the beam's width and height, while the sextupole magnets refocus the beam chromaticity caused by momentum changes in the bunches [42].

Finally, eight inner triplet magnet systems, each containing three quadrupole magnets, are located 23 m from the interaction point in both directions. They are used to 'squeeze' the beams, making them 12.5 times narrower, focusing them to the collision point.

3.1.3 Collisions

Collisions in the LHC occur at four interaction points located within the main detectors, ALICE (A Large Ion Collider Experiment) [43], ATLAS (Section 3.2), CMS (Compact Muon Solenoid) [44] and LHCb [45], a specialised flavour physics experiment. During Run-I and very early Run-II, bunches were brought to collision within these detectors every 50 ns, however this later increased to every 25 ns, resulting in over forty million collisions per second. The instantaneous luminosity, which refers to the number of particles per centimetre squared with the potential of colliding per second, can be defined as:

$$\mathcal{L} = f \frac{N_1 N_2}{4\pi \sigma_x \sigma_y}, \tag{3.1}$$

where N_1 and N_2 refer to the number of particles in each beam, f is the frequency of bunch crossings and σ_x and σ_y are the horizontal and vertical widths of the beam. This instantaneous luminosity can relate the event rate dN/dt to the cross section σ

of a specific process via:

$$\frac{dN}{dt} = \mathcal{L}\sigma. \tag{3.2}$$

For pp collisions during Run-II, the LHC operated with a peak instantaneous luminosity of $\sim 2 \times 10^{34}\,\mathrm{cm}^{-2}\,\mathrm{s}^{-1}$, an increase from the Run-I maximum of $7.7 \times 10^{33}\,\mathrm{cm}^{-2}\,\mathrm{s}^{-1}$. Figure 3.2 displays the total cumulative, or integrated, luminosity delivered by the LHC in 2015 and 2016, as well as the total recorded by the ATLAS experiment. Although data-taking will continue until late 2018, the results presented in this thesis only use data from 2015 and 2016.

The number of interactions per bunch crossing μ, known as *pile-up* [48], can be expressed as

$$\mu = \frac{\mathcal{L}\sigma_{\mathrm{inel.}}}{n_{\mathrm{bunch}}f_r}, \tag{3.3}$$

where $\sigma_{\mathrm{inel.}}$ is the total inelastic cross-section, n_{bunch} is the number of circulating bunches, and f_r is the bunch frequency. The mean number of interactions per bunch crossing $\langle \mu \rangle$ is averaged over a specific luminosity block. Figure 3.3 shows the luminosity-weighted mean number of interactions per bunch crossing in the ATLAS detector during 2015 and 2016, and during Run-I for comparison.

(a) Data-taking during 2015 [46]   **(b)** Data-taking during 2016 [47]
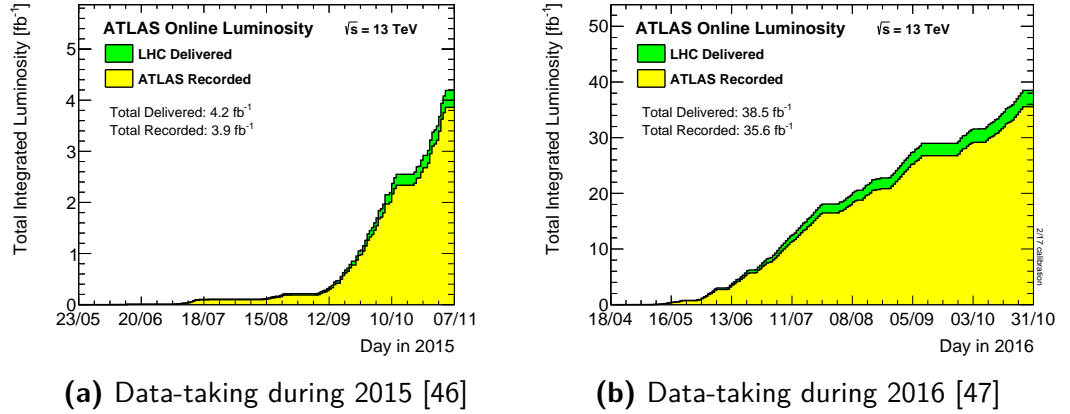
Fig. 3.2: Total integrated luminosity as a function of time delivered by the LHC and recorded by the ATLAS experiment during stable beams for pp collisions with a centre-of-mass energy $\sqrt{s} = 13$ TeV during (a) 2015 and (b) 2016. The differences between LHC delivered and ATLAS recorded luminosity results from inefficiencies of the detector trigger system, as well as the inefficiency of ramping up the tracking detectors when stable beams are declared by the LHC.

(a) Run-I (2011-2012) Luminosity [49]   **(b)** Run-II (2015-2016) Luminosity [50]
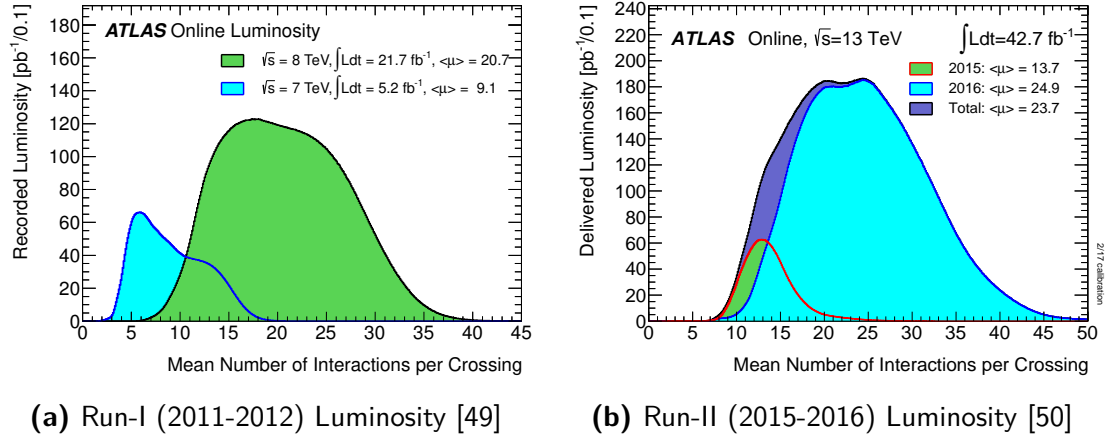
Fig. 3.3: Luminosity-weighted mean number of interactions per bunch crossing in the ATLAS detector during stable beams for *pp* collisions during (a) 2015 and 2016 and (b) 2011 and 2012.

3.2 The ATLAS Detector

The ATLAS detector [51] is a $44\,\mathrm{m}$ long and $25\,\mathrm{m}$ wide cylindrical arrangement of layered sub-detectors located approximately $100\,\mathrm{m}$ below ground at one of the LHC's four interaction points. With CMS, it is one of the two general purpose LHC detectors, being able to measure different properties of particles that are produced during high energy collisions with the aim to both prove the validity of the SM, such as the discovery of the Higgs boson, as well as searching for new physics beyond the SM, such as supersymmetry.

Figure 3.4 displays the ATLAS detector layout. Section 3.2.1 details the ATLAS detector geometry and nomenclature used to measure particle properties, while Sections 3.2.2 to 3.2.6 detail each sub-system separately.

3.2.1 Detector Geometry and Nomenclature

The origin of the ATLAS right-handed coordinate system is defined as the nominal particle-interaction point. The z-axis runs along the beam line, with positive z being termed the "A-Side", and negative z the "C-Side". The x-y plane is perpendicular to the z-axis with positive x pointing directly from the origin towards the centre of the LHC ring and positive y pointing directly up to the surface of the Earth.

Spherical coordinates are also adopted, with the azimuthal angle ϕ being measured around the beam axis, and the polar angle θ measured from the positive z-axis. The angle ϕ is invariant under a boost in the beam direction, however, additional coordinates known as rapidity y and pseudorapidity η are used instead of θ. Rapidity,
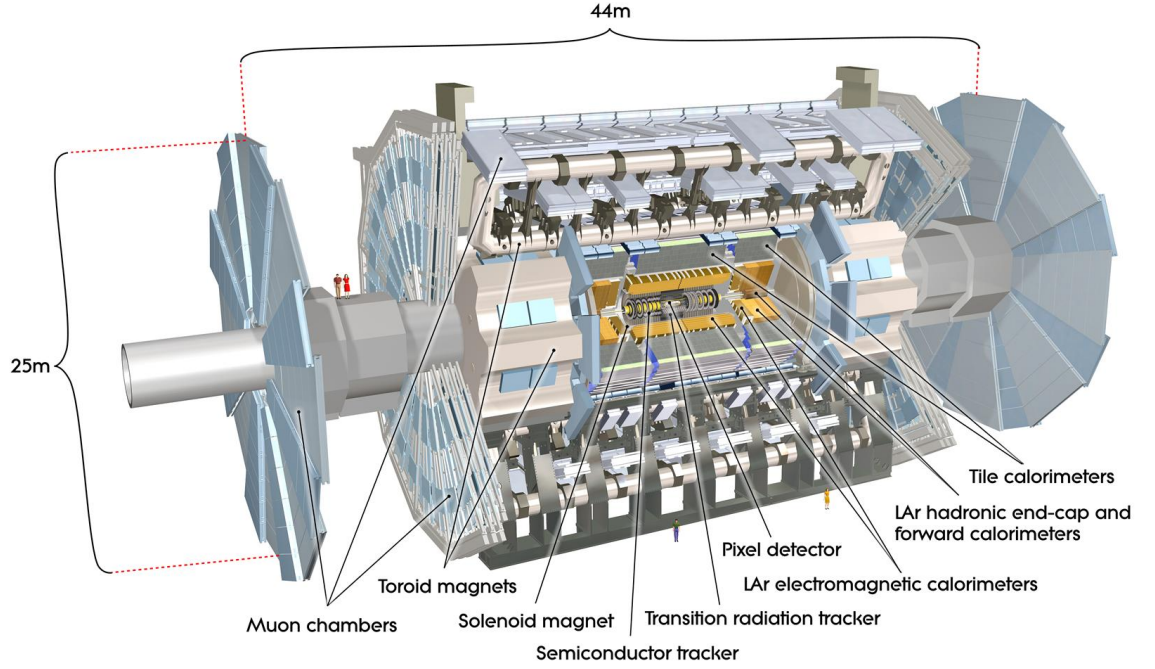
Fig. 3.4: Overview of the layout of the different subsystems of the ATLAS detector [51].

which can be used for massive objects, such as jets, is defined as

$$y = \frac{1}{2} \cdot \ln \left[\frac{E + p_z}{E - p_z} \right], \tag{3.4}$$

where E and p_z are the particle's energy and z-component of momentum, respectively. The sum and difference in rapidities is invariant under beam line boosts. However, particles in LHC collisions are assumed to be highly relativistic and therefore their masses are assumed to be negligible. For massless particles, rapidity can be reduced to pseudorapidity, defined as

$$\eta = -\ln \left[\tan \left(\frac{\theta}{2} \right) \right]. \tag{3.5}$$

The distance between two objects in psuedorapidity-azimuthal angle space is then defined as

$$\Delta R = \sqrt{\Delta \eta^2 + \Delta \phi^2}, \tag{3.6}$$

where $\Delta \eta$ and $\Delta \phi$ are the distances in η and ϕ.

Another widely used kinematic variable is the transverse momentum, p_{T}, measured

in the x-y plane and defined as

$$p_\text{T} = \sqrt{p_x^2 + p_y^2}, \tag{3.7}$$

where p_x and p_y refer to the x and y components of momentum. The use of this transverse component leads to the definition of missing transverse energy. Unlike the z-plane whereby initial momentum can not be known, the initial transverse momentum is known to be zero, and due to conservation of momentum, its final momentum must also be zero. A measured non-zero 'visible' momentum $\vec{p}_\text{T}^{\,\text{vis}}$ indicates that the event must have an equivalent missing transverse momenta $\vec{p}_\text{T}^{\,\text{miss}}$ with magnitude E_T^{miss}, caused by an unknown momentum component such that

$$E_\text{T}^{\text{miss}} = |\vec{p}_\text{T}^{\,\text{miss}}| = |\vec{p}_\text{T}^{\,\text{vis}}| = |\sum_i \vec{p}_T^{\,\text{vis},i}|, \tag{3.8}$$

where $\sum \vec{p}_T$ is the measured sum of all visible particles' transverse momenta components.

Other important kinematic variables used in the analysis are defined in Section 5.3.1.

3.2.2 Detector Magnet System

The ATLAS magnet system [51] is responsible for bending the trajectories of charged particles so that their charge and momentum can be determined by measuring their direction and curvature. Three separate magnets are employed at different stages throughout the detector. In-between the inner detector and the calorimeter (detailed in Sections 3.2.3 and 3.2.4), is the central solenoid, a 5.3 m long, 4.5 cm thick superconducting magnet wrapped around the beam pipe at a radius of 1.4 m. Its 2 T magnetic field acts parallel to the beam pipe and is the first to deflect the charged particles within the inner detector after the collision. On the outer edge of the detector, with an inner and outer diameter of 9.4 m and 20.1 m respectively, is the 25.3 m long barrel toroid, consisting of eight separate superconducting coils. It provides a 4 T magnetic field to the muon spectrometer, detailed in Section 3.2.5, acting perpendicularly to the beam-pipe. Also providing a 4 T magnetic field are the two 5 m long end-cap toroids, each 10.7 m in diameter and holding eight coils in a common cryostat. They are positioned at either end of the detector to take measurements of highly energetic muons travelling close to the beam pipe.

As with the LHC magnet system, the ATLAS superconducting magnets are also cooled by liquid helium. They reach temperatures of 4.7 K, which in necessary to achieve the required magnetic fields. Figure 3.5 displays the magnetic setup.
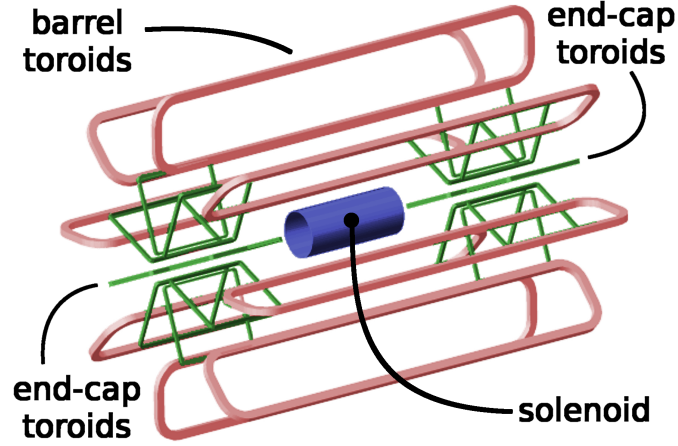
Fig. 3.5: Overview of the layout of the magnet system in the ATLAS detector [52].

3.2.3 Inner Detector

The Inner Detector (ID) is the closest sub-detector to the beam pipe and first to measure the products of collisions, including decays of short-lived particles. It is immersed in the 2 T magnetic field produced by the central solenoid magnet. There are three separate elements of the ID, as displayed in Figure 3.6, consisting of: a main barrel part, with concentric cylindrical layers; and, two disk end-caps, to ensure that all particles within a range of $|\eta| < 2.5$ and $p_\mathrm{T} > 0.5$ GeV can be measured. Primary- and secondary-particle vertices are first measured accurately in the Silicon Pixel Detector and Insertable B-Layer (IBL) before reaching the Semiconductor Tracker (SCT). The final layer is the Transition Radiation Tracker (TRT), which, in addition to tracking, can be used for particle identification.
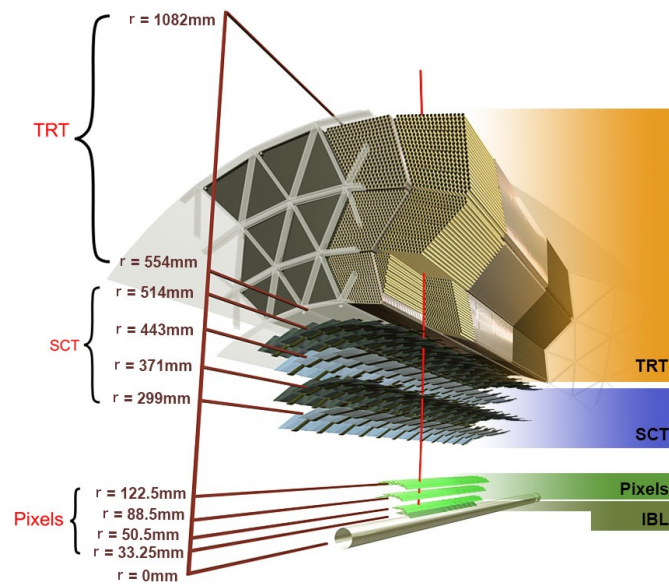
Fig. 3.6: A cross-section of the centre of the Inner Detector [53].

3.2.3.1 Silicon Pixel Detector

Both the Silicon Pixel Detector's barrel and end-caps have three layers of silicon pixels which are formed into 1,456 and 288 modules, respectively. Each module contains 46,080 readout channels, or pixels, each with a surface area of $50 \times 400\,\mu\text{m}^2$. Having pixels of this size allows the ID to make very high-resolution spatial measurements in high particle-multiplicity environments. Each pixel has separate circuits and electronics that record a current, or 'hit', when highly energetic charged particles knock out electron-hole pairs from the silicon. Three layers are needed to gain three space-points for each particle traversing the detector, which are then used to reconstruct the particle tracks and vertices.

For Run-II, the IBL [54], a fourth layer of pixels, was added to the outside of the beam pipe at a radius of $3.3\,\text{cm}$ to improve tracking precision by supplying an additional space-point and also to prevent damage to the inner layers due to higher radiation levels.

3.2.3.2 Semiconductor Tracker

The Semiconductor Tracker (SCT) barrel consists of four concentric layers of silicon detectors with 2,112 modules, while the end-caps have nine layers each and a total of 1,976 modules. Each module comprises two-sides of 768 silicon-strip detectors at a stereo angle of $40\,\text{mrad}$ to each other. For each traversing charged particle, both sides of the module will record a hit, and both hits are combined together to build a single space-point. The SCT layers are positioned so that a total of four space-points will always be recorded within the $|\eta| < 2.5$ range.

3.2.3.3 Transition Radiation Tracker

The Transition Radiation Tracker (TRT) barrel has three rings, each comprising 32 modules, while the end-caps each have 18 units, called wheels, with 224 layers. There are a total of 370,000 cylindrical drift tubes, or straws, that are $4\,\text{mm}$ in diameter and $1.44\,\text{m}$ in length, and are positioned parallel to the beam pipe in the barrel and radial in the end-caps. The straws are filled with gas made from Xenon (70%), for good X-ray absorption, and CO_2 (27%) and O_2 (3%), to increase the electron drift velocity and photon quenching. The straws are coated in aluminium to form a cathode, with a $30\,\mu\text{m}$ gold-plated tungsten wire anode through the centre. As charged particles traverse the TRT, the electrons from the ionised gas atoms drift towards the anode and register a hit. Polypropylene fibres (foils) interleave the straws in the barrel (end-caps), enabling the production of transition radiation in

the form of X-rays. The X-rays are then recorded by the straws as high-threshold hits and can thus identify electrons which have p_T between 1-150 GeV.

3.2.4 Calorimeters

The ATLAS calorimeter system [51] is designed to fully absorb particles and translate their energies into measurable quantities. The system is displayed in Figure 3.7 and consists of an inner electromagnetic calorimeter (ECal) with fine granularity, which absorbs photons and electrons, plus an outer hadronic calorimeter (HCal) with coarser granularity, to absorb particles that interact via the strong force. Finally, one encounters the forward calorimeter (FCal), which absorbs both electromagnetic and hadronic particles that are traversing the detector close to the beam pipe. The combined coverage of the calorimeters is $|\eta| < 4.9$. The only known particles that do not interact with the calorimeter system are neutrinos.

The first layer of both calorimeters is a high-density absorbing material that produces a shower of lower energy secondary particles. These secondary particles continue on to the second *active* material layer that measures the progressively degraded energy, either through ionisation or scintillation.

The radiation length of the material, X_0, which corresponds to the length (in cm) to reduce the energy of an electron by the factor $^1/_e$, is used to define the thickness of the ECal. The equivalent for the HCal is the nuclear interaction length, λ_I.
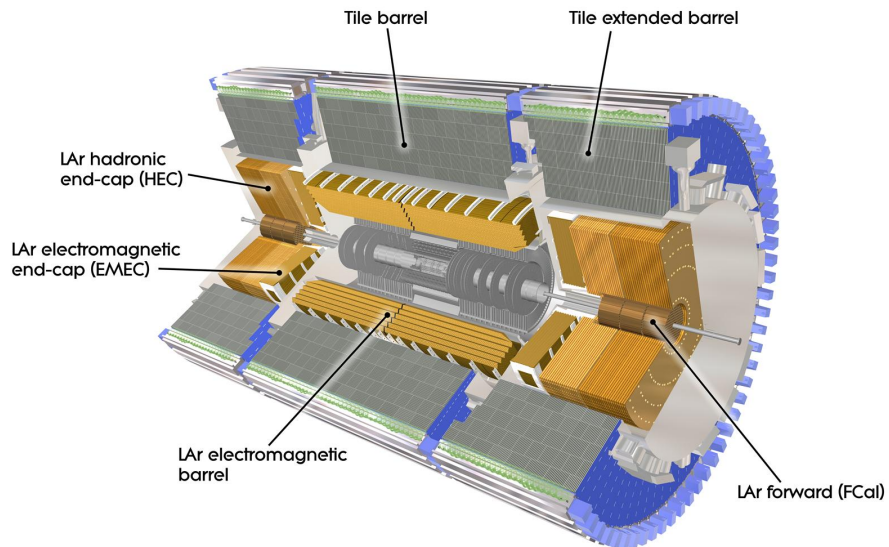
Fig. 3.7: An overview of the calorimeter system consisting of the ECal (LAr electromagnetic barrel and end-cap), HCal (tile barrels and LAr hadronic end-cap) and the FCAL [51].

The ECal and HCal are both able to contain the developing showers, which improves energy measurements and prevents particles *punching-through* to the muon spectrometer.

3.2.4.1 Electromagnetic Calorimeter

The ECal is divided into a barrel region (with range $|\eta| < 1.475$) and two end-caps, each in their own cryostat (with $|\eta|$ range between 1.375 and 3.2). They all use lead and liquid argon (LAr) as their absorbing and active materials, respectively. The LAr is cooled to $\sim 90\,$K and is ionised by the particle showers, allowing the liberated electrons to be collected and recorded by 101,760 copper electrode readout channels in the barrel, and 62,208 in either end-cap. The lead and LAr are structured in an accordion-shape, as shown in Figure 3.8, to provide complete ϕ coverage.

The barrel is 6.4 m in length, has an outer radius of 2.25 m and is 53 cm thick, corresponding to $> 22\ X_0$, while the end-caps are each 63 cm in length along the beam pipe, have an outer radius of 2.10 m and are 1.77 m thick, equivalent to $> 24 X_0$.

To reduce the amount of energy loss from particles going through matter before reaching the ECal, the ECal and the solenoid magnet share a common vacuum vessel. An additional thin active LAr presampler layer, with 10,880 readout channels in the $|\eta| < 1.8$ region, is included in front of the ECal, to correct for the energy that has been lost in the ID, solenoid and cryostat walls.
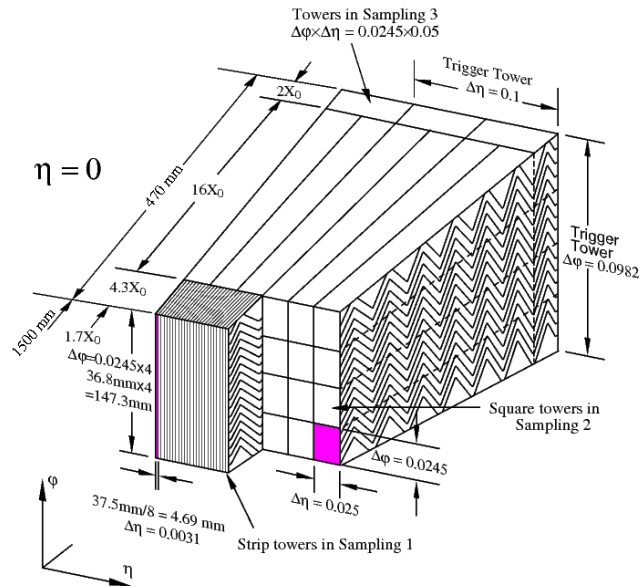
Fig. 3.8: Systematic view of the ECal accordion-structure [55].

3.2.4.2 Hadronic Calorimeter

The HCal is divided into a central barrel (with range $|\eta| < 1.0$), two moveable extended barrels either side (which, when fixed in place have an $0.8 > |\eta| > 1.7$ range), and two end-caps located directly behind the ECal end-caps sharing the same LAr cryostat (with $1.5 < |\eta| < 3.2$). The end-caps are positioned to overlap with the extended barrels, to account for the drop in material density at these locations. The barrels use steel as the absorber, interleaved with plastic scintillating tiles as the active medium. The scintillating tiles use photomultiplier tubes at either side as readout channels. Of these, 5,760 are located in the main barrel and 4,092 in each extended barrel. The end-caps use copper plates and LAr as their respective absorbing and active materials, connected to 5,632 readout channels each.

The central barrel is $5.8\,\mathrm{m}$ in length, while the two extended barrels are $2.6\,\mathrm{m}$ each. They all have an outer radius of $4.25\,\mathrm{m}$ and are $1.97\,\mathrm{m}$ thick. The end-caps are both $1.78\,\mathrm{m}$ in length along the beam pipe, are $2.03\,\mathrm{m}$ in radius and $1.70\,\mathrm{m}$ thick.

3.2.4.3 Forward Calorimeter

The two FCals are divided into an electromagnetic module and two hadronic modules, each $45\,\mathrm{cm}$ in length along the beam pipe, with a combined coverage of $3.1 < |\eta| < 4.9$. They are located in the same cryostats as the end-caps at a distance of $4.7\,\mathrm{m}$ from the interaction point. All modules use LAr as the active material, with copper plates and tungsten as the absorber for the electromagnetic and hadronic modules, respectively. Electrodes consisting of concentric rods and tubes parallel to the beam axis can readout 1,008 channels within the electromagnetic module, and 754 channels in the hadronic modules. The modules are $27.6\ X_0$ and $7.28\ \lambda_I$ deep, respectively. To avoid problems with ion buildup caused by higher particle fluxes, the LAr gaps in the FCals are made substantially smaller than in other parts of the calorimeter ($0.25\,\mathrm{mm}$ compared to $8.5\,\mathrm{mm}$ in the end-caps).

3.2.5 Muon Spectrometer

The outermost layer of the ATLAS detector is the Muon Spectrometer (MS) [51], designed to measure the tracks of penetrating muons. The MS is located within the $4\,\mathrm{T}$ magnetic field generated by the long barrel toroid, described previously in Section 3.2.2. As with the ID, the muons trajectories are bent so that their charge and momenta can be determined. The large barrel toroid magnet deflects the tracks where $|\eta| < 1.4$, the two magnet end-caps deflect the tracks between $1.6 < |\eta| < 2.7$, and a combination of both magnets in the "transition" region between $1.4 < |\eta| < 1.6$.
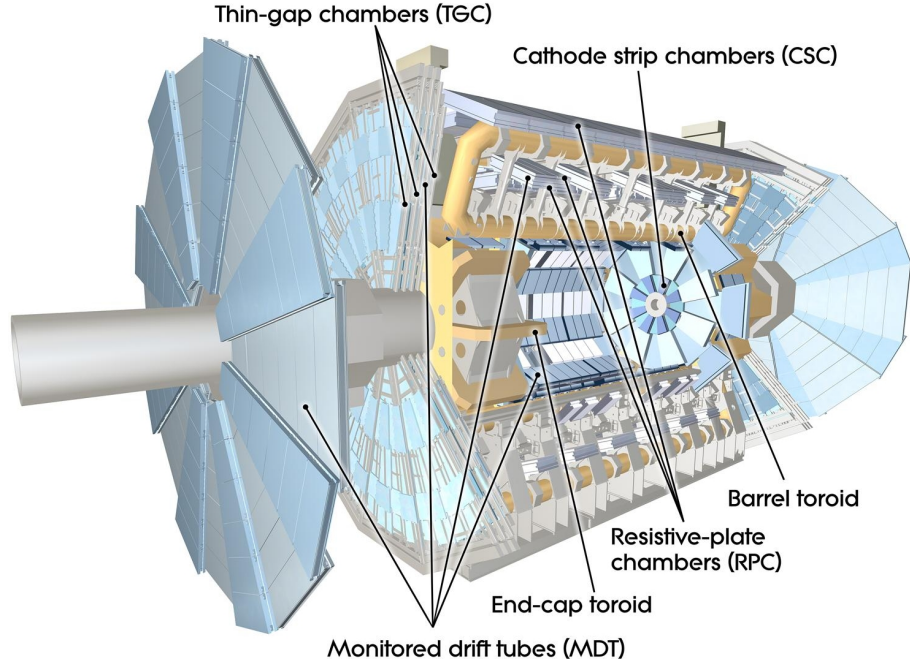
Fig. 3.9: An overview of the MS [51].

Tracks are measured by three layers of concentric chambers in the barrel region with an outer radius of 10 m, and three layers of chamber planes perpendicular to the beam pipe in the end-caps, at a maximum distance of 21.5 m from the interaction point, as shown in Figure 3.9. There are two types of chambers in the barrel, Monitored Drift Tubes (MDTs) and Resistive Plate Chambers (RPCs). The MDTs are also located in the end-caps, along with Cathode Strip Chambers (CSCs) and Thin Gap Chambers (TGCs).

3.2.5.1 Monitored Drift Tubes

The MDTs are pressurised drift tubes with a 29.97 mm diameter, filled with Argon (93%) and CO_2 (7%) gas. Once the gas is ionised by the muons, the free electrons drift towards and are collected by a central tungsten-rhenium anode wire which is kept at a potential to register a hit which provides precision measurements of the track coordinates for $|\eta| < 2.7$. There are three to eight layers of drift tubes which are able to take a total of twenty measurements for each track in both the barrel and end-caps.

3.2.5.2 Cathode Strip Chambers

Due to higher rates of particles in the end-cap regions, precision measurements are also performed by the higher granularity CSCs for $2.0 < |\eta| < 2.7$. The CSCs consist of two disks, each with eight multi-wire proportional chambers that have four CSC plates giving four measurements for an individual track. The chambers are filled

with Argon (80%) and CO_2 (20%) gas, with cathode strips aligned both parallel and perpendicularly to the anode wires, so that particle hit positions can be measured.

3.2.5.3 Resistive Plate Chambers

Muon triggering and secondary complementary coordinates, orthogonal to the precision measurements, are performed in the RPCs in the barrel for $|\eta| < 1.05$ and by the TGCs in the end-caps for $1.05 < |\eta| < 2.7$. The RPCs are gaseous parallel electrode-plate detectors filled with $C_2H_2F_4$ (94.7%), $Iso-C_4H_{10}$ (5%) and SF_6 (0.3%). The plates are made of a plastic laminate and are a distance of $2\,mm$ apart. An electric field between the plates allows avalanches to form along the ionised tracks towards the anode, which is read out by capacitive coupling to metallic strips. A maximum of six space-points are recorded for every track.

3.2.5.4 Thin Gap Chambers

Like the CSCs, the TGCs are also multi-wire proportional chambers. They are filled with CO_2 (55%) and n-pentane (45%) gas, with the cathode plates $2.8\,mm$ apart. The anode wires are only $1.8\,mm$ apart, which, along with a high electric field, leads to very good time resolution, which is essential for the triggering. The TGC provides nine space-points for each track.

3.2.6 Trigger, Data Acquisition and Computing Grid

The purpose of the Trigger and Data Acquisition (TDAQ) system [51, 56] is to reduce the rate of data stored from $\sim 40\,MHz$ down to a manageable $\sim 1\,kHz$ by only storing data for very high energy events that may contain potentially "interesting" physics. Implemented for Run-II, events pass through an online two-tiered trigger system consisting of the Level 1 (L1) trigger and the High Level Trigger (HLT), with each tier requiring events to meet increasingly demanding criteria. The flow of data through these online tiers is managed by the data acquisition system, which eventually passes all accepted events into data streams for offline physics analysis, trigger level analysis and monitoring or detector calibration. Objects that do not meet the requirements are permanently discarded. An offline four-tiered computing infrastructure (Tier-0,1,2,3, described in Section 3.2.6.4) is then employed to reconstruct the data from the streams into meaningful information.

The rest of this section will describe both trigger tiers, trigger software algorithms as well as the computing grid. A schematic representation of the TDAQ system and the first tier of the computing infrastructure is displayed in Figure 3.10.
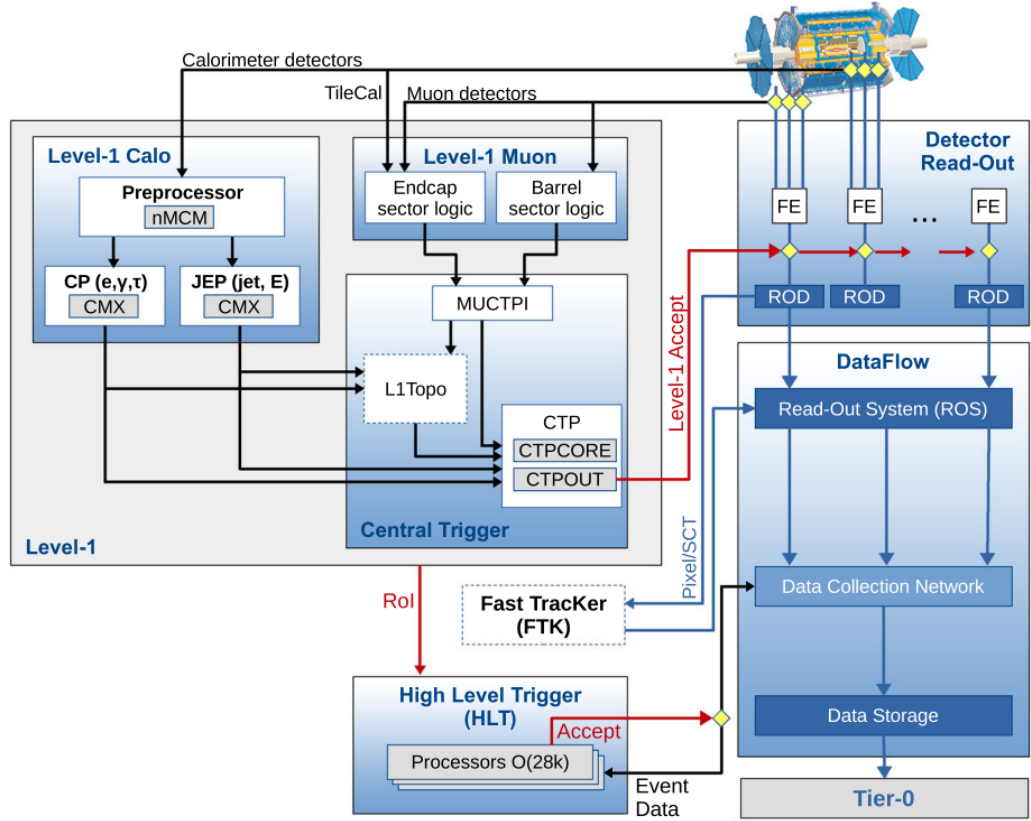
Fig. 3.10: A schematic of the ATLAS TDAQ system along with Tier-0 of the LHC computing infrastructure. All relevant acronyms are described in this section, all others are described in Ref. [57].

3.2.6.1 Level 1 Trigger

The L1 trigger is hardware based and relies on the calorimeters (L1Calo) and muon spectrometer (L1Muon) triggers to determine whether particles come from interesting high energy collisions. L1Calo can do this within low granularity *trigger towers* by directly measuring electron, photon and jet energies, or by inferring a weak interaction has occurred by identifying hadronically decaying taus using the distribution of their showers in core and isolated cones. L1Muon also infers an electroweak interaction when triggering on muons within its RPCs and TGCs. When the L1Calo or L1Muon trigger, data from the entire detector is readout by fast electronics and stored in front-end pipelines on or near to the detector to await further processing.

For Run-II, new topological trigger modules (L1Topo) were introduced to reduce the event rate before reaching a Central Trigger Processor (CTP), a necessity at increased luminosities. The CTP can only make selections based on the multiplicity and thresholds of candidate objects identified by the L1Calo and L1Muon triggers, whereas the new L1Topo can select events based on topological relationships, such as

angular variables and invariant masses. The L1Topo processes data using algorithmic firmware which is loaded onto integrated circuits (FPGAs) before being passed to the CTP. As a result, the L1Muon required a firmware upgrade to send coarse η, ϕ and p_T information to the L1Topo modules. The L1Calo also received an upgraded processing module for Run-II to deal with the higher occupancies in the calorimater system which causes an increase in pile-up events [58].

Once data from all L1 components reach the CTP, a trigger 'menu' made up of 512 distinct items (increased from 256 during Run-1) is implemented, each item being logical combinations of requirements for accepting events based on thresholds, multiplicities and L1Topo flags. Regions-of-Interest (RoIs) using η and ϕ coordinates obtained by the L1Calo and L1Muon are coupled with the passing events, which will later be used for reconstruction and tracking within the HLT. When an object meets all criteria, an *accept* signal is sent and event information is buffered in the Read-Out System (ROS) and sent along with the RoI information to the second-tier HLT. The total latency from the time of bunch crossing until the signal being sent is 2.5 µs.

To prevent an overwhelming rate of data flow and to avoid overlapping readout windows, the CTP enforces two types of dead-time: simple and complex. The simple dead-time limits the minimum time between two consecutive accepts which is set to 4 bunch-crossings (100 ns), while the complex dead-time restricts the number of signals within a given period. The full outcome is that the L1 trigger is able to reduce the rate of data storage from 40 MHz to 100 kHz.

3.2.6.2 High Level Trigger

To reduce the complexity and allow for dynamic resource-sharing between algorithms, Run-II amalgamated the Level 2 trigger and Event Filter farms from Run-I [59] into a single HLT stage which runs on several thousand CPUs. It has two subdivisions: fast tracking and precision tracking. During the 2015 and 2016 data taking periods, fast tracking was performed by the software based Fast Track Finder (FTF). The FTF provided approximately 2,500 independent trigger chains, each chain a sequence of offline-like pattern recognition algorithms executed within the RoIs which was good at reconstructing well-separated object tracks (e.g. electron, photon, muon, tau) and match them with their finer granularity calorimeter information. The muon spectrometer information was used in the FTF to to find *MS-only* muon candidates and back-extrapolate to the ID tracks within the RoI.

In 2017, a new hardware Fast TracKer (FTK) system [60] was installed to assist with the CPU challenges presented with increased luminosities. The aim of the FTK was to provide track reconstruction using particle look-up tables stored in

hardware memory chips for pattern recognition for $|\eta| < 2.4$. This allowed the rate of reconstruction of charged particles to be on par with L1 trigger rates. However as this thesis only presents results using data from 2015 and 2016, only trigger processes associated with the FTF are described within the following.

Following on from fast tracking is the slower precision tracking software which uses track (instead of pattern recognition) algorithms. Refined tracks and space-points are seeded from the FTF to reduce the CPU usage. Full access to object reconstruction information is available so that precision tracking is not limited by RoIs. This means that full calorimeter information can be used to fully reconstruct jets and global quantities such as $E_\mathrm{T}^\mathrm{miss}$. The identification of secondary vertices that can be indicative of a *b*-quark decay (Section 4.3.4), are also very well refined at this stage. As with the fast tracking stage, muons are again reconstructed as MS-only candidates but then combined with the refined RoIs identified by the FTF. The HLT has a latency of $300\,\mathrm{ms}$ and can reduce the rate of data stored from $100\,\mathrm{kHz}$ to $1\,\mathrm{kHz}$.

Once the event is accepted by the HLT, it is written into different data streams to be used for physics analysis (which is subdivided into muon, electron/photon, jet/tau/$E_\mathrm{T}^\mathrm{miss}$, and minimum bias streams), trigger level analysis and monitoring, or detector calibration. Streams are inclusive, meaning an event can feature in more than one, although the overlap between streams is kept to a minimum, with approximately only 10-15% of events being duplicated. To reduce bandwidth further, only the full event information for physics analysis is written to the streams, and only partially written for non-physics analysis.

3.2.6.3 Trigger Menus and Chains

The trigger menu [56] comprises a full list of all combined L1 and HLT trigger chains, which, as previously mentioned, are sequences of algorithms. These algorithms target a multitude of important physics signatures, reflecting the physics goals of the many ATLAS working groups.

The menu consists of primary trigger chains which are used for physics analysis; support trigger chains, used for efficiency and performance measurements, background estimation and monitoring; alternative trigger chains which run alternative online reconstruction algorithms for both the primary and support chains; and backup trigger chains that apply tighter selection requirements to reduce the rate of the primary chains if they become too high.

HLT chains consist of two types of algorithms, *feature extracting* (FEX) and *hypothesis*

testing (HYPO). FEX algorithms are used to reconstruct objects such as tracks or calorimetry clusters, while HYPO algorithms apply selection criteria to the reconstructed object. To reduce the processing time of the trigger system, features extracted from one chain can be reused in additional chains due to caching.

3.2.6.4 Computing Grid

Raw data from the online DAQ system is passed to Tier-0 [61], the first stage of the offline LHC computing grid, where it undergoes a first-pass reconstruction of raw data before being saved into numerous different file formats (raw and derived) and registered with the ATLAS Distributed Data Management (DDM) system. The data is then passed from Tier-0 onto 13 major Tier-1 computing centres around the world, which, not only store a large portion of raw data, but also perform and store final-pass event reconstruction. The data is then distributed to 155 Tier-2 centres, typically universities and scientific institutes that can provide sufficient storage and computing power to perform specific analysis tasks. The final tier, Tier-3, consists of local computing clusters used by individual scientists to access the grid and perform physics analysis.

4. Simulation and Reconstruction

The ATLAS software framework Athena [62], which is based on the Gaudi [63] framework developed by LHCb [45], is used for all aspects of the ATLAS software, including both the triggering of data in the HLT, as previously detailed in Section 3.2.6, and for producing Monte Carlo (MC) simulated data. Due to the complex nature of physics processes, detailed simulations of all processes involved have become crucial tools to understand particle interactions and decays, referred to as an "event" in what follows. These MC simulations can be used to model both background and signal processes, possibly in conjunction with other methods, such as data-driven methods of certain SM background estimation.

The production of simulated events is typically performed in three steps: event generation, which simulates events based on physics models as implemented in so-called event generators, described in Section 4.1; detector simulation, which propagates generated events through a detector simulation to mimic the response of the real detector, described in Section 4.2; and, physics object reconstruction, involving algorithms that are run on both real and simulated data, described in Section 4.3. A detailed schematic of the flow of MC generation is depicted in Figure 4.1, with each part being discussed in more detail in the following sections.
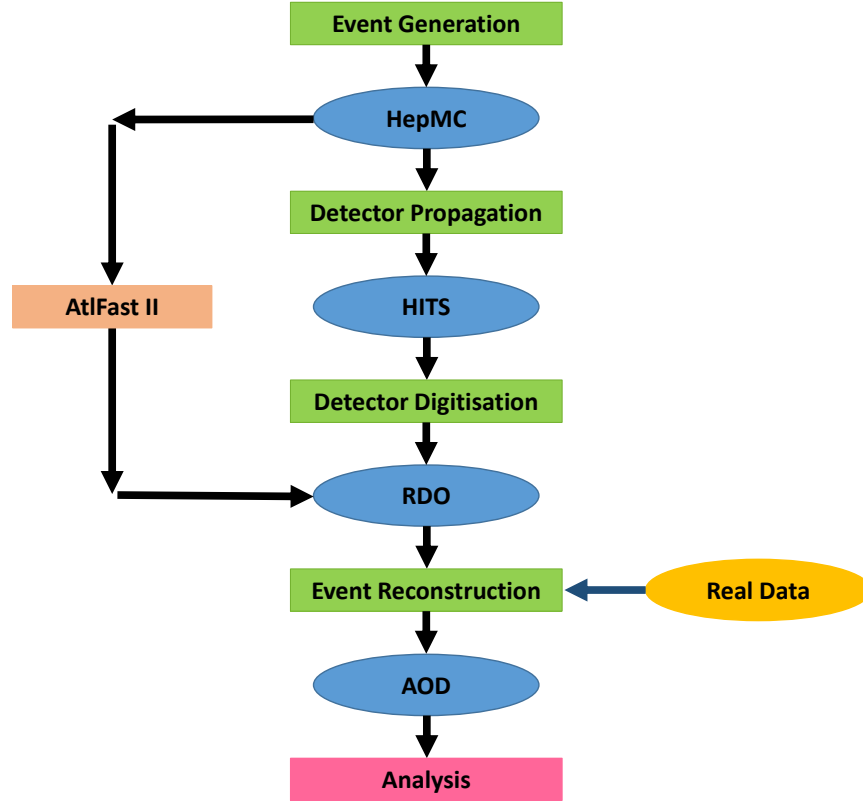
Fig. 4.1: A schematic of the full data production, showing processes in green, orange and pink and output-file-formats in blue.

4.1 Event Generation

Multiple event generators [64], each adopting varying theoretical approaches, can be used to simulate the many physics processes that are expected to be important during proton-proton collisions at the LHC. However, instead of the laborious task of simulating typical events and waiting for the production of one required type based on their cross-sections, simulations are built around a target process.

Processes result from the interactions between the partons in each of the protons. Partons include: the *valence quarks*, which give rise to the colliding particle's quantum numbers; gluons, which mediate the strong interactions between the valence quarks; and, virtual quark-antiquark pairs, known as *sea quarks*, which originate from fluctuations in the strong field within the hadron. The initial state of the hadron, whereby the momentum is shared amongst the partons, can be described mathematically by parton distribution functions (PDFs), which are briefly discussed in Section 4.1.1.

Target processes typically originate from central hard scattering events between

the colliding protons, defined by having either a large momentum transfer Q^2 (as defined in Section 4.1.1), large p_T, or a large mass scale. Particles involved in the hard scattering can emit *Initial State Radiation* (ISR) pre-scattering, or *Final State Radiation* (FSR) post-scattering. ISR and FSR are described as soft scattering processes. Another type of soft scattering includes *beam-beam* remnants produced from the breakup of the protons. All processes that are not directly involved in the primary hard scattering, such as ISR, FSR and beam-beam remnants, are described collectively as part of the *underlying event.*

The term *pile-up*, which was introduced in Section 3.1.3, is used to describe all non-primary interactions, including: additional *pp* collisions coming from the same bunch-crossing as the collision of interest (in-time pile-up); *pp* collisions from bunches before or after the collision of interest (out-of-time pile-up); random hits in the muon spectrometer from free neutrons and photons in the cavern during a typical run of the LHC (cavern background); muon sprays from protons scraping against the FCal (beam halo events); and, protons colliding with residual gas inside the beam-pipe (beam gas events).

Section 4.1.2 gives a brief overview of how general-purpose generators treat the different phases of SM event generation, while Section 4.1.3 looks at the generation of SUSY samples. Finally, Section 4.1.4 details the different generators used for the samples in this thesis.

4.1.1 Parton Distribution Functions

In high energy collisions, a proton's substructure is probed via *Deep Inelastic Scattering* (DIS) when an exchange boson transfers a four momentum of modulus q between two interacting partons. PDFs, denoted $f_i(x_i, Q^2)$, describe the probability of finding a constituent parton i, carrying a fraction of the protons total longitudinal momentum x. Additionally, PDFs depend on the transfer momentum, or energy scale, Q^2, which is equal and opposite to that of the exchanged boson $(-q^2)$.

As constituent partons are dominated by low energy, soft QCD effects, perturbative theory cannot be applied to determine the PDF's shape. Instead, PDF shapes are obtained by fitting observables to hard scattering data from the HERA, Tevatron-collisions and fixed target experiments. Dokshitzer-Gribov-Lipatov-Altarelli-Parisi (DGLAP) differential equations [65–67] are then used to compute the evolution of the PDF in Q^2, allowing the measured PDF to be transferred to experiments, such as the LHC, with much higher Q^2 regions. Currently, several theoretical groups work on determining PDFs, such as CTEQ [68] and NNPDF [69], both contribute to the

datasets presented in this thesis.

The total cross-section for a given process can then be defined as a combination of all allowed parton combinations, such that:

$$\mathrm{d}\sigma = \sum_{i,j} \frac{1}{x_i x_j s} |M_{ij}|^2 f_i(x_i, Q^2) f_j(x_j, Q^2) \mathrm{d}x_i \mathrm{d}x_j \mathrm{d}\Phi_n, \tag{4.1}$$

where i and j are the indices of the interacting partons with momentum fractions x_i and x_j, s is the centre-of-mass energy, M_{ij} is the matrix element (discussed in Section 4.1.2.1) for the given process, and Φ_n is a point in phase-space of the process.

4.1.2 Phased Simulation of pp Collisions

The generation of events can be described as an energy scale evolution and is split into a multi-phase process. The phases coincide with the transition from very high energies, where perturbation theory can be used as a good approximation, down to lower energies, which rely on phenomenological modelling, as depicted in Figure 4.2.
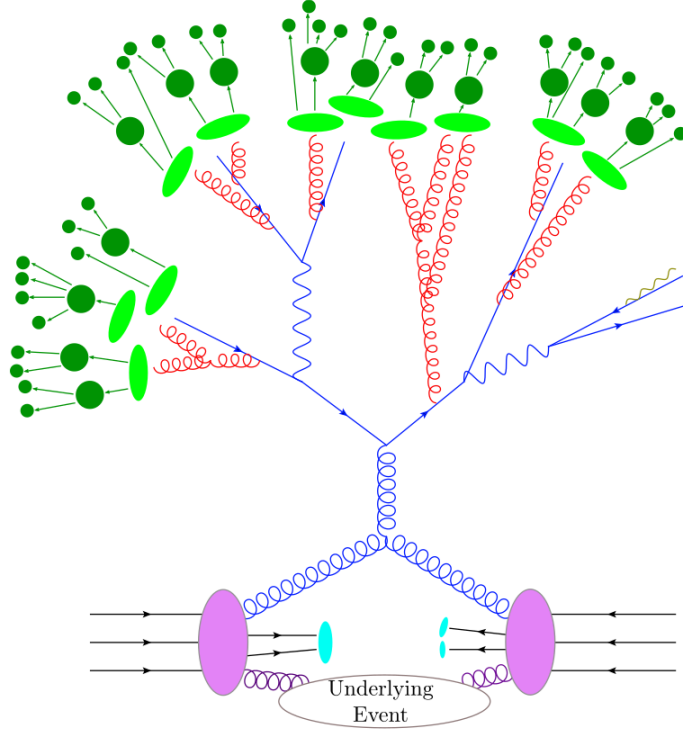
Fig. 4.2: A depiction of MC event generation, showing the colliding protons (purple), hard scattering processes (dark blue), parton showering (red), hadronisation (light green), hadronic or leptonic decays (dark green) and beam remnants (light blue).

4.1.2.1 Matrix Element

At high energy scales where $Q^2 > \mathcal{O}(1\,\text{GeV})$, the QCD running coupling reduces to the order of ~ 0.1 and can be described, as with all other interactions, from first principles using matrix elements involving quantum field perturbation theory. Equation 4.1 provides the input to the matrix element. All hard processes are considered, including *hard emissions* where a quark radiates a gluon ($q \rightarrow gq$), and when a gluon decays into two gluons ($g \rightarrow gg$) or a quark-antiquark pair ($g \rightarrow q\bar{q}$).

All multi-purpose event generators provide an extensive list of leading-order (LO) matrix elements in the framework of the SM and some BSM extensions. For higher-order final states, dedicated generators are employed. However due to their complexity, calculations are usually only carried out to next-to-leading order (NLO), and can be normalised to next-to-next-to-leading order (NNLO) if required. Next-to-leading logarithms (NLL) and next-to-next-to-leading logarithms (NNLL) can be used to increase accuracy [70]. For illustration, the Feynman diagrams in Figure 4.3 give an example of two production channels of a top quark pair from two interacting quarks via LO and NLO processes.

(a)   **(b)**
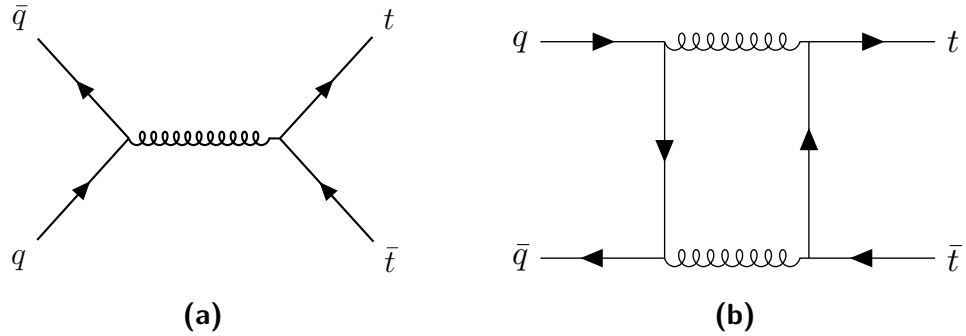
Fig. 4.3: Feynman diagrams showing the production of a top quark pair from two interacting quarks via (a) a LO channel, and (b) a NLO channel with a loop correction.

4.1.2.2 Parton Showers

As the energy scale softens, QCD processes become non-perturbative and can no longer be approximated by matrix elements. At this stage, phenomenological models are employed to simulate processes using algorithms based on step-wise Markov chains [71]. These algorithms probabilistically decide whether a gluon is radiated, or a quark-antiquark pair is produced, in what is termed parton showering. At intermediate Q^2, where emissions could be calculated via both perturbative and non-perturbative methods, Catani-Krauss-Kuhn-Webber (CKKW) [72] and Michelangelo L. Mangano (MLM) [73] algorithms are used to identify any double-counting, and assign emissions to either the matrix element, or parton shower.

4.1.2.3 Hadronisation

At very low energy scales, QCD colour confinement comes into effect, causing all evolved soft partons to hadronise (with the exception of the t-quark which decays too fast). As with parton showers, hadronisation is non-perturbative, requiring separate, independent phenomenological modelling. The two most common are the cluster model [74] and the Lund string model [75]. These models contain many more parameters than the parton showers, and thus are *tuned* using experimental data.

This phase of the generation also considers the decay of any unstable hadrons using phenomenological models based on information from the Particle Data Group's (PDG) Review of Particle Physics [3]. However, as this information is often incomplete (e.g. in the case of B-mesons), additional non-trivial parameterisation decisions are required to simulate decay chains.

The final state of the hadronisation phase consists of objects that are stable on collider timescales and can be propagated through a detector simulation.

4.1.2.4 Underlying Events and Pile-up

As already mentioned, underlying events collectively describe processes that were not directly involved in the hard scattering, while pile-up describes all non-primary interactions. The hadronisation of these processes are simulated using similar phenomenological models. As with the case of evolved, hard scatter, primary interactions, both models include a multitude of parameterisations, and thus are also tuned using experimental data [48, 76].

The modelling of underlying events is performed in the event generators and included within the MC samples. Only in-time and out-of-time pile-up is modelled in the event generators and later overlaid, while cavern background is reconstructed during the detector simulation, described in Section 4.2.

4.1.3 SUSY Generation

SUSY contains a large number of heavy new particles which give way to a multitude of different decay channels. The approach used to simulate the samples in this thesis starts by simulating the production of these new particles, usually only to a leading-order $2 \rightarrow 2$ scattering process. This is followed by the simulated decay using theoretical predictions based on the R-parity conserving simplified models described in Section 2.3.5.

4.1.4 Monte Carlo Generators

ATLAS simulated events are generated by a number of well known MC generators. The following gives a brief description of the relevant generators used to simulate all the processes within this thesis. An overview of which generators were used for specific background and signal processes be found in Section 5.1.

PYTHIA [77], HERWIG [78] and SHERPA [64, 79] are all general-purpose generators that evolve a hard scattering process through the full energy scale. PYTHIA and HERWIG use matrix element calculations at LO, while SHERPA calculates at both LO and NLO. Both HERWIG and SHERPA use the cluster model for hadronisation, while PYTHIA uses the Lund string model, both of which were introduced in Section 4.1.2.3. All of the generators include parton showers, underlying events and can produce complex multi-particle final states. In addition, PYTHIA is responsible for generating in-time and out-of-time pile-up events that are later overlaid during detector simulation (see Section 4.2).

The MADGRAPH [80] and POWHEG [81] generators are exclusively for simulating the hard scatter process using perturbative matrix element calculations, MADGRAPH at both LO and NLO (with version aMC@NLO [82]), and POWHEG at NLO. Both generators require interfacing with either PYTHIA or HERWIG for the ensuing soft scattering phenomenological modelling.

The EVTGEN package [83] interfaces with PYTHIA or HERWIG and is designed to simulate the more complex b-meson decays in the final state. As a result of this increased accuracy, all target processes in this thesis containing *b*-tagged jets (see Section 4.3.4) in the final state, employ EVTGEN.

The output-format for event generators is a HepMC file [84], which is passed on for detector simulation.

4.2 Detector Simulation

GEANT4 [85] is a toolkit, integrated within the ATLAS ATHENA framework, offering a two stage detector simulation. The first stage simulates the propagation of MC generated particles through a detector, described in Section 4.2.1, while the second stage simulates the detector's electrical response, or *digitisation*, described in Section 4.2.2. GEANT4 also offers a fast simulation method, described in Section 4.2.3. A recap of the schematic focusing on the detector simulation flow is presented in Figure 4.4.
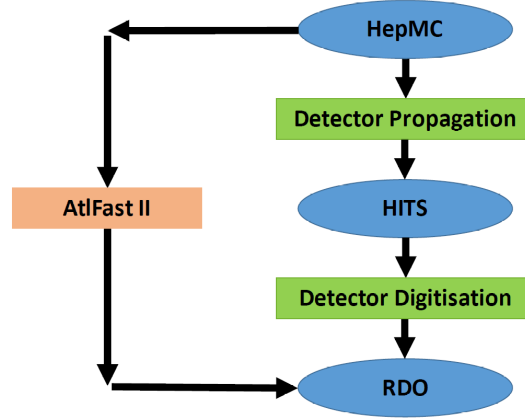
Fig. 4.4: A schematic of MC simulated data through detector simulation. Each stage is described in the following section.

4.2.1 Propagation

As MC generated particles propagate through a detector simulation, they are subjected to equivalent conditions as real particles within ATLAS. The simulated particles can undergo, for example, scattering, and intermediate particle decays, while the detector will react accordingly by simulating ionisation and radiation, etc. These detector interactions are recorded by GEANT4 as hits, in the form of track positions and energy depositions in the sub-detectors. Generated "HIT files" containing all simulated data, are passed on to be "digitised".

4.2.2 Digitisation

Digitisation subjects hits to a simulation of the detector's electrical response, producing digitised values for associated times, currents, voltages, etc. At this stage, to avoid unnecessary CPU usage caused by re-simulating independent events, the pre-generated pile-up interaction, and a model of the detector noise is overlaid. Cavern background, which includes low energy neutron physics too slow for standard MC simulation, is at this point simulated using high-precision phenomenological models. Data is saved into Raw Data Object (RDO) files, the default format used by the ATLAS TDAQ system, so that MC samples and real data can be processed by the same trigger and reconstruction software.

Generated in parallel to RDOs, are Simulated Data Object (SDO) files. These contain the "true" identity of particles at each vertex and all corresponding track and decay information. Truth objects can later be matched to reconstructed events to determine the efficiencies of algorithms to accurately reconstruct objects.

4.2.3 Fast Simulation

ATLAS uses the fast simulation software ALTFASTII [86] to reduce the full simulation time by one order of magnitude. The simulation of particle interactions with the detector has a CPU requirement of several minutes for every event, of which more than 90% is inside the calorimeters. To reduce this, ALTFASTII uses the FastCaloSim package [87] to provide a parametrised simulation of a particle's energy response and distribution in the ATLAS calorimeter, reducing CPU time to a few seconds for every event. This is particularly useful when large numbers of events are required, such as signal requests.

4.3 Object Reconstruction

Physics objects (electrons, muons, taus, jets and E_T^{miss}) are reconstructed from the digitised RDO files using reconstruction algorithms in exactly the same way for real data and MC simulated events. Initially, reconstruction is loose enough that the resulting objects can be used for many analyses. Additional selection criteria, or *object definitions*, based on performance study guidelines provided by ATLAS, can then be introduced by individual analysis groups to increase object purity for specific analysis needs. The object definitions used throughout this thesis are presented in the Analysis Strategy, Chapter 5. The output format, as previously shown in Figure 4.1 is an Analysis Object Data (AOD) file, ready for physics analysis.

In the following, Sections 4.3.1 to 4.3.6 present the reconstruction methods for each physics object relevant to this thesis. Figure 4.5 shows a pictorial representation of each of these physics object signatures in the different ATLAS sub-detectors. Details of the specific object definitions used in this thesis, are presented in Section 5.2.3.

4.3.1 Tracks and Primary Vertices

In this thesis, "tracks" are the reconstructed charged-particle trajectories within the ID, while "vertices" are the points at which two particles interact (e.g. pile-up) or where a single particle decays. A "primary vertex" is the vertex of the hardest event interaction. Tracks and vertices are reconstructed and combined first, before being matched to physics objects.

Three different algorithms are employed to reconstruct tracks [89]. Primary particles, defined as those from the initial *pp* interaction, or from short-lived particles that decay prior to the ID, use an *inside-out* approach. This involves identifying three consistent hits with $p_T > 1\,\mathrm{GeV}$ within the silicon pixel detector and/or SCT, and
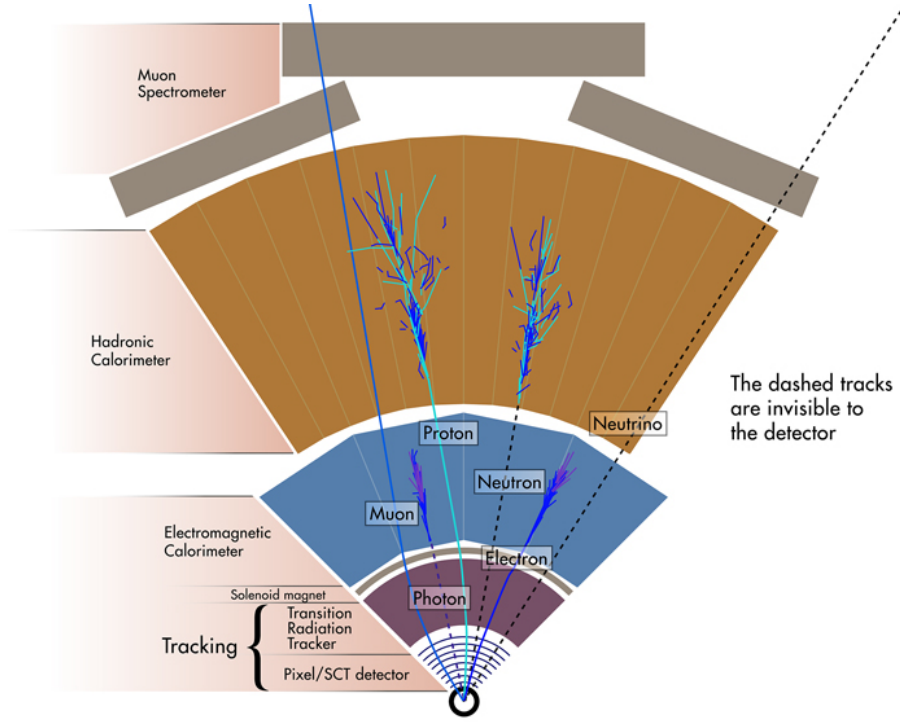
Fig. 4.5: A pictorial representation of each physics objects signatures in the different ATLAS sub-detectors [88].

using a combinatorial Kalman filter [90] to propagate towards, and extend into, the TRT, if compatible hits are present. A *back-tracking* algorithm, targeting late decays of neutral particles and photon conversions to e^+e^- pairs, operates in reverse, starting from the TRT and extrapolating back towards the pixel detector. Finally, TRT-only tracks are formed entirely from hits in the TRT.

The tracks, following a helicoid trajectory within the magnetic field, can be parameterised using a set of five track parameters relative to an origin. They include:

- Space co-ordinates: η and ϕ (see Section 3.2.1).
- Impact parameters: d_0 [mm], z_0 [mm], where d_0 is the distance of closest approach of the track to the origin, and z_0 is the component of d_0 on the z-plane.
- Transverse momentum: p_{T} [GeV], which equals $0.3 \cdot BR$, where B is the magnitude of the magnetic field in Tesla, and R is the bending radius in metres.

Vertices can be reconstructed by extrapolating at least two tracks back to a common interaction point. In order to suppress background events, such as particle decays not from a *pp* collision, primary vertices can be required to have more emanating tracks. Pile-up interactions can also lead to multiple vertices meeting the chosen criteria, in which case, the primary vertex is distinguished as having the largest $\sum p_T^2$

from all associated tracks. Tracks emanating from a measurably displaced secondary vertex, infers that a decay of a short-lived particle has taken place. These secondary vertices are important for physics object identification purposes.

4.3.2 Electrons

Electron reconstruction [91–93] begins by identifying energy deposits, or *seed-clusters*, within the central ECal region ($|\eta| < 2.47$) using a *sliding-window* algorithm [94]. This involves defining a fixed longitudinal ECal tower as a window corresponding to the granularity of the middle layer of the ECal ($3{\times}5$ cells of size $0.025{\times}0.025$ in $\eta \times \phi$), and moving this tower throughout the entire ECal, one step at a time. A seed-cluster is identified when the window contains a local energy maxima above $2.5\,\mathrm{GeV}$. After an energy comparison of nearby seeds, any duplicates will be removed.

Seed clusters are then geometrically matched to reconstructed tracks (see Section 4.3.1) by extrapolation from the middle ECal layer to the last track measurement in the silicon pixel detector. To form an electron candidate, tracks must have $|\Delta\eta| < 0.05$ from the reconstructed seed cluster, and meet $\Delta\phi$ requirements to account for bremsstrahlung losses. If more than one track meets these criteria, the track with the smallest ΔR is chosen. Clusters with no associated tracks, or with TRT-only tracks, can be identified or reconstructed as photon candidates.

The full electron cluster is then recomputed using larger $3{\times}7$ ($5{\times}5$) towers in the barrel region (end-caps) around the original seed cluster centre. The total energy of the cluster is determined using four contributions: the estimated energy deposit in the material in front of the ECal; the measured energy deposit in the cluster; the estimated energy deposit inside the ECal, but outside the cluster (lateral leakage); and, the estimated energy deposit beyond the ECal (longitudinal leakage).

Electron Identification

Electron candidates can be separated into two categories: *real* electrons; or falsely reconstructed *fake* electrons, such as muons, photons (both converted and unconverted), pion decays, and other hadrons. The reliability of reconstructing real electrons can be increased by applying additional cut-based selection criteria, designed to provide good separation between isolated or non-isolated real and fake electrons.

Three sets of identification selection criteria have been defined, Loose++, Medium++, and Tight++, each with increasing background rejection power. Loose++ focuses on shower shape variables of the middle ECalo layer and hadronic leakage. Medium++ adds to these with track quality, and track-cluster matching requirements. Finally,

(a) 2015 [95]   **(b)** 2016 [96]
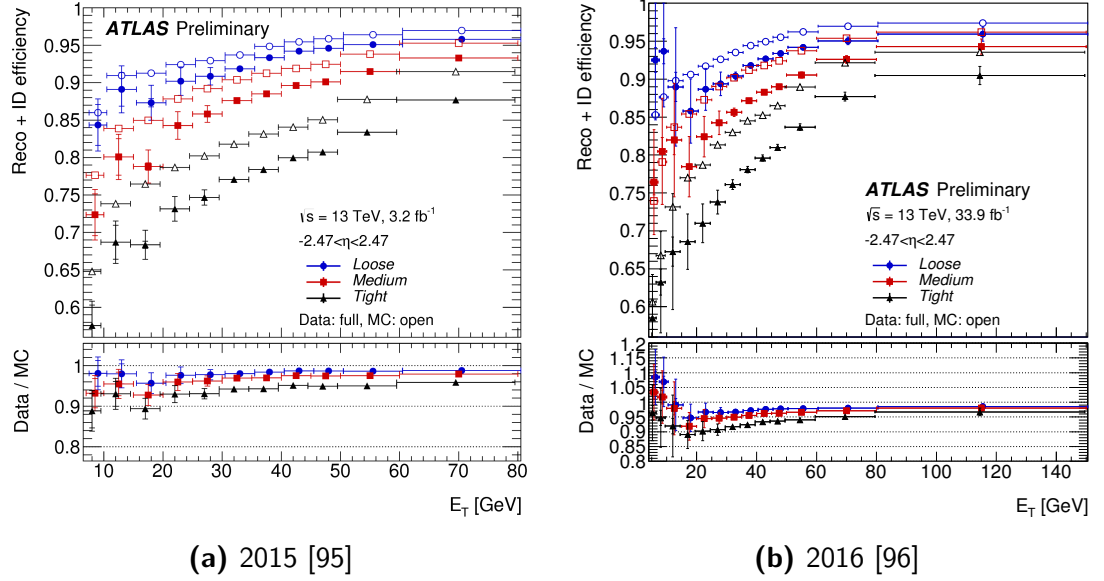
Fig. 4.6: Electron reconstruction and identification efficiencies as a function of E_T. Efficiencies have been measured in $3.2\,\text{fb}^{-1}$ from 2015 (left) and $33.9\,\text{fb}^{-1}$ from 2016 (right) of data recorded by the ATLAS experiment in 2016 at a centre-of-mass energy of $\sqrt{s} = 13\,\text{TeV}$ and compared to MC simulation. The reduction in efficiency seen in data is due to the MC simulations not properly representing the TRT conditions and mis-modelling of calorimeter shower shapes in the detector simulation.

Tight++ uses particle identification using the TRT, and discriminates against photon conversions via a IBL hit requirement. In the forward (and backward) regions (defined as $2.5 < |\eta| < 4.9$), where there are no tracking detectors, electron identification relies on cluster shapes, which give sufficient discrimination against hadrons, and have their own *forward loose* and *forward tight* selections. Figure 4.6 displays the electron reconstruction and identification efficiency using 2015 and 2016 data.

4.3.3 Muons

Muon reconstruction [97–99] begins by identifying tracks in the ID and MS independently. In the MS, muon track candidates are built by seeding segments in the middle layers where more trigger hits are available, and then combining with matching hits in segments from the inner and outer layers. All tubes crossed by a segment must contain a hit for the segment to be considered, and at least two segments are required to build a track (three in the transition region between the barrel and end-cap). Track quality is increased by performing a global χ^2 fit of hits. Hits contributing significantly to the χ^2 are removed and the fit is performed again.

Four different algorithms can then be employed to reconstruct the full muon information. A "combined" approach performs a global fit using hits from both the ID and MS within the tracking range $|\eta| < 2.5$. An outside-in pattern recognition

algorithm is preferred, starting from the MS and extrapolating back to the ID to match tracks that are also compatible in p_{T}. A "stand-alone" approach can be used for the $2.5 < |\eta| < 2.7$ range where ID tracks are not present. MS-only tracks are loosely extrapolated back to an interaction point on the beam-line, taking into account the estimated energy loss of the muon in the calorimeters. "Segment-tagged" muon reconstruction involves matching an ID track with a singular MS segment track, which can occur when the muons have low p_{T}, or in regions where the MS acceptance is reduced. Finally, to recover acceptance for muons in the $|\eta| < 1.0$ region, where the MS is only partially instrumented due to a crack, a "calorimeter-tagged" approach can be implemented. This involves matching an ID track to an energy deposit in the calorimeter that is compatible with a minimum-ionising particle.

Muon Identification

Muon candidates can also be non-prompt, originating from charged pion and kaon decays instead of from the primary vertex. As with electrons, a set of three identification criteria, *loose*, *medium* and *tight* are defined with increasing background rejection power. In the case of muons, medium muons define the default selection, minimising systematic uncertainties associated with reconstruction and calibration. The next selection are loose muons, with the aim of maximising reconstruction efficiency. Finally, tight muons are selected to maximise the purity of muons. A detailed description of each set of criteria is presented in Ref. [97]. Figure 4.7 displays the muon reconstruction efficiency using 2015 and 2016 data.

(a) 2015 [97] **(b)** 2016 [100]
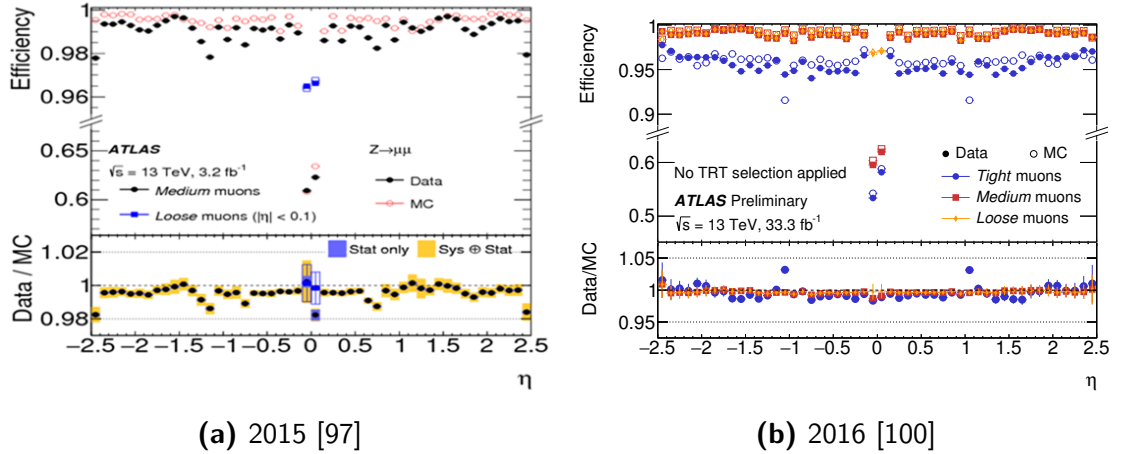
Fig. 4.7: Muon reconstruction efficiencies for loose/medium/tight identification algorithms measured in $Z \to \mu\mu$ as a function of η for muons with $p_{\mathrm{T}} > 10\,\mathrm{GeV}$. Efficiencies have been measured in $3.2\,\mathrm{fb}^{-1}$ from 2015 (left) and $33.3\,\mathrm{fb}^{-1}$ from 2016 (right) of data recorded by the ATLAS experiment in 2016 at a centre-of-mass energy of $\sqrt{s} = 13\,\mathrm{TeV}$ and compared to MC simulation. The bottom panel shows the ratio between expected and observed efficiencies.

4.3.4 Hadronic Jets

Jets, formed during the hadronisation stage (Section 4.1.2.3), can traverse the detector and leave tracks in the ID and energy deposits in both the ECal and HCal. Jet reconstruction [94, 101] begins by using a topological clustering approach to form *topo-clusters*. Cells that are identified as having energy exceeding pile-up and electronic noise by 4σ, are seeded, and neighbouring cells that have energy above 2σ are iteratively added to the topo-cluster. Unlike the sliding-window approach, which was used for the reconstruction of electrons and was limited in size, topo-clusters can grow accordingly, however, to avoid overlapping showers, any cell with energy above $500\,\mathrm{MeV}$ is used as a trial seed for a new topo-cluster and the cluster is split. The mass of all resulting topo-clusters is taken to be zero, and the energy is a summed total of all constituent cells. Topo-clusters are then calibrated using a *local cluster weighting* (LCW) based on whether they originated from either electromagnetic or hadronic showers.

The final stage of jet reconstruction is performed by the standard ATLAS anti-k_t algorithm [102]. LCW calibrated topo-clusters are inputted, and the two with a minimum distance parameter are iteratively combined. The distance parameter is defined as:

$$d_{ij} = \left(\frac{1}{k_{t_i}^2}, \frac{1}{k_{t_j}^2} \right) \frac{\Delta R_{ij}}{R^2}, \tag{4.2}$$

where i and j are the topo-cluster indices, k_t is the transverse momentum of each topo-cluster, ΔR_{ij} is the angular distance between the two clusters (see Section 3.2.1), and R is a free parameter determining the angular width of the, commonly cone-shaped, reconstructed jets. In this thesis, jets are reconstructed with $R = 0.4$. The iterative combination continues until all topo-cluster pairs satisfy $\Delta R_{ij} > R$.

Jet Identification

Jets originating from the initial *pp* collision must be identified from fake backgrounds, such as pile-up. Discriminatory selection criteria designed to suppress pile-up, can be made on energy and momentum fractions in the calorimeters and ID, respectively. Additional methods can be used to specifically associate jets with the primary vertex. A newly developed multivariate discriminant, the Jet Vertex Tagger (JVT) [103] has been built using two older jet variables that provide information on how much jet energy is associated with the primary vertex, making it a good discriminator. Tagging heavy flavour jets, such as those originating from *b*- and *c*-hadrons, can also

be used to identify jets from the initial primary interaction.

b-tagged Jets

Due to the longer lifetime of b-quarks ($\sim1.5\,\mathrm{ps}$), b-hadrons are able to travel a measurable distance from the primary vertex before decaying in cascades to lighter hadrons or leptons. The presence of a secondary vertex within the jet cone is significant in identifying b-tagged jets, or *b-jets*, where the impact parameters d_0 and R, can be used as discriminants (these differ from secondary vertices caused by c-hadron decays due to the shorter lifetime of c-quarks). If a secondary jet vertex is identified, reconstructed tracks within the jet cone can be examined for compatibility with b-hadron decays. Figure 4.8 shows a representation of a b-jet.
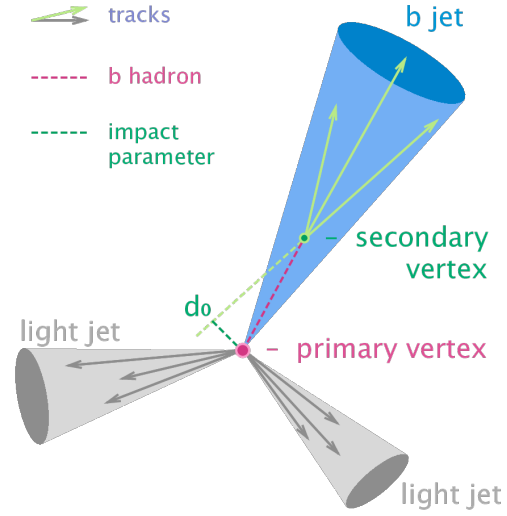
Fig. 4.8: Representation of a *b*-jet, showing a secondary decay vertex of a *b*-hadron within the jet cone, resulting in increased impact parameters. Two jets originating from light hadrons are also displayed [104].

The identification of b-jets used in this thesis is based on three distinct tagging algorithms, which use the secondary vertices and track reconstructions as input. These include an impact parameter-based algorithm (IP2D and IP3D), a secondary vertex reconstruction algorithm (SV), and a decay chain multi-vertex reconstruction (JETFITTER). The outputs of these three algorithms are combined into a multivariate discriminant (MV2), with the MV2c20 variant being used within this thesis. A detailed description of each set of criteria is presented in Refs. [105, 106].

4.3.5 Taus

Tau reconstruction [107, 108] is a more challenging task due to the lepton's heavy mass, shown previously in Table 2.3, and shorter lifetime ($\sim0.29\,\mathrm{ps}$), resulting in taus decaying in the beam-pipe before reaching the detector. Decays are either leptonic with a 35.2% probability, or hadronic 64.7% of the time. In ATLAS, leptonic tau decays are indistinguishable from light leptons originating promptly from the event, while the presence of hadronic taus must be inferred through the reconstruction of their decay products. As the searches in this thesis do not consider hardonic taus, their reconstruction is not discussed.

4.3.6 Missing Transverse Energy

Missing transverse energy E_T^{miss}, is defined as the imbalance of momentum in the x-y plane after calibration and resolution effects have been considered, where conservation is expected (see Section 3.2.1). The detection of E_T^{miss} infers the presence of weakly-interacting particles, such as the SM neutrino or stable supersymmetric particles.

E_T^{miss} reconstruction [109–111] involves summing the energy deposits in the calorimeters and reconstructed muons from the MS, calculated in the x (and y) axis as:

$$E_{x(y)}^{\text{miss}} = E_{x(y)}^{\text{miss, calo}} + E_{x(y)}^{\text{miss, }\mu}. \tag{4.3}$$

The calorimeter term is defined as:

$$
\begin{aligned}
E_{x(y)}^{\text{miss, calo}} = E_{x(y)}^{\text{miss, }e} + E_{x(y)}^{\text{miss, }\gamma} + E_{x(y)}^{\text{miss, }\tau} + E_{x(y)}^{\text{miss, jets}} + E_{x(y)}^{\text{miss, soft jets}} \\
+ E_{x(y)}^{\text{miss, }\mu(\text{calo})} + E_{x(y)}^{\text{miss, CellOut}},
\end{aligned}
\tag{4.4}
$$

where:

- $E_{x(y)}^{\text{miss, }e}$, $E_{x(y)}^{\text{miss, }\gamma}$ and $E_{x(y)}^{\text{miss, }\tau}$ terms are calculated energy deposits in the calorimeter cells associated with the electrons, photons and hadronic taus, respectively;
- $E_{x(y)}^{\text{miss, jets}}$ and $E_{x(y)}^{\text{miss, soft jets}}$ terms are calculated energy deposits from jets with $p_T > 20\,\text{GeV}$ and $7\,\text{GeV} < p_T < 20\,\text{GeV}$, respectively;
- $E_{x(y)}^{\text{miss, }\mu(\text{calo})}$ is calculated from the energy lost by muons in the calorimeters;
- $E_{x(y)}^{\text{miss, CellOut}}$ is all energy clusters not associated with reconstructed objects listed above.

The muon term is calculated as the sum of muon track momenta (within $\eta < 2.7$), and is defined as:

$$E_{x(y)}^{\text{miss},\mu} = \sum_{muons} p_{x(y)}^{\mu}. \tag{4.5}$$

Finally, the values of E_T^{miss} and its azimuthal co-ordinate ϕ_{miss} can be defined as

$$E_T^{miss} = \sqrt{(E_x^{miss})^2 + (E_y^{miss})^2}, \tag{4.6}$$

$$\phi_{miss} = \arctan(E_y^{miss}, E_x^{miss}). \tag{4.7}$$

4.3.7 Overlap Removal

One of the final stages of object reconstruction involves an *overlap removal* procedure [112] designed to discard objects that may have been reconstructed by several algorithms due to close spatial proximities in the detector. Like object definitions, the overlap removal procedure is defined independently by physics working groups to best suit specific analyses requirements. It is implemented at the same time as object definitions. Sections 5.2.3 details the criteria used for objects within this thesis.

5. Strategy for Three-Lepton SUSY Searches

The analyses presented in this thesis focus on the search for electroweak pair production of the SUSY particles $\tilde{\chi}_1^\pm$ and $\tilde{\chi}_2^0$, as detailed in Section 2.3.4, with exactly three electrons or muons, two $\tilde{\chi}_1^0$ particles and a neutrino in the final state. The motivation for this search is discussed in Section 2.3.6.2. Three intermediate decay channels are considered: via sleptons (Figure 2.14); SM W and Z bosons (Figure 2.15); and, SM W and Higgs bosons (Figure 2.16). These channels will be referred to as $\tilde{\ell}$, W/Z and W/h, respectively.

This chapter details the general search strategy adopted for all three channels. Sections 5.1 and 5.2 introduce the datasets used and common pre-selection requirements of events, respectively. Section 5.3 explains the different approaches used to define kinematic regions high in SUSY signals and low in SM background processes, termed *signal regions* (SRs). Section 5.4 details the methods used to estimate and validate

background processes, while Section 5.5 discusses associated uncertainties. Finally, Section 5.6 gives an overview of the statistical procedures used to interpret the results.

5.1 Datasets

The data recorded by the ATLAS detector, along with the Monte Carlo samples used for the SM backgrounds that can replicate the three-lepton signature final state, as well as the samples used for the SUSY signals, are presented. A discussion on the corrections applied to Monte Carlo samples is also given.

5.1.1 Recorded Data

The data used was recorded during 2015 and 2016 with a centre-of-mass energy of $\sqrt{s} = 13\,\mathrm{TeV}$. *Data Quality flags* are issued by each sub-detector for events recorded in *luminosity blocks*. Luminosity blocks are rejected if they have not been recorded during nominal detector conditions (i.e. stable beams, voltages, temperature, humidity), or are from inactive regions of the detector. Conversely, events that pass the flags join a *Good Runs List* (GRL), which is provided to analysts by the ATLAS Data Preparation Group [113]. This thesis presents main results for the $\tilde{\ell}$- and W/Z-mediated searches using the full integrated luminosity of $3.2\,\mathrm{fb}^{-1}$ of data on the GRL from 2015, as well as the full $32.9\,\mathrm{fb}^{-1}$ from 2016, giving a total integrated luminosity of $36.1\,\mathrm{fb}^{-1}$. An early Run-II $\tilde{\ell}$-mediated search also using the full integrated luminosity from 2015, and only $10.1\,\mathrm{fb}^{-1}$ from 2016, giving a subset total of $13.3\,\mathrm{fb}^{-1}$, is also presented.

5.1.2 Monte Carlo Samples

5.1.2.1 SM Backgrounds

Background processes with exactly three reconstructed leptons in the final state can be categorised as either *irreducible* or *reducible*. Irreducible backgrounds are those that have three real leptons from the primary vertex, termed *prompt*. Reducible backgrounds are those that have at least one fake lepton, typically a misidentified jet of hadronising quarks. The jets can themselves be misidentified as leptons, or the hadrons within the jet cone can decay to leptons that are detected, but not from the primary vertex, termed *non-prompt*. All irreducible backgrounds are modelled using event generated simulations, previously described in Chapter 4. All reducible background processes, use simulations to extract the efficiencies of real

Category	Background
Irreducible	WZ, ZZ, Top+Boson, Higgs, Triboson
Reducible	Boson+Jets, Boson+γ, Top Pair, Single Top

Tab. 5.1: Dominant backgrounds that can produce exactly three reconstructed leptons in the final state, categorised as either irreducible or reducible. Backgrounds are listed in ascending order of expected contributions.

and fake leptons which can be applied to modelling using data-driven techniques, described later in this Chapter, in Section 5.4.1. Table 5.1 displays the non-negligible backgrounds that can produce exactly three reconstructed leptons in the final state. A description of each process follows, with all branching ratios, $\mathcal{B}$, taken from the Particle Data Group's (PDG) Review of Particle Physics [3].

Dibosons: the most dominant background is the irreducible $WZ \to \ell\ell\ell\nu$ process, followed by the $ZZ \to \ell\ell\ell\ell$ (where the fourth lepton is either missed or misidentified). The W boson decays to an electron or muon 21.3% of the time, while the Z boson has a 6.7% branching ratio to electrons or muons. Feynman diagrams for both these processes are presented in Figure 5.1.
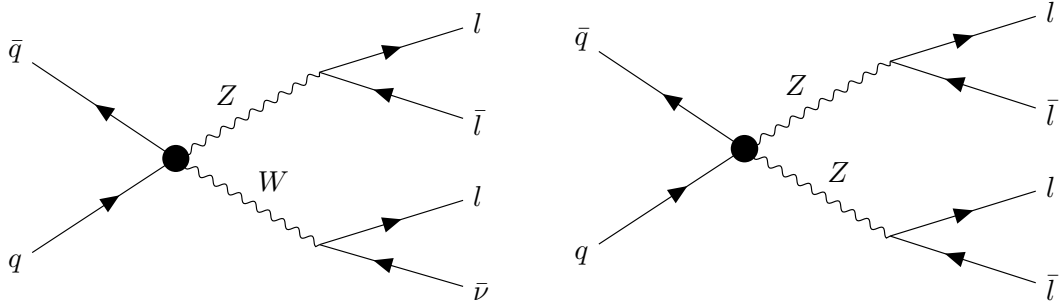
Fig. 5.1: Feynman diagrams for the two most dominant SM background processes: WZ (left) and ZZ (right).

Top + Boson: t-quarks originate predominantly in $t\bar{t}$ pairs produced in association with gauge bosons, such as the irreducible $t\bar{t}Z$, $t\bar{t}W$ and $t\bar{t}WW$ processes. When a $Z \to \ell\ell$ process is involved, as displayed in Figure 5.2 (left), only one t-quark is required to decay leptonically. In the absence of a Z boson, both t-quarks are required to produce leptons in order to give three real leptons in the final state. A single t-quark in association with a Z boson can also replicate the three-lepton signature.

Higgs: the SM Higgs boson can have three real leptons in the final state when produced as $t\bar{t}H$, ZH or WH. Along with a leptonic decay of at least one of the associated t-quarks or gauge bosons, the Higgs is required to decay di-leptonically,
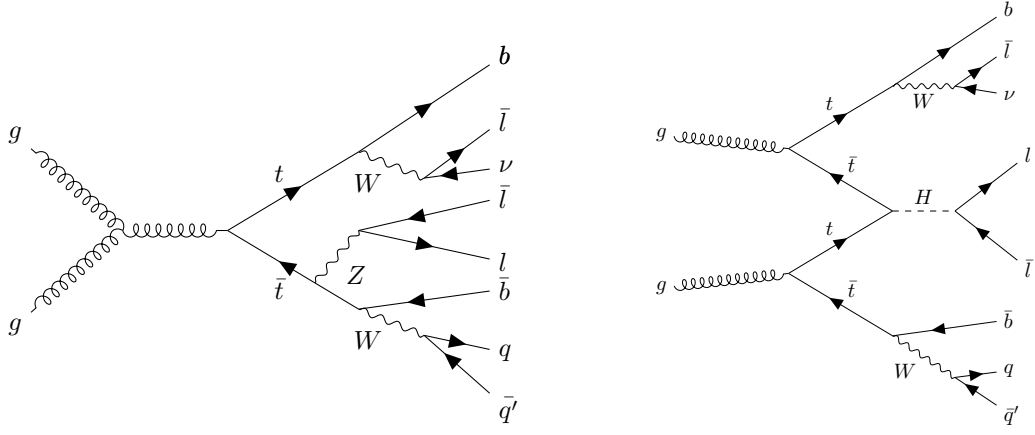
Fig. 5.2: Feynman diagrams for the two t-quark pairs in association with bosons: $t\bar{t}Z$ (left) and $t\bar{t}H$ (right).

either directly or via intermediate decay channels: $H \to WW$ ($\mathcal{B} = 21.4\%$); $H \to \tau\tau$ ($\mathcal{B} = 6.27\%$); $H \to ZZ$ ($\mathcal{B} = 2.62\%$); $H \to Z\gamma$ ($\mathcal{B} = 0.15\%$); and $H \to \mu\mu$ ($\mathcal{B} = 0.02\%$). A diagram of the $t\bar{t}H$ process is presented in Figure 5.2.

Tribosons: the remaining processes that contribute to the irreducible background are the multiple combinations of three gauge bosons, where up to six charged leptons can be in the final state (where extra leptons are missed or misidentified). Two examples are shown in Figure 5.3.
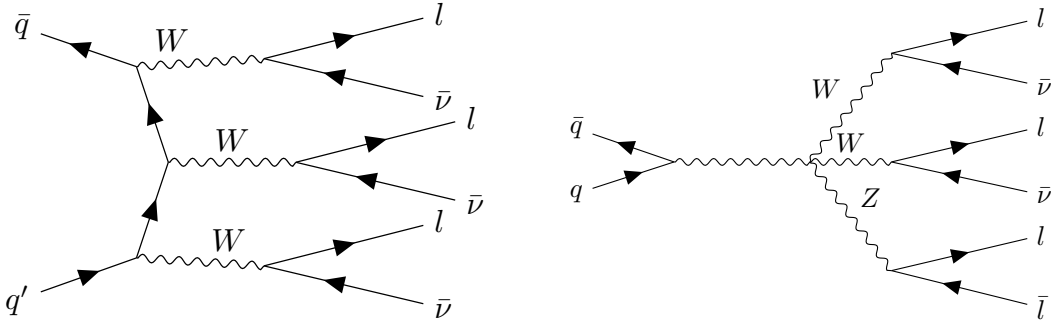
Fig. 5.3: Feynman diagrams for two examples of triboson processes producing at least three real leptons: WWW (left) and ZWW (right).

Boson + Jets: the dominant reducible background is Z+jets, displayed in Figure 5.4 (left), whereby the Z boson decays leptonically and a jet is misidentified as a lepton. The W+jets scenario can also reconstruct three leptons if two jets are misidentified, however this contribution is negligible.

Boson + γ: photon conversions decaying to non-prompt electron pairs, which, when in association with a Z boson, can give a significant contribution to reducible backgrounds, shown in Figure 5.4 (right).

Top Pair: t-quark pairs that are not produced in association with bosons, contribute
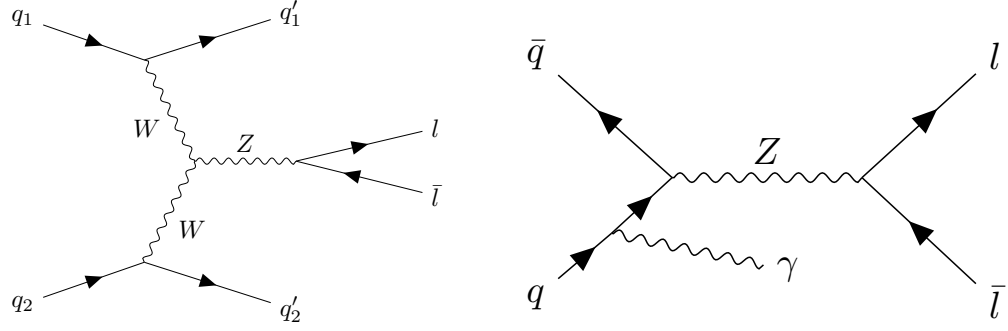
Fig. 5.4: Feynman diagrams for two dominant reducible backgrounds: Z+jets (left) and $Z + \gamma$ (right).

significantly to the reducible backgrounds. Decays can be: fully hadronic, $t\bar{t} \rightarrow Wb\,Wb \rightarrow qqb\,qqb$, with a branching ratio of 45.7%; via lepton+jets, $t\bar{t} \rightarrow Wb\,Wb \rightarrow \ell\nu b\,qqb$, which occurs 43.8% of the time; or di-leptonically, $t\bar{t} \rightarrow Wb\,Wb \rightarrow \ell\nu b\,\ell\nu b$, which accounts for a 10.5% branching ratio. In all instances jets are required to be misidentified as leptons.

Single Top: the last reducible background to be considered is the production of a single t-quark, either via: the exchange of a time-like W boson (s-channel), $q\bar{q} \rightarrow t\bar{b}$; an exchange of a space-like W boson (t-channel), $qb \rightarrow tq'$; or in association with a W boson emission (tW-channel), $gb \rightarrow tW$. Feynman diagrams are presented in Figure 5.5. In all cases, jets must be misidentified as leptons.

Table 5.2 gives a breakdown of the generators (described in Section 4.1.4) used to simulate non-negligible background processes.
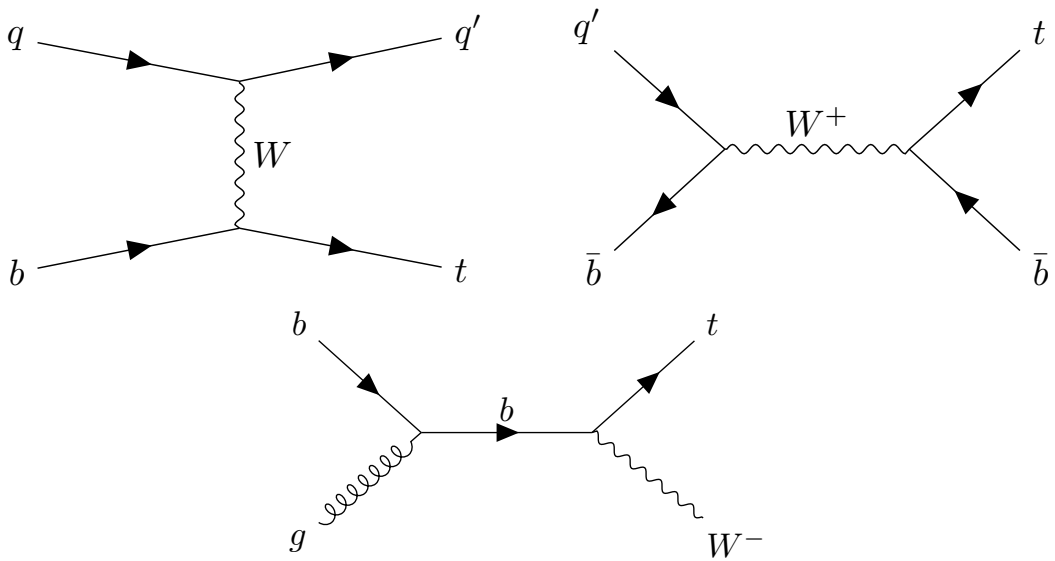
Fig. 5.5: Feynman diagrams showing the different channels of single t-quark production: t-channel (top left), s-channel (top right) and tW-channel (bottom).

Process	Generators	PDF set	Cross-section
$WZ(\to lll\nu)$	SHERPA 2.2	NNPDF3.0	NLO*
$ZZ(\to llll)$			
WWW, WWZ			
WZZ, ZZZ			
V+Jets			NNLO*
$WZ(\to lll\nu jj)$	SHERPA 2.1	CT10	LO
$ZZ(\to ggllll)$			
$V\gamma$			
$t\bar{t}V$	MADGRAPH5_aMC@NLO	NNPDF2.3	NLO*
tZ	+ PYTHIA		LO
$t\bar{t}H$	MADGRAPH5_aMC@NLO	CTEQ6 (CT10ME)	NLO
	+ HERWIG++		
VH	PYTHIA 8	NNPDF2.3	NLO
$t\bar{t}$	POWHEG + PYTHIA 8	CT10	NNLO+NNLL*
Single Top			NLO+NLL
Pile-up	PYTHIA	MSTW2008	

Tab. 5.2: Different generators and PDF sets used to simulate the dominant background processes with three reconstructed leptons in the final state, where V can be with a W or Z boson. All b- and c-hadron events are modelled using the EVTGEN package. The order of the calculations are also given. Starred terms indicate that the cross-sections were first calculated to LO and have been normalised to the final order displayed [114, 115].

5.1.2.2 SUSY Signals

In this thesis, simplified SUSY models (explained in Section 2.3.5) are considered, where mass ranges of the $\tilde{\chi}_1^{\pm}$, $\tilde{\chi}_2^0$ and $\tilde{\chi}_1^0$ sparticles that have not previously been accessible or excluded (see Section 2.3.6.1) are targeted. The difference in mass between the $\tilde{\chi}_1^{\pm}, \tilde{\chi}_2^0$ (where $m_{\tilde{\chi}_1^{\pm}} = m_{\tilde{\chi}_2^0}$) and the $\tilde{\chi}_1^0$, is termed the "mass-splitting" Δm. Intermediate mass-splittings range from 50-200 GeV, while high mass-splittings are above 300 GeV. Table 5.3 details the various combinations that have been used

Decay Channel	$m_{\tilde{\chi}_1^{\pm},\tilde{\chi}_2^0}$ [GeV]	$m_{\tilde{\chi}_1^0}$ [GeV]	Δm [GeV]
$\tilde{\ell}$	150-1200	0-1000	50-1200
W/Z	150-700	0-400	50-700
W/h	150-575	0-110	130-550

Tab. 5.3: Masses of signal samples considered in each of the three analyses. Intermediate mass-splittings range from 50-200 GeV, while high mass-splittings are above 300 GeV.

Group	Channel	Generator	PDF set	Cross-section
$\tilde{\chi}_1^\pm \tilde{\chi}_2^0$	$\tilde{\ell}$, W/Z, W/h	MADGRAPH +PYTHIA	NNPDF2.3	NLO+NLL

Tab. 5.4: Generators used to simulate the three intermediate decay channels presented in this thesis. The order of the cross-section calculations are also given [70].

for the $\tilde{\ell}$, W/Z and W/h channels. The generators and PDF sets employed for SUSY signals are presented in Table 5.4. To increase data statistics, events are required to have at least two light letpons, resulting in hadronic events from the W boson in the latter W/Z and W/h channels being suppressed.

5.1.2.3 MC Event Weight Corrections

Scale factors (SFs) are applied to MC samples to account for discrepancies that can arise between simulated events and real data. Pile-up distributions are matched to those observed in data. Lepton reconstruction and flavour-tagging efficiencies are provided by ATLAS performance groups [116, 117]. The uncertainties that arise from applying these SFs are described in Section 5.5.

5.2 Event Pre-selection

This section gives a description of the analysis preselection requirements, such as analysis-based object definitions, the trigger strategy and event "cleaning".

5.2.1 Trigger Strategy

As discussed in Section 3.2.6, all events used for physics analyses must pass trigger chains. Chains are chosen by individual analysis groups in accordance to analysis specific requirements. The triggers used for all analyses are listed in Table 5.5, and consist of a variety of single and di-lepton triggers, which ensures that all events have leptons above a given p_T threshold. Additional *offline* p_T thresholds are chosen to provide assurance that the particle p_T is above the trigger *turn-on-curve* (i.e. within the plateau of efficiency for the trigger it has fired). Multiple trigger chains are selected to target the various possible lepton flavour combinations; all events are required to pass at least one of these chains.

The trigger chains, presented in Table 5.5, are predominantly defined by the HLT triggers, which can apply "loose", "medium" and "tight" selection criteria, similar to the identification requirements used for object reconstruction in Section 4.3. The inclusion of "nod" indicates that no transverse impact parameter cuts are required.

Tab. 5.5: A list of trigger chains. The 2015 chains were used for both the $13.3\,\text{fb}^{-1}$ and $36.1\,\text{fb}^{-1}$ searches, while the 2016 chains for $13.3\,\text{fb}^{-1}$ are given in brackets. The offline p_T thresholds for each analysis are presented in Section 5.3.1.1 (Analysis Preselection).

Year	Flavour	Trigger Chain
	ee	HLT_2e12_lhloose_L12EM10VH
2015	$\mu\mu$	HLT_mu18_mu8noL1
	$e\mu$	HLT_e17_lhloose_mu14
	ee	HLT_2e17_lhloose_nod0
		(HLT_2e15_lhloose_nod0)
2016	$\mu\mu$	HLT_mu22_mu8noL1
		(HLT_mu20_mu8noL1)
	$e\mu$	HLT_e17_lhloose_nod0_mu14

The di-electron triggers also have L1 requirements whereby "VH" specifies that electrons are vetoed if they have left significant deposits within the HCal.

5.2.2 Event Cleaning

Having passed the trigger chains, events are subjected to further event quality requirements involving the removal of events that could still be considered invalid for physics analysis. Data is already required to pass the GRL, as mentioned in Section 5.1, however additional requirements are imposed to both data and simulated events. Reasons for removal could be: low quality muon events from cavern background; fake muons caused by energetic jets punching through into the MS; or, badly measured ID tracks wrongly matched to the MS. More explicitly, any events with a muon that does not satisfy the impact parameters $z_0^{PV} < 1\,\text{mm}$, $d_0^{PV} < 0.2\,\text{mm}$ and $\sigma_{q/p}/|q/p| < 0.2$ are removed (where PV refers to the primary vertex). Real and fake jets can also be reconstructed from non-collision background processes leaving energy deposits in the calorimeters. These can be removed by making requirements on known jet properties.

5.2.3 Object Definitions

The final stage of preselection is the assignment of analysis-based object definitions. This section is dedicated to defining the main physics objects, as outlined in Sections 4.3.2 to 4.3.6. They are included as a separate section because they are unique to the analyses presented in this thesis. Loose criteria, provided by ATLAS, are first implemented to define *baseline objects*, which undergo the overlap removal procedure introduced in Section 4.3.7. These baseline objects can be used for data-driven

background estimation and validation purposes (discussed in Section 5.4.1). Once passed overlap removal, events are subjected to more stringent criteria to define *signal objects*, a subset of baseline objects with higher purity and better isolation. Signal object definitions are typically provided by ATLAS working groups so that harmonised physics analyses can be performed.

Overlap Removal

The following overlap removal conditions are applied to all baseline events in the order presented:

1. Electrons sharing an ID track with muons are discarded;
2. Electrons within $\Delta R < 0.2$ of a b-jet are discarded, as it is likely to be from a semi-leptonic b-hadron decay;
3. Light jets (non-b-jets) within $\Delta R < 0.2$ of an electron candidate are discarded, as they most likely originate from electron showers depositing energy in the calorimeters;
4. Electrons within $\Delta R < 0.4$ of a jet candidate are discarded to suppress electrons from the semi-leptonic decays of b- and c-hadrons;
5. Jets with fewer than three associated tracks are discarded to suppress non-prompt events;
6. Jets are discarded if they are within $\Delta R < 0.2$ of a muon, or if the muon is matched to a track associated with the jet, and the muon carries 70% of the total traverse momenta of all the jet tracks;
7. Muons within $\Delta R < 0.4$ of a jet candidate are discarded to suppress muons from the semi-leptonic decays of b- and c-hadrons.

Light Leptons

Baseline electrons and muons are required to have $p_\text{T} > 10\,\text{GeV}$, with electrons within $|\eta| < 2.47$, and muons within $|\eta| < 2.7$. Both need to pass loose likelihood based identification criteria. Signal electrons and muons add to the baseline selections by requiring a total p_T efficiency of 95% at $25\,\text{GeV}$, and up to 99% at $60\,\text{GeV}$, termed *GradientLoose* Isolation [118], while also having impact parameters in the range of $|z_0\sin\theta| < 0.5\,\text{mm}$ and $|d_0/\sigma_{d_0}| < 5$ (3) for electrons (muons). Signal electrons also tighten the identification criteria by requiring a medium likelihood, while signal muons decrease the $|\eta|$ range to < 2.4.

Hadronic Jets

Baseline jets use the anti-k_t 4EMTopo algorithm, with a radius parameter $R = 0.4$, and are required to have $p_T > 20\,\text{GeV}$, with $|\eta| < 4.5$. Signal jets reduce the $|\eta|$ range to < 2.4 and also implement a $|\text{JVT}| > 0.59$ requirement for jets with $p_T < 60\,\text{GeV}$ in order to suppress pile-up events. Signal b-jets use the MV2c10 tagger algorithm, detailed in Section 4.3.4, with a 77% average efficiency.

Missing Transverse Energy

The missing transverse momentum vector $\vec{p}_T^{\,\text{miss}}$, with magnitude E_T^{miss}, is the negative vector sum of all identified physics objects' (electrons, photons, muons and jets) transverse momenta, and an additional soft term (see Section 4.3.6). All physics objects are required to satisfy the baseline criteria defined above. In addition, jets are also required to originate from the hard scatter using the JVT.

5.3 Signal Region Optimisation

All events that pass the preselection criteria are ready for physics analysis. Multiple signal regions (SRs) can be defined, designed to be high in SUSY signal contributions and low in background processes. Each SR is optimised to target different areas of parameter-space, typically with either high ($> 300\,\text{GeV}$) or intermediate ($50\text{-}200\,\text{GeV}$) mass splittings between the $\tilde{\chi}_1^\pm \tilde{\chi}_2^0$ and $\tilde{\chi}_1^0$. A set of selections, or cuts, can be made on kinematic variables to isolate the signal by only discriminating against and suppressing background processes. Variables used within this thesis are described in Section 5.3.1.

The amount of signal isolation within a SR can be numerically measured as a significance value Z, which indicates the likelihood that an excess is from a real signal, rather than background fluctuations. In its simplest form, significance can be expressed as:

$$Z_N = \frac{N_{\text{sig}}}{\sqrt{N_{\text{bkg}} + (\sigma_{\text{bkg}} N_{\text{bkg}} + 1)^2}}, \tag{5.1}$$

where N_{sig} is the number of expected signal events, N_{bkg} is the number of expected background events, and σ_{bkg} is the relative systematic uncertainty on the background, which is conservatively assumed to be 30% for optimisation. This thesis uses a data analysis framework called ROOT [119], which can implement a variety of possible significance calculations, as described in Ref. [120]. To optimise a SR, Z must be

maximised to the extent that an excess in data should be observed if a SUSY signal is present. To avoid statistical fluctuations dominating the background yield, at least one background event is required in each SR. A discussion on the statistical interpretation of the significance is presented in Section 5.6.

Two different approaches can be adopted to define SRs. The early Run-II $\tilde{\ell}$ analysis, which had lower luminosities, used an *inclusive approach*, which allowed events to feature in more than one SR. Later analyses, also presented in this thesis, use an *exclusive approach*, whereby several SRs are designed to be orthogonal to each other, resulting in events being univocally separated into exclusive SRs. This exclusive approach has the benefit of allowing the significances of the individual SRs to be easily statistically combined for greater sensitivities.

The specific SR definitions for the $\tilde{\ell}$ and W/Z analyses are presented in their corresponding chapters.

5.3.1 Discriminant Variables

The following section details the common discriminant variables that can be used for general three-lepton signature searches.

Flavour and Charge

Events can be described by the flavour and charge of the three final state leptons. For both the $\tilde{\ell}$ and W/Z channels, the lepton pair originating from the $\tilde{\chi}_2^0$ will be of same-flavour and opposite-charge-sign, and are known as SFOS pairs, $(e^\pm, e^\mp)$ or $(\mu^\pm, \mu^\mp)$ and can be generalised as $\ell^\pm \ell^\mp \ell'$. The third lepton, which can be any flavour, is a product of the $\tilde{\chi}_1^\pm$ decay.

Invariant and Transverse Mass

The invariant mass of the SFOS lepton pair originating from the $\tilde{\chi}_2^0$ or $\tilde{\ell}$ is used, along with the transverse mass, which is constructed with the remaining lepton, expected to originate from the $\tilde{\chi}_1^\pm$. Transverse mass is given by

$$m_T = \sqrt{2p_T^\ell E_T^{\text{miss}} - 2\vec{p}_T^{\,\ell}.\vec{p}_T^{\,miss}} = \sqrt{2p_T^\ell E_T^{\text{miss}}[1 - \cos(\phi_\ell - \phi_{miss})]}. \qquad (5.2)$$

As m_T is correlated to lepton p_T and E_T^{miss}, it can be used as a good discriminator against lower energy events.

If all three leptons have the same flavour, two SFOS pairs can be formed. In this

scenario, the searches in this thesis employ two approaches to assign the leptons. The first approach, which was used for the early $\tilde{\ell}$ analysis, was to take the SFOS pair as the pair having an invariant mass closest to the Z-boson mass, termed m_{SFOS}. The second approach, which is utilised for all searches using $36.1\,\text{fb}^{-1}$ of data, is to take the SFOS pair as the pair which minimises the transverse mass, named $m_{\text{T}}^{\text{min}}$, having associated invariant mass $m_{\text{SFOS}}^{\text{min}}$.

In both cases, requiring events to have m_{SFOS} or $m_{\text{SFOS}}^{\text{min}}$ within a close range of the Z-boson mass ($\pm 10\,\text{GeV}$), termed *on-Z*, would target the W/Z channel, where, the $\tilde{\chi}_2^0$ decays intermediately via the Z boson. In the $\tilde{\ell}$ channel, the $\tilde{\chi}_2^0$ decays directly to a SFOS lepton-slepton pair, with the slepton decaying further to a corresponding SM lepton. In this instance, the range of m_{SFOS} or $m_{\text{SFOS}}^{\text{min}}$ has no consequence to the signal, and so requiring it to be away from the Z-boson mass, termed *off-Z*, is a good discriminator against the dominant SM WZ background.

The invariant mass of all three leptons, $m_{\ell\ell\ell}$, is also used to remove residual low-mass resonances, and to avoid the use of low-mass Drell-Yan MC samples.

Missing Transverse Energy

The presence of high $E_{\text{T}}^{\text{miss}}$ is of utmost importance in SUSY searches. Events that do not contain this signature will be removed. This is a particular good discriminator against boson+jet background events.

b-tagged Jet Multiplicity

Since signal events are not expected to have significant hadronic activity, the vetoing of b-jets is a simple method to remove dominant background processes which contain the top quark that will decay via b-hadrons.

Light Flavour Jet Multiplicity

Defining SRs that either veto or require jets, is used for the W/Z analysis. It was found that vetoing jets made looser $E_{\text{T}}^{\text{miss}}$ cuts more optimal, which allowed SRs to target lower mass signals.

Transverse Momenta

Both lepton and jet transverse momenta, $p_{\text{T}}^{\ell(n)}$ and $p_{\text{T}}^{j(n)}$, respectively, where n refers to the nth leading lepton or jet, are used within this thesis.

The $p_\mathrm{T}^{\ell(n)}$ can be used as a good discriminator to optimise sensitivity to higher and intermediate mass splittings.

The $p_\mathrm{T}^{jet(n)}$ has been found to be correlated to the transverse momenta of the vector sum of leptons $p_\mathrm{T}^{\ell\ell\ell}$, which is also considered.

5.3.1.1 Analysis Preselection

The discriminant variables described above can be used to remove undesirable events prior to SR optimisation. The preselections for each analysis are listed in Table 5.6. Due to kinematic limitations in the earlier $\tilde{\ell}$ analysis, a requirement of $40\,\mathrm{GeV}$ was imposed on m_SFOS, however this was reduced to $20\,\mathrm{GeV}$ for the higher luminosity $\tilde{\ell}$ and W/Z analyses, and a first glance optimisation of W/h. The increase in $p_\mathrm{T}^{\ell 2}$ requirement for these searches is a consequence of the higher trigger p_T thresholds, previously presented in Table 5.5.

Tab. 5.6: Preselections for each analysis using the discriminant variables described above. Units are in GeV.

Variable	$13.3\,\mathrm{fb}^{-1}$	$36.1\,\mathrm{fb}^{-1}$
	$\tilde{\ell}$	$\tilde{\ell}$, W/Z & W/h
Leptons	$\ell^\pm \ell^\mp \ell'$	$\ell^\pm \ell^\mp \ell'$
$p_\mathrm{T}^{\ell 1}$	> 25	> 25
$p_\mathrm{T}^{\ell 2}$	> 20	> 25
$p_\mathrm{T}^{\ell 3}$	> 20	> 20
$m_{\ell\ell\ell}$	> 20	> 20
m_SFOS	> 40	-
$m_\mathrm{SFOS}^\mathrm{min}$	-	> 20
b-jets	Veto	Veto
$E_\mathrm{T}^\mathrm{miss}$	> 20	> 20

5.4 Background Modelling

The notion of irreducible and reducible backgrounds was introduced in Section 5.1, with consequent descriptions on how each background process can be observed as one or the other. The aim of this section is to outline the various methods involved in estimating and validating the different backgrounds. The associated uncertainties will be discussed in the next section.

5.4.1 Background Estimation

The two categories of background, irreducible and reducible, are estimated separately. Simulations are predominantly used for irreducible, where the reconstruction of events has lower rates of misidentification, while data-driven techniques are preferred for reducible backgrounds where misidentification rates are higher. An additional semi data-driven approach is also typically employed for the estimation of the primary irreducible background, which uses data to tune simulations to correct for potential mismodelling. However it is not limited to irreducible backgrounds, and can be used to estimate reducible backgrounds as well. The following section will first detail the semi data-driven method that was used to estimate the SM WZ background in the later analyses, followed by an overview of two fully data-driven techniques that were used by different channels to estimate the reducible backgrounds.

5.4.1.1 Semi Data-Driven Methods

Semi data-driven methods use kinematically defined control regions (CRs) designed to be enriched with the dominant background process, in this case, SM WZ, while minimising SUSY signal contamination. The dominant background is fitted, so that the CR distribution matches observed data, and then extrapolated to SRs via derived scale factors. In the most simplified case, considering one background process, in one SR and one CR, the scale factor μ_{MC} is given by:

$$\mu_{\mathrm{MC}} \equiv \frac{N_{\mathrm{CR}}^{\mathrm{data}}}{N_{\mathrm{CR}}^{\mathrm{MC}}}, \tag{5.3}$$

This type of fit is known as a *background-only* fit, an overview for the specific application used in this thesis is given in Section 5.6.2. CRs are designed to be similar to SRs so that the fitting of distributions to data can be performed reliably, yet, they must remain orthogonal to avoid any bias in unintentionally "unblinding" partial results. All the later analyses in this thesis use this method, with specific definitions for the $\tilde{\ell}$ and W/Z channels presented in Chapter 6.

5.4.1.2 Data-Driven Methods

Two different data-driven approaches have been used to estimate the reducible backgrounds. The main $\tilde{\ell}$ and W/Z analyses use a "Fake-Factor" approach, while the early Run-II low luminosity $\tilde{\ell}$ analysis used the "Matrix Method".

Fake Factor Method

A fully data-driven control sample of events enriched in the reducible backgrounds being estimated, is used to derive an extrapolation factor, or "Fake Factor" that will be extrapolated to estimate the background events in each SR. The control sample is measured in a kinematic region designed to consist of fake leptons with a similar composition as the reducible background in the SRs. The fake factor is a ratio of two sets of lepton identification criterion found within the control sample: tight "ID" criteria, corresponding to the standard identification used for signal leptons in the analysis; and, an orthogonal, loose "anti-ID" criterion, designed to increase the rate of misidentification and be enriched with fake and non-prompt leptons. Fake factors (F), which have dependences on kinematics such as p_{T} and η, can be binned and measured in these kinematic variables, taking the form

$$F(i) = \frac{N_{ID}^{\mathrm{data},i}}{N_{anti-ID}^{\mathrm{data},i}} \; , \tag{5.4}$$

where N is the number of events, and i refers to the ith bin in a given kinematic distribution. The control sample is contaminated with irreducible backgrounds, contributing primarily to the ID selection. These are removed using MC estimations, modifying Equation 5.4 to

$$F(i) = \frac{N_{\mathrm{ID}}^{\mathrm{data},i} - N_{\mathrm{ID}}^{\mathrm{MC\ irred.},i}}{N_{\mathrm{anti\text{-}ID}}^{\mathrm{data},i} - N_{\mathrm{anti\text{-}ID}}^{\mathrm{MC\ irred.},i}} \; . \tag{5.5}$$

Once the Fake Factors have been measured in the control sample, they can be used to obtain the reducible background estimations in the SRs. To do so, each SR has corresponding CRs, which, in this analysis are designed to be identical except that one of the ID leptons is replaced with an anti-ID lepton. The number of events in the CRs is multiplied by the Fake Factor to find the total reducible background in the SR, given as

$$N_{\mathrm{red.}}^{\mathrm{SR}} = \sum_i (N_{CR}^{\mathrm{data},i} - N_{CR}^{\mathrm{other},i}) \cdot F(i), \tag{5.6}$$

where i is again referring to the ith kinematic bin, and $N_{CR}^{\mathrm{other},i}$ is an optional term referring to any reducible backgrounds that may have been estimated separately using alternative techniques.

Matrix Method

Similar to the Fake Factor, the Matrix Method also uses two lepton identification criteria as its basis: a tight criterion (T), which is the standard identification of the signal leptons in the analysis; and, loose (L), which follows the exact criteria used for baseline leptons. In addition, two probabilities are defined:

- real efficiency r, which gives the probability that a real lepton will pass both the loose and tight criteria;
- fake rate f, which is the probability that a fake lepton will pass both tight and loose criteria.

The methods used to obtain these efficiencies are briefly discussed at the end of this section. Using these efficiencies, the sample compositions can be expressed as a linear combination of samples with real (R) and fake (F) leptons, for example, the total number of events where all three leptons pass the tight criteria can be expressed as:

$$N_{\text{TTT}} = r^3 N_{\text{RRR}} + r^2 f N_{\text{RRF}} + r f^2 N_{\text{RFF}} + f^3 N_{\text{FFF}}, \tag{5.7}$$

where the subscripts indicate whether each lepton is real or fake, and are in order of p_{T} based on the highest first. In this instance, it is assumed that each of the three leptons have the same associated r and f, however, in reality each lepton has an individual probability denoted r_1, r_2, r_3, f_1, f_2 and f_3. Eight compositions are possible in various combinations (N_{TLL}, N_{TLT} etc) that can be described by matrix equations. In three-lepton events, where the highest-p_{T} lepton has been found to be real for the majority of time ($> 95\%$ of events [33]), a simplified 4×4 matrix equation can be used to describe the remaining two leptons:

$$\begin{bmatrix} N_{\text{TT}} \\ N_{\text{TL}} \\ N_{\text{LT}} \\ N_{\text{LL}} \end{bmatrix} = \text{M}(r_1, r_2, f_1, f_2) \begin{bmatrix} N_{\text{RR}} \\ N_{\text{RF}} \\ N_{\text{FR}} \\ N_{\text{FF}} \end{bmatrix}, \tag{5.8}$$

where

$$
M = \begin{bmatrix}
r_1 r_2 & r_1 f_2 & f_1 r_2 & f_1 f_2 \\
r_1(1-r_2) & r_1(1-f_2) & f_1(1-r_2) & f_1(1-f_2) \\
(1-r_1)r_2 & (1-r_1)f_2 & (1-f_1)r_2 & (1-f_1)f_2 \\
(1-r_1)(1-r_2) & (1-r_1)(1-f_2) & (1-f_1)(1-r_2) & (1-f_1)(1-f_2)
\end{bmatrix}.
$$

(5.9)

The number of events with varying combinations of real and fake leptons can be found by inverting Equation 5.8, giving:

$$
\begin{aligned}
N_{\text{RR}} &= (1-f_1)(1-f_2)N_{\text{TT}} - [f_2(1-f_1)]N_{\text{TL}} - [f_1(1-f_2)]N_{\text{LT}} + f_1 f_2 N_{\text{LL}}, \\
N_{\text{RF}} &= -(1-f_1)(1-r_2)N_{\text{TT}} + [r_2(1-f_1)]N_{\text{TL}} + [f_1(1-r_2)]N_{\text{LT}} + f_1 r_2 N_{\text{LL}}, \\
N_{\text{RF}} &= -(1-f_2)(1-r_1)N_{\text{TT}} + [f_2(1-r_1)]N_{\text{TL}} + [r_1(1-f_2)]N_{\text{LT}} + f_2 r_1 N_{\text{LL}}, \\
N_{\text{FF}} &= (1-r_1)(1-r_2)N_{\text{TT}} - [r_2(1-r_1)]N_{\text{TL}} - [r_1(1-r_2)]N_{\text{LT}} + r_1 r_2 N_{\text{LL}}.
\end{aligned}
$$

(5.10)

The final total number of tight events with at least one fake lepton $N_{\text{Fake|TT}}$, can be computed by:

$$
N_{\text{Fake|TT}} = r_1 f_2 N_{\text{RF}} + f_1 r_2 N_{\text{FR}} + f_1 f_2 N_{\text{FF}} \; .
$$

(5.11)

Efficiencies: the real-efficiencies that have been used throughout this section, are obtained using the Z *tag-and-probe method* from a $Z \to l^{\pm} l^{\mp}$ enriched control region. This method requires a tag lepton to pass tight identification criterion, and a probe lepton to pass loose criterion. An invariant mass of the leptons within $\pm 10\,\text{GeV}$ of the Z boson mass indicates that the tag lepton is real. The efficiency is defined as the ratio between the number of probe leptons passing the tight requirements, and the number of probe leptons passing the loose requirements.

Measuring the fake-rates is more complex and requires separate consideration for the different types of fake lepton: heavy-flavour fakes from the semi-leptonic decays of b and c hadrons in jets; light-flavour fakes from misidentified jets or semi-leptonic decays of light-quark hadrons in jets; and, the pair production of electrons from photon conversions. The relative contribution of each type of fake lepton is measured in simulation in dedicated control regions, with the MC truth information being used for classification. The efficiency is defined as the ratio between the number of fakes based on the MC truth information, and the number of fakes in the simulation.

5.4.2 Background Validation

To avoid any mis-modelling, background estimates and normalisations require validating before the analyses are unblinded and expected yields are compared to observable data in the SRs. This is performed in dedicated validation regions (VRs), which are designed to lie within an orthogonal extrapolation region between CRs and SRs, depicted in Figure 5.6. In this way, VRs serve as a mid-point to validate the extrapolation. Only once agreement within uncertainty is observed within the VRs between background and data, can the analyses be unblinded.

Fig. 5.6: A qualitative depiction of the orthogonal nature of the extrapolation of background from CRs, through VRs, to the SRs [121].
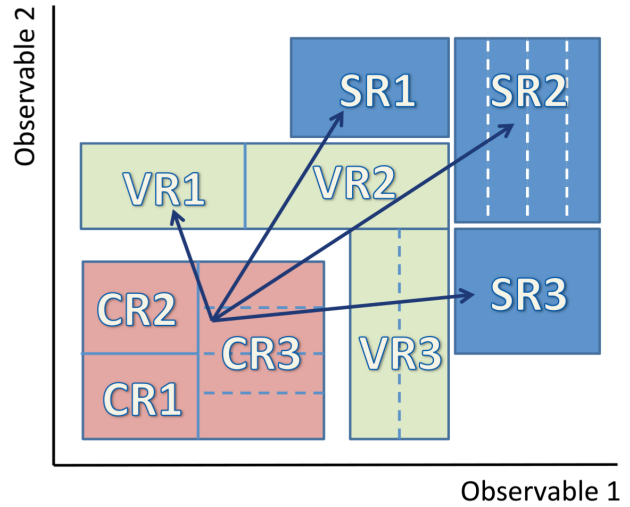
5.5 Systematic Uncertainties

Further to statistical uncertainties, additional systematic uncertainties are considered. Systematic uncertainties play a key role in the measurement of physical quantities, and are often more sizeable than their statistical counterparts. They can be categorised as either originating from experimental effects (i.e. detector calibration or physics object reconstruction etc), or they can be due to imperfect theoretical predictions (i.e. resulting from PDF and QCD scale uncertainties, and theoretical calculations etc). An overview of each will be given in the following.

5.5.1 Experimental Systematics

Experimental systematic uncertainties are assumed to be fully correlated across all backgrounds, and are implemented within the MC by calculating the disparity between the nominal yield and expected variations caused by the following given sources. Breakdown estimates of systematic uncertainties for each SR are presented in Chapter 6.

Jets

Due to the important role of jet multiplicities and E_T^{miss} calculations in the analyses presented in this thesis, uncertainties stemming from the measurements of jet energy, give one of the most dominant contribution of systematic uncertainties. The precision and scale calibration of a jet's energy measurement are referred to as the Jet Energy Resolution (JER) and Jet Energy Scale (JES), respectively. A jet's p_T distribution in MC tends to be more precise than in the real detector. As a result, the MC p_T distribution is smeared by a Gaussian JER function for improved agreement with data. The uncertainty on this smearing is the JER uncertainty and can be calculated as a variation in the mean and width of the Gaussian [122]. JES calibration involves the use of test-beams and MC simulations to extrapolate particle's actual energy from the measured energy, and the uncertainty on these procedures is the JES uncertainty [123].

b-tagging Efficiency

b-jets are tagged using the algorithm detailed in Section 4.3.4. The tagging efficiency measurements are provided by the ATLAS flavour-tagging performance group [124] in the form of jet p_T dependent scale factors extracted in dileptonic $t\bar{t}$ events, which match the b-tagging performance in simulation to that observed in data [125].

Jet Vertex Tagger

This multivariate variable, described in Section 4.3.4, has uncertainties assigned to account for any potential mis-modelling of the hard-scatter jets, based on distribution shapes and generator comparisons [126].

Pile-up

As discussed in Section 5.1.2.3, a pile-up reweighting scale factor is applied to MC simulations to match distributions with those observed in data. The uncertainty on this scale factor is taken by varying the distribution of the number of interactions per bunch crossing overlaid in the MC samples by $\pm 10\%$.

Missing Transverse Energy

The energy measurement uncertainties described above all contribute to an overall uncertainty in the E_T^{miss} calculation given in Equations 4.3. These uncertainties are propagated to E_T^{miss}, while the uncertainty on the $E_{x(y)}^{CellOut}$ term, which describes all

energy clusters not associated with reconstructed objects, is taken from comparisons of 2015 data to MC simulations [127].

Leptons

Electrons have two uncertainties originating from the energy: the electron scale which arises from any miscalibration of the electron energy using MC; and, the electron energy resolution, which considers the resolution of the ECal subdetector. Both are calculated using an E_T and η dependent function with $Z \to ee$ and $W \to e\nu$ events in data, and $J/\Psi \to ee$ events to estimate these uncertainties for low-p_T electrons [128].

Muons have two uncertainties originating from the muon energy scale with contributions from the ID track and the MS track. They are both calculated using data events for $J/\Psi \to \mu\mu$, $Z \to \mu\mu$ and $\Upsilon \to \mu\mu$ compared to MC [129].

Reducible Background

The Fake Factor method, which is discussed in Section 5.4.1.2, has several sources of systematic uncertainty. One of the main sources originates from the subtraction of irreducible processes using MC simulation (Equation 5.5). To evaluate this, the irreducible processes are scaled by $\pm 15\%$ and the Fake Factor is recalculated. The largest difference with respect to the nominal Fake Factor is taken as the uncertainty. The kinematic and composition differences between the Fake Factor region and the signal regions must also be considered. To do so, MC simulations are used to compute the Fake Factor in both kinematic regions and the difference between these two MC-based Fake Factors is used as the uncertainty. All uncertainties are then statistically combined to determine a total Fake Factor systematic uncertainty.

The uncertainty on the Matrix Method, which is also discussed in Section 5.4.1.2, is determined by varying the fake rate, real efficiencies and weight component of each reducible processes by $\pm 1\,\sigma$ around nominal in the control regions. An additional uncertainty on the number of tight and loose events in Equation 5.10, is calculated by taking the sum of the square of the weights in each region. All uncertainties are then statistically combined to determine a total Matrix Method systematic uncertainty.

5.5.2 Theory Systematics

Theoretical uncertainties in QCD energy scales, arise from the different choice of parameter values for the calculations. The *renormalisation scale* μ gives the

dependence for the running strong coupling constant α_s, and is normally set to equal the momentum transfer Q of the scattering. The *factorisation scale* refers to the separation of the hard scattering QCD effects from the PDF, and is often set to μ. The choice of scales also affects the cross-section calculation of the processes. Additionally, PDFs have an associated theoretical uncertainty due to the choice of Q^2, a measured value provided by the different experiments, as previously discussed in Section 4.1.1.

For diboson backgrounds in this thesis, the QCD scale, α_s and PDF contributions are calculated for each VR and SR independently. The MC simulated datasets used for this process contain generator-level weights that allow for the reweighting of the samples to different renormalisation and factorization scales. These weight variations can be used to calculate the theory uncertainties on transfer factors for the SM WZ background using the dedicated CRs.

The uncertainty on the signal cross-section is assigned by using cross-section predictions from different PDF sets. These uncertainties are added to the signal samples, and applied as weights.

5.6 Statistical Interpretation

The statistical analysis of results presented in this thesis has been performed using HistFitter [121, 130], a widely used software framework in ATLAS. Having estimated and validated the background modelling using a background-only fit with control regions, described in Sections 5.4.1 and 5.4.2, and having observed agreement within uncertainty between background and data in the validation regions, the analysis can be unblinded by comparing background to data in the signal regions. Two outcomes are possible: an excess in data is observed, which would suggest the presence of new physics beyond the SM; or, agreement within uncertainty is observed, and SUSY mass models can be excluded. In both cases, limits on the models can be set. In this section, the idea of hypothesis testing is introduced, followed by a discussion on the techniques adopted by HistFitter to set discovery and exclusion limits.

5.6.1 Treatment of Systematics

As discussed in Section 5.5, systematic uncertainties are calculated by MC simulations as the disparity between the nominal yield and expected variations caused by a given source. The variation range, which extends both positively and negatively relative to nominal, can be rescaled to have a typical mean value of zero, and expected 1σ spread corresponding to one. The rescaled variation is treated as an

independent "nuisance" parameter ν_i, where i indicates the systematic source, and is used during the statistical interpretation of results, to unify the magnitudes of systematic uncertainties.

5.6.2 Background-only Fits

As previously discussed in Section 5.4.1, background-only fits are employed in semi data-driven background estimations using CRs, to normalise MC simulations to observed data. HistFitter uses a likelihood fit to achieve this by varying a scale factor for the dominant process being fitted in both the CRs and VRs simultaneously. The nuisance parameters, introduced in Section 5.5, for all backgrounds are also used to constrain the fit.

5.6.3 Hypothesis Testing

Each SUSY model, based on the different mass-splittings listed in Table 5.3, is a hypothesis that requires testing for validity. Hypothesis testing [132] is a statistical procedure to test which hypothesis best describes observed data. *P-values* are used to define the probability that an experimental outcome, which can be referred to as a test statistic q, agrees with a given hypothesis. Two hypotheses are considered: a *null hypothesis H_0*, which is considered true by default, and in the case of particle physics, is the SM, or the background-only hypothesis; or, an *alternative hypothesis H_i*, which describes signal-plus-background hypotheses, where in this thesis, i denotes the different SUSY models. *P*-values for H_0 and H_i are calculated as integrals of the test statistic probability density functions, $f(q|b)$ and $f(q|s+b)$, respectively, from an observed test statistic q_{obs}. A one-sided representation is shown in Figure 5.7.
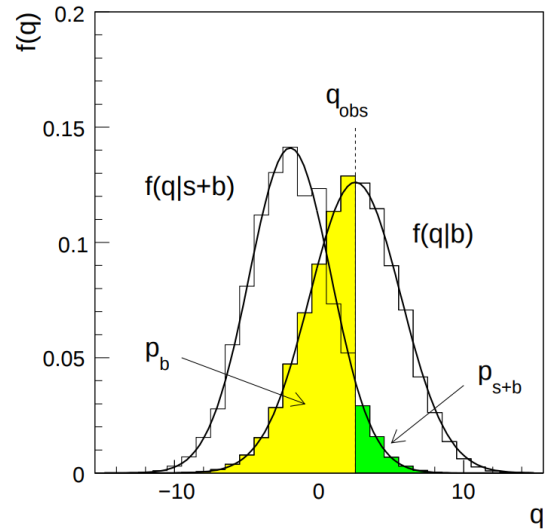

Fig. 5.7: A distribution of a test statistic q under the null hypothesis $f(q|b)$, and alternative hypothesis $f(q|s+b)$ [131].

The *p*-values can be defined as:

$$p_b = P(q \leq q_{obs}|H_0) = \int_{-\infty}^{q_{obs}} f(q|b)dq, \tag{5.12}$$

$$p_{s+b} = P(q \geq q_{obs}|H_i) = \int_{q_{obs}}^{\infty} f(q|s+b)dq, \tag{5.13}$$

where p_b is a measure of the compatibility between the data and background-only hypthosis, and p_{s+b} is the measure between signal hypothesis and observed data and is often referred to as the *discovery p*-value.

5.6.3.1 Statistical Optimisation

Another way to express a *p*-value is to redefine it as a significance level Z, which was discussed in Section 5.3 and used to optimise signal regions. This Z value is defined as the number of standard deviations σ the observed test statistic is above the mean of a Gaussian distribution [131]. The relationship between the *p*-value and Z is shown in Figure 5.8. Signal regions are optimised by maximising Z. The aim is to define regions, where, if the SUSY model is present, its test statistic would be observed as far from the mean as possible to avoid statistical background fluctuations interfering with the results. To avoid falsely claiming discovery of new physics, it is convention that discoveries can only be claimed if q_{obs} is beyond $Z = 5$, corresponding to a *p*-value $< 2.87 \times 10^{-7}$, while significant evidence for new physics can be claimed when q_{obs} is beyond $Z = 3$ (*p*-value $< 1.3 \times 10^{-3}$). A signal model that is expected to have $Z > 1.64$, corresponding to a *p*-value < 0.05, is excluded if no excess in data is observed to fulfill these requirements. *P*-values can also be expressed as *confidence levels*, which is discussed in Section 5.6.5.

Fig. 5.8: A Gaussian distribution showing the relationship between the significance *Z* and the p-value [131].
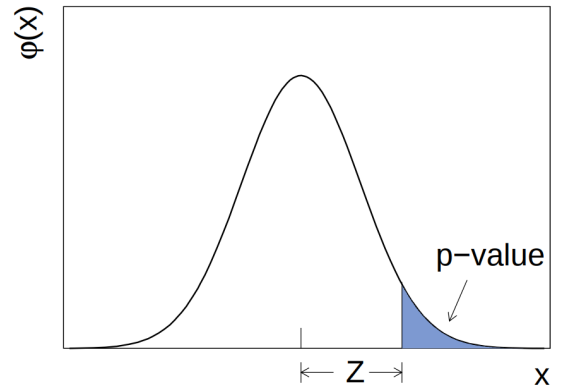
5.6.4 Profile Likelihood Ratio

The analyses in this thesis define a test statistic based on a maximum profile likelihood ratio [131, 132], with a likelihood function in its simplest form given as

$$\mathcal{L}(n_{obs}|\mu_s S, B, \nu) = \mathrm{P}(n_{obs}|\mu_s S + B) \times \prod_i \mathrm{G}(\nu_i, \mu_{\nu_i} = 0, \sigma_{\nu_i} = 1), \qquad (5.14)$$

where

- n_{obs} is the number of observed data events;
- $\mu_s S$ is the expected number of signal events, with signal strength μ_s (explained in the following);
- B is the expected number of background events;
- $\mathrm{P}(n_{obs}|\mu_s S + B)$ is a Poisson distribution;
- ν is an associated nuisance parameter, introduced in Section 5.6.1;
- $\mathrm{G}(\nu_i, \mu_{\nu_i} = 0, \sigma_{\nu_i} = 1)$ is a Gaussian distribution of each individual nuisance parameter i, with a mean μ_{ν_i} of zero, and standard deviation σ_{ν_i} of one.

With the inclusion of multiple orthogonal regions, such as control and signal regions, the combined likelihood can be expressed as

$$\mathcal{L}(n_{obs}|\mu_s S, B, \nu) = \left[\prod^N \mathrm{P}(n_{obs}|\mu_s S + B)\right] \times \left[\prod_i \mathrm{G}(\nu_i, \mu_{\nu_i} = 0, \sigma_{\nu_i} = 1)\right],$$
$$(5.15)$$

where N represents the regions being simultaneously fitted. The notation can be condensed by referring to the signal and background model (and associated nuisance parameters) as $\boldsymbol{\theta}$, and the likelihood as $\mathcal{L}(\mu_s, \boldsymbol{\theta})$. In turn, this causes the profile likelihood ratio to become

$$\lambda_p(\mu_s) = \frac{\mathcal{L}(\mu_s, \hat{\hat{\boldsymbol{\theta}}})}{\mathcal{L}(\hat{\mu_s}, \hat{\boldsymbol{\theta}})}, \qquad (5.16)$$

where the denominator is maximised over all parameters and is absolute, and the numerator is maximised for a given value of the parameter, which, in the case above is μ_s. A signal strength $\mu_s = 0$ corresponds to the SM without SUSY (background-only hypothesis), while a signal strength $\mu_s = 1$ corresponds to the presence of the SUSY model being tested (signal-plus-background hypothesis). As maximising the likelihood is equivalent to minimising the negative log likelihood, we can redefine

Equation 5.16 and assign it as our test statistic:

$$q = -\ln(\lambda_p(\mu_s)). \tag{5.17}$$

For the calculation of the p-value, and in order to generate a distribution of test statistics, the HistFitter software randomly generates thousands of pseudo-data from a Poisson distribution. It does this for all models of μ_s that are being tested, resulting in independent p-values for every hypothesis, including background-only. At this point, the compatibility of q_{obs} can be evaluated.

5.6.5 Exclusion Limits

A p-value can also be defined as a *confidence level* (CL), and as discussed earlier, a signal model is excluded if its p-value p_{s+b} is < 0.05; this corresponds to a 95% CL. However, this approach, which is sufficient for the optimisation of signal regions, can lead to falsely excluding models which the analysis has little or no sensitivity to. To avoid this, interpretation of results is performed using the CL_s method [133], which, in addition to p_{s+b}, incorporates the p-value of the background-only hypothesis p_b, and is given as

$$\text{CL}_s = \frac{\text{CL}_{s+b}}{\text{CL}_b} = \frac{p_{s+b}}{1 - p_b}. \tag{5.18}$$

Figure 5.9 illustrates the relationship between the confidence levels and the test statistic probability distribution. It is comparable to the p-value relationship, shown previously in Figure 5.7. While the CL_s is technically not a CL, it has been conventionally adopted by the ATLAS Collaboration to exclude models if $\text{CL}_s < 0.05$. So far, the statistical techniques discussed have used the signal strength μ_s as the

Fig. 5.9: A distribution of a test statistic q, illustrating the confidence levels used to quantify the compatibility of q_s to either hypothesis. Image based on [131].
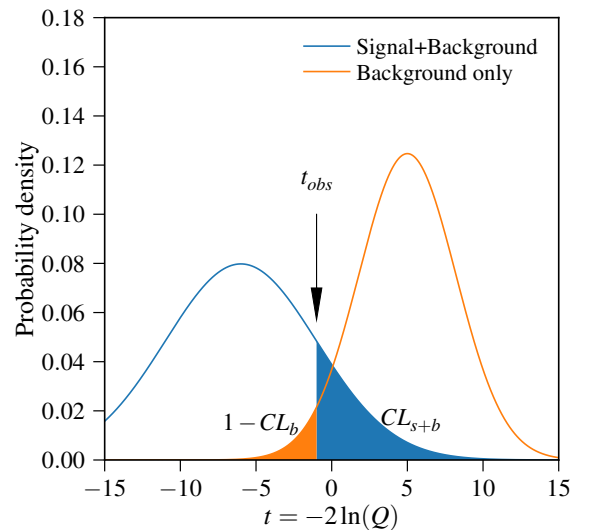
function of the test statistic, inferring that μ_s is the parameter being excluded. To translate this to mass-splitting models, only p_{s+b} corresponding to $\mu_s = 1$ is used to calculate the CL_s values for all possible signal samples. The outcome is *Exclusion Limits* on the masses of the $\tilde{\chi}_1^\pm \tilde{\chi}_2^0$ and $\tilde{\chi}_1^0$ sparticles.

5.6.6 Discovery Limits

Discovery Limits, or more concisely, model-independent limits, are used to consider how compatible the observed data is with the background-only hypothesis ($\mu_s = 0$), and is particularly significant when estimating the sensitivity to new physics scenarios if an excess in data is observed. Limits include: an upper limit on how many events can be observed before compatibility with the SM breaks down; along with an upper limit on the visible signal cross-section, which is defined as the product of the signal cross-section (given by $\mu_s S/\mathcal{L}$, where $\mathcal{L}$ is the luminosity), the detector acceptance and the analysis efficiency. The visible signal cross-section limit is obtained by performing a scan of μ_s in each signal region independently, starting at large, excluded values, and reducing until the p-value equals 0.05. In this way, μ_s acts as a dummy signal to test scenarios not considered in this thesis.

6. Results for $\tilde{\chi}_1^\pm \tilde{\chi}_2^0$ with Three-Lepton Final States

In Chapter 5, the general search strategy for all three analysis channels was detailed. In this chapter, the unique prescriptions adopted, along with the final results, are presented for the $\tilde{\ell}$ and W/Z channels in Sections 6.1 and 6.2, respectively. All results are public, with the early Run-II $\tilde{\ell}$ analysis in an ATLAS conference paper [114], while the higher luminosity $\tilde{\ell}$ and W/Z analyses have been submitted to European Physicals Journal C [115].

In addition to the public analyses, a preliminary first look optimisation for the W/h scenario, previously detailed in Section 2.3.5, is presented in Section 6.3

6.1 Searches for $\tilde{\chi}_1^\pm \tilde{\chi}_2^0$ via Sleptons

The early Run-II analysis is featured in Section 6.1.1. As this uses only a subset of data and the results are vastly improved in the later higher luminosity analysis, only a brief overview is given. The main $\tilde{\ell}$ analysis follows, with the SR optimisation and definition in Section 6.1.2, the definition of CRs and VRs, along with data to background comparisons in Section 6.1.3, and the results in Section 6.1.5.

6.1.1 Early Run-II Search

This early Run-II analysis, which used $13.3\,\text{fb}^{-1}$, focused solely on the $\tilde{\ell}$ channel due to the higher associated branching ratios compared to alternative three-lepton models. The following section gives an overview of the optimisation of signal regions, which was my primary contribution, along with the unblinded results. The background modelling follows the standard procedure detailed in the analysis strategy, with the use of the Matrix Method to estimate the reducible background.

Signal Regions

Eight benchmark signal points were used during the early Run-II search, to construct two inclusive signal regions, defined in Table 6.1. An intermediate region was designed to target the parameter space where slepton masses are similar to that of the Z boson, labelled SR3ℓ-I, and a high region to target the mass spectrum beyond that of the Z boson, labelled SR3ℓ-H. Both regions were constructed to be off-Z. Further requirements were made on lepton p_T, E_T^miss and m_T using "N-1" distributions with one-dimensional Z_N curves, whereby all kinematic requirements have been implemented, with the exception of the variable being plotted. These distributions are presented in Figures 6.1 to 6.5. High m_T requirements were applied to target heavy $\tilde{\chi}_1^\pm \tilde{\chi}_2^0$ and discriminate against diboson backgrounds. SR3ℓ-I kept a soft lepton p_T requirement to retain signal events with softer leptons, while conversely implementing a high E_T^miss requirement to target heavy $\tilde{\chi}_1^0$. SR3ℓ-H targeted both harder leptons and heavy $\tilde{\chi}_1^0$, by imposing high cuts on both lepton p_T and E_T^miss. The full yield breakdown for both SRs is presented in Table 6.2.

Tab. 6.1: Signal Region definitions for the early Run-II search using $13.3\,\text{fb}^{-1}$ of data.

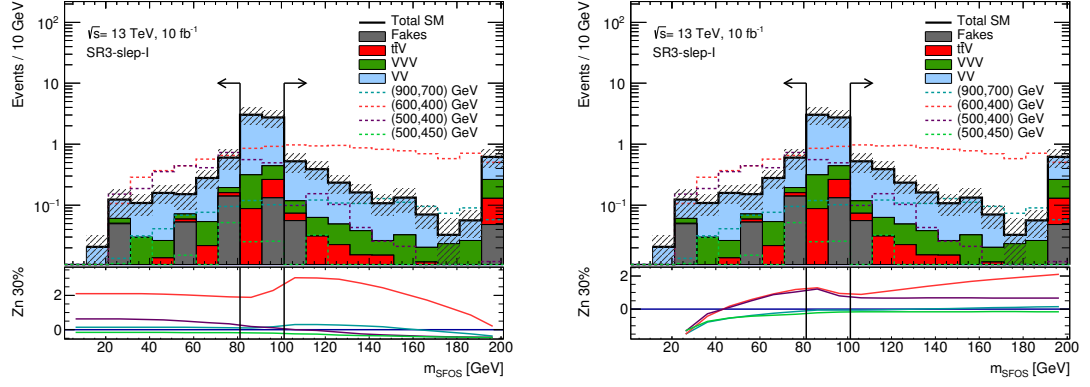| Variable	m_T [GeV]	m_SFOS [GeV]	$p_\text{T}^{\ell 3}$ [GeV]	E_T^miss [GeV]
SR3ℓ-I	> 110	$\notin$[81.2-101.2]	> 30	> 120
SR3ℓ-H	> 110	> 101.2	> 80	> 60

Fig. 6.1: Early Run-II N-1 distributions for variables used in SR3ℓ-I signal region. Arrows indicate SR cut. The ratio plot shows the one-dimensional Z_N curves for four benchmark signal points, which read from left to right for (left), indicating optimal lower cuts, and right to left for (right) indicating optimal upper cuts.
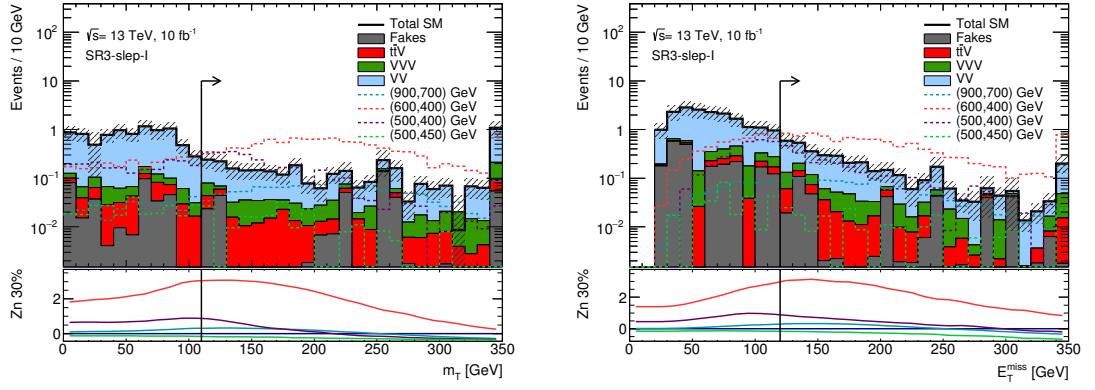

Fig. 6.2: Early Run-II N-1 distributions for variables used in SR3ℓ-I signal region. Arrows indicate SR cut. The ratio plot shows the one-dimensional Z_N curves for four benchmark signal points.
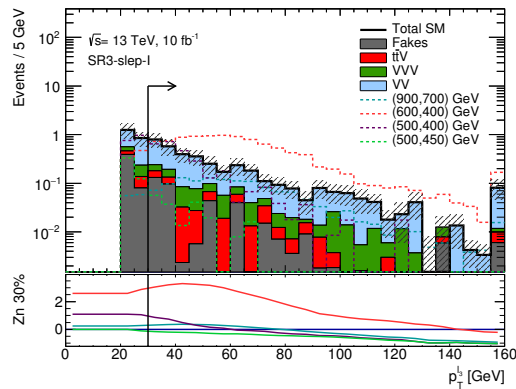

Fig. 6.3: Early Run-II N-1 distributions for variables used in SR3ℓ-I signal region. Arrows indicate SR cut. The ratio plot shows the one-dimensional Z_N curves for four benchmark signal points.

Fig. 6.4: Early Run-II N-1 distributions used in SR3ℓ-H signal region. Arrows indicate SR cut. The ratio plot shows the one-dimensional Z_N curves for four benchmark signal points.

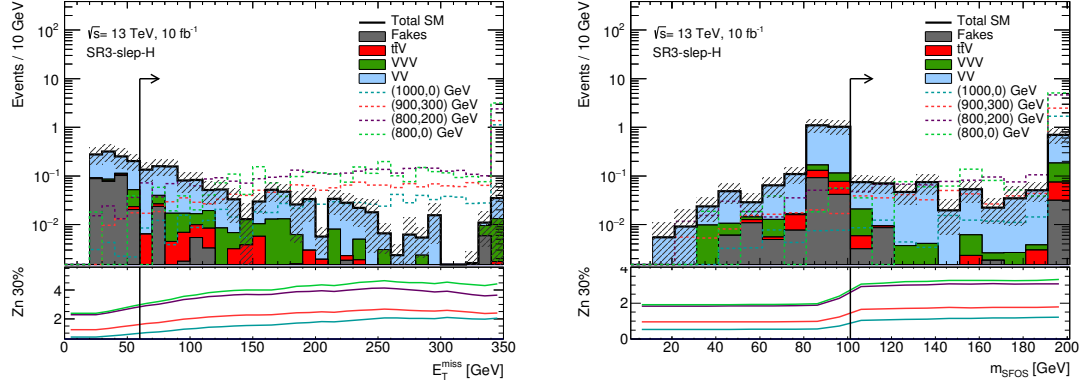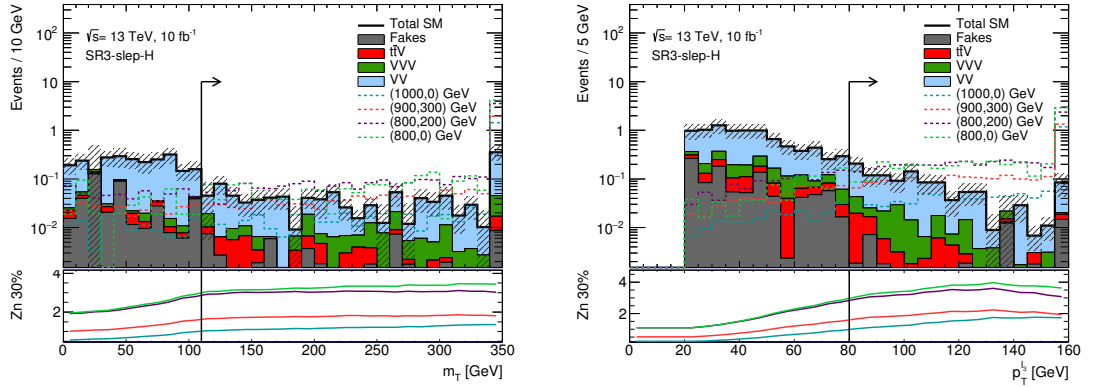
Fig. 6.5: Early Run-II N-1 distributions used in SR3ℓ-H signal region. Arrows indicate SR cut. The ratio plot shows the one-dimensional Z_N curves for four mass benchmark signal points.

Process	SR3ℓ-I	SR3ℓ-H
VV	2.52 ± 0.16	0.91 ± 0.09
VVV	0.43 ± 0.03	0.14 ± 0.02
$t\bar{t}V$	0.26 ± 0.02	0.05 ± 0.01
Higgs	0.02 ± 0.01	0.0 ± 0.0
Reducible	0.31 ± 0.12	0.05 ± 0.01
Total background	3.53 ± 0.21	1.14 ± 0.1
via Slep (1000,0)	1.92 ± 0.05	1.78 ± 0.04
via Slep (900,300)	3.2 ± 0.06	2.82 ± 0.05
via Slep (800,200)	5.96 ± 0.11	5.33 ± 0.1
via Slep (800,0)	6.24 ± 0.35	5.65 ± 0.33

Tab. 6.2: Early Run-II optimisation yields for the SM background processes and four benchmark signal points in the four SFOS SRs. Reducible is MC only. The uncertainties are statistical only.

Results

Unblinded results for the early Run-II SRs are presented in Table 6.3, with the kinematic distributions shown in Figures 6.6 and 6.7. No excess in the number of data events was observed, and there was good agreement between data and the SM background within uncertainties. In the absence of an excess, model-dependent exclusion limits were set, and are shown in Figure 6.8. As signal regions were inclusive, the combination was performed by selecting the most sensitive SR per SUSY mass point. The exclusion of $\tilde{\chi}_1^{\pm}\,\tilde{\chi}_2^0$ masses was increased to ~1 TeV, an improvement of ~300 GeV from Run-I, while the mass of the $\tilde{\chi}_1^0$ could be excluded up to ~580 GeV, an increase of ~200 GeV [134]. Table 6.4 presents the upper limits on BSM events (N_{BSM}) and the visible signal cross-section ($\langle\epsilon\sigma\rangle_{obs}^{95}$). These results are improved upon in the following section using increased luminosity.

	SR3ℓ-I	SR3ℓ-H
Observed events	2	0
Total SM	4.41 ± 1.14	0.98 ± 0.50
VV	1.49 ± 0.45	0.69 ± 0.47
VVV	0.68 ± 0.36	0.20 ± 0.11
$t\bar{t}V$	0.34 ± 0.11	0.09 ± 0.03
Higgs	0.03 ± 0.01	0.00 ± 0.00
Reducible	1.87 ± 0.72	0.00 ± 0.21

Tab. 6.3: Breakdown of SM background and data yields in the three lepton signal regions. The "reducible" component refers to the data-drive estimates coming from the Matrix Method. Errors are statistical and systematic [114].
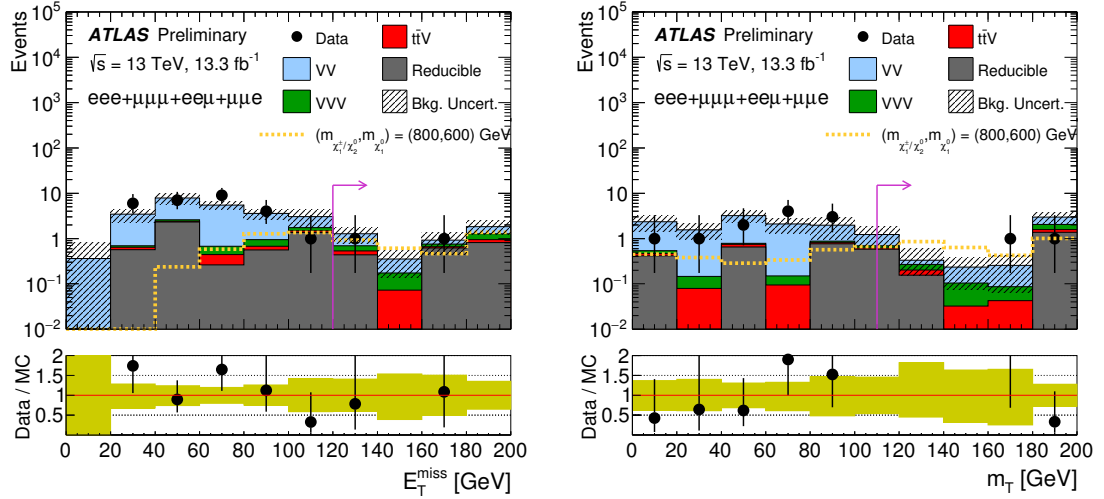
Fig. 6.6: Early Run-II distributions for E_T^{miss} (left) and m_{SFOS} (right) in SR3ℓ-I. Reducible backgrounds have been taken from the Matrix Method. The arrows indicate the cut value defining the SRs. Both statistical and systematic uncertainties are included [114]. These results have been improved using an increased luminosity, presented in the following section.

Fig. 6.7: Early Run-II distributions for m_T (left) and $p_T^{\ell 3}$ (right) in SR3ℓ-H. Reducible backgrounds from the Matrix Method. The arrows indicate the cut value defining the SRs. Both statistical and systematic uncertainties are included [114]. These results have been improved using an increased luminosity, presented in the following section.
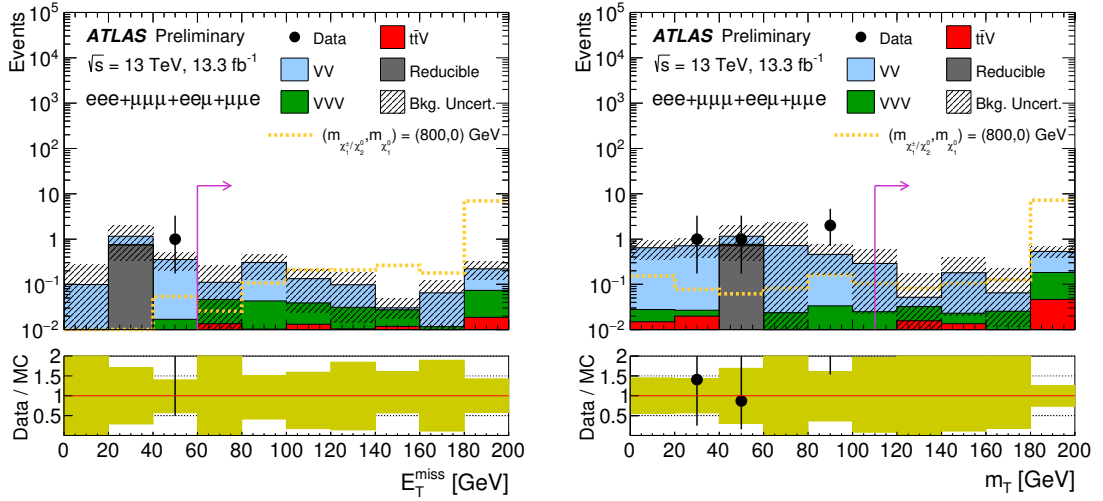
Fig. 6.8: Early Run-II observed and expected exclusion limits on the $\tilde{\chi}_2^0 \tilde{\chi}_1^\pm$ and $\tilde{\chi}_1^0$ masses in the context of SUSY scenarios with simplified mass spectra [114]. The contours of the band around the expected limit are the $\pm 1\sigma$ results, including all uncertainties except theoretical uncertainties on the signal cross-section. The dotted lines around the observed limit illustrate the change in the observed limit as the nominal signal cross-section is scaled up and down by the theoretical uncertainty. All limits are computed at 95% CL. The observed limits obtained from ATLAS during LHC Run I are also shown [134]. These results have been improved using an increased luminosity, presented in the following section.
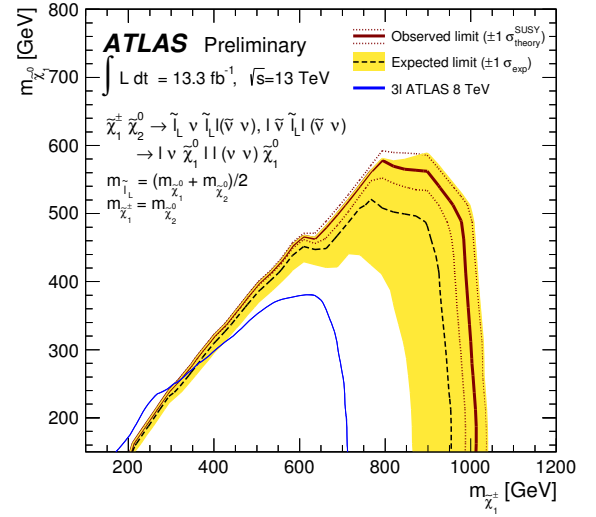
Signal Region	N_{obs}	N_{exp}	$\langle \epsilon\sigma \rangle_{obs}^{95}$[fb]	S_{obs}^{95}	S_{exp}^{95}
SR3ℓ-I	2	4.41 ± 1.14	0.28	3.7	$5.5^{+3.0}_{-1.8}$
SR3ℓ-H	0	0.98 ± 0.50	0.18	3.0	$3.4^{+2.2}_{-0.4}$

Tab. 6.4: Early Run-II signal model-independent upper limits on the number of beyond-the-SM events (N_{BSM}) and the visible signal cross-section ($\langle \epsilon\sigma \rangle_{obs}^{95}$). Also shown are the observed and expected upper limits at 95% CL on the number of beyond-the-SM events (S_{exp}^{95} and S_{obs}^{95}) for each signal region calculated using pseudo-experiments. The $\pm 1\,\sigma$ variations on the expected limit are due to the statistical and systematic uncertainties in the background prediction are also shown [114]. These results have been improved using an increased luminosity, presented in the following section.

6.1.2 Signal Region Definition for $\tilde{\chi}_1^\pm \tilde{\chi}_2^0$ via Sleptons

For this analysis, using the full $36.1\,\text{fb}^{-1}$ from 2015 and 2016, my primary contribution was to define signal regions that offer optimal sensitivity to $\tilde{\chi}_1^\pm \, \tilde{\chi}_2^0$ decays via slepton-mediated channels. Cases where the mass difference between the $\tilde{\chi}_1^\pm \, \tilde{\chi}_2^0$ and the $\tilde{\chi}_1^0$ are close to and larger than the Z boson mass are considered. The optimisation studies are presented in the following.

6.1.2.1 Optimisation of Signal Regions

The following section motivates the SR definitions, presented in Table 6.5. A selection of benchmark signal points that each reside in different areas of parameter space outside of previously excluded ranges are utilised. As with the earlier Run-II analysis,

Tab. 6.5: Full 2015 and 2016 Run-II summary of the exclusive signal regions targeting both intermediate and high mass spectrum.

Region	$m_{\text{SFOS}}^{\min}$ [GeV]	$m_{\text{T}}^{\min}$ [GeV]	$E_{\text{T}}^{\text{miss}}$ [GeV]	$p_{\text{T}}^{\ell 3}$ [GeV]
SR-slep-a				20-30
SR-slep-b	<81.2	>110	>130	>30
SR-slep-c				20-50
SR-slep-d	>101.2	>110	>130	50-80
SR-slep-e				>80

an off-Z requirement is applied for the $m_{\text{SFOS}}^{\min}$ variable in order to veto the peak in the distribution caused by background events comprised of Z bosons, shown in Figure 6.9. Two exclusive regions with $m_{\text{SFOS}}^{\min}$ either above of below the off-Z window are defined to target either heavy or light $\tilde{\chi}_1^\pm \tilde{\chi}_2^0$, respectively.

High $E_{\text{T}}^{\text{miss}}$ and $m_{\text{T}}^{\min}$ are also good discriminators to target $\tilde{\chi}_1^\pm \tilde{\chi}_2^0$ and $\tilde{\chi}_1^0$. As these two variables are highly correlated, the choice of cuts was initially considered by using two-dimensional correlation plots. As the SR with $m_{\text{SFOS}}^{\min} < 81.2\,\text{GeV}$ is sensitive to lower SUSY masses with intermediate mass-splittings $(50 - 200\,\text{GeV})$, correlation plots for benchmark signal points with $m(\tilde{\chi}_1^\pm \tilde{\chi}_2^0, \tilde{\chi}_1^0) = (600,500)$ GeV and $(800,600)$ GeV are shown in Figure 6.10. Kinematic N-1 distributions with one-dimensional Z_N curves, which were introduced in the early Run-II search, are utilised to further tune the choice of $E_{\text{T}}^{\text{miss}}$ and m_T, and are shown in Figure 6.11. The arrows at $E_{\text{T}}^{\text{miss}} > 130\,\text{GeV}$ and $m_T > 110\,\text{GeV}$ indicate the position of the cuts, which were chosen to coincide with an observable increase in sensitivity while retaining high signal yields for all benchmark signal points.
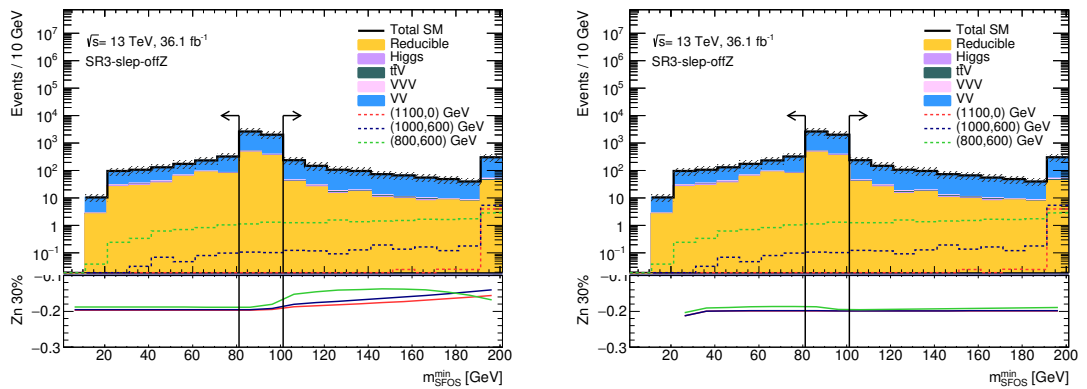
Fig. 6.9: Full 2015 and 2016 Run-II N-1 distributions for $m_{\text{SFOS}}^{\min}$ after baseline and $E_{\text{T}}^{\text{miss}}$ and $m_{\text{T}}^{\min}$ cuts. The arrows indicate the SR cuts. The ratio plot shows the one-dimensional Z_N curves for three benchmark signal points, which read from left to right for (left), indicating optimal lower cuts, and right to left for (right) indicating optimal upper cuts.
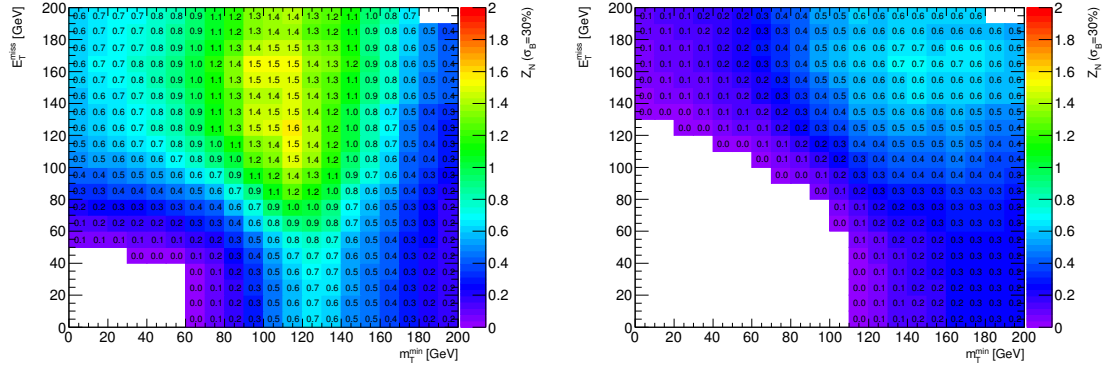
Fig. 6.10: Two-dimensional correlation plots showing the significance for E_T^{miss} vs. m_T^{min} in the $m_{SFOS}^{min} < 81.2$ GeV bin for $m(\tilde{\chi}_1^\pm/\tilde{\chi}_2^0, \tilde{\chi}_1^0) = (600,500)$ GeV (left) and $m(\tilde{\chi}_1^\pm/\tilde{\chi}_2^0, \tilde{\chi}_1^0) = (800,600)$ GeV (right). MC simulations have been used for both irreducible and reducible backgrounds. A 30% uncertainty is included in the Z_N calculations. White indicates less than one background event.
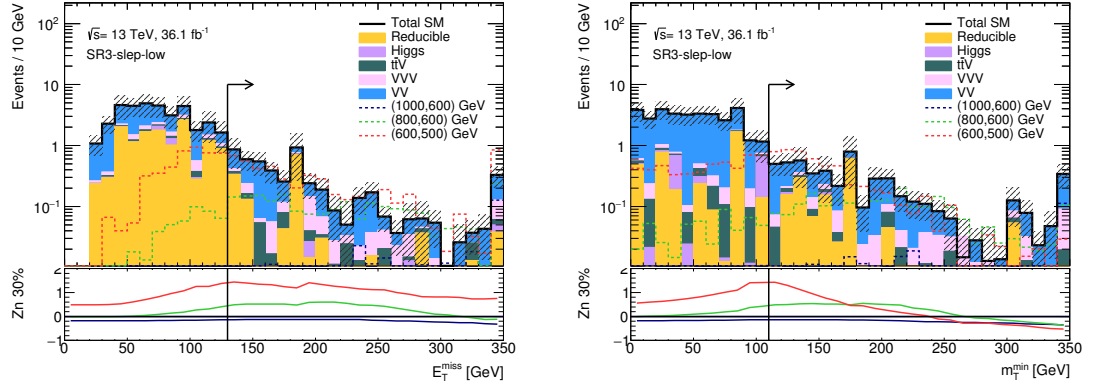

Fig. 6.11: Full 2015 and 2016 Run-II N-1 distributions for E_T^{miss} (left) and m_T^{min} (right) in the $m_{SFOS}^{min} < 81.2$ GeV SR. The arrows indicates the SR cuts. The ratio plot shows the one-dimensional Z_N curves for three benchmark signal points.

The SR with $m_{SFOS}^{min} > 101.2$ GeV targets both intermediate and high mass-splittings (> 300 GeV), with higher SUSY masses. Correlation plots for benchmark signal points with $m(\tilde{\chi}_1^\pm \tilde{\chi}_2^0, \tilde{\chi}_1^0) = (800,600)$ GeV and $(1000,600)$ GeV are shown in Figure 6.12, with corresponding N-1 distributions with the additional $m(\tilde{\chi}_1^\pm \tilde{\chi}_2^0, \tilde{\chi}_1^0) = (1100,0)$ GeV benchmark point included in Figure 6.13. The cuts were again chosen to coincide with an observable increase in sensitivity while retaining high signal yields for all benchmark signal points, and also remaining harmonised with the $m_{SFOS}^{min} < 81.2$ GeV SR.
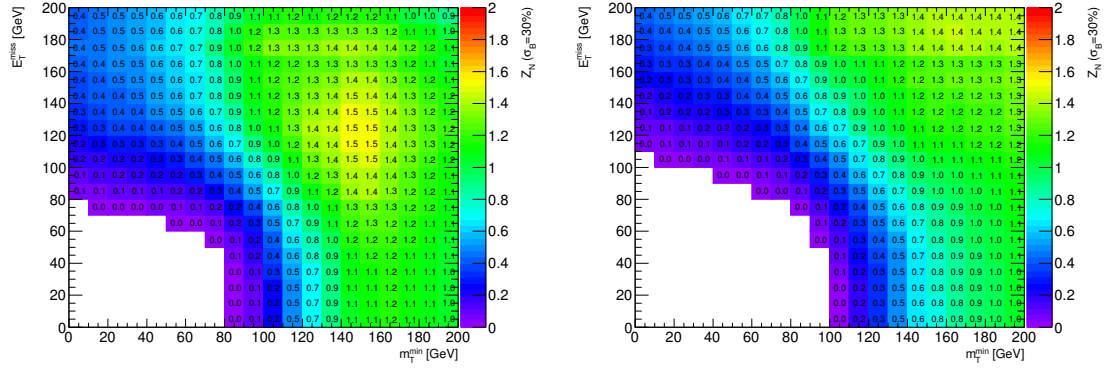
Fig. 6.12: Two-dimensional correlation plots showing the significance for E_T^{miss} vs. m_T^{min} in the $m_{SFOS}^{min} > 101.2$ GeV bin for $m(\tilde{\chi}_1^\pm/\tilde{\chi}_2^0, \tilde{\chi}_1^0) = (800,600)$ GeV (left) and $m(\tilde{\chi}_1^\pm/\tilde{\chi}_2^0, \tilde{\chi}_1^0) = (1000,600)$ GeV (right). MC simulations have been used for both irreducible and reducible backgrounds. A 30% uncertainty is included in the Z_N calculations. White indicates less than one background event.
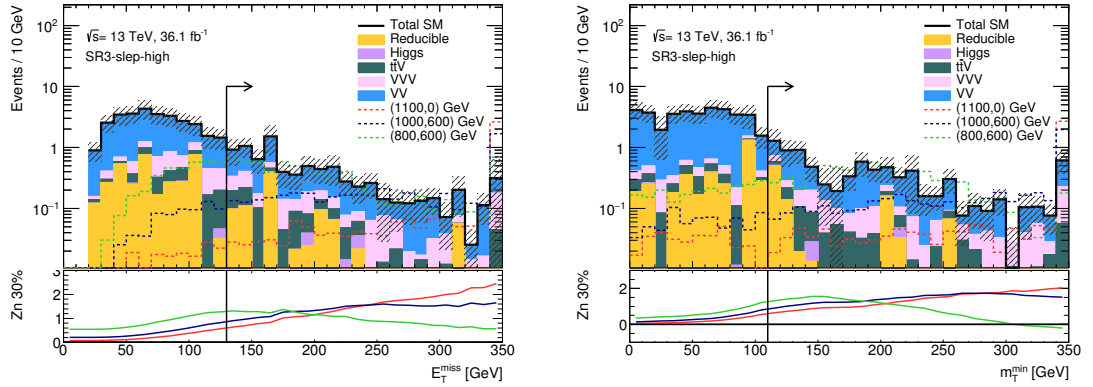

Fig. 6.13: Full 2015 and 2016 Run-II N-1 distributions for E_T^{miss} (left) and m_T^{min} (right) in the $m_{SFOS}^{min} > 81.2$ GeV SR. The arrows indicate the SR cuts. The ratio plot shows the one-dimensional Z_N curves for three benchmark signal points.

Kinematic N-1 distributions with one-dimensional Z_N curves were utilised to further improve sensitivity with additional requirements on $p_T^{\ell 3}$. The lower m_{SFOS}^{min} region is divided into two $p_T^{\ell 3}$ SRs: 20-30 GeV, to retain signal events with soft leptons; and > 30 GeV, to target harder leptons, shown in Figure 6.14. The higher m_{SFOS}^{min} region is divided into three $p_T^{\ell 3}$ bins: 20-50 GeV; 50-80 GeV; and, > 80 GeV, shown in Figure 6.15. Each targeting the different regions of lepton p_T parameter space. The full yield breakdown for all SRs is presented in Table 6.6.
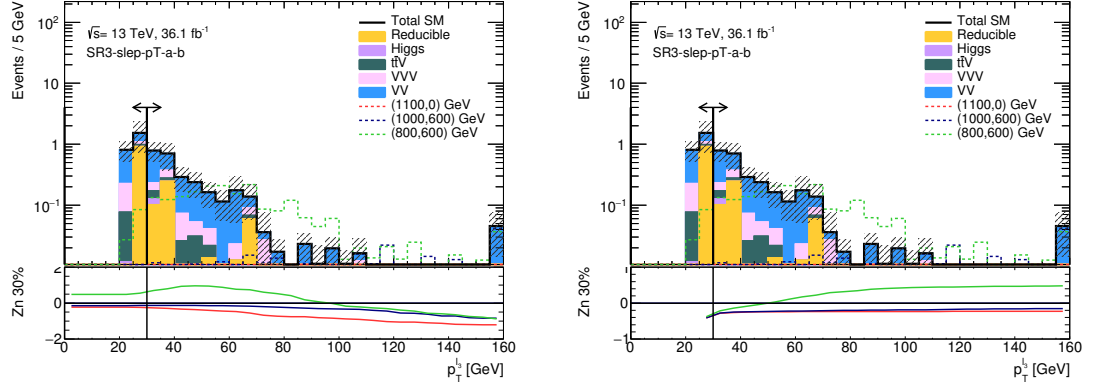
Fig. 6.14: Full 2015 and 2016 Run-II N-1 distributions for $p_T^{\ell 3}$ in the low off-Z region. The arrows indicate the SR cuts. The ratio plot shows the one-dimensional Z_N curves for three benchmark signal points, which read from left to right for (left), indicating optimal lower cuts, and right to left for (right) indicating optimal upper cuts.

Fig. 6.15: Full 2015 and 2016 Run-II N-1 distributions for $p_T^{\ell 3}$ in the high off-Z region. The arrows indicate the SR cuts. The ratio plot shows the one-dimensional Z_N curves for three benchmark signal points, which read from left to right for (left), indicating optimal lower cuts, and right to left for (right) indicating optimal upper cuts.
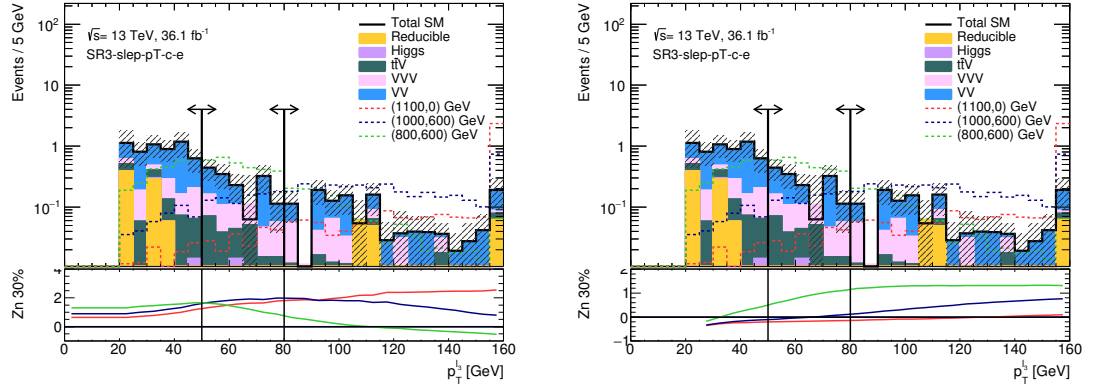
Process	SR3-slep-a	SR3-slep-b	SR3-slep-c	SR3-slep-d	SR3-slep-e
WZ	1.09 ± 0.17	2.02 ± 0.24	3.93 ± 0.52	0.94 ± 0.36	0.78 ± 0.17
ZZ	0.02 ± 0.01	0.01 ± 0.02	0.13 ± 0.03	0.06 ± 0.02	0.03 ± 0.01
VVV	0.25 ± 0.05	0.33 ± 0.05	0.7 ± 0.08	0.36 ± 0.06	0.25 ± 0.05
$t\bar{t}V$	0.14 ± 0.03	0.17 ± 0.03	0.48 ± 0.05	0.22 ± 0.04	0.09 ± 0.02
Higgs	0.01 ± 0.01	0.01 ± 0.02	0.03 ± 0.02	0.01 ± 0.01	–
Reducible	0.80 ± 0.46	0.36 ± 0.18	0.48 ± 0.25	–	0.08 ± 0.04
Total SM	2.31 ± 0.49	2.90 ± 0.31	5.76 ± 0.59	1.6 ± 0.36	1.22 ± 0.18
via $\tilde{\ell}$					
(1100,0)	–	0.02 ± 0.01	0.1 ± 0.01	0.2 ± 0.02	3.27 ± 0.08
(1000,600)	0.01 ± 0.01	0.26 ± 0.03	0.39 ± 0.04	0.89 ± 0.06	3.53 ± 0.11
(800,600)	0.11 ± 0.03	1.99 ± 0.11	2.53 ± 0.13	3.01 ± 0.14	1.25 ± 0.09
(600,500)	2.09 ± 0.17	3.28 ± 0.22	0.26 ± 0.07	0.06 ± 0.03	0.0 ± 0.0
(600,400)	0.52 ± 0.08	7.07 ± 0.31	10.31 ± 0.38	11.87 ± 0.4	5.3 ± 0.27
(400,300)	9.36 ± 0.87	16.94 ± 1.19	1.69 ± 0.37	0.26 ± 0.15	0.11 ± 0.11
Z_N					
(1100,0)	0	0	0	0	2.00
(1000,600)	0	0	0	0.34	2.13
(800,600)	0	0.72	0.61	1.57	0.75
(600,500)	0.89	1.07	0	0	0
(600,400)	0.02	2.44	2.63	4.91	3.04
(400,300)	3.43	4.59	0.41	0	0

Tab. 6.6: Yields for the SM background processes and six benchmark signal points for the five SFOS SRs targeting models with intermediate decays via the slepton. Z_N values are included for the signal points. The uncertainties are statistical only.

6.1.2.2 Sensitivity

Figure 6.16 shows the expected significance Z_N values for the $\tilde{\chi}_1^\pm\,\tilde{\chi}_2^0$ decays via sleptons when statistically combining all five SRs. For this scenario the masses of the $\tilde{\chi}_1^\pm\,\tilde{\chi}_2^0$ are expected to be excluded up to 1.1 TeV, an increase of $\sim$400 GeV from Run-I and $\sim$100 GeV from the early Run-II analysis presented in Section 6.1.1. The mass of the $\tilde{\chi}_1^0$ is expected to be excluded up to $\sim$600 GeV, an increase of $\sim$250 GeV from Run-I and $\sim$50 GeV from early Run-II. All benchmark signal points are expected to be excluded if no excess in data is observed.
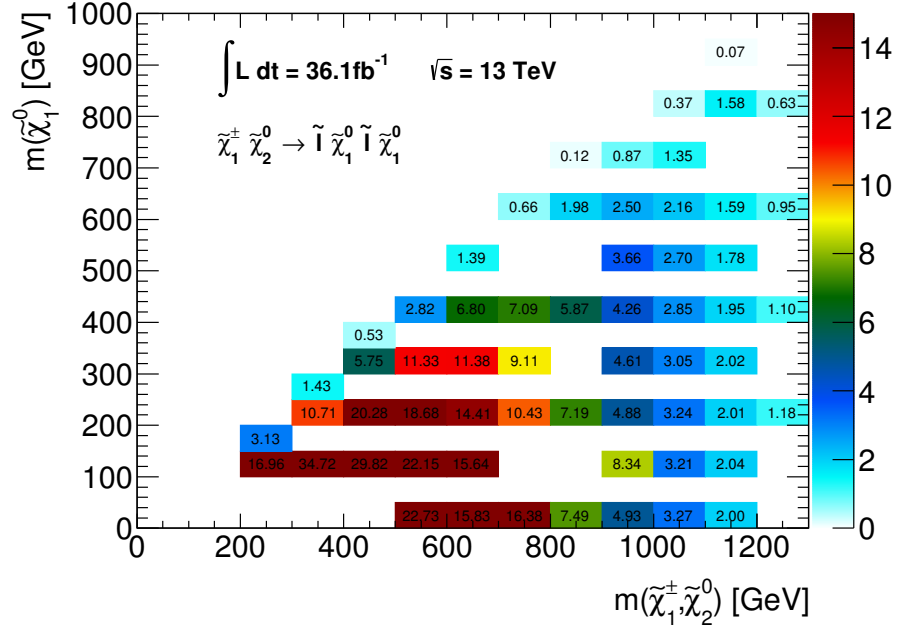
Fig. 6.16: Full 2015 and 2016 Run-II two-dimensional sensitivity plot showing the expected combined significances Z_N for the SR binned selection in the C1N2 via sleptons simplified model. MC simulation is used for both irreducible and reducible backgrounds. A 30% uncertainty is included in the Z_N calculations.

6.1.3 Background Validation for $\tilde{\chi}_1^\pm\tilde{\chi}_2^0$ via Sleptons

This section is devoted to validating the SM background processes that have already been described in the general strategy in Chapter 5. My contribution was to assist in defining CRs and VRs, to provide support in running the background-only fits and generating the tables presented, and also producing all of the distributions for visual interpretation. The data-driven Fake Factor method is used to model the reducible Z+jets and $Z+\gamma$ processes, while the "top-like" reducible backgrounds use the semi data-driven methods with dedicated CRs to derive scale factors. Both have been estimated together and are combined into one total reducible sample. The most dominant SM background, WZ, also uses the semi data-driven method with CRs, and is described and validated in the following.

6.1.3.1 Control Regions

One CR is defined, which is orthogonal to the SR by inverting the $m_{\text{SFOS}}^{\min}$ requirement to be on-Z. As cutting on high values of $m_{\text{T}}^{\min}$ reduces the contribution of the WZ background, a $m_{\text{T}}^{\min} < 110\,\text{GeV}$ requirement is applied to ensure the CR is enriched with the target background. Preserving the high $E_{\text{T}}^{\text{miss}}$ selection ensures that the CR is kinematically close to the SRs and limits the contamination of fake backgrounds, therefore improving the WZ purity. Table 6.7 gives a summary of the CR definition.

Tab. 6.7: Full 2015 and 2016 Run-II CR definition, in addition to the preselection requirements. Units are in GeV.

Region	m_{SFOS} [GeV]	$E_{\mathrm{T}}^{\mathrm{miss}}$ [GeV]	$m_{\mathrm{T}}^{\mathrm{min}}$ [GeV]
CR3ℓ-slep	$\in[81.2, 101.2]$	>120	<110

As described in Section 5.6, observed data is used to tune the SM WZ background so that the total estimated background matches. The scale factor for the WZ background in CR3ℓ-slep was calculated to be 0.924 ± 0.060. Section 6.1.3.3 presents an extrapolated background-only fit, using both CR3ℓ-slep and the VRs, defined in the following section.

6.1.3.2 Validation Regions

To validate the background models, four VRs are designed to target different dominant processes. A low-$E_{\mathrm{T}}^{\mathrm{miss}}$, on-$Z$ region, labelled VR3-Za, is defined to be rich in WZ and/or Z bosons in order to validate the bulk of their distributions. A high-$E_{\mathrm{T}}^{\mathrm{miss}}$ on-Z, and low-$E_{\mathrm{T}}^{\mathrm{miss}}$ off-Z region, labelled VR3-Zb and VR3-offZa, respectively, are designed to target the distribution tails of the WZ process, with VR3-Zb also requiring at least one b-tagged jet to include the $t\bar{t}$ background. A final region, VR3-offZb, which is off-Z, $E_{\mathrm{T}}^{\mathrm{miss}}$-inclusive and requires b-tagged jets, predominantly targets the fake $t\bar{t}$ background process that was modelled using data-driven techniques. The definitions of the VRs are shown in Table 6.8. Distributions in $E_{\mathrm{T}}^{\mathrm{miss}}$, $m_{\mathrm{T}}^{\mathrm{min}}$, $m_{\mathrm{SFOS}}^{\mathrm{min}}$ and lepton p_{T} are presented in Figures 6.17 to 6.28, with the derived scale factor applied. All data to background comparisons show good agreement within uncertainty.

Region	$p_{\mathrm{T}}^{\ell 3}$ [GeV]	$m_{\ell\ell\ell}$ [GeV]	$m_{\mathrm{SFOS}}^{\mathrm{min}}$ [GeV]	$E_{\mathrm{T}}^{\mathrm{miss}}$ [GeV]	N(b-jets)
VR3-Za	>30	$\notin [81.2, 101.2]$	$\in[81.2, 101.2]$	40–60	–
VR3-Zb	>30			>60	>0
VR3-offZa	>30	$\notin [81.2, 101.2]$	$\notin [81.2, 101.2]$	40–60	–
VR3-offZb	>20			>40	>0

Tab. 6.8: Full 2015 and 2016 Run-II selection requirements for four VRs targeting different background processes.
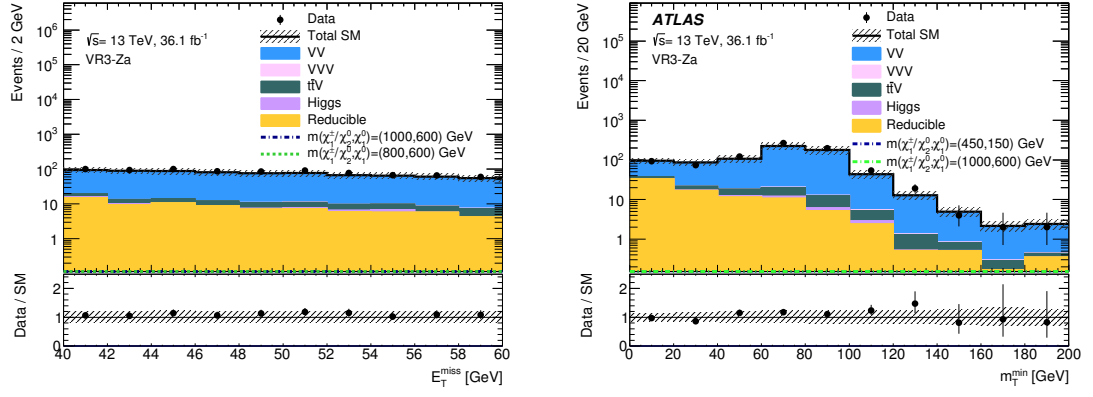
Fig. 6.17: Full 2015 and 2016 Run-II E_T^{miss} (left) and m_T^{min} (right) [115] distributions in VR3-Za with scale factor applied to WZ background. The uncertainties are inclusive of both statistical and systematic.
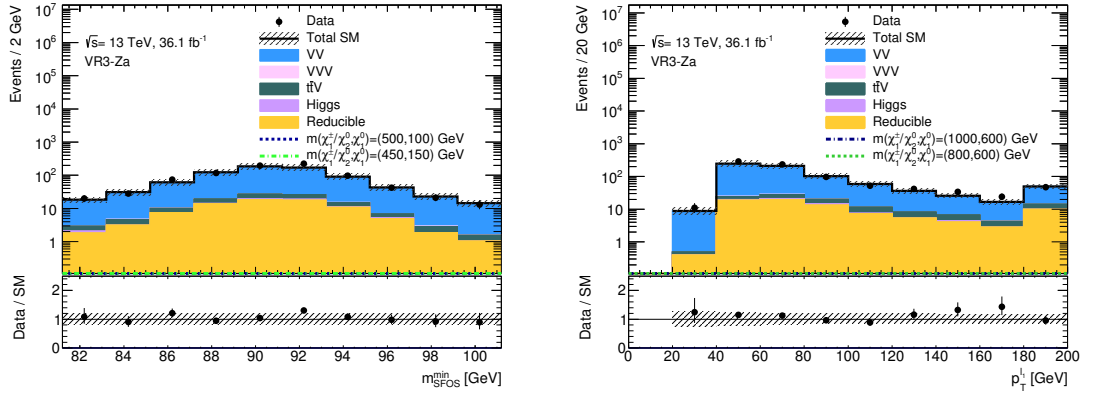

Fig. 6.18: Full 2015 and 2016 Run-II distributions in VR3-Za with scale factor applied to WZ background. The uncertainties are inclusive of both statistical and systematic.

Fig. 6.19: Full 2015 and 2016 Run-II distributions in VR3-Za with scale factor applied to WZ background. The uncertainties are inclusive of both statistical and systematic.
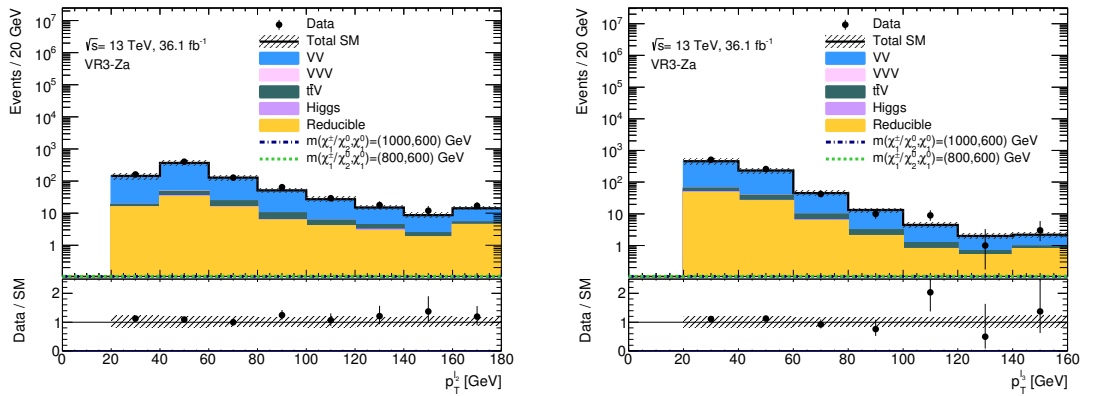
Fig. 6.20: Full 2015 and 2016 Run-II E_T^{miss} (left) [115] and m_T^{min} (right) distributions in VR3-Zb with scale factor applied to WZ background. The uncertainties are inclusive of both statistical and systematic.

Fig. 6.21: Full 2015 and 2016 Run-II distributions in VR3-Zb with scale factor applied to WZ background. The uncertainties are inclusive of both statistical and systematic.
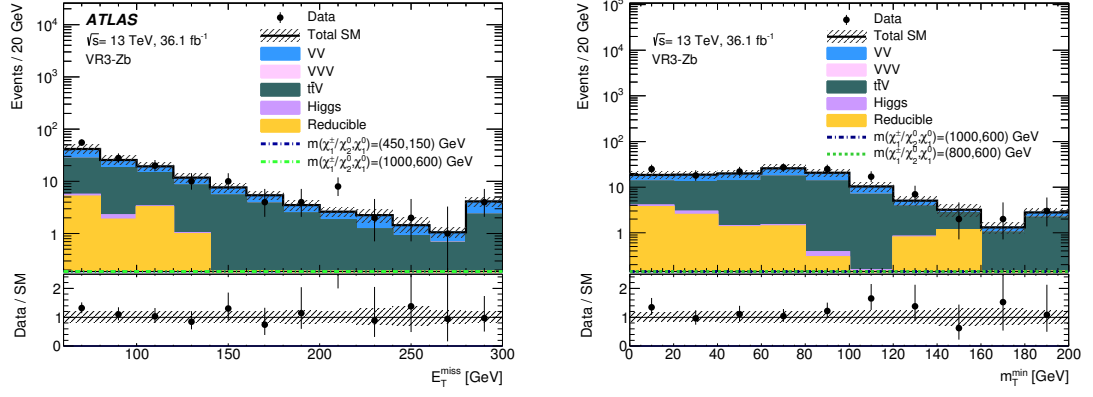

Fig. 6.22: Full 2015 and 2016 Run-II distributions in VR3-Zb with scale factor applied to WZ background. The uncertainties are inclusive of both statistical and systematic.

Fig. 6.23: Full 2015 and 2016 Run-II distributions in VR3-offZa with scale factor applied to WZ background. The uncertainties are inclusive of both statistical and systematic.
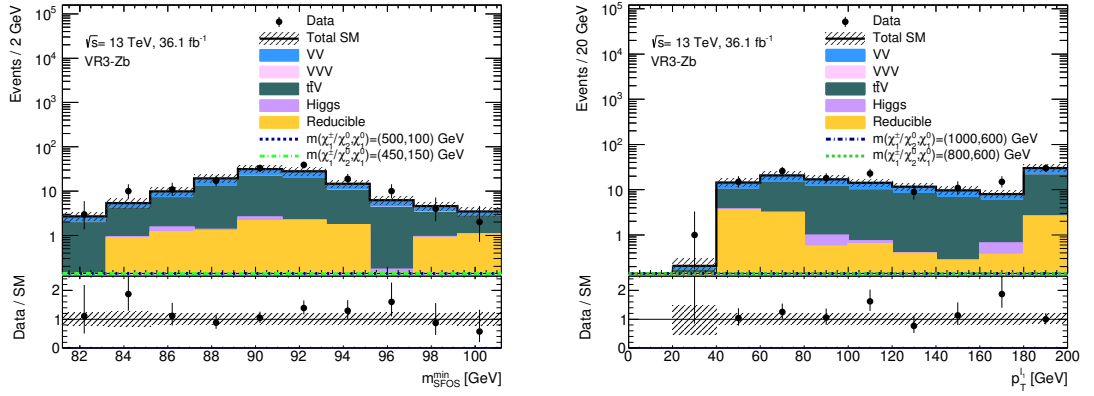

Fig. 6.24: Full 2015 and 2016 Run-II distributions in VR3-offZa with scale factor applied to WZ background. The uncertainties are inclusive of both statistical and systematic.
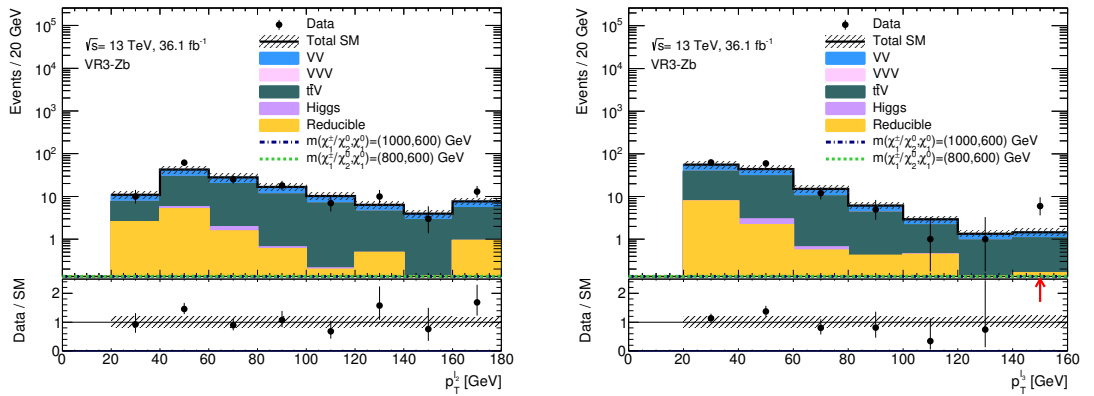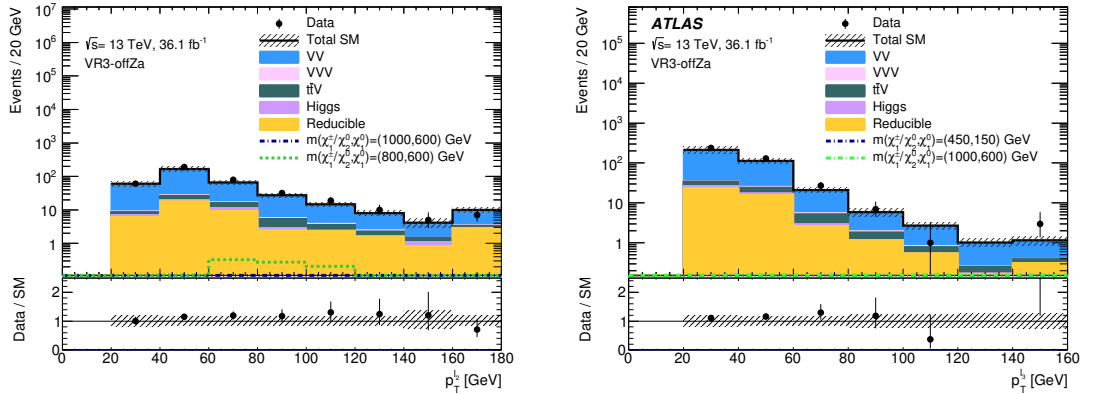

Fig. 6.25: Full 2015 and 2016 Run-II sub-leading lepton p_T (left) and third-leading lepton p_T (right) [115] distributions in VR3-offZa with scale factor applied to WZ background. The uncertainties are inclusive of both statistical and systematic.
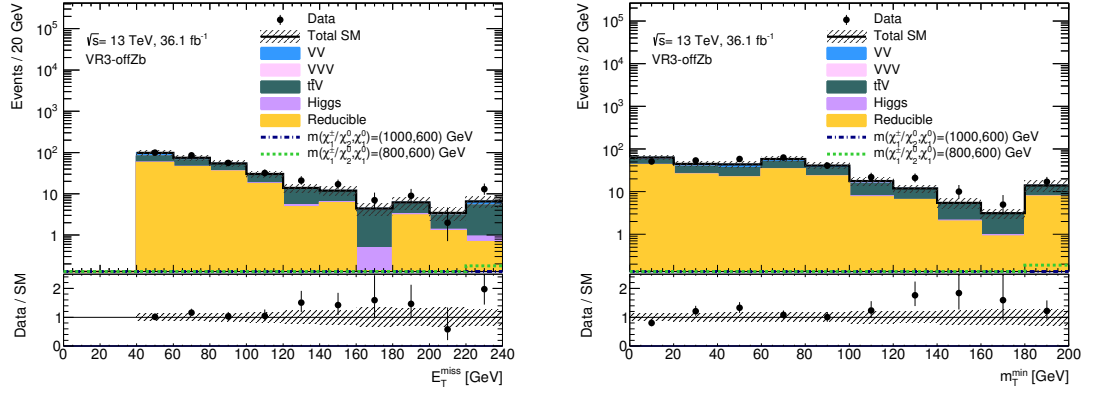
Fig. 6.26: Full 2015 and 2016 Run-II distributions in VR3-offZb with scale factor applied to WZ background. The uncertainties are inclusive of both statistical and systematic.
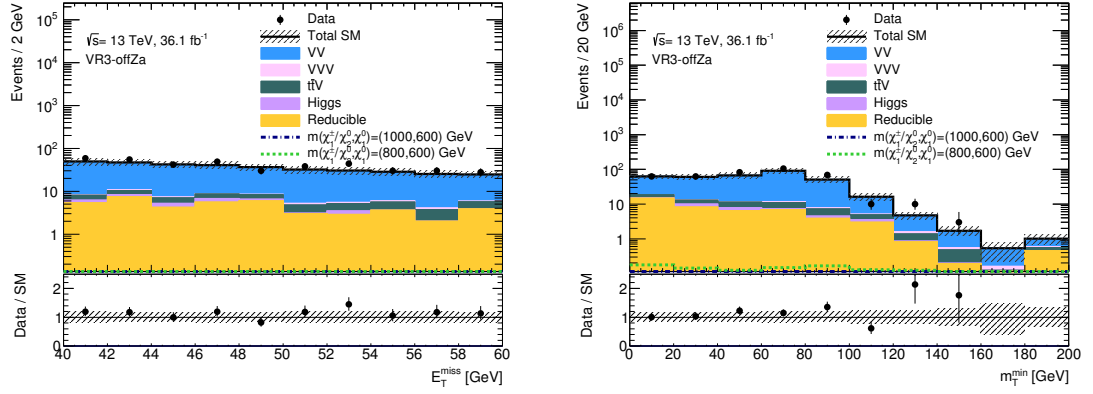

Fig. 6.27: Full 2015 and 2016 Run-II distributions in VR3-offZb with scale factor applied to WZ background. The uncertainties are inclusive of both statistical and systematic.
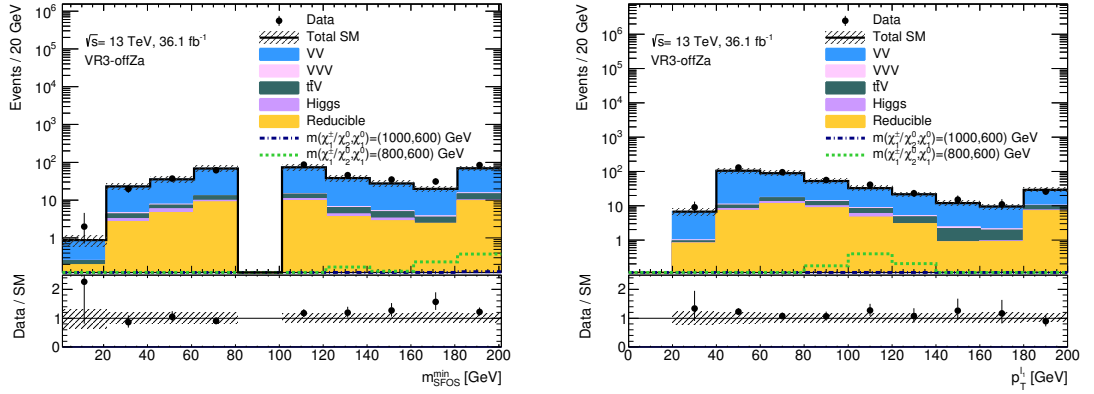

Fig. 6.28: Full 2015 and 2016 Run-II sub-leading lepton p_T (left) and third-leading lepton p_T (right) [115] distributions in VR3-offZb with scale factor applied to WZ background. The uncertainties are inclusive of both statistical and systematic.
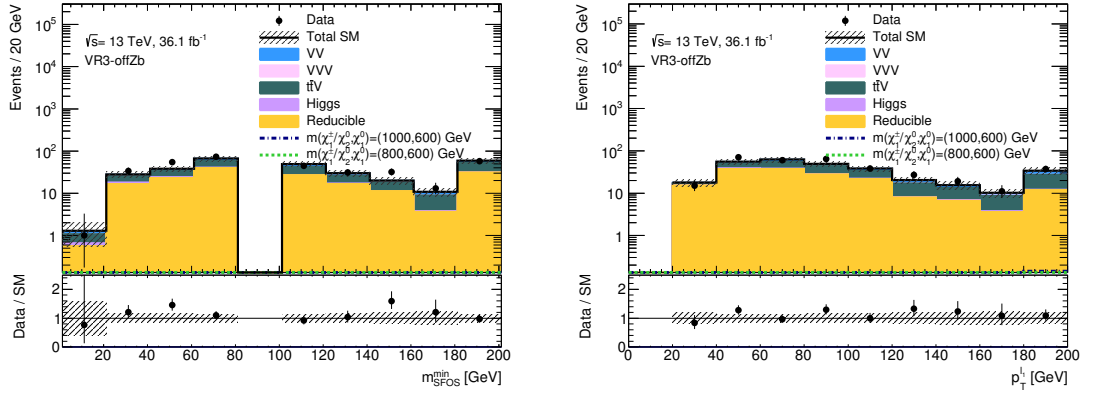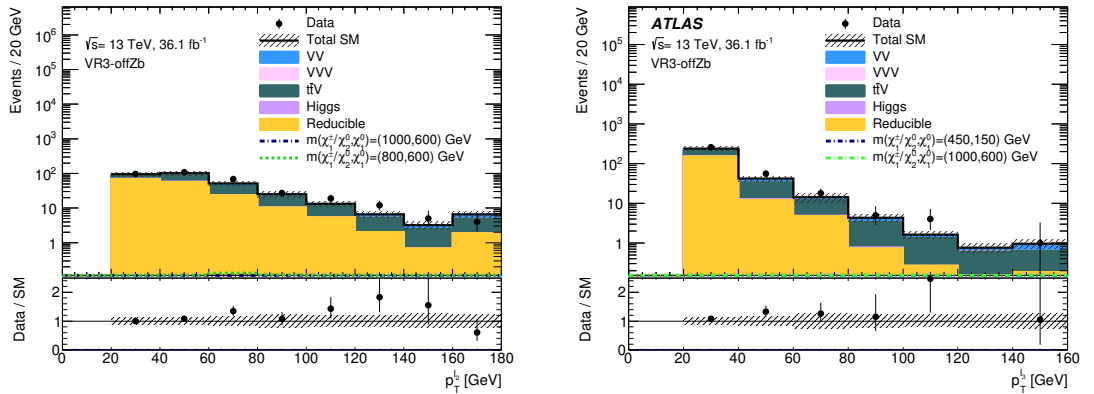
6.1.3.3 Background-only Fit

The CR defined in Table 6.7 and VRs defined in Table 6.8 have been used for the extrapolation of the fit results as detailed in Section 5.6, shown in Table 6.9. Both statistical and systematic uncertainties are included. The total expected SM yields are in good agreement with the number of observed events in each region.

	CR3ℓ-slep	VR3-Za	VR3-Zb	VR3-offZa	VR3-offZb
Observed events	324	829	148	404	342
Total SM	324 ± 18	790 ± 90	140 ± 70	370 ± 40	280 ± 100
WZ	298 ± 25	640 ± 80	45 ± 10	290 ± 40	42 ± 10
ZZ	7 ± 6	38 ± 32	2.0 ± 1.7	18 ± 15	2.7 ± 2.3
VVV	2.0 ± 1.7	1.3 ± 1.1	0.32 ± 0.28	3.5 ± 3.0	0.9 ± 0.8
$t\bar{t}V$	7 ± 6	33 ± 28	80 ± 70	15 ± 13	60 ± 50
Higgs	3.5 ± 3.0	4 ± 4	1.2 ± 1.0	5 ± 5	5 ± 4
Reducible	6.4 ± 3.2	81 ± 40	11 ± 6	44 ± 22	170 ± 80

Tab. 6.9: Full 2015 and 2016 Run-II background-only fit for the slepton-mediated CR and VRs. All systematic and statistical uncertainties are included [115].

6.1.4 Systematic Uncertainties for $\tilde{\chi}_1^\pm \tilde{\chi}_2^0$ via Sleptons

A summary of the dominant sources of systematic uncertainties in the background and signal estimates for each SR are listed in Table 6.10. Systematic uncertainties on the reducible background estimations are consistently the most significant, followed by the theoretically modelling of the WZ background.

Uncertainty	SR3-slep-a	SR3-slep-b	SR3-slep-c	SR3-slep-d	SR3-slep-e
Reducible	17.9%	6.45%	4.44%	16.9%	3.51%
WZ Modelling	4.13%	4.66%	5.23%	4.28%	5.62%
Jets	7.64%	2.32%	2.82%	2.54%	3.04%
E_T^{miss}	2.33%	2.82%	1.38%	4.28%	4.47%
Leptons	0.78%	1.64%	1.36%	2.34%	5.82%
b-tagging Eff.	0.45%	1.48%	0.55%	1.00%	–

Tab. 6.10: Breakdown of the dominant systematic uncertainties on background estimates. Percentages are quoted relative to the total background estimates for each SR defined in Section 6.1.2 and assume no correlation between the combined sub-categories to give an approximate idea of magnitudes for illustrative purposes.

6.1.5 Results for $\tilde{\chi}_1^\pm\,\tilde{\chi}_2^0$ via Sleptons

This section is dedicated to presenting and interpreting the results for the $36.1\,\mathrm{fb}^{-1}$ $\tilde{\ell}$-mediated channel at a centre-of-mass energy of $\sqrt{s}=13\,\mathrm{TeV}$. All the statistical strategies adopted have previously been discussed in the general analysis strategy, in Section 5.6. In addition to generating distributions for visual interpretation, and providing support for the background-only fits, I was responsible for running the discovery-fit to set the model-independent upper limits.

6.1.5.1 Observations in Signal Regions

The observed number of events in all signal regions, along with the total background expectations and uncertainties are shown in Table 6.11. The uncertainties include both statistical and systematic components. It is also interesting to compare the shape of the important kinematic distributions for variables that were used for optimisation. The $E_\mathrm{T}^\mathrm{miss}$ and $m_\mathrm{T}^\mathrm{min}$ distributions are presented in Figures 6.29 to 6.33 for each of the five independent SRs, while Figure 6.34 presents orthogonal $p_\mathrm{T}^{\ell 3}$ distributions. Two $\tilde{\chi}_1^\pm\tilde{\chi}_2^0$ via $\tilde{\ell}$ benchmark points with $m(\tilde{\chi}_1^\pm\tilde{\chi}_2^0,\tilde{\chi}_1^0)=(1000,600)$ and $(800,600)$ GeV are also included as they are within an area of parameter space that is expected to be excluded by the analysis.

In general, the statistics are low as expected, and the agreement between data events and background is good within systematic uncertainties. There are some upward fluctuations, as in the case of SR3-slep-a and SR3-slep-c, which expected 2.2 ± 0.8 and 5.4 ± 0.9 events and observed 4 and 9 events, respectively. While there were also

SR3-	slep-a	slep-b	slep-c	slep-d	slep-e
Observed	4	3	9	0	0
Total SM	2.2 ± 0.8	2.8 ± 0.4	5.4 ± 0.9	1.4 ± 0.4	1.14 ± 0.23
WZ	1.1 ± 0.4	1.98 ± 0.31	3.9 ± 0.7	0.91 ± 0.26	0.76 ± 0.17
ZZ	0.02 ± 0.01	0.01 ± 0.01	0.13 ± 0.03	0.06 ± 0.02	0.03 ± 0.01
VVV	0.26 ± 0.08	0.34 ± 0.05	0.72 ± 0.12	0.36 ± 0.10	0.25 ± 0.05
$t\bar{t}V$	0.07 ± 0.03	0.09 ± 0.02	0.20 ± 0.04	0.07 ± 0.02	0.02 ± 0.01
Higgs	0.01 ± 0.00	0.01 ± 0.01	0.03 ± 0.02	0.01 ± 0.00	–
Reducible	0.80 ± 0.46	0.36 ± 0.18	0.48 ± 0.25	–	0.08 ± 0.04

Tab. 6.11: Full 2015 and 2016 Run-II background-only fit results for SR3-slep-a to SR3-slep-e in the 3ℓ channel. All systematic and statistical uncertainties are included in the fit [115].
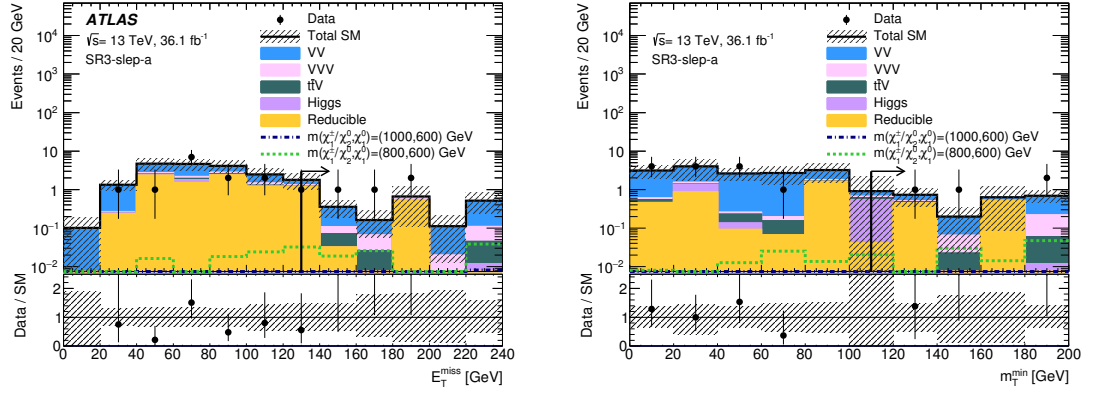
Fig. 6.29: Full 2015 and 2016 Run-II E_T^{miss} (left) [115] and m_T^{min} (right) N-1 distribution in SR3-slep-a with the scale factor applied to WZ background. The uncertainties are inclusive of both statistical and systematic.

Fig. 6.30: Full 2015 and 2016 Run-II E_T^{miss} (left) [115] and m_T^{min} (right) N-1 distribution in SR3-slep-b with the scale factor applied to WZ background. The uncertainties are inclusive of both statistical and systematic.

Fig. 6.31: Full 2015 and 2016 Run-II E_T^{miss} (left) and m_T^{min} (right) N-1 distribution in SR3-slep-c with the scale factor applied to WZ background. The uncertainties are inclusive of both statistical and systematic.

6.1 Searches for $\tilde{\chi}_1^\pm\,\tilde{\chi}_2^0$ via Sleptons
111
6 Results for $\tilde{\chi}_1^\pm\tilde{\chi}_2^0$ with Three-Lepton Final States

Fig. 6.32: Full 2015 and 2016 Run-II E_T^{miss} (left) and m_T^{min} (right) N-1 distribution in SR3-slep-d with the scale factor applied to WZ background. The uncertainties are inclusive of both statistical and systematic.
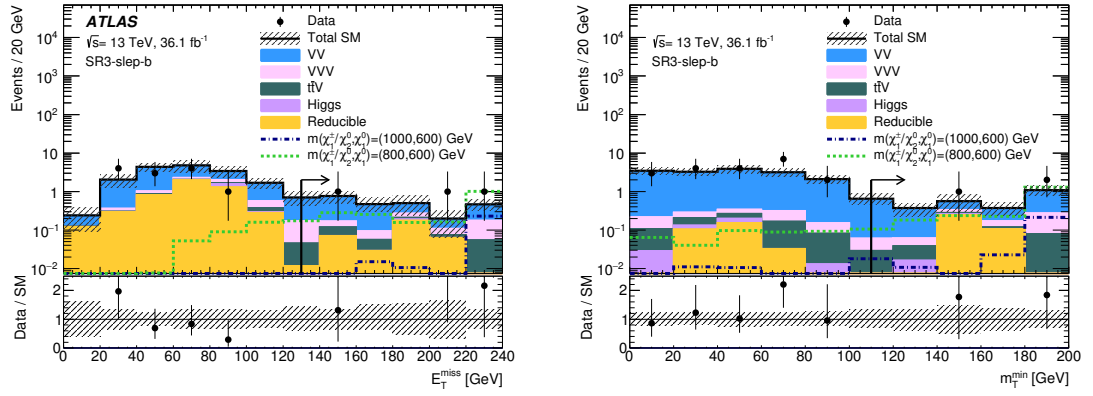

Fig. 6.33: Full 2015 and 2016 Run-II E_T^{miss} (left) and m_T^{min} (right) N-1 distribution in SR3-slep-e with the scale factor applied to WZ background. The uncertainties are inclusive of both statistical and systematic.
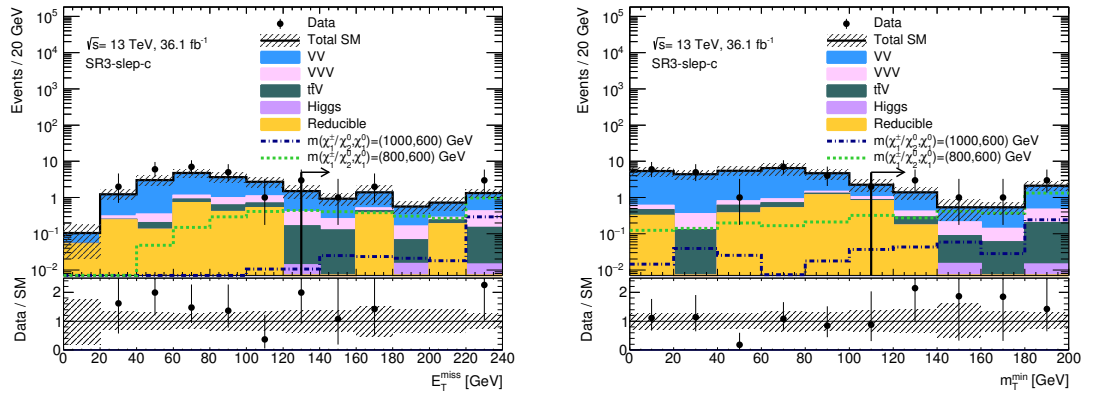

Fig. 6.34: Full 2015 and 2016 Run-II $p_T^{\ell 3}$ distributions in SR3-slep-a and SR3-slep-b (left) and SR3-slep-c to SR3-slep-e (right) [115] with the scale factor applied to WZ background. The uncertainties are inclusive of both statistical and systematic.

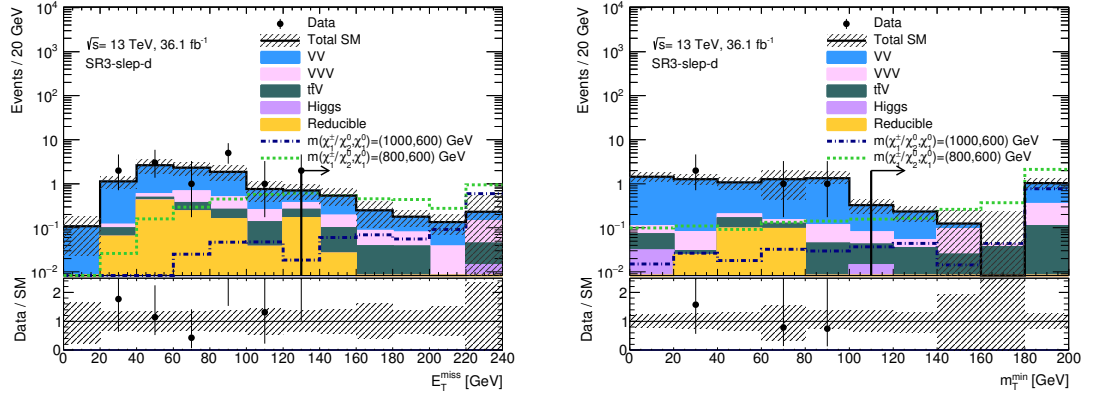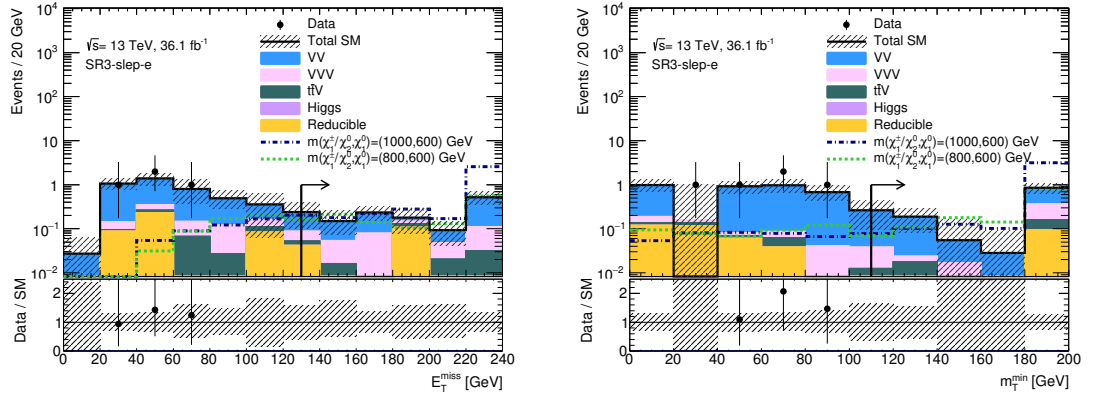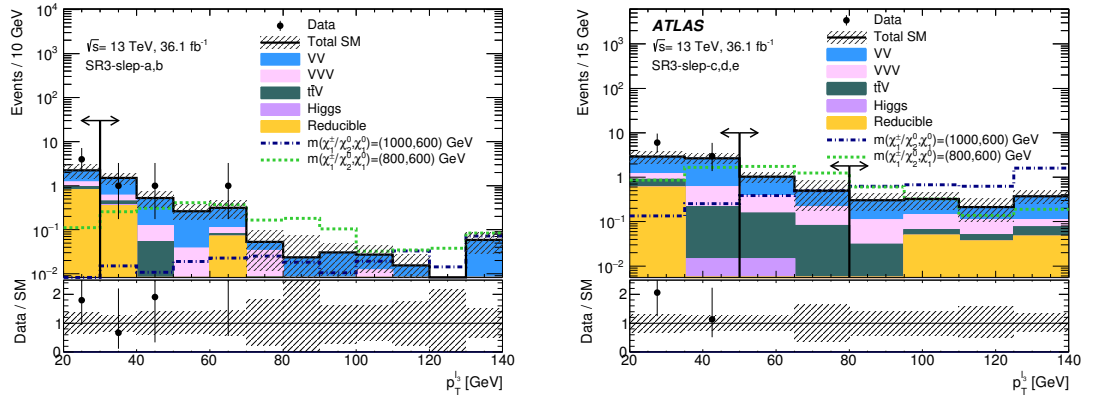downward fluctuations in SR3-slep-d and SR3-slep-e, which expected 1.4 ± 0.4 and 1.14 ± 0.23 events, respectively, and both observed zero events. However no significant excess can be claimed. The quantified statistical interpretation of these results follows.

6.1.5.2 Statistical Interpretation

In the absence of any significant excess, exclusion limits on the masses of the charginos and neutralinos are set, and are presented in Figure 6.35. The observed limit, which is indicated by the solid red line, exceeded the expected limit indicated by the dashed blue line, and gives exclusion of $\tilde{\chi}_1^{\pm}$ $\tilde{\chi}_2^0$ masses up to ~ 1.13 TeV. This is an improvement of ~ 400 GeV from Run-I and ~ 100 GeV from the early Run-II lower luminosity analysis. The exclusion of $\tilde{\chi}_1^0$ masses up to ~ 700 GeV has been achieved, which is an improvement of ~ 350 GeV from Run-I and ~ 150 GeV from the early Run-II analysis. The model-independent upper limits on the number of beyond-the-SM events and the visible signal cross-section are also presented in Table 6.12. The p-value and the corresponding significance for the background-only hypothesis are also evaluated.
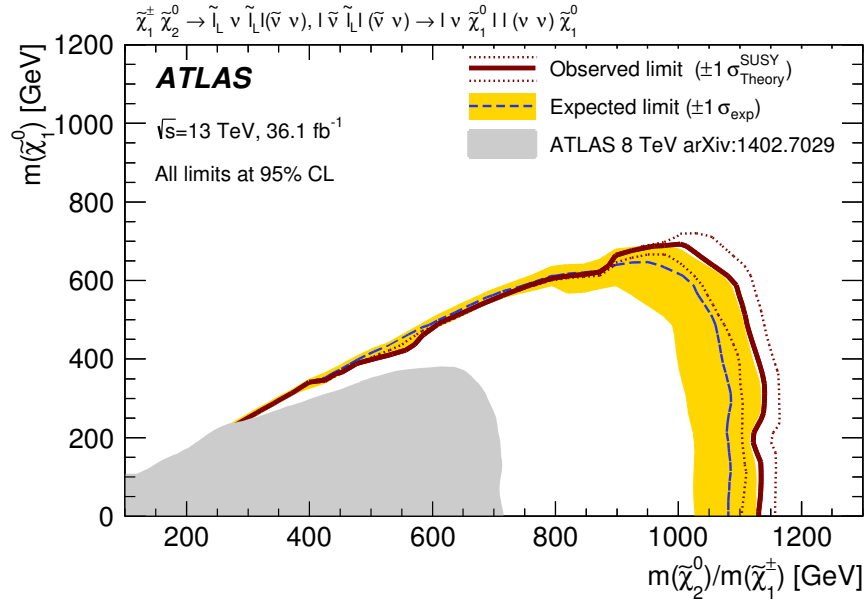
Fig. 6.35: Full 2015 and 2016 Run-II observed and expected exclusion limits on the $\tilde{\chi}_2^0\tilde{\chi}_1^{\pm}$ and $\tilde{\chi}_1^0$ masses in the context of SUSY scenarios with simplified mass spectra. The observed (solid thick red line) and expected (thin dashed blue line) exclusion contours are indicated [115]. The shaded band corresponds to the $\pm 1\sigma$ variations in the expected limit, including all uncertainties except theoretical uncertainties in the signal cross-section. The dotted lines around the observed limit illustrate the change in the observed limit as the nominal signal cross-section is scaled up and down by the theoretical uncertainty. All limits are computed at 95% confidence level. The observed limits that were obtained from ATLAS during Run-I are also shown [134].

Region	N_{obs}	N_{exp}	$\langle\epsilon\sigma\rangle^{95}_{obs}$[fb]	S^{95}_{obs}	S^{95}_{exp}	$p(s{=}0)$	Z
slep-a	4	2.2 ± 0.8	0.19	6.8	$4.7^{+2.3}_{-0.5}$	0.23	0.72
slep-b	3	2.8 ± 0.4	0.14	5.2	$5.1^{+1.9}_{-1.2}$	0.47	0.08
slep-c	9	5.4 ± 0.9	0.29	10.5	$6.8^{+2.9}_{-1.3}$	0.09	1.4
slep-d	0	1.4 ± 0.4	0.08	3.0	$3.6^{+1.2}_{-0.6}$	0.5	0
slep-e	0	1.1 ± 0.2	0.09	3.3	$3.6^{+1.3}_{-0.5}$	0.5	0

Tab. 6.12: Summary of results and model-independent limits for the $\tilde{\ell}$-mediated channel. The observed (N_{obs}) and expected background (N_{exp}) yields in the signal regions are indicated. Signal model-independent upper limits at 95% confidence level on the the visible signal cross-section ($\langle\epsilon\sigma\rangle^{95}_{obs}$), and the observed and expected upper limit on the number of BSM events (S^{95}_{obs} and S^{95}_{exp}, respectively) are also shown. The $\pm 1\sigma$ variations of the expected limit originate from the statistical and systematic uncertainties in the background prediction. The last two columns show the p-value and the corresponding significance for the background-only hypothesis. For SRs where the data yield is smaller than expected, the p-value is truncated at 0.5 and the significance is set to 0 [115].

6.2 Searches for $\tilde{\chi}_1^\pm \tilde{\chi}_2^0$ via W and Z Bosons

The $\tilde{\chi}_1^\pm \tilde{\chi}_2^0$ via the W/Z-mediated channel is presented in this section and follows the same structure as the $\tilde{\ell}$ channel. The SR optimisation and definition is in Section 6.2.1, the definition of CRs and VRs, along with data to background comparisons are in Section 6.2.2, and the results are in Section 6.2.4. The data-driven Fake Factor has been used to estimate the reducible backgrounds.

6.2.1 Signal Region Definition for $\tilde{\chi}_1^\pm \tilde{\chi}_2^0$ via W and Z Bosons

As with the $\tilde{\ell}$ analysis, my primary contribution was to define SRs that offer optimal sensitivity to $\tilde{\chi}_1^\pm \tilde{\chi}_2^0$ decays via the W/Z-mediated channels. Cases where the mass difference between the $\tilde{\chi}_1^\pm \tilde{\chi}_2^0$ and the $\tilde{\chi}_1^0$ are close to and larger than the Z boson mass are again considered, with integrated luminosity of $36.1\,\mathrm{fb}^{-1}$ used throughout. I worked along side another analyst from a different institute, performing numerous iterations until we converged on the final signal region definitions presented here.

6.2.1.1 Optimisation of Signal Regions

The SR definitions are presented in Table 6.13. A selection of benchmark signal points that each reside in different areas of parameter space outside of previously excluded ranges are utilised for the different SRs. Contrary to the $\tilde{\ell}$ analysis, $m^{\mathrm{min}}_{\mathrm{SFOS}}$

Bin	$m_{\mathrm{SFOS}}^{\min}$ [GeV]	n_{Jets}	$m_{\mathrm{T}}^{\min}$ [GeV]	$E_{\mathrm{T}}^{\mathrm{miss}}$ [GeV]	$p_{\mathrm{T}}^{\ell 3}$ [GeV]	$p_{\mathrm{T}}^{\ell\ell\ell}$ [GeV]	p_{T}^{jet1} [GeV]
SR3-WZ-0Ja				60-120			
SR3-WZ-0Jb	$\in[81.2, 101.2]$	0	>110	120-170			
SR3-WZ-0Jc				>170			
SR3-WZ-1Ja			>110	120-200		<120	> 70
SR3-WZ-1Jb	$\in[81.2, 101.2]$	> 0	110-160	>200			
SR3-WZ-1Jc			>160		>35		

Tab. 6.13: Full 2015 and 2016 Run-II summary of the exclusive signal regions targeting both intermediate and high mass spectrum.

is required to be on-Z in order to target the intermediate decay via the Z boson. To optimise for lower $E_{\mathrm{T}}^{\mathrm{miss}}$ values and to access the intermediate mass-splittings, this region is divided into orthogonal jet multiplicities, requiring either no jets, or at least one jet.

The $E_{\mathrm{T}}^{\mathrm{miss}}$ and $m_{\mathrm{T}}^{\min}$ variables are again utilised, and two-dimensional correlation plots are used to initially consider the choice of cuts. Figures 6.36 to 6.38 present six correlation plots requiring $n_{\mathrm{Jets}} = 0$ for benchmark signal points $m(\tilde{\chi}_1^\pm \tilde{\chi}_2^0, \tilde{\chi}_1^0)$ = (200,100), (300,150), (400,200), (450,150), (500,0) and (500,100) GeV. These figures show the significance maximas are fixed around $m_T > 110\,\mathrm{GeV}$ while shifting to increasing $E_{\mathrm{T}}^{\mathrm{miss}}$ values as the mass-splittings of the signal points increase. For this reason, three exclusive SRs are defined with the assistance of kinematic N-1 distributions with one-dimensional Z_N curves, presented in Figures 6.39 to 6.41, with $E_{\mathrm{T}}^{\mathrm{miss}}$ of 60-120 GeV, 120-170 GeV and $> 170\,\mathrm{GeV}$.

Figures 6.42 to 6.44 show correlation plots for the same six benchmark signal points with $n_{\mathrm{Jets}} > 0$. In this case, the significance maximas are seen to shift to both higher $E_{\mathrm{T}}^{\mathrm{miss}}$ and m_T values with increasing mass-splittings. Kinematic N-1 distributions with one-dimensional Z_N curves, presented in Figures 6.45 to 6.47, are used to determine optimal access to the different areas of parameter space. Figure 6.45 shows SR3-WZ-1Ja, with $E_{\mathrm{T}}^{\mathrm{miss}}$ with 120-200 GeV and $m_{\mathrm{T}}^{\min} > 110\,\mathrm{GeV}$, is able to target intermediate mass-splittings. While the N-1 distributions in Figures 6.46 and 6.47 for SR3-WZ-1Jb and SR3-WZ-1Jc, have $E_{\mathrm{T}}^{\mathrm{miss}} > 200\,\mathrm{GeV}$ and are binned in m_T to target the higher mass-splitting scenarios.

Additional variables to improve sensitivity were investigated. The $p_{\mathrm{T}}^{\ell\ell\ell}$ and p_{T}^{jet1} variables were found to be highly correlated and benefical to increase sensitivity to SUSY scenarios with intermediate mass-splittings in the SR3-WZ-1Ja region. An
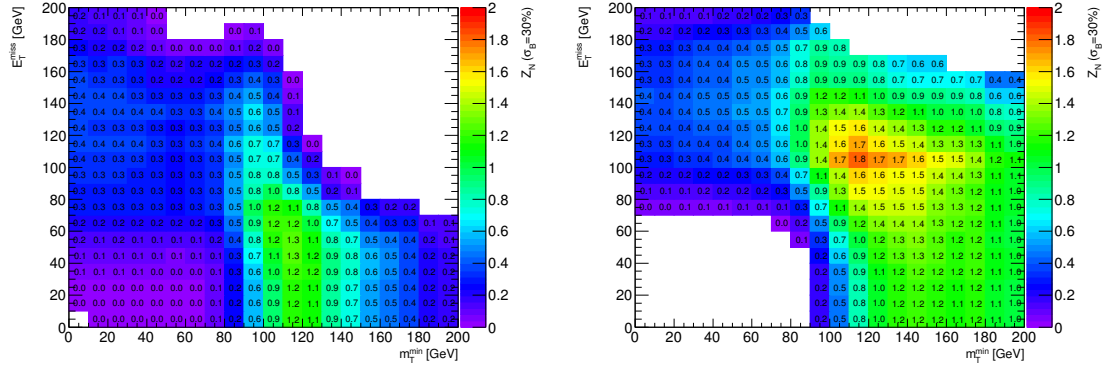
Fig. 6.36: Two-dimensional correlation plots showing the significance for E_T^{miss} vs. m_T^{min} with $n_{Jets} = 0$ for $m(\tilde{\chi}_1^\pm/\tilde{\chi}_2^0, \tilde{\chi}_1^0) = (200,100)$ GeV (left) and $(300,150)$ GeV (right). MC simulations have been used for both irreducible and reducible backgrounds. A 30% uncertainty is included in the Z_N calculations. White indicates less than one background event.

Fig. 6.37: Two-dimensional correlation plots showing the significance for E_T^{miss} vs. m_T^{min} with $n_{Jets} = 0$ for $m(\tilde{\chi}_1^\pm/\tilde{\chi}_2^0, \tilde{\chi}_1^0) = (400,200)$ GeV (left) and $(450,150)$ GeV (right). MC simulations have been used for both irreducible and reducible backgrounds. A 30% uncertainty is included in the Z_N calculations. White indicates less than one background event.
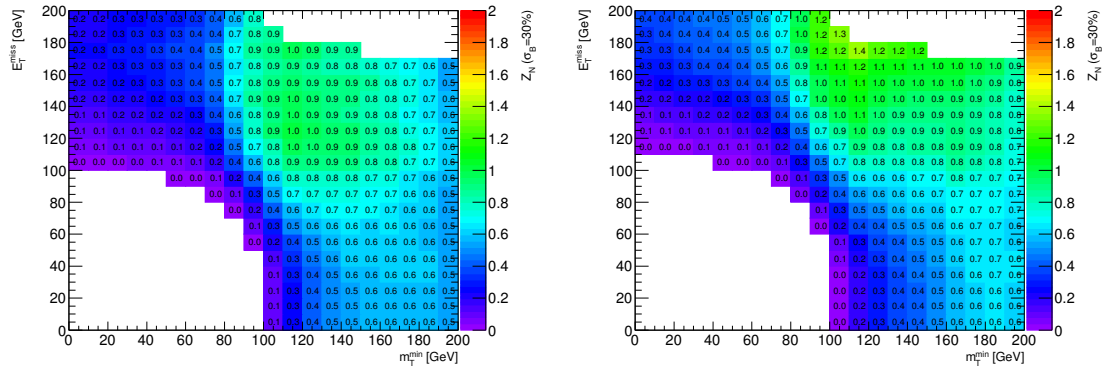
upper cut of $120\,\text{GeV}$ on $p_T^{\ell\ell\ell}$ and a lower cut of $70\,\text{GeV}$ on p_T^{jet1} are applied, based on the findings of the correlation plots shown in Figure 6.48. Finally, Figure 6.49 presents a kinematic N-1 $p_T^{\ell 3}$ distribution with one-dimensional Z_N curves for SR3-WZ-1Jc, with a requirement of $> 35\,\text{GeV}$, designed to target very high mass points. The full yield breakdown for both SRs is presented in Table 6.14.
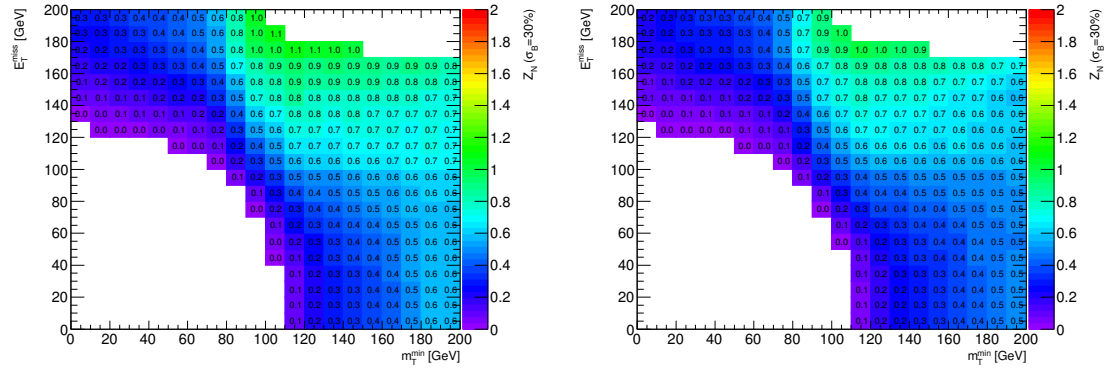
Fig. 6.38: Two-dimensional correlation plots showing the significance for E_T^{miss} vs. m_T^{min} with $n_{Jets} = 0$ for $m(\tilde{\chi}_1^\pm/\tilde{\chi}_2^0, \tilde{\chi}_1^0) = (500,0)$ GeV (left) and $(500,100)$ GeV (right). MC simulations have been used for both irreducible and reducible backgrounds. A 30% uncertainty is included in the Z_N calculations. White indicates less than one background event.
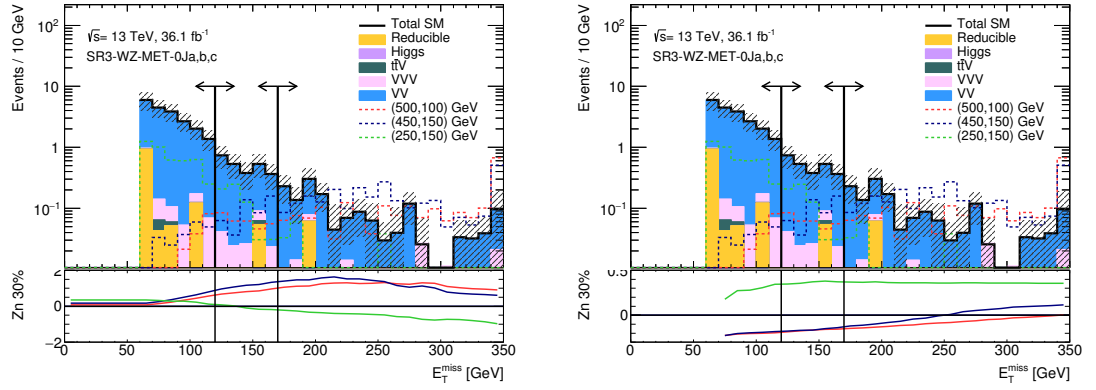
Fig. 6.39: Full 2015 and 2016 Run-II N-1 distributions for E_T^{miss} for the $n_{Jets} = 0$ bins. The arrows indicate the SR cuts. The ratio plot shows the one-dimensional Z_N curves for three benchmark signal points, which read from left to right for (left), indicating optimal lower cuts, and right to left for (right) indicating optimal upper cuts.

Fig. 6.40: Full 2015 and 2016 Run-II N-1 distributions for m_T^{min} for SR3-WZ-0Ja (left) and SR3-WZ-0Jb (right). The arrows indicate the SR cuts. The ratio plot shows the one-dimensional Z_N curves for three benchmark signal points.

Fig. 6.41: Full 2015 and 2016 Run-II N-1 m_T^{min} distributions for SR3-WZ-0Jc. The arrows indicate the SR cuts. The ratio plot shows the one-dimensional Z_N curves for three benchmark signal points.
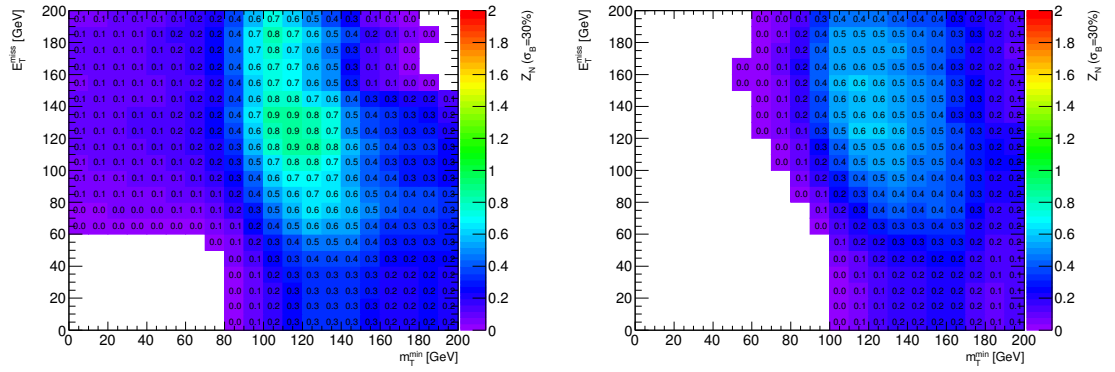
Fig. 6.42: Two-dimensional correlation plots showing the significance for E_T^{miss} vs. m_T^{min} with $n_{\mathrm{Jets}} > 0$ for $m(\tilde{\chi}_1^\pm/\tilde{\chi}_2^0, \tilde{\chi}_1^0) = (200,100)$ GeV (left) and $(250,150)$ GeV (right). MC simulations have been used for both irreducible and reducible backgrounds. A 30% uncertainty is included in the Z_N calculations. White indicates less than one background event.
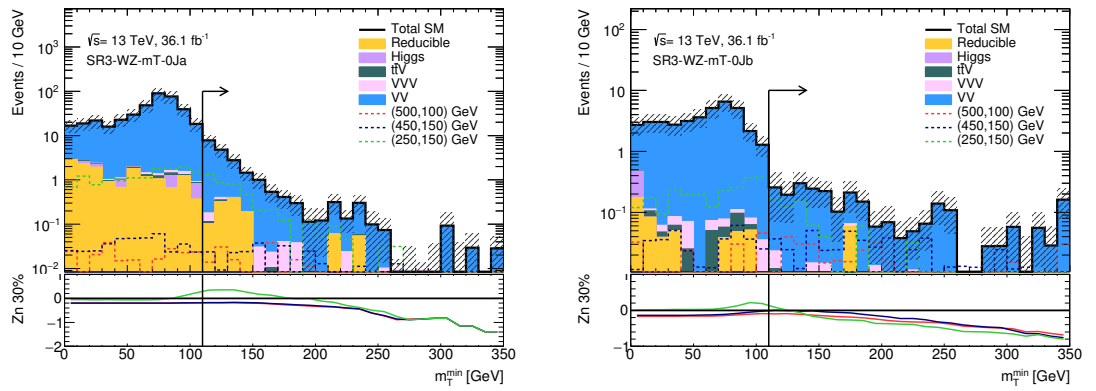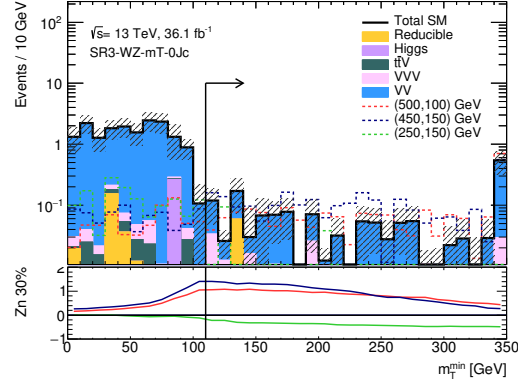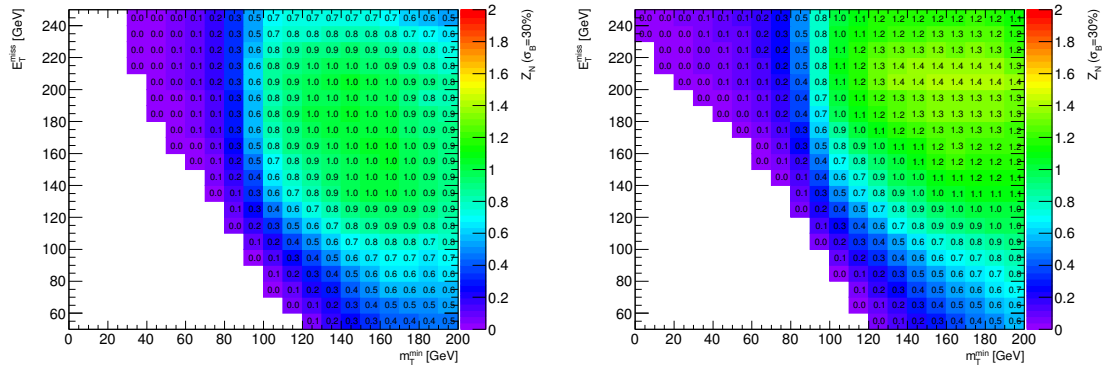

Fig. 6.43: Two-dimensional correlation plots showing the significance for E_T^{miss} vs. m_T^{min} with $n_{\mathrm{Jets}} > 0$ for $m(\tilde{\chi}_1^\pm/\tilde{\chi}_2^0, \tilde{\chi}_1^0) = (400,200)$ GeV (left) and $(450,150)$ GeV (right). MC simulations have been used for both irreducible and reducible backgrounds. A 30% uncertainty is included in the Z_N calculations. White indicates less than one background event.

Fig. 6.44: Two-dimensional correlation plots showing the significance for E_T^{miss} vs. m_T^{min} with $n_{Jets} > 0$ for $m(\tilde{\chi}_1^\pm/\tilde{\chi}_2^0, \tilde{\chi}_1^0) = (500,0)$ GeV (left) and $(500,100)$ GeV (right). MC simulations have been used for both irreducible and reducible backgrounds. A 30% uncertainty is included in the Z_N calculations. White indicates less than one background event.

Fig. 6.45: Full 2015 and 2016 Run-II N-1 E_T^{miss} distributions for SR3-WZ-1Ja. The arrows indicate the SR cuts. The ratio plot shows the one-dimensional $Z_N$ curves for three benchmark signal points, which read from left to right for (left), indicating optimal lower cuts, and right to left for (right) indicating optimal upper cuts.
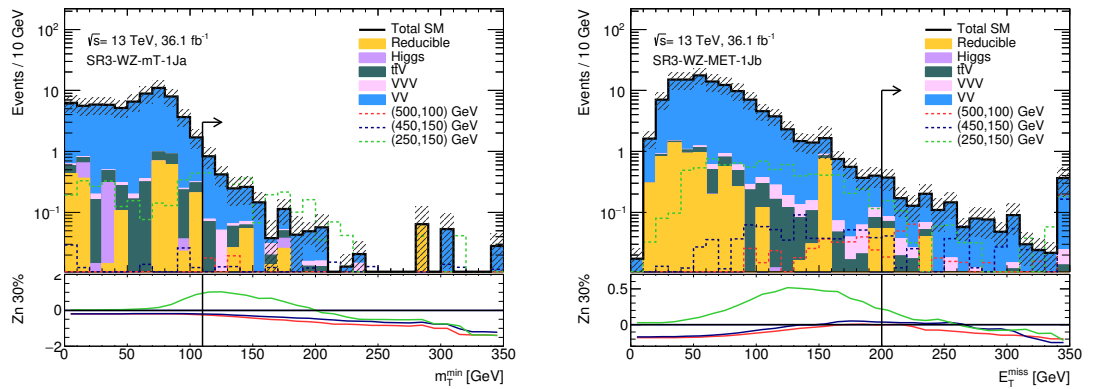
Fig. 6.46: Full 2015 and 2016 Run-II N-1 distributions for SR3-WZ-1Ja (left) and SR3-WZ-1Jb (right). The arrows indicate the SR cuts. The ratio plot shows the one-dimensional Z_N curves for three benchmark signal points.
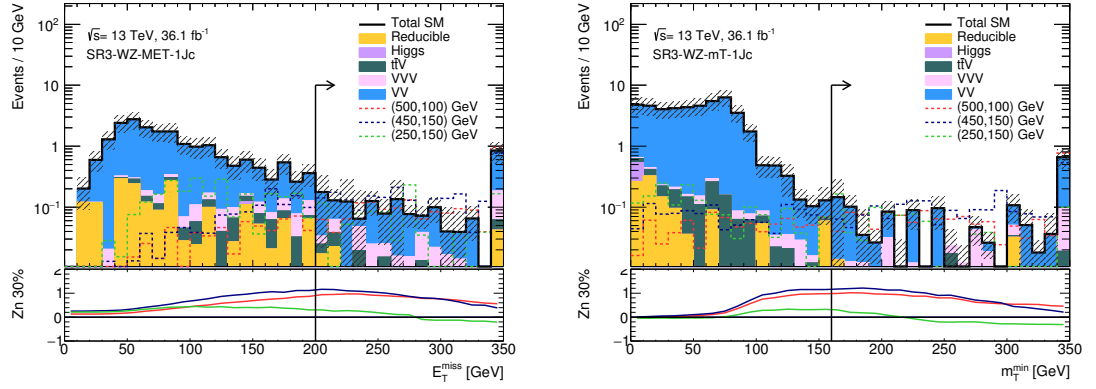
Fig. 6.47: Full 2015 and 2016 Run-II N-1 E_T^{miss} (left) and m_T^{min} (right) distributions for SR3-WZ-1Jc. The arrows indicate the SR cuts. The ratio plot shows the one-dimensional Z_N curves for three benchmark signal points.
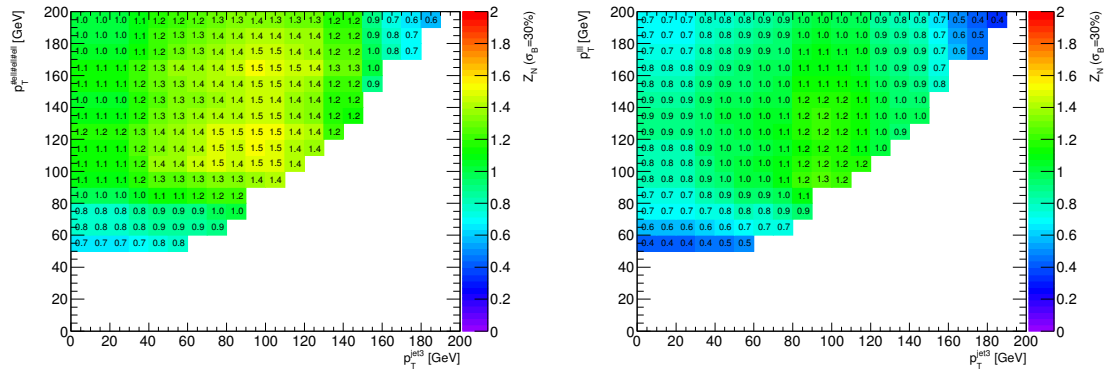
Fig. 6.48: Two-dimensional correlation plots showing the significance for $p_T^{\ell\ell\ell}$ vs. p_T^{jet1} in the SR3-WZ-01Ja region for the two intermediate mass splitting scenarios $m(\tilde{\chi}_1^\pm/\tilde{\chi}_2^0, \tilde{\chi}_1^0) =$ (200,100) GeV (left) and (250,150) GeV (right). MC simulations have been used for both irreducible and reducible backgrounds. A 30% uncertainty is included in the Z_N calculations. White indicates less than one background event.
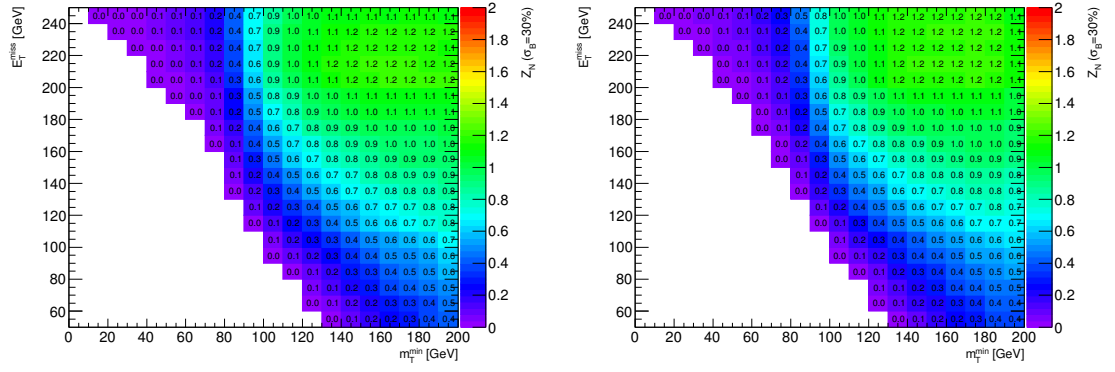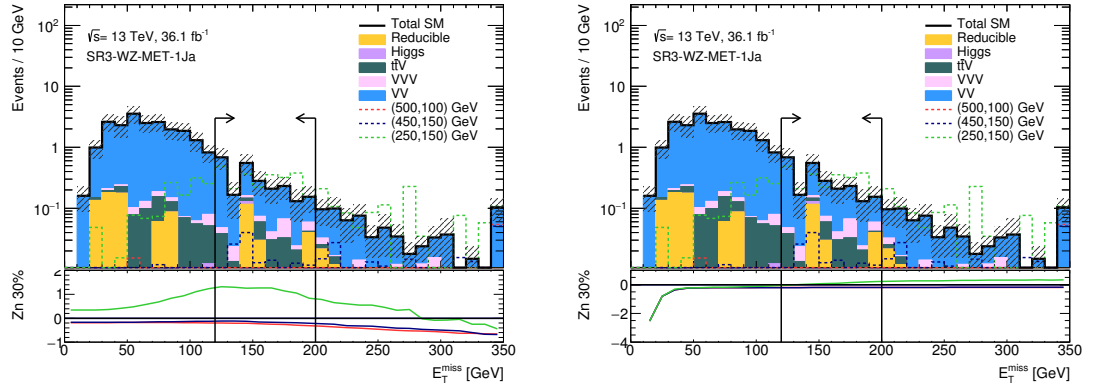

Fig. 6.49: Full 2015 and 2016 Run-II N-1 $p_T^{\ell3}$ distribution for SR3-WZ-1Jc. The arrows indicate the SR cuts. The ratio plot shows the one-dimensional Z_N curves for three benchmark signal points.

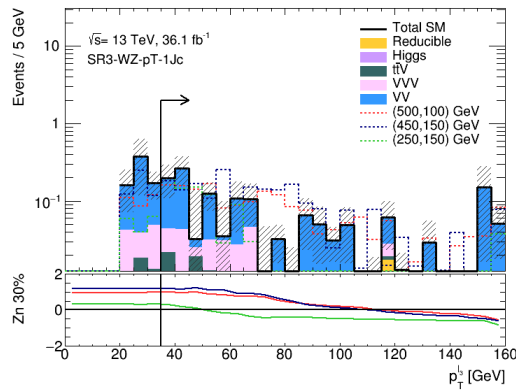| Process	WZ-0Ja	WZ-0Jb	WZ-0Jc	WZ-1Ja	WZ-1Jb	WZ-1Jc
WZ	18.15 ± 0.9	2.29 ± 0.33	1.23 ± 0.24	1.9 ± 0.24	1.58 ± 0.21	0.96 ± 0.27
ZZ	0.81 ± 0.09	0.06 ± 0.02	0.05 ± 0.02	0.05 ± 0.01	0.02 ± 0.01	0.01 ± 0.01
VVV	0.31 ± 0.05	0.13 ± 0.03	0.13 ± 0.03	0.12 ± 0.03	0.12 ± 0.03	0.23 ± 0.04
$t\bar{t}V$	0.05 ± 0.02	0.02 ± 0.01	0.01 ± 0.01	0.18 ± 0.03	0.13 ± 0.02	0.09 ± 0.02
Higgs	–	–	–	0.01 ± 0.01	–	–
Reducible	1.10 ± 0.5	0.02 ± 0.01	0.04 ± 0.02	0.11 ± 0.06	0.07 ± 0.04	0.01 ± 0.0
Total SM	20.41 ± 1.04	2.51 ± 0.33	1.46 ± 0.24	2.37 ± 0.25	1.91 ± 0.21	1.31 ± 0.28
via W/Z						
(500,100)	0.16 ± 0.04	0.31 ± 0.05	2.05 ± 0.13	0.04 ± 0.02	0.43 ± 0.06	1.79 ± 0.12
(500,0)	0.11 ± 0.03	0.29 ± 0.05	2.09 ± 0.13	0.05 ± 0.02	0.37 ± 0.05	1.85 ± 0.12
(450,150)	0.21 ± 0.05	0.48 ± 0.08	2.68 ± 0.18	0.12 ± 0.04	0.48 ± 0.08	2.09 ± 0.17
(400,200)	0.81 ± 0.09	1.42 ± 0.12	2.08 ± 0.14	0.24 ± 0.05	0.61 ± 0.08	1.31 ± 0.12
(300,150)	3.93 ± 0.35	3.1 ± 0.31	1.88 ± 0.24	1.07 ± 0.2	1.44 ± 0.22	0.81 ± 0.17
(250,150)	4.37 ± 0.37	0.64 ± 0.14	0.13 ± 0.07	2.46 ± 0.3	0.75 ± 0.16	0.78 ± 0.17
(200,100)	8.85 ± 0.79	1.21 ± 0.31	0.5 ± 0.19	3.53 ± 0.52	1.44 ± 0.34	0.36 ± 0.19
Z_N						
(500,100)	0	0	0.76	0	0.09	1.39
(500,0)	0	0	0.76	0	0.06	1.45
(450,150)	0	0	1.07	0	0.16	1.68
(400,200)	0	0.26	0.73	0	0.24	1.01
(300,150)	0.46	0.91	0.69	0.40	0.80	0.43
(250,150)	0.49	0	0	1.07	0.22	0.37
(200,100)	1.16	0	0	1.61	0.71	0

Tab. 6.14: Yields for the SM background processes and seven benchmark signal points for the four SFOS SRs targeting models with intermediate decays via the W and Z bosons. Z_N values are included for the signal points. The uncertainties are statistical only.

6.2.1.2 Sensitivity

Figure 6.50 shows the expected significance Z_N values for the $\tilde{\chi}_1^\pm \tilde{\chi}_2^0$ decays via gauge bosons when combining all six SRs. For this scenario the masses of the $\tilde{\chi}_1^\pm \tilde{\chi}_2^0$ are expected to be excluded up to $500\,\text{GeV}$, an increase of $\sim 150\,\text{GeV}$ from Run-I. The mass of the $\tilde{\chi}_1^0$ is expected to be excluded up to $\sim 150\,\text{GeV}$, which is an increase of $\sim 40\,\text{GeV}$ obtained from Run-I. Three of the benchmark signal points, $m(\tilde{\chi}_1^\pm \tilde{\chi}_2^0, \tilde{\chi}_1^0)$
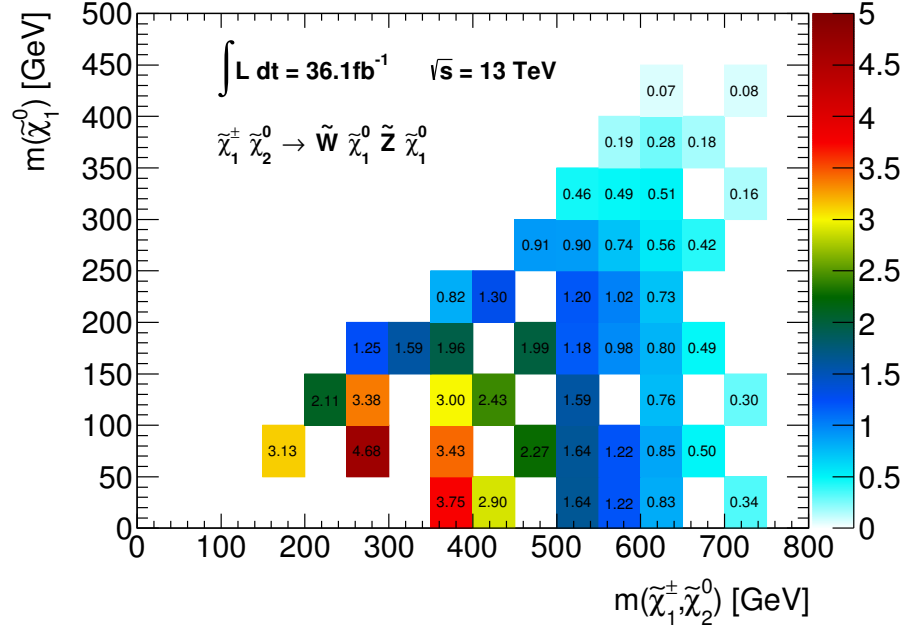
Fig. 6.50: Full 2015 and 2016 Run-II two-dimensional sensitivity plot showing the expected combined significances Z_N for the SR binned selection in the C1N2 via gauge bosons simplified model. MC simulation is used for all backgrounds. A 30% uncertainty is included in the Z_N calculations.

= (200,100), (450,150) and (500,0) GeV are expected to be excluded if no excess is observed, while $m(\tilde{\chi}_1^\pm \tilde{\chi}_2^0, \tilde{\chi}_1^0)$ = (300,150) and (500,100) GeV have the potential to be excluded.

6.2.2 Background Validation for $\tilde{\chi}_1^\pm \tilde{\chi}_2^0$ via W and Z Bosons

This section is devoted to validating the SM background processes that have already been described in the general strategy in Chapter 5. Similarly to the $\tilde{\ell}$ analysis, I contributed towards defining CRs and VRs, I provided support in running the background-only fits and generating the tables presented, and also producing all of the distributions for visual interpretation. As with the $\tilde{\ell}$ analysis, the data-driven Fake Factor is used to model the reducible processes, while the most dominant SM background, WZ, uses dedicated CRs to derive scale factors.

6.2.2.1 Control Regions

Although the W/Z analysis uses the same data and background samples as the $\tilde{\ell}$ analysis, two new CRs are required, tailored to determine separate scale factors for events with $n_{\text{Jets}} = 0$ and $n_{\text{Jets}} > 0$, as per the W/Z SRs. To keep the CRs orthogonal to the SRs, both require $m_{\text{T}}^{\text{min}} < 110\,\text{GeV}$. Conversely, to keep the regions kinematically similar and to increase WZ purity by reducing the number of

Tab. 6.15: Full 2015 and 2016 Run-II definitions of CRs with either zero jets or at least one jet. Al requirements are in addition to the preselection. Units are in GeV.

Region	n_{Jets}	m_{SFOS} [GeV]	$m_{\text{T}}^{\text{min}}$ [GeV]	$E_{\text{T}}^{\text{miss}}$ [GeV]
CR3ℓ-0J	0	$\notin [81.2, 101.2]$	<110	>60
CR3ℓ-1J	>0			>120

fake backgrounds, both maintain their corresponding $E_{\text{T}}^{\text{miss}}$ cuts of $>60\,\text{GeV}$ and $>120\,\text{GeV}$, respectively. Table 6.15 gives a summary of the CR definitions.

As described in Section 5.6, observed data is used to tune the SM WZ background so that the total estimated background matches. The scale factors for the WZ background was calculated to be 1.017 ± 0.054 for events with $n_{\text{Jets}} = 0$, and 0.907 ± 0.065 for events with $n_{\text{Jets}} > 0$.

6.2.2.2 Validation Regions

In order to validate the new CRs, two corresponding VRs with $n_{\text{Jets}} = 0$ and $n_{\text{Jets}} > 0$ are defined, presented in Table 6.16. To remain orthogonal to the CR and SRs, a low-$E_{\text{T}}^{\text{miss}}$ is enforced. Distributions in $E_{\text{T}}^{\text{miss}}$, $m_{\text{T}}^{\text{min}}$, $m_{\text{SFOS}}^{\text{min}}$ and lepton p_{T} are presented in Figures 6.51 to 6.56, with the derived scale factor applied. All data to background comparisons show good agreement within uncertainty.

Tab. 6.16: Full 2015 and 2016 Run-II VR definitions. All requirements are in addition to the preselection. Units are in GeV.

Region	n_{Jets}	$m_{\ell\ell\ell}$ [GeV]	m_{SFOS} [GeV]	$E_{\text{T}}^{\text{miss}}$ [GeV]
VR3-Za-0J	0	$\notin [81.2, 101.2]$	$\in [81.2, 101.2]$	40-60
VR3-Za-1J	>0			
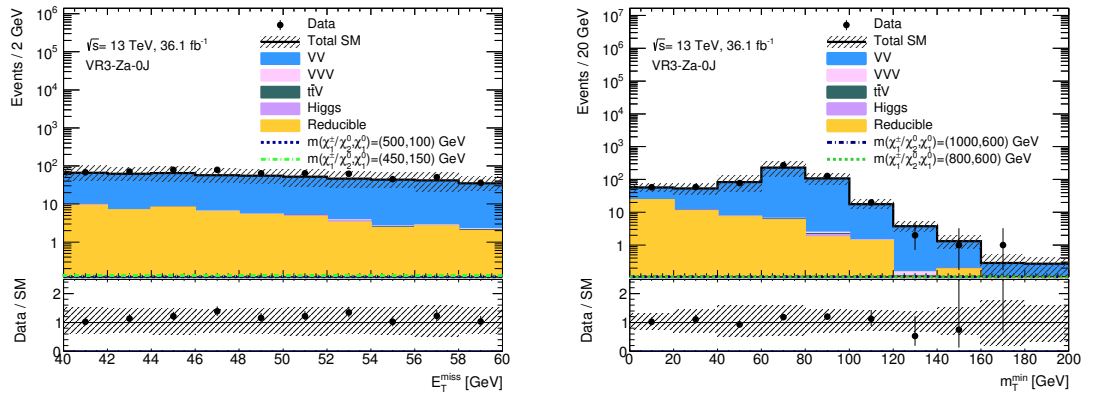
Fig. 6.51: Full 2015 and 2016 Run-II distributions in VR3-Za-0J with scale factor applied to WZ background. The uncertainties are inclusive of both statistical and systematic.
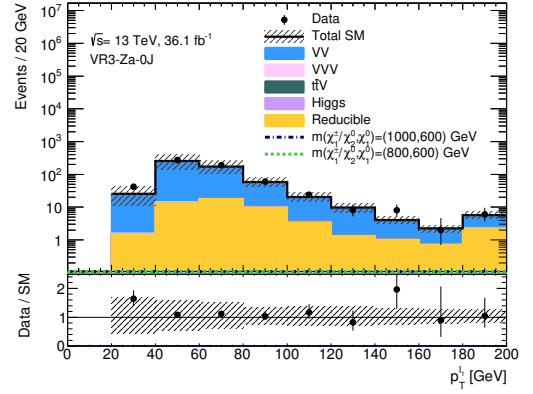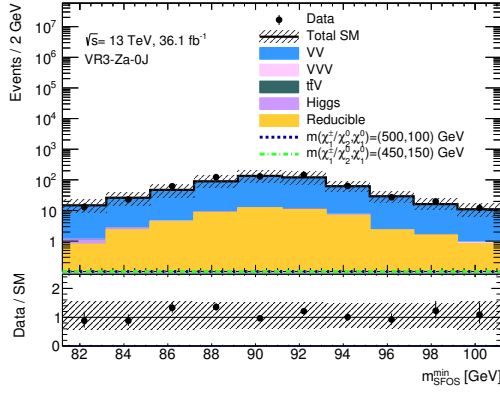
Fig. 6.52: Full 2015 and 2016 Run-II distributions in VR3-Za-0J with scale factor applied to WZ background. The uncertainties are inclusive of both statistical and systematic.
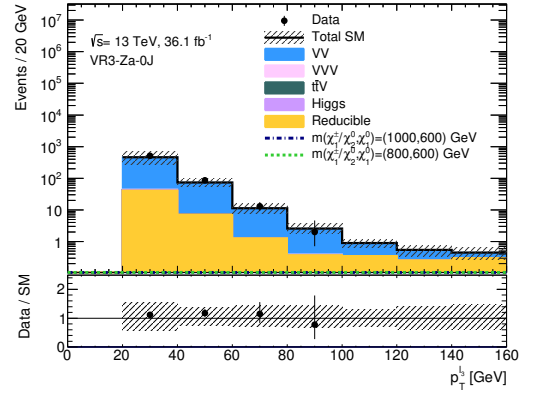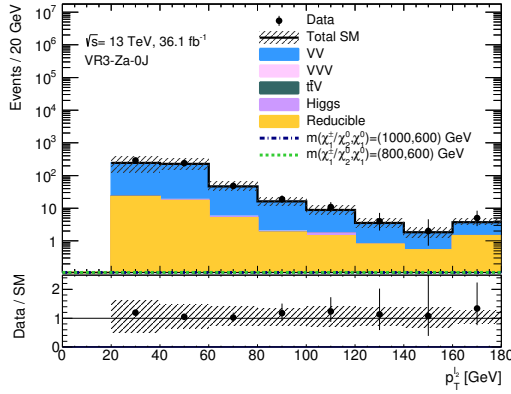
Fig. 6.53: Full 2015 and 2016 Run-II distributions in VR3-Za-0J with scale factor applied to WZ background. The uncertainties are inclusive of both statistical and systematic.
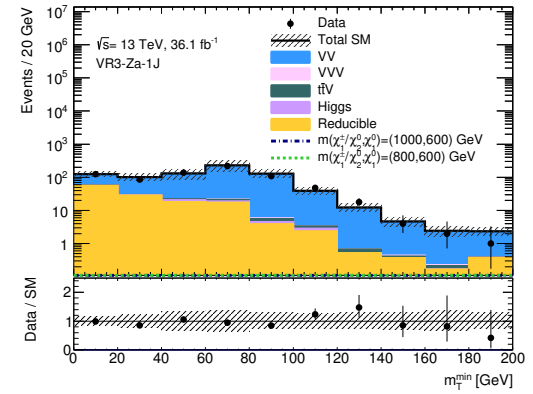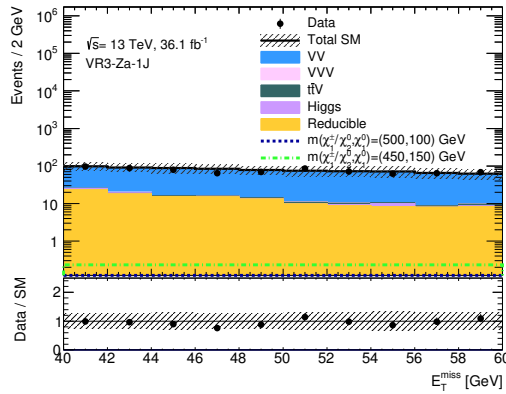
Fig. 6.54: Full 2015 and 2016 Run-II distributions in VR3-Za-1J with scale factor applied to WZ background. The uncertainties are inclusive of both statistical and systematic.
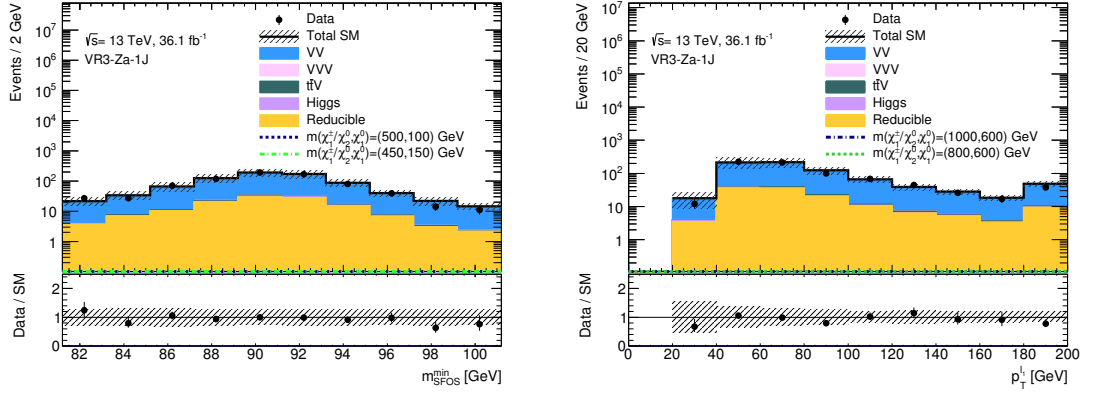
Fig. 6.55: Full 2015 and 2016 Run-II distributions in VR3-Za-1J with scale factor applied to WZ background. The uncertainties are inclusive of both statistical and systematic.
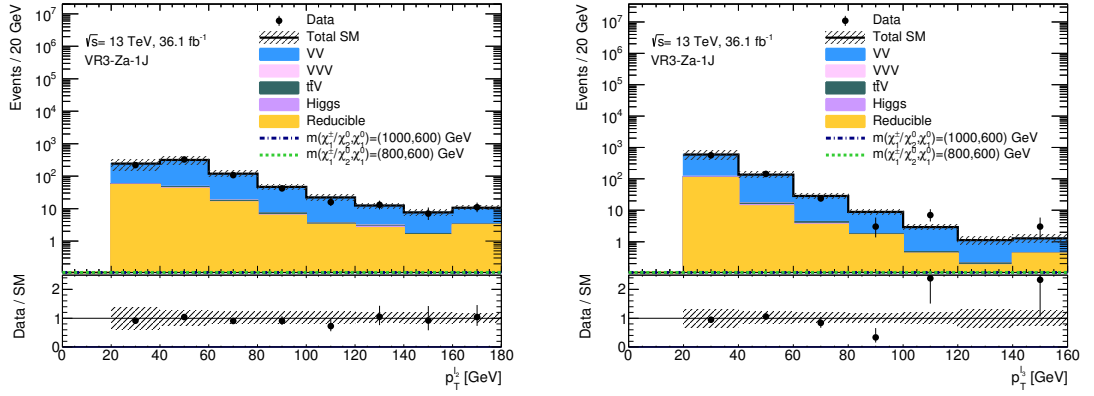
Fig. 6.56: Full 2015 and 2016 Run-II distributions in VR3-Za-1J with scale factor applied to WZ background. The uncertainties are inclusive of both statistical and systematic.

6.2.2.3 Background-only Fit

The CRs defined in Table 6.15 and VRs defined in Table 6.16 have been used for the extrapolation of the fit results as detailed in Section 5.6. The results are shown in Tables 6.17 and 6.18. Both statistical and systematic uncertainties are included. The total expected SM yields are in good agreement with the number of observed events in each region.

	CR3-WZ-0J	VR3-Za-0J
Observed events	486	618
Total SM	486 ± 22	598 ± 61
WZ0j	453 ± 27	520 ± 61
ZZ	12 ± 10	24 ± 20
VVV	1.6 ± 1.3	0.93 ± 0.77
$t\bar{t}V$	1.4 ± 1.1	0.79 ± 0.66
Higgs	2.5 ± 2.1	1.21 ± 1.01
Reducible	15 ± 8	51 ± 25

Tab. 6.17: Full 2015 and 2016 Run-II background-only fit for the WZ-mediated CRs. All systematic and statistical uncertainties are included.

	CR3-WZ-1J	VR3-Za-1J
Observed events	264	746
Total SM	264 ± 16	809 ± 95
WZ1j	241 ± 22	620 ± 84
ZZ	5 ± 5	48 ± 40
VVV	1.6 ± 1.3	1.5 ± 1.3
$t\bar{t}V$	7 ± 6	7.3 ± 6.1
Higgs	2.9 ± 2.4	5.6 ± 4.6
Reducible	5.9 ± 2.9	127 ± 63

Tab. 6.18: Full 2015 and 2016 Run-II background-only fit for the WZ-mediated CRs. All systematic and statistical uncertainties are included.

6.2.3 Systematic Uncertainties for $\tilde{\chi}_1^\pm \tilde{\chi}_2^0$ via W and Z Bosons

A summary of the dominant sources of systematic uncertainties in the background and signal estimates for each SR are listed in Table 6.19. The systematic uncertainty associated with jets can be seen to be a consistently significant contribution, followed by both WZ modelling and $E_\mathrm{T}^\mathrm{miss}$ contributions.

Uncertainty	WZ-0Ja	WZ-0Jb	WZ-0Jc	WZ-1Ja	WZ-1Jb	WZ-1Jc
Reducible	2.48%	0.37%	1.28%	2.26%	2.20%	–
WZ Modelling	5.37%	5.20%	5.51%	8.34%	5.74%	12.8%
Jets	7.79%	7.59%	8.60%	14.0%	4.18%	6.83%
E_T^{miss}	7.10%	3.77%	5.66%	12.6%	2.75%	5.38%
Leptons	1.06%	3.10%	3.27%	3.94%	2.33%	3.27%
b-tagging Eff.	–	–	–	1.28%	0.78%	0.79%

Tab. 6.19: Breakdown of the dominant systematic uncertainties on background estimates. Percentages are quoted relative to the total background estimates for each SR defined in Section 6.1.2 and assume no correlation between the combined sub-categories to give an approximate idea of magnitudes for illustrative purposes.

6.2.4 Results for $\tilde{\chi}_1^\pm \tilde{\chi}_2^0$ via W and Z Bosons

This section is dedicated to presenting and interpreting the results for the $36.1\,\text{fb}^{-1}$ W/Z-mediated channel at a centre-of-mass energy of $\sqrt{s} = 13\,\text{TeV}$. All the statistical strategies adopted have previously been discussed in the general analysis strategy, in Section 5.6. As with the $\tilde{\ell}$ analysis, in addition to generating distributions for visual interpretation, and providing support for the background-only fits, I was responsible for running the discovery-fit to set the model-independent upper limits.

6.2.4.1 Observations in Signal Regions

The observed number of events in all signal regions, along with the total background expectations and uncertainties are shown in Table 6.20. The uncertainties include both statistical and systematic components. As with the $\tilde{\ell}$ analysis, it is also interesting to compare the shape of the important kinematic distributions for variables that were used for optimisation. The E_T^{miss}, m_T^{min} and $p_T^{\ell 3}$ distributions, are presented for each of the six signal regions in Figures 6.57 to 6.60. Two $\tilde{\chi}_1^\pm \tilde{\chi}_2^0$ via W/Z benchmark points with $m(\tilde{\chi}_1^\pm \tilde{\chi}_2^0, \tilde{\chi}_1^0) = (500,100)$ and $(450,150)$ GeV are also included as they are within an area of parameter space that is expected to be excluded by the analysis.

In general, the agreement between data events and background is good within systematic uncertainties. As with the $\tilde{\ell}$ channel there are some upward fluctuations, as in the case of SR3-WZ-1Jb and SR3-WZ-1Jc, which expected 1.82±0.26 and 1.26±0.34 events and observed 3 and 4 events, respectively. There were also downward fluctuations in SR3-WZ-0Jb and SR3-WZ-1Ja.

SR3-	WZ-0Ja	WZ-0Jb	WZ-0Jc	WZ-1Ja	WZ-1Jb	WZ-1Jc
Observed	21	1	2	1	3	4
Total SM	21.7 ± 2.9	2.7 ± 0.5	1.56 ± 0.33	2.2 ± 0.5	1.82 ± 0.26	1.26 ± 0.34
WZ	19.5 ± 2.9	2.5 ± 0.5	1.33 ± 0.31	1.8 ± 0.5	1.49 ± 0.22	0.92 ± 0.28
ZZ	0.81 ± 0.23	0.06 ± 0.03	0.05 ± 0.01	0.05 ± 0.02	0.02 ± 0.01	–
VVV	0.31 ± 0.07	0.13 ± 0.04	0.13 ± 0.03	0.11 ± 0.02	0.12 ± 0.03	0.23 ± 0.05
$t\bar{t}V$	0.04 ± 0.02	0.01 ± 0.01	0.01 ± 0.01	0.14 ± 0.04	0.12 ± 0.02	0.08 ± 0.02
Higgs	–	–	–	0.01 ± 0.00	–	–
Reducible	1.1 ± 0.5	0.02 ± 0.01	0.04 ± 0.02	0.11 ± 0.06	0.07 ± 0.04	0.01 ± 0.00

Tab. 6.20: Full 2015 and 2016 Run-II background-only fit results for all six W/Z signal regions. All systematic and statistical uncertainties are included in the fit.
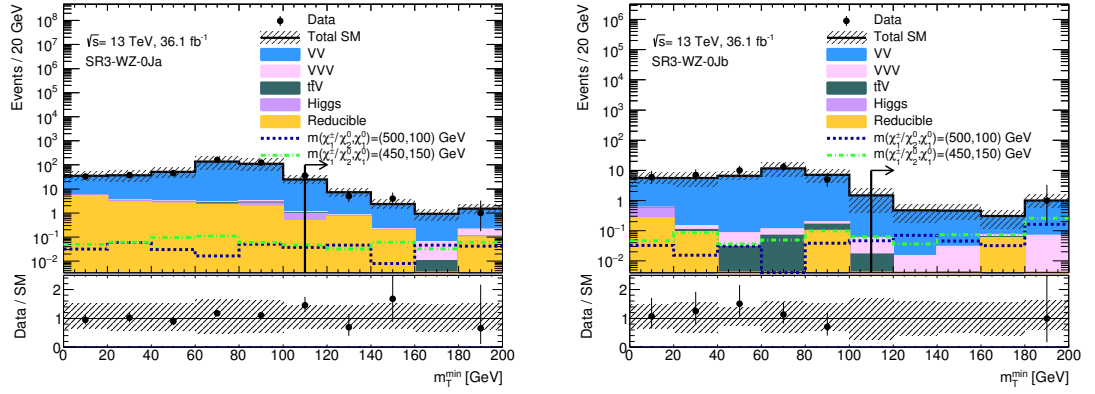
Fig. 6.57: Full 2015 and 2016 Run-II m_T^{min} N-1 distributions in SR3-WZ-0Ja (left) and SR3-WZ-0Jb (right) with the scale factor applied to WZ background. The uncertainties are inclusive of both statistical and systematic.

Fig. 6.58: Full 2015 and 2016 Run-II N-1 distributions for m_T^{min} in SR3-WZ-0Jc (left) and E_T^{miss} for all $n_{Jets} =0$ bins (right) [115] with the scale factor applied to WZ background. The uncertainties are inclusive of both statistical and systematic.
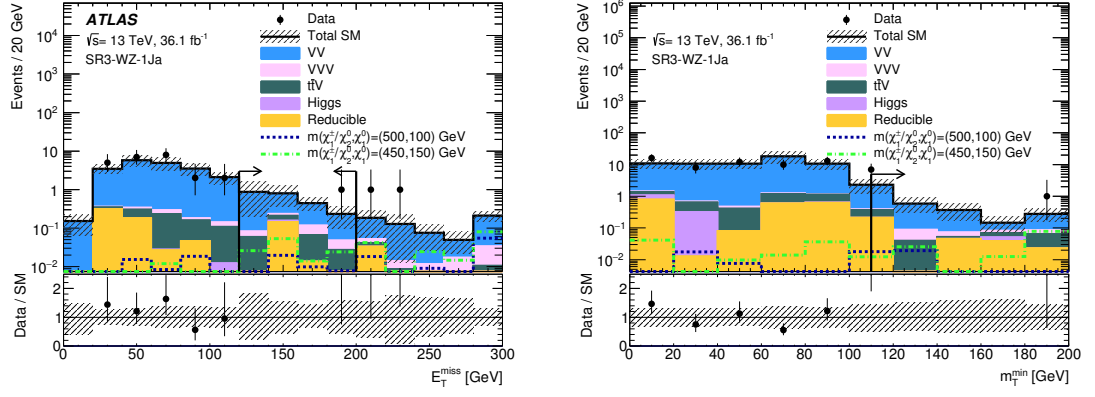
Fig. 6.59: Full 2015 and 2016 Run-II E_T^{miss} (left) [115] and m_T^{min} (right) N-1 distribution in SR3-WZ-1Ja with the scale factor applied to WZ background. The uncertainties are inclusive of both statistical and systematic.
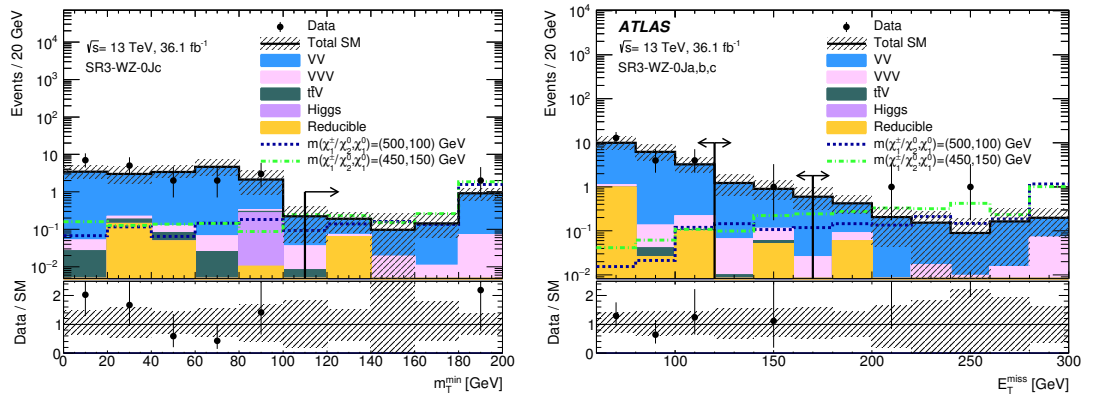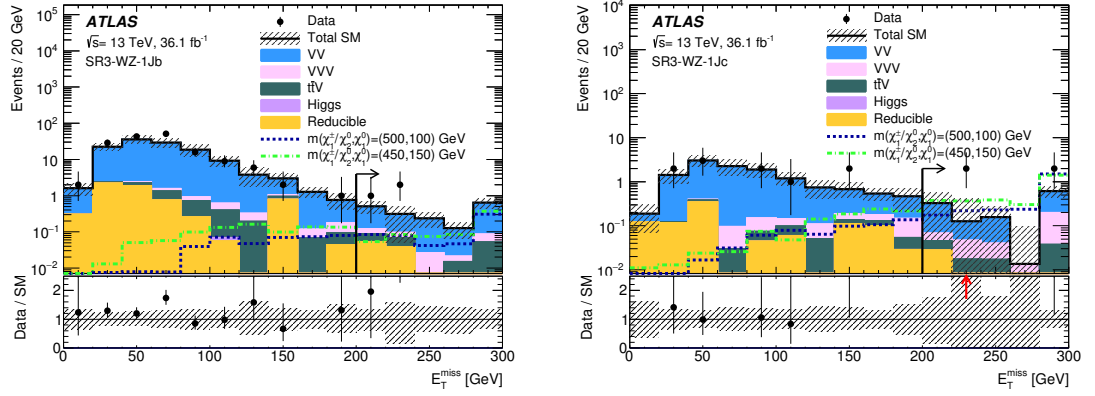

Fig. 6.60: Full 2015 and 2016 Run-II E_T^{miss} N-1 distributions in SR3-WZ-1Jb (left) [115] and SR3-WZ-1Jc (right) [115] with the scale factor applied to WZ background. The uncertainties are inclusive of both statistical and systematic.

6.2.4.2 Statistical Interpretation

In the absence of any significant excess, exclusion limits on the masses of the charginos and neutralinos are set. Figure 6.61 presents the exclusion contours for SUSY scenarios with exactly three-leptons in the final state. The observed limit excludes $\tilde{\chi}_1^\pm \, \tilde{\chi}_2^0$ masses up to $\sim$380 GeV, which is an increase of $\sim$30 GeV compared to Run-I. The upper limit is not as high as expected due to the number of events observed in SR3-WZ-1Jc. The model-independent limits are presented in Table 6.21.

Fig. 6.61: Full 2015 and 2016 Run-II observed and expected exclusion limits on the $\tilde{\chi}_2^0 \tilde{\chi}_1^\pm$ and $\tilde{\chi}_1^0$ masses for simplified mass spectra SUSY scenarios with exactly three leptons in the final state [115]. The observed (solid thick red line) and expected (thin dashed blue line) exclusion contours are indicated. The shaded band corresponds to the $\pm 1\sigma$ variations in the expected limit, including all uncertainties except theoretical uncertainties in the signal cross-section. The dotted lines around the observed limit illustrate the change in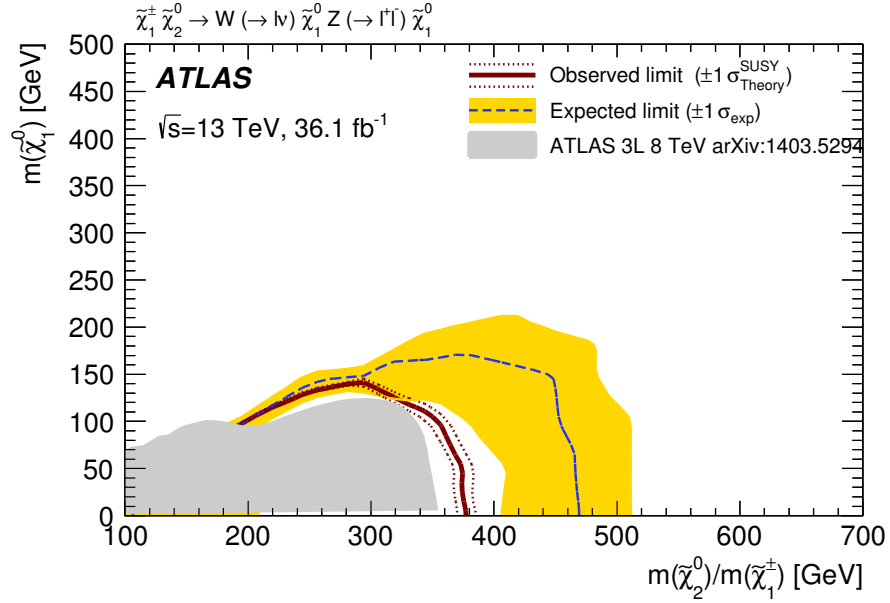 the observed limit as the nominal signal cross-section is scaled up and down by the theoretical uncertainty. All limits are computed at 95% confidence level. The observed limits that were obtained from ATLAS during Run-I are also shown [134].

Region	N_{obs}	N_{exp}	$\langle \epsilon\sigma \rangle_{obs}^{95}$[fb]	S_{obs}^{95}	S_{exp}^{95}	$p(s=0)$	Z
WZ-0Ja	21	21.7 ± 2.9	0.35	12.8	$13.5^{+2.7}_{-5.3}$	0.5	0
WZ-0Jb	1	2.7 ± 0.5	0.10	3.7	$4.6^{+2.1}_{-0.9}$	0.5	0
WZ-0Jc	2	1.6 ± 0.3	0.13	4.8	$4.1^{+1.7}_{-0.7}$	0.28	0.57
WZ-1Ja	1	2.2 ± 0.5	0.09	3.2	$4.5^{+1.6}_{-1.3}$	0.5	0
WZ-1Jb	3	1.8 ± 0.3	0.16	5.6	$4.3^{+1.7}_{-0.9}$	0.18	0.91
WZ-1Jc	4	1.3 ± 0.3	0.20	7.2	$4.2^{+1.7}_{-0.4}$	0.03	1.8

Tab. 6.21: Full 2015 and 2016 Run-II summary of results and model-independent limits for the $\tilde{\ell}$-mediated channel. The observed (N_{obs}) and expected background (N_{exp}) yields in the signal regions are indicated. Signal model-independent upper limits at 95% confidence level on the the visible signal cross-section ($\langle \epsilon\sigma \rangle_{obs}^{95}$), and the observed and expected upper limit on the number of BSM events (S_{obs}^{95} and S_{exp}^{95}, respectively) are also shown. The $\pm 1\sigma$ variations of the expected limit originate from the statistical and systematic uncertainties in the background prediction. The last two columns show the p-value and the corresponding significance for the background-only hypothesis. For SRs where the data yield is smaller than expected, the p-value is truncated at 0.5 and the significance is set to 0 [115].

Statistical Combination with Two-Lepton Final States

As discussed in the experimental landscape, earlier in Section 2.3.6, the results from W/Z-mediated three-lepton searches can be statistically combined with the results from the W/Z-mediated two-lepton searches due to the orthogonality of their SRs. Figure 2.17 shows the combined upper exclusion limits of the chargino and neutralino masses achieved during Run-I. For Run-II the two-lepton search defined SRs that targeted jets in the final state, and is documented in Ref. [115]. Figure 6.62 presents the combined upper mass limits for two and three-lepton searches. The masses of the $\tilde{\chi}_1^\pm$ $\tilde{\chi}_2^0$ are excluded up to $\sim$580 GeV, a significant increase of $\sim$160 GeV from Run-I.
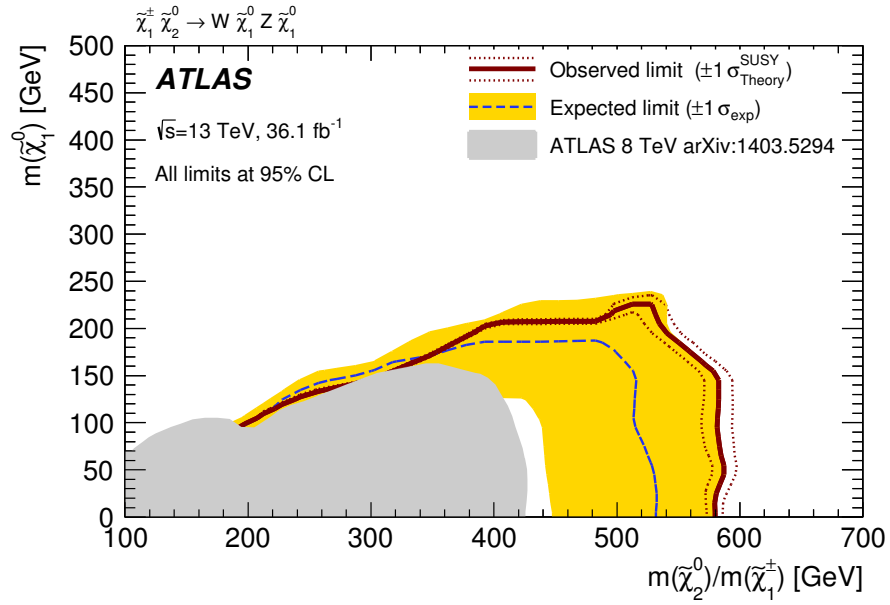
Fig. 6.62: Full 2015 and 2016 Run-II observed and expected exclusion limits on the $\tilde{\chi}_2^0 \tilde{\chi}_1^\pm$ and $\tilde{\chi}_1^0$ masses for simplified mass spectra SUSY scenarios with exactly two or three leptons in the final state [115]. The observed (solid thick red line) and expected (thin dashed blue line) exclusion contours are indicated. The shaded band corresponds to the $\pm 1\sigma$ variations in the expected limit, including all uncertainties except theoretical uncertainties in the signal cross-section. The dotted lines around the observed limit illustrate the change in the observed limit as the nominal signal cross-section is scaled up and down by the theoretical uncertainty. All limits are computed at 95% confidence level. The observed limits that were obtained from ATLAS during Run-I are also shown [134].

6.3 Future Outlook for Electroweak SUSY

Complimentary searches for electroweak SUSY can be carried out to cover maximal SUSY scenarios with three electrons or muons in the final state. As detailed in Section 2.3.5, scenarios with intermediate decays via the W and Higgs bosons can also produce this signature. This section introduces a preliminary first-look optimisation of SRs targeting this scenario. Run-I results for this channel, presented in Section 2.3.6, shows exclusion of $\tilde{\chi}_1^\pm$ $\tilde{\chi}_2^0$ masses up to $\sim 150\,\mathrm{GeV}$. The aim of this preliminary glance is to gage how well the W/h-mediated scenario can isolate SUSY signal from background SM processes at an increased total luminosity of $80\,\mathrm{fb}^{-1}$, as was collected during Run-II by the end of 2017.

6.3.1 Preliminary Glance at $\tilde{\chi}_1^\pm \tilde{\chi}_2^0$ via W and Higgs Bosons

As the analyses presented in Sections 6.1 and 6.2 focus solely on SUSY scenarios that require a SFOS lepton pair in the final state, this section follows a similar approach by motivating a preliminary optimisation of SRs targeting only events that also require a SFOS lepton pair. Section 6.3.1.1 details the instances when SFOS lepton pairs can occur, while Section 6.3.1.2, presents the first-look optimisation study. The optimisation strategy follows the same procedure as detailed in Chapter 5 with the reducible background being MC only.

6.3.1.1 $\tilde{\chi}_1^\pm \tilde{\chi}_2^0$ via W and Higgs Bosons with SFOS Events

The Higgs boson can decay di-leptonically, either directly or via intermediate decay channels: $H \to WW$ ($\mathcal{B} = 21.4\%$); $H \to \tau\tau$ ($\mathcal{B} = 6.27\%$); $H \to ZZ$ ($\mathcal{B} = 2.62\%$); $H \to Z\gamma$ ($\mathcal{B} = 0.15\%$); and $H \to \mu\mu$ ($\mathcal{B} = 0.02\%$) [3]. When in association with a leptonically decaying W boson, three leptons can be produced in the final state. All these scenarios can result in a SFOS lepton pair, and so SRs to target this are an interesting aspect of a W/h-mediated SUSY search.

The alternative to requiring a SFOS lepton pair is to request a different-flavour opposite-charge-sign (DFOS) lepton pair. Additional SRs requiring a DFOS lepton pair can be made orthogonal to their SFOS SR counterparts by also requiring a same-flavour same-charge-sign (SFSS) lepton pair. Orthogonal DFOS-plus-SFSS SRs (which will be referred to solely as DFOS from now on), would target the highest branching ratio scenario whereby the Higgs boson decays to a W boson pair, leaving SFOS SRs to target all others.

6.3.1.2 SFOS Signal Region Optimisation

The SR definitions for SFOS are presented in Table 6.22 and are inspired by the W/Z SRs presented in Table 6.13. Three benchmark signal points with $m(\tilde{\chi}_1^\pm \tilde{\chi}_2^0, \tilde{\chi}_1^0)$ = (175,25), (187.5,37.5) and (200,0) GeV are utilised as they each reside in areas of parameter space not previously excluded. Similar to the $\tilde{\ell}$ analysis, the $m_{\mathrm{SFOS}}^{\mathrm{min}}$ variable is required to be off-Z in order to veto the peak in the distribution arising from background events comprised of Z bosons. A $m_{\mathrm{SFOS}}^{\mathrm{min}}$ distribution with only baseline requirements applied, is shown in Figure 6.63. In order to optimise for lower $E_{\mathrm{T}}^{\mathrm{miss}}$ values, which allow access to the intermediate mass splittings residing along the horizontal of the signal grid, this region is binned in jet multiplicity, requiring either no jets, or at least one jet. A high $m_{\mathrm{T}}^{\mathrm{min}}$ requirement is also imposed. Finally, the SRs are binned in E_T^{miss} to maximise the significance. Kinematic N-1 distributions are presented in Figures 6.64 to 6.65, and the yield breakdown for each SR is given in Table 6.23.

Region	$m_{\mathrm{SFOS}}^{\mathrm{min}}$ [GeV]	nJets	m_T^{min} [GeV]	E_T^{miss} [GeV]
SR-SFOS-0Ja	$\notin [81.2, 101.2]$	0	>110	80-120
SR-SFOS-0Jb				>120
SR-SFOS-1Ja	$\notin [81.2, 101.2]$	>0	>110	110-160
SR-SFOS-1Jb				>160

Tab. 6.22: Summary table of SFOS SR selection criteria
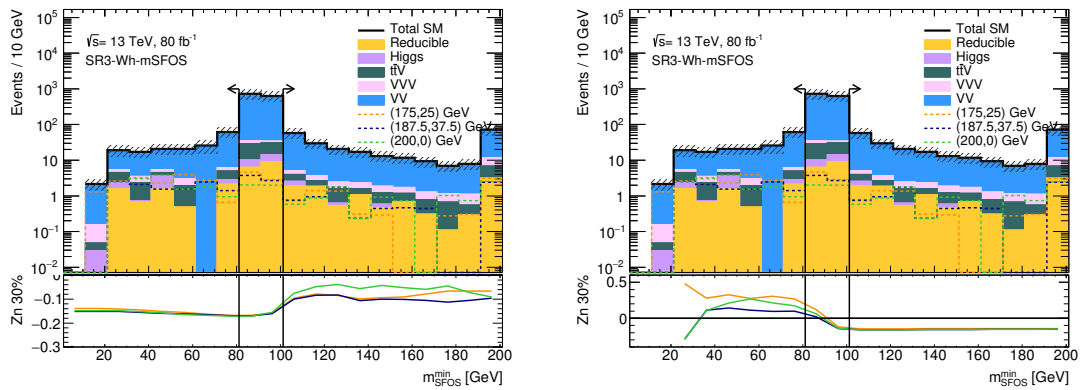
Fig. 6.63: N-1 plots for the SFOS preselection criteria. The arrows indicate bin edges. The panels below the main distributions show one-dimensional Z_N curves for three benchmark signal points. These curves indicate how the significance changes as a function of threshold when either a lower or upper cut on the variable in question is applied to the SR definition. Data-driven reducible backgrounds are being used with a flat 30% uncertainty.
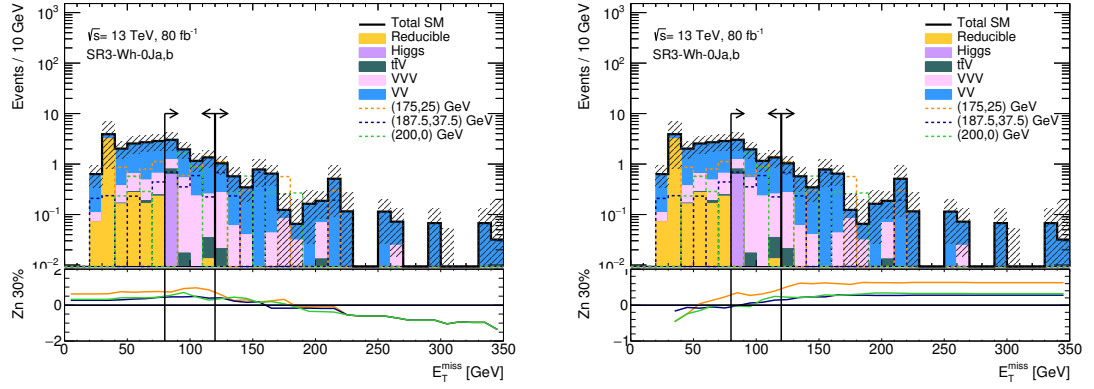
Fig. 6.64: N-1 plots for the zero jet bin (SR3ℓ-SFOS 0Ja,b). The arrows indicate bin edges. The panels below the main distributions show one-dimensional Z_N curves for three benchmark signal points. These curves indicate how the significance changes as a function of threshold. Data-driven reducible backgrounds are being used with a flat 30% uncertainty.
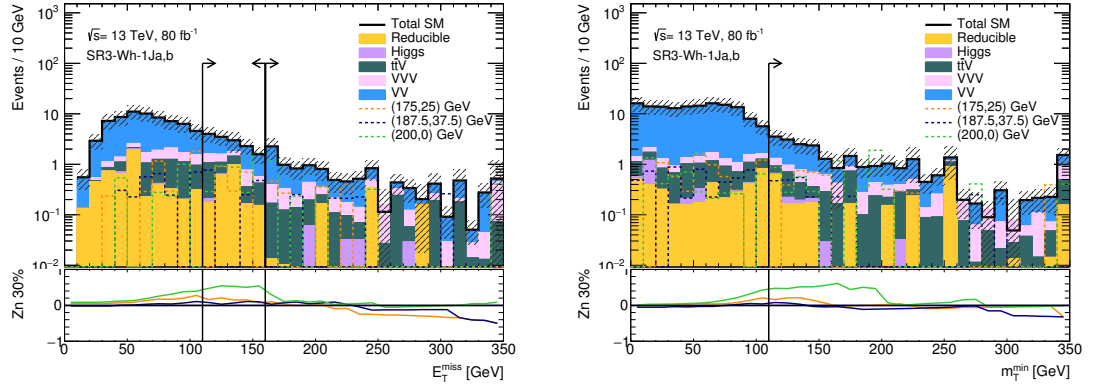
Fig. 6.65: N-1 plots for the at least one jet bin (SR3ℓ-SFOS 1J). The arrows indicate bin edges. The panels below the main distributions show one-dimensional Z_N curves for three benchmark signal points. These curves indicate how the significance changes as a function of threshold when either a lower or upper cut on the variable in question is applied to the SR definition. Data-driven reducible backgrounds are being used with a flat 30% uncertainty.

Process	SFOS-0Ja	SFOS-0Jb	SFOS-1Ja	SFOS-1Jb
WZ	5.01 ± 0.65	4.05 ± 0.75	7.63 ± 0.77	6.23 ± 1.12
ZZ	0.24 ± 0.06	0.15 ± 0.05	0.4 ± 0.09	0.25 ± 0.06
VVV	1.38 ± 0.18	0.59 ± 0.11	1.88 ± 0.19	2.14 ± 0.2
$t\bar{t}V$	0.22 ± 0.15	0.07 ± 0.02	2.26 ± 0.38	1.60 ± 0.30
Higgs	0.62 ± 0.62	0.0 ± 0.0	0.06 ± 0.04	0.12 ± 0.08
Reducible	0.01 ± 0.01	–	1.18 ± 0.42	0.66 ± 0.32
Total background	7.48 ± 0.93	4.86 ± 0.77	14.23 ± 1.2	11.01 ± 1.23
via Wh (175,25)	11.97 ± 3.8	9.4 ± 3.33	7.81 ± 3.21	6.09 ± 3.1
via Wh (187.5,37.5)	7.72 ± 2.6	7.37 ± 2.61	6.11 ± 2.51	4.72 ± 2.12
via Wh (200,0)	6.79 ± 2.27	4.48 ± 1.83	11.1 ± 3.11	6.73 ± 2.41

Tab. 6.23: Yields for the SM background processes and three benchmark signal points for the four SFOS SRs targeting models with intermediate decays via the W and Higgs boson. The uncertainties are statistical only.

6.3.1.3 Sensitivity

Figure 6.66 presents the two-dimensional sensitivity plot for the simplified model with $\tilde{\chi}_1^\pm \tilde{\chi}_2^0$ decaying via intermediate W and Higgs bosons, requiring only events with a SFOS lepton pair in the final state. The significance is calculated assuming a flat 30% systematic uncertainty on the total SM background. The backgrounds used in the optimisation studies are based on MC with statistical uncertainties only.
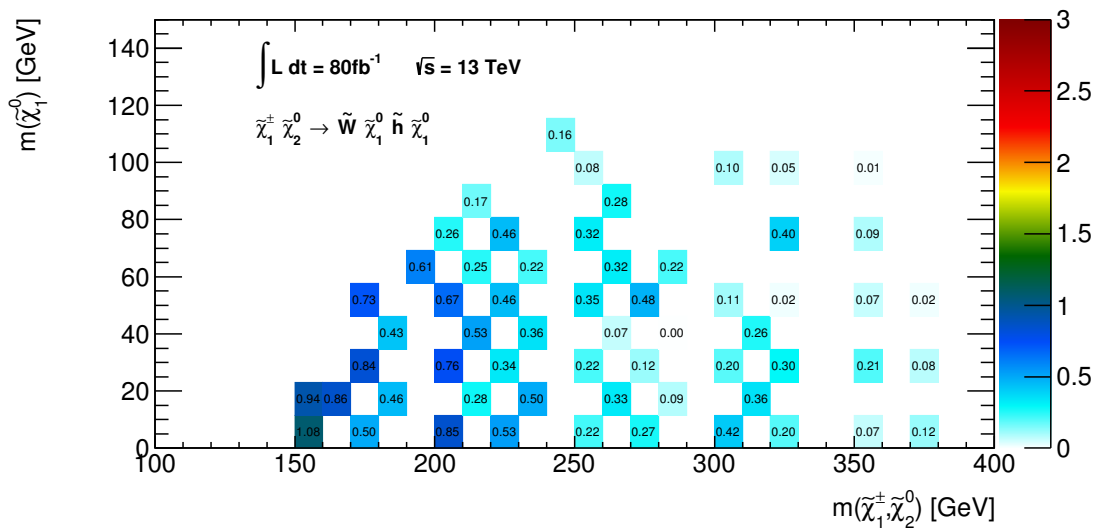

Fig. 6.66: 2D sensitivity plots showing the SFOS significance for the full five bin signal region targeting C1N2 via Wh model.

6.3.1.4 Combined Signal Regions

As previously mentioned, this analysis could be statistically combined with orthogonal SRs which target a DFOS lepton pair. As DFOS SRs target a higher branching ratio decay chain than the orthogonal SFOS lepton pair, much higher sensitivities than those shown in Figure 6.66 can be predicted, resulting in a further increase in sensitivity when statistically combining both the SFOS and DFOS SRs.

6.3.2 Summary

Although the SFOS SRs cannot expect to exclude masses beyond Run-I limits alone, when considered in combination with additional orthogonal DFOS SRs it is indicative that the mass limits of exclusion will improve significantly if no evidence of SUSY is found. Therefore, further optimisation focusing on DFOS SRs should be performed. These regions could investigate new kinematic variables such as invariant mass of the lepton pair originating from the Higgs boson, angular variables between the SFSS or DFOS leptons, and distance between final state leptons.

7. Conclusion and Outlook

This thesis presents the best results to date produced by ATLAS on the search for electroweak production of supersymmetric gauginos, in events with three electrons or muons and missing transverse energy in the final state. Analyses were performed using $13.3\,\text{fb}^{-1}$ and $36.1\,\text{fb}^{-1}$ of data at $\sqrt{s} = 13\,\text{TeV}$.

Optimised selection criteria were applied to target R-parity conserving simplified supersymmetric scenarios with intermediate decays via either sleptons or SM W and Z bosons. No significant excess was observed within statistical and systematic uncertainties, when compared to SM expectations. Statistical interpretation of the results was performed in order to set 95% CL exclusion limits on the mass parameters of each model considered. Model-independent limits on the visible cross-section for beyond-the-SM scenarios were also set with 95% CL.

Early results for scenarios with intermediate decays via sleptons, using a $13.3\,\text{fb}^{-1}$ subset of data was able to exclude $\tilde{\chi}_2^{\pm}$ $\tilde{\chi}_1^0$ masses up to $\sim 1\,\text{TeV}$, a substantial increase of $\sim 300\,\text{GeV}$ compared to Run-I results, providing an insight into the exclusion power of masses at the increased $13\,\text{TeV}$ collision energy. A subsequent analysis using the full $36.1\,\text{fb}^{-1}$ of data collected during 2015 and 2016 improved on this further by setting upper limits on $\tilde{\chi}_2^{\pm}$ $\tilde{\chi}_1^0$ masses of $\sim 1.13\,\text{TeV}$, an increase of $\sim 420\,\text{GeV}$ compared to Run-I. The observed upper mass limit for scenarios with intermediate decays via W and Z bosons was set at $\sim 380\,\text{GeV}$, an increase of $\sim 30\,\text{GeV}$ compared to Run-I. The increase from Run-I was not as large as had been expected, due to a small, but not significant excess, in data, in regions of parameter space that were targeting heavier $\tilde{\chi}_2^{\pm}$ $\tilde{\chi}_1^0$'s. When these results for the W and Z mediated decay were statistically combined with results from an orthogonal two-lepton final state scenario, upper $\tilde{\chi}_2^{\pm}$ $\tilde{\chi}_1^0$ masses were set at $\sim 580\,\text{GeV}$, a substantial increase of $\sim 160\,\text{GeV}$ compared to the equivalent combined Run-I results.

Even though it is disappointing not to have observed evidence of new physics at the LHC in this first iteration at $\sqrt{s} = 13\,\text{TeV}$, the work presented shows clear advancement in strategy, and an improvement of the upper mass limits compared to Run-I, all of which will play a vital role in contributing to the evolution of the theory of supersymmetry. Looking ahead, with the full Run-II integrated luminosity expected to reach $\sim 150\,\text{fb}^{-1}$, there is still much potential to observe evidence of the production of electroweak supersymmetric particles, and analyses with the objective to build on the results presented in this thesis are already underway.

A. Inner Detector Trigger

This section gives an overview of the technical work performed to obtain the ATLAS authorship qualification. The work was within the ID Trigger group detailed in Chapter 3, and was split into three parts. Early contributions involved the evaluation of changes made to the trigger framework, and is discussed in Section A.1, while the dominant contribution was to adapt the trigger software to use a new format for the input files, discussed in Section A.2. The final contribution was the development of an automated system to submit and process data collected from the ID in order to monitor the performance, detailed in Section A.3.

A.1 ID Trigger Performance

The ID tracking algorithms used for the HLT trigger reconstruction are continuously updated to optimise the performance of the experiment. Monitoring and evaluation of this performance is a crucial part of data-taking to ensure the reliability of the software before any updates are released for online use. This evaluation is performed offline by emulating online conditions using benchmark runs and mimicking the reconstruction that would occur during normal data-taking [135].

I was tasked with the first stage of this evaluation, which involved running the updated software locally and comparing the results to those from the original setup. Often, bugs in the software would be present that would require attention, for example missing software libraries or undefined dataset lists. Once all software bugs had been fixed and good agreement was observed, the updates were passed to the ATLAS Nightly Build System [136] for further testing.

The ATLAS Nightly Build System is responsible for testing the repeatability of new releases, accumulating results on webpage interfaces, and giving feedback to the responsible developers if an error is detected. If no error occurs, the new release is passed to the final stage of validation, the RunTimeTester (RTT) framework [137].

The RTT is used to run much longer tests up to approximately 24 hours. It has the ability to submit, run and test jobs using different computing resources, and report results to developers, similarly as the ATLAS Nightly Build System. Once an update has been validated, the development release goes into a new patch release that can be deployed for online use.

A.2 Migration to New Offline Data Formats

As discussed in Chapter 4, the ID Trigger software runs on the Athena computing framework. This framework is able to read in data files and write out ntuples. In 2014 a new dataset format, known as xAODs, designed for use with a ROOT [119] based physics analysis framework called RootCore, was introduced. However, this new format was not fully compatible with Athena, namely a crucial function that selected ID tracks and used all the corresponding properties for reconstruction. My initial task was to develop this function in RootCore, which would eventually be paired to run in parallel with the Athena framework.

A.2.1 Track Selection

The track selection within Athena was designed to first check whether a chain (see Section 3.2.6) passes a given trigger. For each passing chain, a "Trigger Decision Tool" (TDT) looped through all RoI combinations to retrieve track collections. Finally, a function was implemented to select and retrieve all track properties from the collections.

The development in RootCore was held up by a separate delay in developing a compatible TDT, however an improved solution was realised. Instead of running RootCore in parallel, a stripped down version of Athena was provided with the necessary functionality to run RootCore and the newly developed track selection function within the Athena framework itself.

A.2.2 Outcomes

The result of integrating RootCore into Athena was that the newly developed track selecting function could run much faster than if it required two separate frameworks running in parallel, and much faster than running standalone in Athena due to the time it would take to setup the full Athena framework.

A.3 Automated Performance Analysis Development

The ID Trigger group carries out analyses on the tracking performance of the ID. This involves sending the entire list of Run-II collected data to the computing grid (see Section 3.2.6), process it and produce performance plots, each stage of which was performed and checked manually, making it a very time-consuming endeavour. I was given the task of developing an automated system that would perform the following:

- Send dataset jobs to the grid;
- Check whether the jobs had completed successfully;
- Re-submit if jobs had failed;
- Download all successfully completed jobs;
- Process all new jobs daily.

The electron chain performance plots generated by this automated system are displayed in Figures A.1 and A.2. This system was later developed by the ID Trigger group for muon and tau chains.
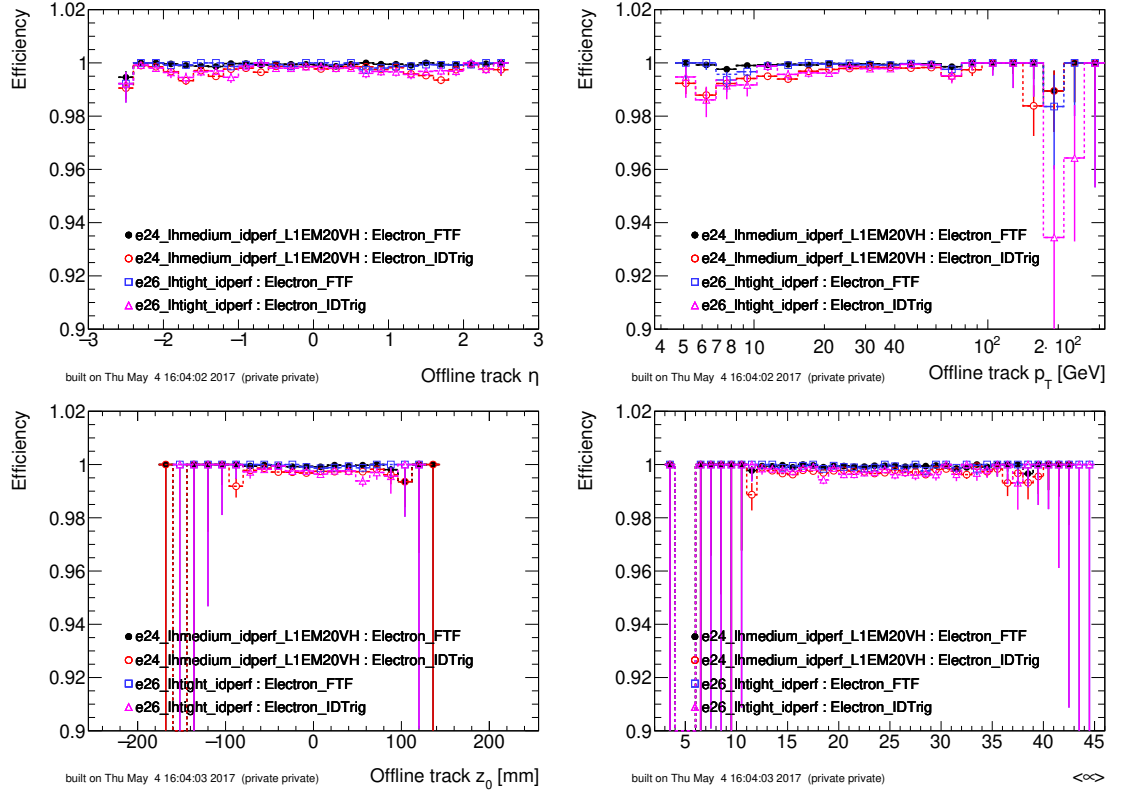
Fig. A.1: The ID tracking efficiency for electrons selected by the 24 GeV and 26 GeV electron support triggers, with respect to offline electron candidates with $p_T > 0$ GeV. The efficiency is shown as a function of: (a) the offline reconstructed muon η, (b) the offline reconstructed muon p_T, (c) the offline reconstructed muon z_0, and (d) the mean number of pile-up vertices, $< \mu >$. Efficiencies are shown for both the fast tracking and precision tracking algorithms. Bayesian uncertainties are shown.
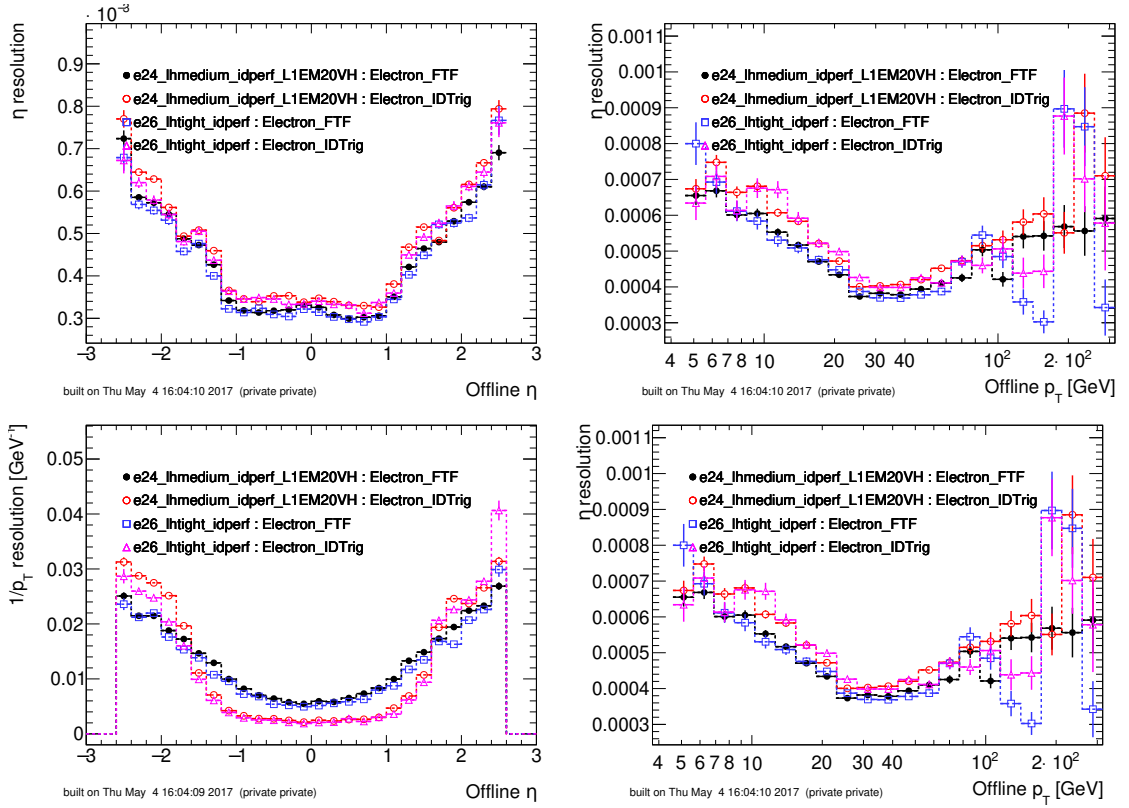
Fig. A.2: The differential resolution for pseudorapidity and inverse transverse momentum as a function of offline track psuedorapidity and transverse momentum. The resolutions are shown for electrons selected by the $24\,\mathrm{GeV}$ and $26\,\mathrm{GeV}$ electron support triggers for both the fast tracking and precision tracking algorithms. Bayesian uncertainties are shown.

The primary neutralino and chargino producing processes detailed in Section 2.3.5 are predicted to be incredibly rare events with production cross-sections many orders of magnitude smaller than the total produced by the LHC. Being able to separate a SUSY signal from the SM background requires a good understanding of the most dominant processes so that accurate estimations can be made. As mentioned in Section 5.1, $t\bar{t}V$ is one of the most significant processes that can replicate three leptons and high $E_{\mathrm{T}}^{\mathrm{miss}}$ in the final state, and so it is of crucial importance for this thesis that the cross-sections are accurate.

The production cross-section at $\sqrt{s} = 8\,\mathrm{TeV}$ was measured to be $\sigma_{t\bar{t}Z} = 0.176^{+0.058}_{-0.052}\,\mathrm{pb}$ observed with a $4.5\,\sigma$ significance [138]. This was achieved using a combination of SRs targeting same-sign di-muons, tri-leptons or tetra-leptons in the final state. At $\sqrt{s} = 13\,\mathrm{TeV}$, theoretical calculations estimated an increased production cross-section of $\sigma_{t\bar{t}Z} = 0.84 \pm 0.1\,\mathrm{pb}$ [139].

This section introduces an early Run-II re-optimisation study that I contributed as part of the $t\bar{t}V$ analysis team. Using a subset of $3.2\,\mathrm{fb}^{-1}$ of data recorded in 2015, the aim was to increase sensitivity to $t\bar{t}Z$ processes in the SRs, allowing further constraints on the $t\bar{t}V$ production cross-section. The full publication of this early Run-II study is in Ref. [140].

B.1 Signal Region Optimisation

In Section B.1.1, a recap of the SR definitions used during Run-I is given, while Section B.1.2 presents a re-optimisation strategy based on the Run-I definitions.

B.1.1 Run-I Signal Regions

The discriminant variables utilised for the Run-I $t\bar{t}Z$ signal regions, have all been introduced in Section 5.3.1, and were used in the previously presented SUSY searches. A SFOS lepton pair is required, with the invariant di-lepton mass required to be

Tab. B.1: Summary of the exclusive Run-I signal regions targeting the $t\bar{t}Z$ process.

Variable	3ℓ-Z-1b4j	3ℓ-Z-2b3j	3ℓ-Z-2b4j
Leptons		$\ell^{\pm}\ell^{\mp}\ell'$	
$p_T^{\ell 1}$		> 25 GeV	
$p_T^{\ell 3}$		> 20 GeV	
m_{SFOS}		$\in [81.2 - 101.2]$ GeV	
n_{jets}	≥ 4	$= 3$	≥ 4
n_{b-jets}	$= 1$	≥ 2	≥ 2

close to the Z boson mass. Additional requirements on the leading, and third-leading lepton p_T are to provide assurance that the particle p_T is above the trigger turn-on-curve. The $t\bar{t}Z$ decay channel which results in three leptons in the final state is $t\bar{t}Z \rightarrow Wb\,Wb\,Z \rightarrow \ell\nu b\,qqb\,\ell\ell$, which also results in four jets, two of which are b-jets. The 3ℓ-Z-2b4j SR is designed to target instances where all jets have been correctly reconstructed, while 3ℓ-Z-1b4j and 3ℓ-Z-2b3j target cases where jets have been missed in reconstruction. Definitions for the three exclusive Run-I SRs are presented in Table B.1.

B.1.2 Re-optimisation Study

A re-optimisation of the SRs defined for the Run-I analysis, was attempted to improve sensitivity for $t\bar{t}V$ processes. A luminosity of $3.32\,\mathrm{fb}^{-1}$ was used, with the significant background arising from fake leptons, diboson production and the production of a single top quark in association with a Z boson.

Using the 3ℓ-Z-1b4j, 3ℓ-Z-2b3j and 3ℓ-Z-2b4j SR definitions as a basis, this study introduces additional jet variables to determine whether an improvement to significance can be achieved, when compared to the original Run-I SR definitions. The additional variables are jet transverse momentum, p_T^{jet1}, p_T^{jet2} and p_T^{jet3}, and the sum of all jet transverse momentum, H_T. In all cases, the lepton p_T is modified to achieve optimal significance. Significance is calculated using the same method presented in Section 5.3 with an uncertainty of 30%. New SR definitions with optimal significance are presented in the following sections.

B.1.2.1 3ℓ-Z-1b4j Optimisation

Requirements of $H_T > 250\,\mathrm{GeV}$ and $p_T^{jet1} > 40\,\mathrm{GeV}$ were introduced in order to target energetic events, while p_T of the leading and third-leading leptons were adjusted

accordingly. A summary of the optimal selections for the 3ℓ-Z-1b4j SR are presented in Table B.2, with the relevant kinematic distributions being displayed in Figures B.1-B.4. The event yield breakdown for both the original Run-I and the re-optimised SR definitions are presented in Table B.3. With this re-optimised SR defintion, a significance of 1.223 was achieved, a slight increase from 1.222 which was obtained for the original Run-I SR definition.

Variable	Cut
H_T	>250 GeV
p_T^{jet1}	>40 GeV
$p_T^{\ell 1}$	>50 GeV
$p_T^{\ell 3}$	>20 GeV

Tab. B.2: Optimal additional and modified selections for the 3ℓ-Z-1b4j SR.
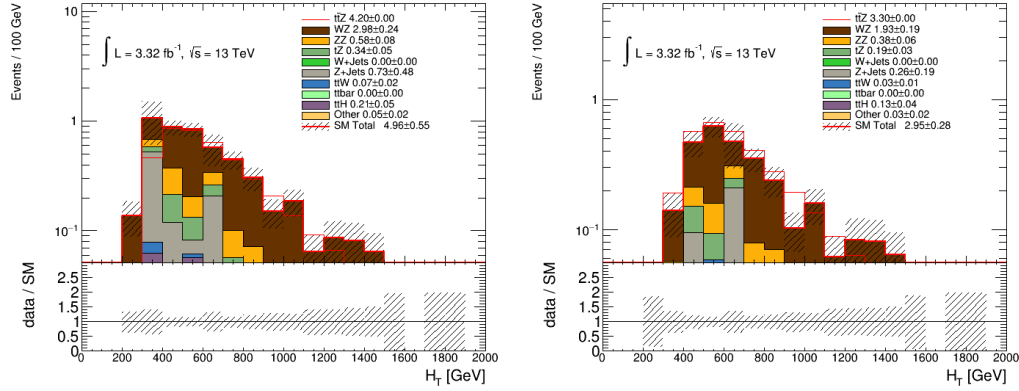

Fig. B.1: H_T distributions before (left) and after (right) the optimal cuts have been applied for the 3ℓ-Z-1b4j SR.

Fig. B.2: p_T distributions for the sub-leading jet before (left) and after (right) the optimal cuts have been applied for the 3ℓ-Z-1b4j SR.
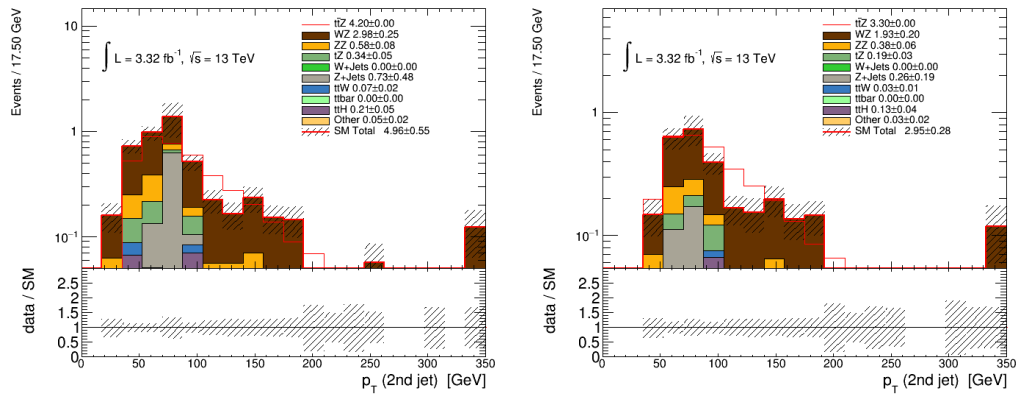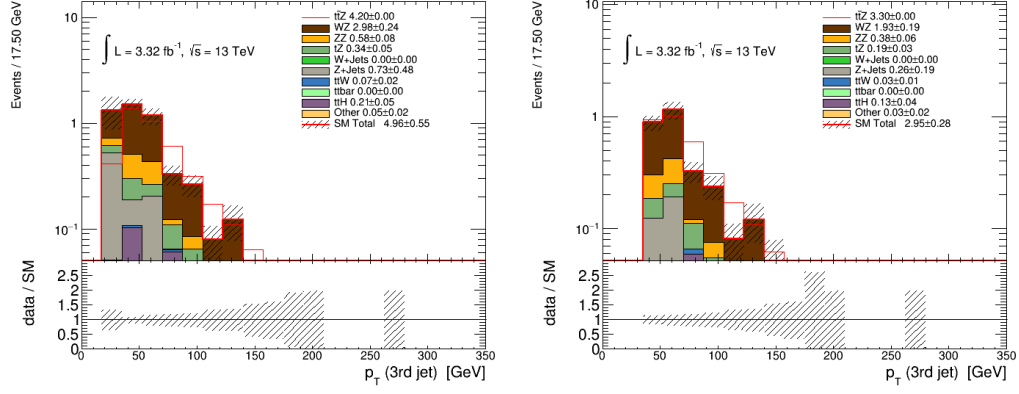
Fig. B.3: p_T distributions for the 3rd-leading jet before (left) and after (right) the optimal cuts have been applied for the 3ℓ-Z-1b4j SR.
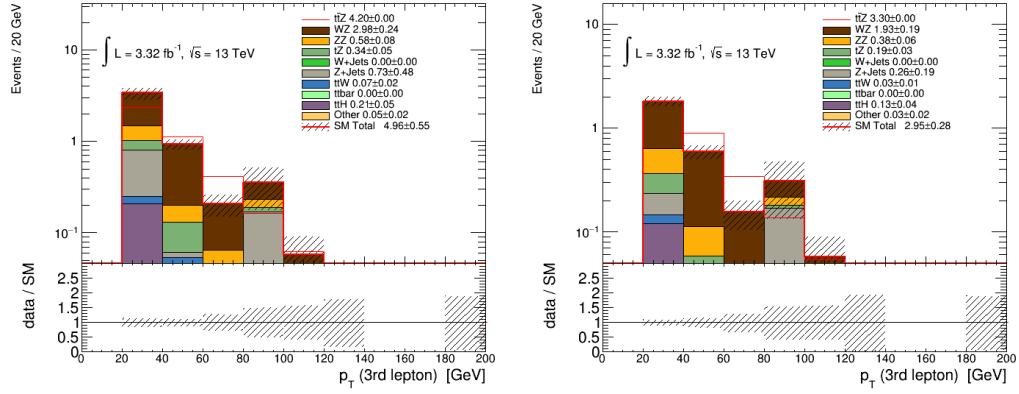

Fig. B.4: p_T distributions for the 3rd-leading lepton before (left) and after (right) the optimal cuts have been applied for the 3ℓ-Z-1b4j SR.

B.1.2.2 3ℓ-Z-2b3j Optimisation

A larger requirement on H_T of $> 300\,\mathrm{GeV}$, along with $p_T^{jet1} > 40\,\mathrm{GeV}$ and $p_T^{jet2} > 30\,\mathrm{GeV}$ requirements were introduced in order to target energetic events, while p_T of the sub-leading and third-leading leptons were adjusted accordingly. A summary of the optimal selections for the 3ℓ-Z-2b3j SR are presented in Table B.4, with the relevant kinematic distributions being displayed in Figures B.5-B.8. The event yield breakdown for both the original Run-I and the re-optimised SR definitions are presented in Table B.5. With this re-optimised SR defintion, a significance of 1.223 was achieved, an increase from 1.213 which was obtained for the original Run-I SR definition.

Process	Run-I SR	Re-optimised SR
WZ	2.86±0.23	1.927 ± 0.194
ZZ	0.40±0.18	0.383 ± 0.063
tZ	0.303±0.017	0.188 ± 0.033
Z+jets	0.012±0.005	0.257 ± 0.186
$t\bar{t}W$	0.036±0.005	0.034 ± 0.005
$t\bar{t}$	0.25±0.07	–
$t\bar{t}H$	0.129±0.009	0.129 ± 0.040
Other	0.743±0.042	0.034 ± 0.016
Total SM	4.733±0.300	2.952 ± 0.537
$t\bar{t}Z$	4.33 ± 0.04	3.301 ± 0.032
Significance	1.222	1.223

Tab. B.3: Event breakdown for Run-I SR and re-optimised SR for 3ℓ-Z-1b4j.

Variable	Cut
H_T	>300 GeV
p_{T}^{jet1}	>40 GeV
p_{T}^{jet2}	>30 GeV
$p_{\mathrm{T}}^{\ell2}$	>30 GeV
$p_{\mathrm{T}}^{\ell3}$	>20 GeV

Tab. B.4: Optimal additional and modified selections for the 3ℓ-Z-2b3j SR.

Fig. B.5: H_T distributions before (left) and after (right) the optimal cuts have been applied for the 3ℓ-Z-2b3j SR.

Fig. B.6: p_T distributions for the sub-leading jet before (left) and after (right) the optimal cuts have been applied for the 3ℓ-Z-2b3j SR.

Fig. B.7: p_T distributions for the 3rd-leading jet before (left) and after (right) the optimal cuts have been applied for the 3ℓ-Z-2b3j SR.
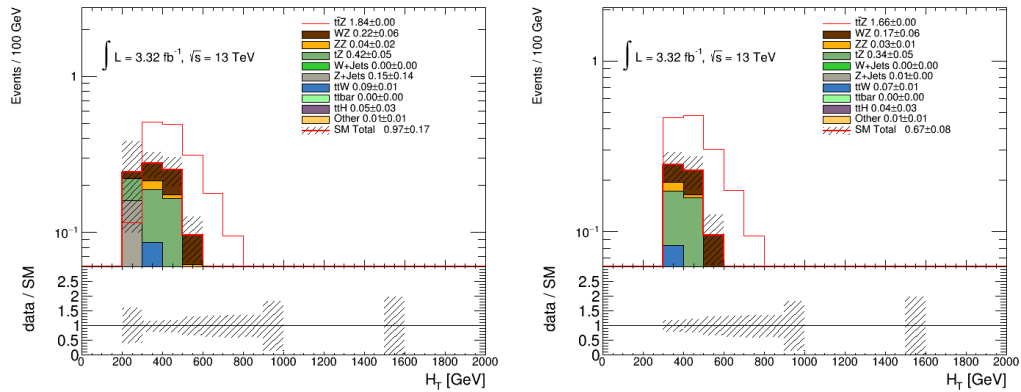

Fig. B.8: p_T distributions for the 3rd-leading lepton before (left) and after (right) the optimal cuts have been applied for the 3ℓ-Z-2b3j SR.

Process	Run-I SR	Re-optimised SR
WZ	0.22±0.06	0.167 ± 0.056
ZZ	0.0022±0.0014	0.031 ± 0.012
tZ	0.348±0.018	0.344 ± 0.048
Z+jets	0.006±0.004	0.006 ± 0.004
$t\bar{t}W$	0.083±0.006	0.073 ± 0.006
$t\bar{t}$	0.10±0.04	0.000 ± 0.000
$t\bar{t}H$	0.055±0.004	0.044 ± 0.034
Other	0.172±0.018	0.008 ± 0.007
Total SM	0.986 ± 0.070	0.672 ± 0.167
$t\bar{t}Z$	1.928 ± 0.023	1.658 ± 0.021
Total Significance	1.213	1.223

Tab. B.5: Event breakdown for Run-I SR and re-optimised SR for 3ℓ-Z-2b3j.

B.1.2.3 3ℓ-Z-2b4j Optimisation

In the final SR that targets events with no missing jets, requirements of $H_T > 250\,\text{GeV}$ and $p_{\text{T}}^{jet3} > 50\,\text{GeV}$ are applied, while p_{T} of the sub-leading and third-leading leptons were adjusted accordingly. A summary of the optimal selections for the 3ℓ-Z-2b4j SR are presented in Table B.6, with the relevant kinematic distributions being displayed in Figures B.9-B.12. The event yield breakdown for both the original Run-I and the re-optimised SR definitions are presented in Table B.7. With this re-optimised SR defintion, a significance of 2.135 was achieved, a decrease from 2.577 which was obtained for the original Run-I SR definition.

Variable	Cut
H_T	>250 GeV
p_{T}^{jet3}	>50 GeV
$p_{\text{T}}^{\ell 1}$	>40 GeV
$p_{\text{T}}^{\ell 3}$	>30 GeV

Tab. B.6: Optimal additional and modified selections for the 3ℓ-Z-2b4j SR.

Fig. B.9: H_T distributions before (left) and after (right) the optimal cuts have been applied for the 3ℓ-Z-2b4j SR.
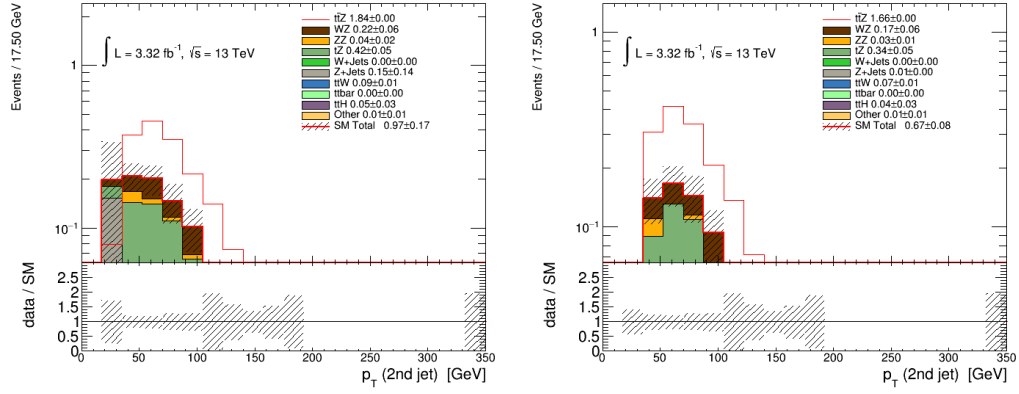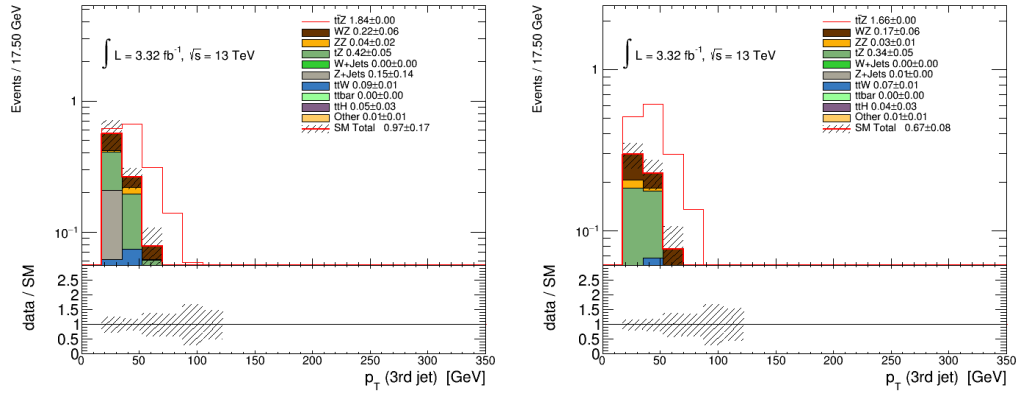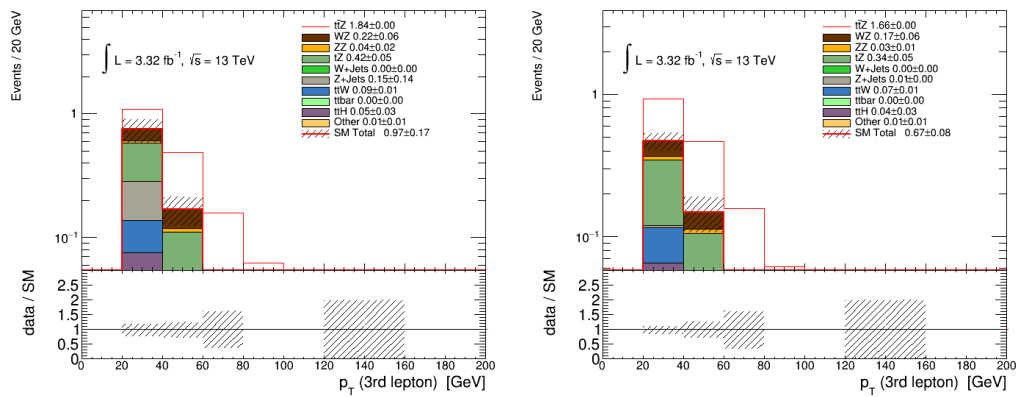

Fig. B.10: p_T distributions for the sub-leading jet before (left) and after (right) the optimal cuts have been applied for the 3ℓ-Z-2b4j SR.

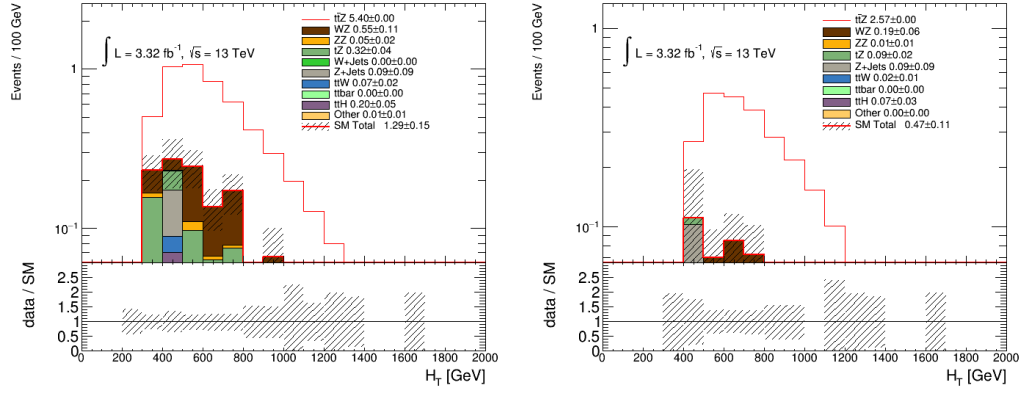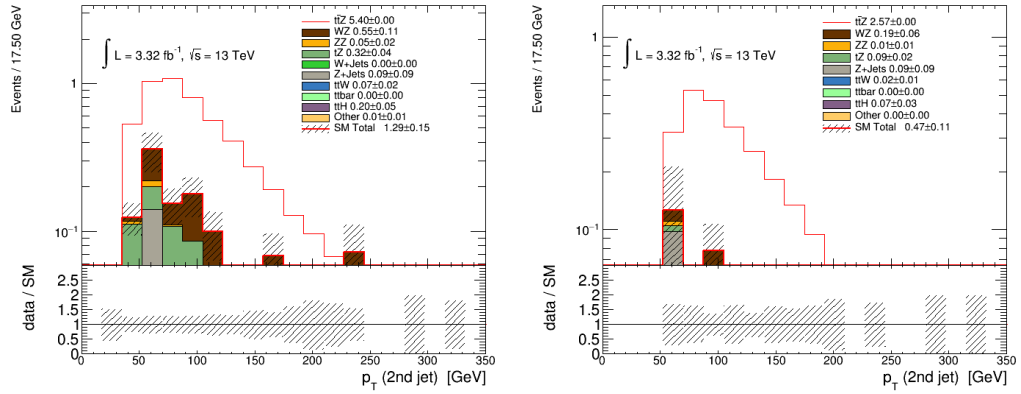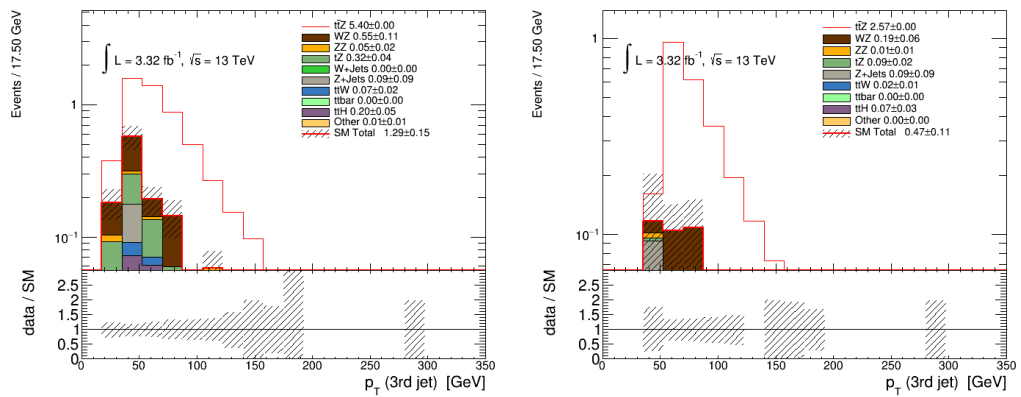**Fig. B.11:** p_T distributions for the 3rd-leading jet before (left) and after (right) the optimal cuts have been applied for the 3ℓ-Z-2b4j SR.
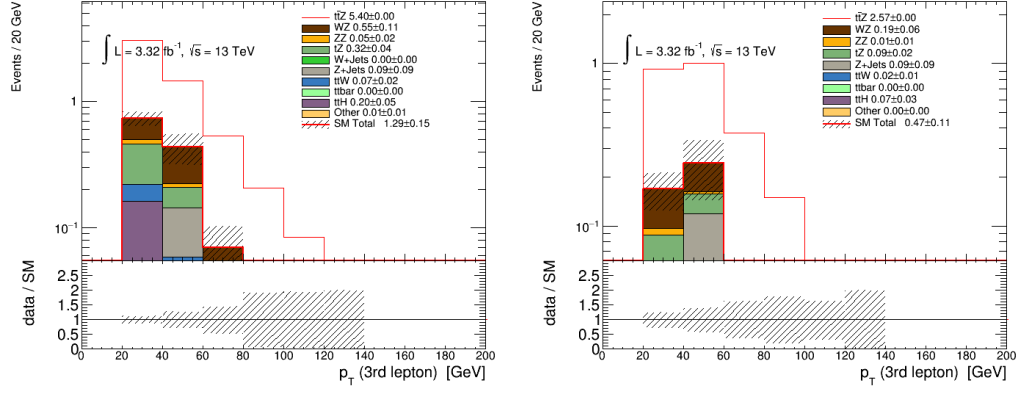
Fig. B.12: p_T distributions for the 3rd-leading lepton before (left) and after (right) the optimal cuts have been applied for the 3ℓ-Z-2b4j SR.

Process	Run-I SR	Re-optimised SR
WZ	0.51±0.10	0.190 ± 0.058
ZZ	0.0028±0.0016	0.014 ± 0.008
tZ	0.337±0.018	0.085 ± 0.022
Z+jets	–	0.085 ± 0.085
$t\bar{t}W$	0.065±0.007	0.018 ± 0.009
$t\bar{t}$	0.034±0.011	0.000 ± 0.000
$t\bar{t}H$	0.166±0.009	0.073 ± 0.033
Other	0.582±0.031	0.003 ± 0.002
Total SM	1.70±0.11	0.468 ± 0.218
$t\bar{t}Z$	5.50 ± 0.04	2.571 ± 0.027
Total Significance	2.577	2.135

Tab. B.7: Event breakdown for Run-I SR and re-optimised SR for 3ℓ-Z-2b4j.

B.2 Outcome

Despite re-optimisation studies of the Run-I SRs using additional jet variables, no clear improvement was seen. In particular, the re-optimised 3ℓ-Z-2b3j and 3ℓ-Z-2b4j SRs had a lack of background statistics which would have resulted in unreliable final results. Consequently, the original Run-I $t\bar{t}Z$ SR definitions were used in the analysis. The final $t\bar{t}Z$ cross-section calculated at $\sqrt{s} = 13\,\text{TeV}$ using $3.2\,\text{fb}^{-1}$ of recorded data, was $\sigma_{t\bar{t}Z} = 0.92 \pm 0.31$ pb with a $3.9\,\sigma$ significance [140]. This was consistent with theoretical calculations. With an increase in luminosity, the inclusion of additional jet variables could yet prove to increase significance further.

References

[1] M. Thomson, *Modern particle physics*, Cambridge University Press, New York, 2013.

[2] MissMJ, *Standard model of elementary particles*, `https://commons.wikimedia.org/wiki/File:Standard_Model_of_Elementary_Particles.svg`. Accessed: 17.04.2018.

[3] Particle Data Group, C. Patrignani *et al.*, *Review of Particle Physics*, Chin. Phys. **C40** (2016) 100001.

[4] M. E. Peskin and D. V. Schroeder, *An Introduction to quantum field theory*, Addison-Wesley, Reading, USA, 1995.

[5] S. Weinberg, *A model of leptons*, Phys. Rev. Lett. **19** (1967) 1264.

[6] A. Salam and J. C. Ward, *Electromagnetic and weak interactions*, Phys. Lett. **13** (1964) 168.

[7] S. L. Glashow, *Partial-symmetries of weak interactions*, Nucl. Phys. **22** (1961) 579.

[8] L. B. Okun, *Leptons and Quarks*, North Holland Publishing, Amsterdam, 1985.

[9] P. W. Higgs, *Broken symmetries and the masses of gauge bosons*, Phys. Rev. Lett. **13** (1964) 508.

[10] F. Englert and R. Brout, *Broken symmetry and the mass of gauge vector mesons*, Phys. Rev. Lett. **13** (1964) 321.

[11] L. Alvarez-Gaume and J. Ellis, *Eyes on a prize particle*, Nature Phys. **7** (2011) 2.

[12] ATLAS collaboration, G. Aad *et al.*, *Observation of a new particle in the search for the Standard Model Higgs boson with the ATLAS detector at the LHC*, Phys. Lett. **B716** (2012) 1, `arXiv:1207.7214`.

[13] CMS collaboration, S. Chatrchyan *et al.*, *Observation of a new boson at a mass of 125 GeV with the CMS experiment at the LHC*, Phys. Lett. **B716** (2012) 30, `arXiv:1207.7235`.

[14] ATLAS collaboration, G. Aad *et al.*, *Measurement of the Higgs boson mass from the $H \to \gamma\gamma$ and $H \to ZZ^* \to 4\ell$ channels with the ATLAS detector using 25 fb^{-1} of pp collision data*, Phys. Rev. **D90** (2014) 052004, `arXiv:1406.3827`.

[15] CMS collaboration, V. Khachatryan *et al.*, *Precise determination of the mass of the Higgs boson and tests of compatibility of its couplings with the standard model predictions using proton collisions at 7 and 8 TeV*, Eur. Phys. J. **C75** (2015) 212, `arXiv:1412.8662`.

[16] K. L. Chan, U. Chattopadhyay, and P. Nath, *Naturalness, weak scale supersymmetry and the prospect for the observation of supersymmetry at the Tevatron and at the CERN LHC*, Phys. Rev. **D58** (1998) 096004, `arXiv:hep-ph/9710473`.

[17] G. Ross, *Grand Unified Theories*, Westview Press, Boulder, Colorado, USA, 2003.

[18] D. Gross, H. Politzer, and F. Wilczek, *The nobel prize in physics 2004 - popular information*, `https://www.nobelprize.org/nobel_prizes/physics/laureates/2004/popular.html`. Accessed: 12-04-2018.

[19] T. S. van Albada, J. N. Bahcall, K. Begeman, and R. Sancisi, *Distribution of dark matter in the spiral galaxy NGC 3198*, The Astrophysical Journal **295** (1985) 305.

[20] R. Massey, T. Kitching, and J. Richard, *The dark matter of gravitational lensing*, Rept. Prog. Phys. **73** (2010) 086901, `arXiv:1001.1739`.

[21] Planck collaboration, R. Adam *et al.*, *Planck 2015 results. I. Overview of products and scientific results*, Astron. Astrophys. **594** (2016) A1, `arXiv:1502.01582`.

[22] S. O. Bilson-Thompson, F. Markopoulou, and L. Smolin, *Quantum gravity and the standard model*, Class. Quant. Grav. **24** (2007) 3975, `arXiv:hep-th/0603022`.

[23] A. D. Sakharov, *Violation of CP Invariance, C asymmetry, and baryon asymmetry of the universe*, Pisma Zh. Eksp. Teor. Fiz. **5** (1967) 32, [Usp. Fiz. Nauk161,no.5,61(1991)].

[24] A. Hocker and Z. Ligeti, *CP violation and the CKM matrix*, Ann. Rev. Nucl. Part. Sci. **56** (2006) 501, `arXiv:hep-ph/0605217`.

[25] W. M. Alberico and S. M. Bilenky, *Neutrino oscillations, masses and mixing*, Phys. Part. Nucl. **35** (2004) 297, `arXiv:hep-ph/0306239`, [Fiz. Elem. Chast. Atom. Yadra35,545(2004)].

[26] A. Signer, *ABC of SUSY*, J. Phys. **G36** (2009) 073002, `arXiv:0905.4630`.

[27] S. P. Martin, *A supersymmetry primer*, Adv. Ser. Direct. High Energy Phys. **18** (1997) 1, `arXiv:hep-ph/9709356`.

[28] M. Mulders and G. Zanderighi, eds., *Proceedings, 2016 European School of High-Energy Physics (ESHEP2016)*, vol. 5 of *CERN Yellow Reports: School Proceedings*, (Geneva), CERN, CERN, 2017. doi: 10.23730/CYRSP-2017-005.

[29] Y. Shadmi, *Supersymmetry breaking*, in *Particle physics beyond the standard model. Proceedings, Summer School on Theoretical Physics, 84th Session, Les Houches, France, August 1-26, 2005*, pp. 147–180, 2006. `arXiv:hep-th/0601076`.

[30] C. Csaki, *The Minimal supersymmetric standard model (MSSM)*, Mod. Phys. Lett. **A11** (1996) 599, `arXiv:hep-ph/9606414`.

[31] A. Djouadi, *The anatomy of electroweak symmetry breaking Tome II: The Higgs bosons in the Minimal Supersymmetric Model*, Physics Reports **459** (2008) 1 .

[32] ATLAS and CMS collaborations, A. Ventura, *Searches for supersymmetry*, Int. J. Mod. Phys. Conf. Ser. **46** (2018) 1860006, `arXiv:1711.00152`.

[33] ATLAS collaboration, G. Aad *et al.*, *Search for direct production of charginos and neutralinos in events with three leptons and missing transverse momentum in $\sqrt{s} = 8TeV$ pp collisions with the ATLAS detector*, JHEP **04** (2014) 169, `arXiv:1402.7029`.

[34] ATLAS collaboration, G. Aad *et al.*, *Search for direct production of charginos, neutralinos and sleptons in final states with two leptons and missing transverse momentum in pp collisions at $\sqrt{s} = 8$ TeV with the ATLAS detector*, JHEP **05** (2014) 071, `arXiv:1403.5294`.

[35] CMS collaboration, V. Khachatryan *et al.*, *Searches for electroweak production of charginos, neutralinos, and sleptons decaying to leptons and W, Z, and Higgs bosons in pp collisions at 8 TeV*, Eur. Phys. J. **C74** (2014) 3036, `arXiv:1405.7570`.

[36] ATLAS collaboration, G. Aad *et al.*, *Search for direct production of charginos and neutralinos in events with three leptons and missing transverse momentum in $\sqrt{s} = 7$ TeV pp collisions with the ATLAS detector*, Phys. Lett. **B718** (2013) 841, `arXiv:1208.3144`.

[37] ATLAS Collaboration, *Search for squarks and gluinos in final states with jets and missing transverse momentum using 36 fb^1 of $\sqrt{s} = 13$ TeV pp collision data with the ATLAS detector*, Tech. Rep. ATLAS-CONF-2017-022, CERN, Geneva, Apr, 2017.

[38] L. Evans and P. Bryant, *LHC Machine*, JINST**3** (2008) S08001.

[39] CERN, *CERN timelines: The Large Hadron Collider*, `https://timeline.web.cern.ch/timelines/the-large-hadron-collider`. Accessed: 08.01.2018.

[40] CERN, *Longer term LHC schedule*, `https://lhc-commissioning.web.cern.ch/lhc-commissioning/schedule/lhc-long-term.htm`. Accessed: 08.01.2018.

[41] CERN, *TE-EPC-LPC in LHC*, `http://te-epc-lpc.web.cern.ch/te-epc-lpc/machines/lhc/general.stm`. Accessed: 10.12.2017.

[42] K. Wille, *The Physics of Particle Accelerators: An Introduction*, Oxford University Press, Oxford, 5, 2001.

[43] ALICE collaboration, *The ALICE experiment at the CERN LHC*, JINST**3** (2008) S08002.

[44] CMS collaboration, *The CMS experiment at the CERN LHC*, JINST**3** (2008) S08004.

[45] LHCb collaboration, *The lhcb detector at the LHC*, JINST **3** (2008) S08005.

[46] ATLAS collaboration, *Luminosity summary plots for 2015 pp data taking*, `https://twiki.cern.ch/twiki/bin/view/atlaspublic/` `luminositypublicresultsrun2#luminosity_summary_plots_for_an3`. accessed: 08.01.2018.

[47] ATLAS collaboration, *Luminosity summary plots for 2016 pp data taking*, `https://twiki.cern.ch/twiki/bin/view/atlaspublic/` `luminositypublicresultsrun2#luminosity_summary_plots_for_an1`. accessed: 08.01.2018.

[48] ATLAS collaboration, Z. Marshall, *Simulation of Pile-up in the ATLAS Experiment*, J. Phys. Conf. Ser. **513** (2014) 022024.

[49] ATLAS collaboration, *Luminosity Public Results*, `https://twiki.cern.` `ch/twiki/bin/view/atlaspublic/luminositypublicresults`. accessed: 08.01.2018.

[50] ATLAS collaboration, *Luminosity Public Results Run2*, `https://twiki.` `cern.ch/twiki/bin/view/atlaspublic/luminositypublicresultsrun2#` `2016_pp_collisions`. accessed: 08.01.2018.

[51] ATLAS collaboration, *The ATLAS Experiment at the CERN Large Hadron Collider*, JINST **3** (2008) S08003.

[52] J. Goodson, *Magnet systems*, `http://www.jetgoodson.com/images/` `thesisImages/magnetSystems.png`. Accessed: 10-05-2018.

[53] J. J. Peña, *Alignment of the ATLAS Inner Detector Upgraded for the LHC Run II*, J. Phys. Conf. Ser. **664** (2015) 072025.

[54] A. La Rosa, *The ATLAS Insertable B-Layer: from construction to operation*, JINST **11** (2016) C12036, `arXiv:1610.01994`.

[55] ATLAS collaboration, *ATLAS liquid-argon calorimeter: Technical Design Report*, Technical Design Report ATLAS, CERN, Geneva, 1996.

[56] L. Heinrich, *The ATLAS Trigger Core Configuration and Execution System in Light of the ATLAS Upgrade for LHC Run 2*, Tech. Rep. ATL-DAQ-PROC-2015-016. 8, CERN, Geneva, May, 2015.

[57] ATLAS collaboration, *Approved plots DAQ*, `https://twiki.cern.ch/twiki/` `bin/view/atlaspublic/approvedplotsdaq#plots_figures_pictures`. Accessed: 08.01.2018.

[58] ATLAS collaboration, *Performance of the atlas trigger system in 2015*, The European Physical Journal C **77** (2017) 317.

[59] ATLAS collaboration, W. Panduro Vazquez, *The ATLAS Data Acquisition System: from Run 1 to Run 2*, Nucl. Part. Phys. Proc. **273-275** (2016) 939.

[60] ATLAS collaboration, N. Ilic, *The ATLAS Fast Tracker and Tracking at the High-Luminosity LHC*, JINST **12** (2017) C02052.

[61] M. Elsing, L. Goossens, A. Nairz, and G. Negri, *The ATLAS Tier-0: Overview and operational experience*, J. Phys. Conf. Ser. **219** (2010) 072011.

[62] M. C. Aleksa *et al.*, *ATLAS Liquid Argon Calorimeter Phase-I Upgrade Technical Design Report*, Tech. Rep. CERN-LHCC-2013-017. ATLAS-TDR-022, Sep, 2013. Final version presented to December 2013 LHCC.

[63] G. Barrand *et al.*, *GAUDI - A software architecture and framework for building HEP data processing applications*, Comput. Phys. Commun. **140** (2001) 45.

[64] A. Buckley *et al.*, *General-purpose event generators for LHC physics*, Phys. Rept. **504** (2011) 145, `arXiv:1101.2599`.

[65] Y. L. Dokshitzer, *Calculation of the Structure Functions for Deep Inelastic Scattering and e^+e^- Annihilation by Perturbation Theory in Quantum Chromodynamics.*, Sov. Phys. JETP **46** (1977) 641.

[66] V. N. Gribov and L. N. Lipatov, *Deep inelastic ep scattering in perturbation theory*, Sov. J. Nucl. Phys. **15** (1972) 438.

[67] G. Altarelli and G. Parisi, *Asymptotic Freedom in Parton Language*, Nucl. Phys. **B126** (1977) 298.

[68] H.-L. Lai *et al.*, *New parton distributions for collider physics*, Phys. Rev. **D82** (2010) 074024, `arXiv:1007.2241`.

[69] NNPDF, R. D. Ball *et al.*, *Parton distributions for the LHC Run II*, JHEP **04** (2015) 040, `arXiv:1410.8849`.

[70] J. H. Kuhn, S. Moch, A. A. Penin, and V. A. Smirnov, *Next-to-next-to-leading logarithms in four fermion electroweak processes at high-energy*, Nucl. Phys. **B616** (2001) 286, `arXiv:hep-ph/0106298`, [Erratum: Nucl. Phys.B648,455(2003)].

[71] *The cambridge dictionary of statistics (2nd ed.)*, Reference Reviews **17** (2003) 29, `arXiv:https://doi.org/10.1108/09504120310455993`.

[72] S. Catani, F. Krauss, R. Kuhn, and B. R. Webber, *QCD matrix elements + parton showers*, JHEP **11** (2001) 063, `arXiv:hep-ph/0109231`.

[73] M. L. Mangano, M. Moretti, and R. Pittau, *Multijet matrix elements and shower evolution in hadronic collisions: $Wb\bar{b} + n$ jets as a case study*, Nucl. Phys. **B632** (2002) 343, `arXiv:hep-ph/0108069`.

[74] A. Kupco, *Cluster hadronization in HERWIG 5.9*, in *Monte Carlo generators for HERA physics. Proceedings, Workshop, Hamburg, Germany, 1998-1999*, pp. 292–300, 1998. `arXiv:hep-ph/9906412`.

[75] B. Andersson, S. Mohanty, and F. Soderberg, *Recent developments in the Lund model*, in *36th Annual Winter School on Nuclear and Particle Physics (PINP 2002) and 8th St. Petersburg School on Theoretical Physics St. Petersburg, Russia, February 25-March 3, 2002*, 2002. `arXiv:hep-ph/0212122`.

[76] P. Z. Skands, *Tuning Monte Carlo Generators: The Perugia Tunes*, Phys. Rev. **D82** (2010) 074018, `arXiv:1005.3457`.

[77] T. Sjöstrand, S. Mrenna, and P. Z. Skands, *A Brief Introduction to PYTHIA 8.1*, Comput. Phys. Commun. **178** (2008) 852, `arXiv:0710.3820`.

[78] M. Bahr *et al.*, *Herwig++ Physics and Manual*, Eur. Phys. J. C **58** (2008) 639, `arXiv:0803.0883`.

[79] T. Gleisberg *et al.*, *Event generation with sherpa 1.1*, Journal of High Energy Physics **2009** (2009) 007.

[80] F. Maltoni and T. Stelzer, *MadEvent: Automatic event generation with Mad-Graph*, JHEP **02** (2003) 027, `arXiv:hep-ph/0208156`.

[81] S. Alioli, P. Nason, C. Oleari, and E. Re, *A general framework for implementing NLO calculations in shower Monte Carlo programs: the POWHEG BOX*, JHEP **06** (2010) 043, `arXiv:1002.2581`.

[82] S. Frixione and B. R. Webber, *Matching NLO QCD computations and parton shower simulations*, JHEP **06** (2002) 029, `arXiv:hep-ph/0204244`.

[83] D. J. Lange, *The EvtGen particle decay simulation package*, Nucl. Instrum. Meth. A **462** (2001) 152.

[84] M. Dobbs and J. B. Hansen, *The HepMC C++ Monte Carlo event record for High Energy Physics*, Comput. Phys. Commun. **134** (2001) 41.

[85] Geant4 collaboration, J. Allison *et al.*, *Geant4 developments and applications*, IEEE Trans. Nucl. Sci. **53** (2006) 270; Geant4 collaboration, S. Agostinelli *et al.*, *Geant4: A simulation toolkit*, Nucl. Instrum. Meth. **A506** (2003) 250.

[86] ATLAS collaboration, W. Lukas, *Fast Simulation for ATLAS: Atlfast-II and ISF*, J. Phys. Conf. Ser. **396** (2012) 022031.

[87] ATLAS, T. Yamanaka, *The ATLAS calorimeter simulation FastCaloSim*, J. Phys. Conf. Ser. **331** (2011) 032053.

[88] L. R. F. Castillo, *The ATLAS and CMS detectors*, in *The Search and Discovery of the Higgs Boson*, 2053-2571, pp. 4–1 to 4–8. Morgan and Claypool Publishers, 2015. doi: 10.1088/978-1-6817-4078-2ch4.

[89] ATLAS collaboration, M. Aaboud *et al.*, *Reconstruction of primary vertices at the ATLAS experiment in Run 1 protonproton collisions at the LHC*, Eur. Phys. J. **C77** (2017), no. 5 332, `arXiv:1611.10235`.

[90] R. Fruhwirth, *Application of Kalman filtering to track and vertex fitting*, Nucl. Instrum. Meth. **A262** (1987) 444.

[91] ATLAS collaboration, M. Aaboud *et al.*, *Electron efficiency measurements with the ATLAS detector using 2012 LHC protonproton collision data*, Eur. Phys. J. **C77** (2017) 195, `arXiv:1612.01456`.

[92] ATLAS collaboration, G. Aad *et al.*, *Electron performance measurements with the ATLAS detector using the 2010 LHC proton-proton collision data*, Eur. Phys. J. **C72** (2012) 1909, `arXiv:1110.3174`.

[93] ATLAS collaboration, G. Aad *et al.*, *Expected Performance of the ATLAS Experiment - Detector, Trigger and Physics*, `arXiv:0901.0512`.

[94] W. Lampl *et al.*, *Calorimeter Clustering Algorithms: Description and Performance*, Tech. Rep. ATL-LARG-PUB-2008-002. ATL-COM-LARG-2008-003, CERN, Geneva, Apr, 2008.

[95] ATLAS collaboration, *Electron efficiency measurements with the atlas detector using the 2015 lhc proton-proton collision data*, `https://atlas.web.cern.ch/Atlas/GROUPS/PHYSICS/CONFNOTES/ATLAS-CONF-2016-024/`. Accessed: 10-05-2018.

[96] ATLAS collaboration, *Electron reconstruction and identification efficiency measurements in 2016 data*, `https://atlas.web.cern.ch/Atlas/GROUPS/PHYSICS/PLOTS/EGAM-2017-003/index.html`. Accessed: 10-05-2018.

[97] ATLAS collaboration, G. Aad *et al.*, *Muon reconstruction performance of the ATLAS detector in protonproton collision data at $\sqrt{s}$ =13 TeV*, Eur. Phys. J. **C76** (2016) 292, `arXiv:1603.05598`.

[98] ATLAS collaboration, B. Resende, *Muon identification algorithms in ATLAS*, PoS **EPS-HEP2009** (2009) 431.

[99] R. Nicolaidou *et al.*, *Muon identification procedure for the atlas detector at the lhc using muonboy reconstruction package and tests of its performance using cosmic rays and single beam data*, Journal of Physics: Conference Series **219** (2010) 032052.

[100] ATLAS collaboration, *Atlas muon combined performance with the full 2016 dataset*, `https://atlas.web.cern.ch/Atlas/GROUPS/PHYSICS/PLOTS/MUON-2017-001/index.html`. Accessed: 10-05-2018.

[101] A. Hrynevich, *Atlas jet and missing energy reconstruction, calibration and performance in lhc run-2*, Journal of Instrumentation **12** (2017) C06038.

[102] M. Cacciari, G. P. Salam, and G. Soyez, *The Anti-k(t) jet clustering algorithm*, JHEP **04** (2008) 063, `arXiv:0802.1189`.

[103] ATLAS collaboration, *Forward Jet Vertex Tagging: A new technique for the identification and rejection of forward pileup jets*, Tech. Rep. ATL-PHYS-PUB-2015-034, CERN, Geneva, Aug, 2015.

[104] N. Bartosik, *Diagram showing the common principle of identification of jets initiated by b-hadron decays*, `http://bartosik.pp.ua/hep_sketches/btagging`. Accessed: 01.02.2018.

[105] ATLAS collaboration, A. Calandri, *Flavour tagging algorithms and performance at the ATLAS experiment*, PoS **LHCP2016** (2016) 180.

[106] ATLAS collaboration, *Optimisation of the ATLAS b-tagging performance for the 2016 LHC Run*, Tech. Rep. ATL-PHYS-PUB-2016-012, CERN, Geneva, Jun, 2016.

[107] ATLAS collaboration, C. F. Galea, *Tau Lepton Reconstruction in ATLAS*, Nucl. Part. Phys. Proc. **287-288** (2017) 111.

[108] ATLAS collaboration, G. Aad *et al.*, *Reconstruction of hadronic decay products of tau leptons with the ATLAS experiment*, Eur. Phys. J. **C76** (2016) 295, `arXiv:1512.05955`.

[109] ATLAS collaboration, A. Hrynevich, *ATLAS jet and missing energy reconstruction, calibration and performance in LHC Run-2*, JINST **12** (2017) C06038.

[110] L. March, *Performance of missing transverse momentum reconstruction in ATLAS studied in proton-proton collisions in 2012 at 8 TeV*, Journal of Physics: Conference Series **645** (2015) 012014.

[111] ATLAS collaboration, G. Aad *et al.*, *Performance of Missing Transverse Momentum Reconstruction in Proton-Proton Collisions at 7 TeV with ATLAS*, Eur. Phys. J. **C72** (2012) 1844, `arXiv:1108.5602`.

[112] ATLAS collaboration, M. Aaboud *et al.*, *Search for squarks and gluinos in events with hadronically decaying tau leptons, jets and missing transverse momentum in protonproton collisions at $\sqrt{s} = 13$ TeV recorded with the ATLAS detector*, Eur. Phys. J. **C76** (2016) 683, `arXiv:1607.05979`.

[113] P. Laycock *et al.*, *Atlas data preparation in run 2*, Journal of Physics: Conference Series **898** (2017), no. 4 042050.

[114] ATLAS collaboration, *Search for supersymmetry with two and three leptons and missing transverse momentum in the final state at $\sqrt{s}$=13 TeV with the ATLAS detector*, Tech. Rep. ATLAS-CONF-2016-096, CERN, Geneva, 2016.

[115] ATLAS collaboration, M. Aaboud *et al.*, *Search for electroweak production of supersymmetric particles in final states with two or three leptons at $\sqrt{s} = 13$ TeV with the ATLAS detector*, `arXiv:1803.02762`.

[116] ATLAS collaboration, G. Aad *et al.*, *Performance of b-Jet Identification in the ATLAS Experiment*, JINST **11** (2016) P04008, `arXiv:1512.01094`.

[117] ATLAS collaboration, G. Aad *et al.*, *Electron reconstruction and identification efficiency measurements with the ATLAS detector using the 2011 LHC proton-proton collision data*, Eur. Phys. J. **C74** (2014) 2941, `arXiv:1404.2240`.

[118] ATLAS collaboration, *Electron efficiency measurements with the ATLAS detector using the 2015 LHC proton-proton collision data*, Tech. Rep. ATLAS-CONF-2016-024, CERN, Geneva, 2016.

[119] CERN, *Root data analysis framework*, `https://root.cern.ch`. Accessed: 17-04-2018.

[120] L. Moneta, K. Cranmer, G. Schott, and W. Verkerke, *The RooStats project*, in *Proceedings of the 13th International Workshop on Advanced Computing and Analysis Techniques in Physics Research. February 22-27, 2010, Jaipur, India*, p. 57, 2010. `arXiv:1009.1003`.

[121] J. M. Lorenz *et al.*, *HistFitter - A flexible framework for statistical data analysis*, J. Phys. Conf. Ser. **608** (2015) 012049.

[122] ATLAS collaboration, G. Aad *et al.*, *Jet energy resolution in proton-proton collisions at $\sqrt{s} = 7$ TeV recorded in 2010 with the ATLAS detector*, Eur. Phys. J. **C73** (2013) 2306, `arXiv:1210.6210`.

[123] ATLAS collaboration, *Jet energy scale and its systematic uncertainty in proton-proton collisions at sqrt(s)=7 TeV with ATLAS 2011 data*, Tech. Rep. ATLAS-CONF-2013-004, CERN, Geneva, Jan, 2013.

[124] ATLAS collaboration, *Performance of b-jet identification in the ATLAS experiment*, Journal of Instrumentation **11** (2016) P04008.

[125] ATLAS collaboration, *Calibration of b-tagging using dileptonic top pair events in a combinatorial likelihood approach with the ATLAS experiment*, Tech. Rep. ATLAS-CONF-2014-004, CERN, Geneva, Feb, 2014.

[126] ATLAS collaboration, *Tagging and suppression of pileup jets*, Tech. Rep. ATLAS-CONF-2014-018, CERN, Geneva, 2014.

[127] ATLAS collaboration, M. Aaboud *et al.*, *Performance of missing transverse momentum reconstruction with the ATLAS detector using proton-proton collisions at $\sqrt{s} = 13$ TeV*, `arXiv:1802.08168`.

[128] G. Aad *et al.*, *Electron performance measurements with the atlas detector using the 2010 lhc proton-proton collision data*, The European Physical Journal C **72** (2012) 1909.

[129] ATLAS collaboration, G. Aad *et al.*, *Electron and photon energy calibration with the atlas detector using lhc run 1 data*, The European Physical Journal C **74** (2014) 3071.

[130] M. Baak *et al.*, *HistFitter software framework for statistical data analysis*, Eur. Phys. J. **C75** (2015) 153, `arXiv:1410.1280`.

[131] G. Cowan, K. Cranmer, E. Gross, and O. Vitells, *Asymptotic formulae for likelihood-based tests of new physics*, Eur. Phys. J. **C71** (2011) 1554, `arXiv:1007.1727`, [Erratum: Eur. Phys. J.C73,2501(2013)].

[132] O. Behnke, K. Kröninger, T. Schörner-Sadenius, and G. Schott, eds., *Data analysis in high energy physics*, Wiley-VCH, Weinheim, Germany, 2013.

[133] A. L. Read, *Presentation of search results: the cl_s technique*, Journal of Physics G: Nuclear and Particle Physics **28** (2002) 2693.

[134] ATLAS collaboration, G. Aad, B. Abbott, and Abdallah, *Search for the electroweak production of supersymmetric particles in $\sqrt{s} = 8$ TeV pp collisions with the atlas detector*, Phys. Rev. D **93** (2016) 052002.

[135] R. Keyes and A. Collaboration, *Development, validation and integration of the atlas trigger system software in run 2*, Journal of Physics: Conference Series **898** (2017) 032008.

[136] A. Undrus, *Evolution of the ATLAS Nightly Build System*, Journal of Physics: Conference Series **396** (2012) 052070.

[137] ATLAS collaboration, *The Run Time Tester User Guide*, `https://atlas-rtt.cern.ch/prod/docs/userguide/`. Accessed: 17-04-2018.

[138] ATLAS collaboration, G. Aad *et al.*, *Measurement of the $t\bar{t}W$ and $t\bar{t}Z$ production cross sections in pp collisions at $\sqrt{s} =8$ TeV with the ATLAS detector*, Journal of High Energy Physics **2015** (2015) 172.

[139] S. Frixione *et al.*, *Electroweak and QCD corrections to top-pair hadroproduction in association with heavy bosons*, Journal of High Energy Physics **2015** (2015) 184.

[140] ATLAS collaboration, M. Aaboud *et al.*, *Measurement of the $t\bar{t}W$ and $t\bar{t}Z$ production cross sections in multiple final states using $3.2fb^{-1}$ of pp collisions at $\sqrt{s} =13$ TeV with the ATLAS detector*, Journal of High Energy Physics **77** (2017) 40.